Discontinuities in materials and structures

A unifying computational approach

DISCONTINUITIES IN MATERIALS AND STRUCTURES

A UNIFYING COMPUTATIONAL APPROACH

PROEFSCHRIFT

ter verkrijging van de graad van doctor
aan de Technische Universiteit Delft,
op gezag van de Rector Magnificus prof. dr. ir. J.T. Fokkema,
voorzitter van het College voor Promoties,
in het openbaar te verdedigen op woensdag 25 oktober 2006 om 10.00 uur

door

Joris Johannes Cornelis REMMERS

ingenieur luchtvaart en ruimtevaart

geboren te Tilburg

DIT PROEFSCHRIFT IS GOEDGEKEURD DOOR DE PROMOTOREN:

Prof. dr. ir. R. de Borst
Prof. dr. A. Needleman

SAMENSTELLING PROMOTIECOMMISSIE:

Rector Magnificus	Voorzitter
Prof. dr. ir. R. de Borst	Technische Universiteit Delft, promotor
Prof. dr. A. Needleman	Brown University, promotor
Prof. dr. O. Allix	École Normale Supérieure de Cachan
Prof. dr. ir. M.G.D. Geers	Technische Universiteit Eindhoven
Prof. dr. ir. A. de Boer	Universiteit Twente
Prof. dr. ir. F. van Keulen	Technische Universiteit Delft
Dr. V.S. Deshpande	Cambridge University

KEYWORDS:

Cohesive zone modelling, partition of unity method, delamination, dynamic crack growth, discrete dislocation analysis.

Cover design: Martijn de Kock

Cover image: Bernard Frize
"Boswell" 2001
Acrylic and resin on canvas
180 × 120 cm
Used with permission

Copyright © 2006 by Joris J.C. Remmers

Printed in The Netherlands by PrintPartners Ipskamp
ISBN-10: 90-9021094-6
ISBN-13: 978-90-9021094-0

Foreword

In 1997 the Board of Delft University of Technology initiated a university wide research programme by the name of DIOC (a Dutch acronym for 'Delft Interfacultary Research Centres') in order to encourage multidisciplinary research activities. One of the 17 programmes that was approved was 'Reliability of Materials and Constructions' which became known as DIOC 10. The programme focused on studies to investigate the reliability of structural materials, such as concrete and fibre-metal laminates. The individual research projects within DIOC 10 were of both experimental and analytical nature.

The project I was involved in was entitled 'Delamination Buckling in Glare' and was in a way intended as a follow-up of the PhD project of Frank Hashagen. Whereas Hashagen's study focused on the development of numerical techniques to model failure mechanisms in laminates, my research aimed at applying and, if necessary, extending these techniques to analyse material failure in combination with the loss of structural stability of laminated materials.

It appeared to be a highly topical subject. Glare was on the verge to be selected as the main material for the skin of the fuselage of Airbus A380 aeroplane. An important factor in the decision making process was the residual strength of the material under different circumstances. The stability of panels with initial delaminations that are subjected to compressive or shear loads was one of the cases under investigation.

The numerical models as developed by Frank Hashagen could be used with hardly any modifications. The first results showed that delamination growth in combination with local buckling did not appear to be a problem for a fibre-metal laminate like Glare. Conclusions that were confirmed by a large number of experimental observations by other people.

The next step in the project was to optimise the numerical model in such a way that it could be used for a detailed failure analysis of large panels. This new model was based on a novel technique for the simulation of crack growth, the partition of unity method. Indeed, the new model appeared to be very efficient. Encouraged by these results, it was decided to use the approach to analyse different failure mechanism on different levels of observation. The development of these models forms the basis of this thesis.

I have been fortunate for having two excellent researchers as thesis advisers. I would like to express my appreciation to René de Borst for his excellent support and guidance, for giving me the opportunity to chart my own course and for sharing his expertise whenever I encountered problems. I am also much indebted to Alan Needleman for inviting me to work with him in Providence. His sparkling enthusiasm encouraged me to further develop the models and explore new areas.

Partition of unity based models can only be implemented in a flexible numerical framework. Most of the models in this thesis have been programmed using the Jem/Jive finite element toolkit which has been developed by Habanera. In particular, I would like to thank Erik-Jan Lingen for designing and supporting this magnificent piece of software. Many thanks go to Garth Wells for introducing me to the basic concepts of the partition of unity approach to cohesive fracture. Miguel Gutiérrez and Clemens Verhoosel are acknowledged for the useful discussions that helped me to implement and fine-tune the energy release control path-following method.

The development of the cohesive segments method led to a collaborative research project in the field of finite strain discrete dislocation analysis. I am most grateful to Vikram Deshpande for inviting me at Cambridge University to work on this new model and I thank the British Council - NWO Partnership Programme in Science for the financial support. Carlos Dávila is acknowledged for inviting me at NASA Langley Research Center to work on fracture in fibre reinforced composites. Many thanks go to Frank Hashagen for writing an excellent thesis that served as a source of inspiration.

A word of appreciation for the members of the DIOC 10 group for their role as a sounding board during the early stages of my research. In particular, I would like to thank scientific director Sybrand van der Zwaag, project leaders Fred van Keulen, Jan van Mier, Erik van der Giessen and Ad Vlot and my

fellow Ph.D. students Michiel Hagenbeek, Carel ten Horn, Jan Bisschop and Arjan Woerden. I am grateful to Eduard Riks for encouraging me to continue my education as a Ph.D. candidate.

This work could not have been completed without the help of a number of people that made sure that all the paperwork was done correctly and the computers were running. In particular, I would like to thank Carla Roovers and Harold Thung at Delft University of Technology and Pat Capece at Brown University.

Finally, I would like to thank all my colleagues who have contributed by means of fruitful discussions, useful comments and, most important, by providing a pleasant working atmosphere: Ido Akkerman, Amine Benzerga, Henk de Boer, Harald van Brummelen, Pedro Camanho, Dominique Chamoret, Doo-Bo Chung, Marcela Cid, Demir Coker, Elena Correa, Otto Heeres, Thomas Hettich, Thomas Hille, Steve Hulshoff, Eelco Jansen, Bart Koene, Ellen Kuhl, Claudio Lopes, Juliana Lopez de la Cruz, Akihiro Matsuda, Christian Michler, Edwin Munts, Marco Nawijn, Julien Réthoré, Reinout van Rooijen, Gillian Saunders-Smits, Edwin Schimmel, Ingrid Schipperen, Alexander Schmetz, Jingyi Shi, Angelo Simone, Bert Sluys, Felicia Stan, Martijn Stroeven, Akke Suiker, Martin Tijssens, Denny Tjahjanto, Albert Turon, Sergio Turteltaub, André Vaders, Tjerk de Vries and Kris van der Zee.

Joris Remmers

Delft, July 2006

Voor Irene en Luc

Contents

Chapter 1

Introduction

Our modern society is completely dominated by mechanical systems and installations. We are protected from floods by civil works such as dams; we use electricity generated by plants and distributed via power lines; we travel on aeroplanes or high speed trains and our communications rely on a network of satellites. If one or more of these systems fail, it will at least disturb our common life. In some circumstances however, it can cause environmental or financial damage, for example in the case of an accident with an oil tanker. The worst case scenario is the failure of critical systems such as dams or large industrial installations in densely populated areas which could possibly result in a large number of casualties.

In order to reduce the probability of failure to an absolute minimum, structures and installations are designed in such a way that, for a given spectrum of expected external loads, no critical damage is suffered. The possibility of damage due to unexpected loading situations, such as extreme gust loads on an aircraft, is prevented by using *safety factors*. The load carrying components of a structure are deliberately designed in such a way that they are stronger than necessary in order to withstand extreme loads. In addition, the safety factor is further increased to compensate for possible material flaws or initial damage in the structure introduced during the production phase.

The use of large safety factors has a significant drawback. Overdimensioning of a structure will restrict its applicability. The possible span of a bridge for example is reduced when the roadway is too thick and too heavy. Apart from that, overdimensioning will irrevocably result in an increase in maintenance and operating costs. These considerations play an important role in the

design of aeroplanes, where every kilogramme that can be gained will save a few litres of kerosene per flight.

The magnitude of safety factors is always a compromise between safety on one hand and economical considerations on the other hand. In the design of civil structures such as bridges, a safety factor around 2.5 is generally used for the most important load carrying parts. When saving weight is a primary goal, for example in the aerospace or automotive industry, safety factors as low as 1.4 are not uncommon. But for nuclear power plants, where safety is of the utmost importance, the most critical parts in the structure, the foundation and the concrete dome that covers the reactor, can be dimensioned with a safety factor as high as 50.0.

A better understanding of the behaviour of materials under high external loads can increase the efficiency of the designs of these structures, without indulging the safety requirements. Therefore, the study of failure mechanisms in engineering materials has become an important part in the design process. Not only the onset of the first damage in a material is analysed, the complete evolution of the fracture process is investigated as well, in order to predict its residual strength and the probability of total failure of the structure.

In this chapter, we will have a closer look at some aspects of fracture mechanisms in materials and we will discuss a number of numerical techniques to model these mechanisms.

§ 1.1 The physics of fracture

From a mechanical point of view, fracture can be described by a number of successive events. The first onset to fracture is the nucleation of micro-separations in a small area around an existing dominant crack, notch or cut-out, the *process zone*, see Figure 1.1. These micro-separations can be considered as small cracks in the micro-structure of the material. They generally nucleate at inhomogeneities such as a cavity or a phase boundary: places where the stresses are high and the inter-atomic bonds are relatively weak. Alternatively, micro-separations can nucleate at imperfections at the free surface of the specimen. These free surface sites play a key role in stress corrosion cracking and fatigue failure in crystalline solids, such as metals and silicon based semi-conductors.

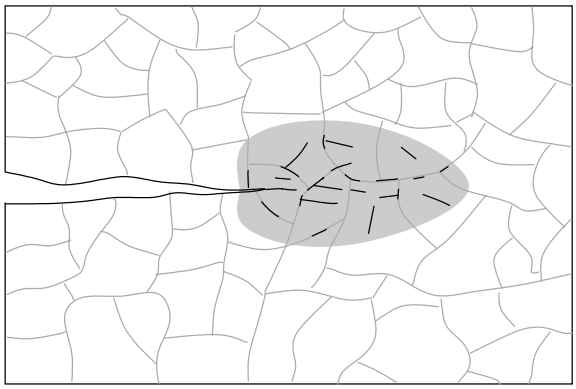

Figure 1.1 Simplified representation of a granular material with an initial crack and process zone (shaded area) with micro-separations.

The nucleation of these micro-separations is an irreversible process, which reduces the strength and the stiffness of the material. It is accompanied by the dissipation of energy through plastic deformation of the surrounding bulk material and the production of heat by means of friction. When the applied load is removed, the micro-separations remain and the structure shows permanent deformations. When the applied load is increased, the existing micro-separations can grow and coalesce forming larger defects, which can become visible for the naked eye. These defects give rise to even higher stress concentrations in the structure. This, in combination with the reduced strength and stiffness of the material, preludes the final failure of the structure.

The evolution from micro-separations to final failure is different for each material type. An important factor is the nature of the micro-structure of the material, or more precisely, the homogeneity of the material and the amount of initial defects (Broberg 1999). A good example of a class of homogeneous materials are ceramics, where the dominating micro-structure consists of atoms that are mutually tied by sharing electrons. The nature of such a bond is extremely rigid. In the special case that the atomic structure is regular, without inhomogeneities or imperfections, for example in materials as quartz or diamond, there are hardly any sources for the nucleation of micro-separations away from the existing crack tip. As a result, the size of the process zone in these materials is of the order of magnitude of the inter-atomic distance and the final crack, if it can be created at all, is extremely sharp.

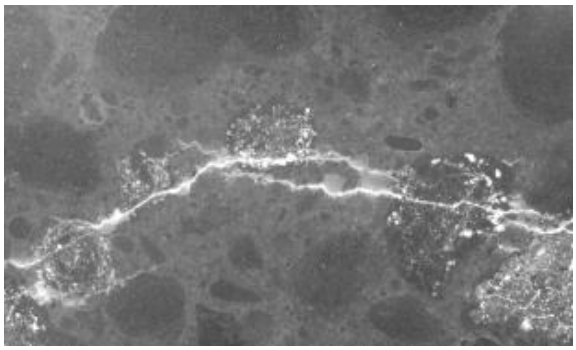

Figure 1.2 Diffuse crack pattern in concrete (Van Mier 1997).

On the other end of the spectrum we find heterogeneous materials such as concrete. This material is composed of hardened cement paste with aggregates of various dimensions and shapes. Due to the differences in stiffnesses and cohesive strengths of the two ingredients, there are many possible sources for the nucleation of micro-separations. Moreover, concrete can contain a large number of initial micro-cracks due to drying shrinkage (Bisschop 2002). It may be obvious that the process zone of this material is relatively wide and the final crack pattern diffuse, as shown in Figure 1.2 (van Mier 1997).

Loading conditions also play an important role in the failure process. Crystalline solids such as metals show a different fracture behaviour under monotonic loading than under repeated (or cyclic) loading. In the latter case, the ultimate load that leads to total failure appears to be much smaller than in the monotonic loading case, a phenomenon that is often referred to as fatigue fracture. Again, this can be explained by investigating the processes in the micro-structure of these materials. Here, the governing process is the creation of micro-slip planes due to collective motion of dislocations, i.e. vacancies in the atomic grid of the material. In the case of cyclic loading, the slip planes created by dislocation-glide in opposite directions give rise to larger imperfections at the free surfaces and therefore a different fracture behaviour at lower external loads.

Finally, environmental conditions can influence the fracture process as well. Aggressive environments such as salt water can accelerate the fracture process in metals at relatively small load levels, a process known as stress-corrosion. Another example is the effect of temperature changes on the failure behaviour

of composite materials such as carbon fibre reinforced plastics. Elevated temperatures can decrease the strength of the adhesive bond between the epoxy and the fibres, which may lead to fibre pull-out or delamination.

§ 1.2 Modelling fracture

Regardless of the micro-structure of the material, the loading state and the environmental conditions, the complete fracture process can be summarised as the nucleation, growth and coalescence of small cracks or slip systems, or more general, discontinuities in the material. In classical mechanical models however, the material is modelled as a continuum. This means that (i) it completely fills the space that it occupies, leaving no pores or empty spaces and (ii) its properties are described by continuous functions (Malvern 1969). It may be obvious that this assumption does not allow the incorporation of detailed information on the micro-structure of the material with its initial imperfections, not to mention the nucleation and coalescence of the micro-separations in the process zone.

Instead of modelling the complete micro-structure and each individual micro-separation, the most common approach is to lump the effects of all micro-separations in the process zone in one single model that governs the propagation of a single dominant crack. Such a model should preferably take into account the following two important properties of the fracture process. First, the stiffness and the strength of the material must be reduced in a realistic way and secondly, this reduction of stiffness and strength must be accompanied by the correct reduction of internal energy in the material.

In early mechanical models, the propagation of a single crack in elastic solids was simulated using the theorem of minimum energy. Griffith (1920) assumed that a crack, which can be modelled as a discontinuity in a smooth displacement field, is only allowed to propagate over a certain length when the surface energy in the structure equals the energy needed for the micro-separations in the process zone to nucleate and grow. The motivation to use this energy criterion instead of the more obvious notion of maximum tensile stress was based on the work of Inglis (1913), who had demonstrated that in a linear elastic mechanical model, the stresses in the vicinity of a sharp notch are unbounded and therefore useless for the determination of crack growth.

Griffith's theory was extended for ductile materials by Irwin (1957) who included small-scale yielding near the crack tip and introduced the concept of stress intensity factors in relation to the energy release rate in order to qualify the stress conditions around the crack tip.

The generalisation of Griffith's work for application to elastic-plastic solids (Rice 1968) and the use of the method in combination with the finite element method, has led to a powerful tool for the simulation of crack growth, often denoted as linear elastic fracture mechanics (LEFM). Despite the successful application in a variety of engineering problems, the method has a number of drawbacks. First, since the phenomena in the process zone are lumped in a single point at the current tip of the crack, the method can only be used in those cases where the process zone is relatively small. Second, the method does not allow for the nucleation of a crack in undamaged material away from a dominant flaw. And finally, the procedure that determines the direction of the crack propagation has never been truly incorporated into the finite element model. Instead, the results of the finite element calculations serve as an input for the prediction of the new crack path and vice versa (Ingraffea and Saouma 1985, Knops 1994). This means that when the crack is extended, the elements in the vicinity of the crack tip need remeshing, a procedure that limits the applicability of LEFM.

On the other hand, the rise of the finite element method in mechanical engineering marked the development of completely new techniques for the simulation of fracture, commonly denoted as nonlinear theories. Over the years, two trends can be distinguished, the *smeared* or *continuous* approach and the *discrete* or *discontinuous* approach.

The smeared approach

The smeared approach to fracture stems from the idea that the micro-mechanical phenomena in the vicinity of an integration point in the finite element model are translated into deterioration of the stiffness and the strength of the material in this point. Initially, the material properties in all integration points in the model are assumed to be linear elastic. When an equivalent stress in an integration point satisfies a specified criterion, e.g. the principal stress exceeds

a yield limit, the linear elastic stress-strain relation is changed.* Total failure of the structure is reached when the stiffness in the material is reduced to zero. Although the global behaviour of the model is in agreement with reality, from a structural point of view, a real crack is never really introduced in the model: neither as a discontinuity in the displacement field, nor as the introduction of a separation in the finite element mesh.

In early studies, the stiffness parameters in the direction tangential to the crack were set to zero (Rashid 1968, Cope *et al.* 1980). It was soon realised that a gradual decrease of the stiffness parameters was needed for a more realistic mechanical behaviour. This is for instance accomplished in continuum damage models where the stiffness of the material point is decreased by means of a damage parameter or damage tensor (Lemaitre and Chaboche 1990). Initially, when the material is completely intact, this damage parameter is equal to zero. As soon as the stress state in a material point exceeds a threshold value, the damage parameter is increased according to a material specific damage law that describes the release of internal energy during the damage process. The maximum value of the damage parameter is equal to 1.0, which corresponds to the situation that the material has completely lost its load carrying capability. The method has become a standard technique for the simulation of fracture and has been used successfully in a variety of applications, e.g. (Mazars 1984, Mazars and Pijaudier-Cabot 1989).

Instead of the creation of a real crack in the material (a discontinuity in the displacement field), the deformations in the process zone will localise and give rise to large deformation gradients in a narrow band in the process zone, which eventually causes numerical problems. Moreover, the width of this band must be at least equal to the width of a specific element in the finite element mesh. Clearly, this imposes serious limitations to the applicability of the method to materials with relatively small process zones. In order to avoid these problems, models have been developed where the large deformation gradient is incorporated in the kinematic relation of the element as an additional strain field. These models are commonly denoted as *embedded discontinuity approaches* (Ortiz *et al.* 1987, Belytschko *et al.* 1988, Simo *et al.* 1993). In-

*The smeared or continuous crack models are members of a much larger family of nonlinear material relations, such as plasticity models. In this section, we will confine attention to those models that eventually simulate total failure of the material.

deed, these approaches enhance the deformational capabilities of the element, but often at the expense of obtaining a non-symmetric (and computationally expensive) stiffness matrix. Furthermore, a true discontinuity is not obtained because the kinematics of the embedded crack band are diffused over the element.

Unfortunately, all previously described models suffer from an additional deficiency. Since the material is considered to be homogeneous, the models fail to describe the correct width of the process zone. Instead, all damage tends to concentrate in a single material point. Since this problem is related to the mathematical formulation of the model, numerical remedies such as mesh-refinement or the aforementioned embedded discontinuity approaches do not offer a solution. Instead, the underlying model must be improved.

Strategies that try to incorporate some information of the micro-structure in the continuum are normally denoted by the term *regularisation models*. An important class of such strategies includes higher order derivatives of the displacement field in the kinematic model (de Borst and Muhlhaus 1992). In the context of damage models, nonlocal models in an integral format (Pijaudier-Cabot and Bažant 1987) or in a differential format (Peerlings *et al.* 1996, Peerlings *et al.* 1998) have been proposed. Anisotropic versions of gradient models have been published as well (Kuhl *et al.* 2000). In all models, the strain term is extended with a higher order derivative (the so-called nonlocal strain), usually by deriving a set of Helmholtz equations. An additional parameter determines the slope of this decaying second order strain term, which sets the length scale that is related to the homogeneity of the material.

Although these formulations adequately repair the loss of well-posedness of the incremental boundary value problem, the application in engineering practice is somewhat limited. This is partly the result of the ongoing discussions on the kind of boundary conditions, which should be adopted for the higher order strain terms, and is partly due to the difficulties in determining the aforementioned nonlocal parameter.

Discrete fracture models

In order to model fracture in materials where the process zone is relatively narrow compared to the structural dimensions, a different class of techniques

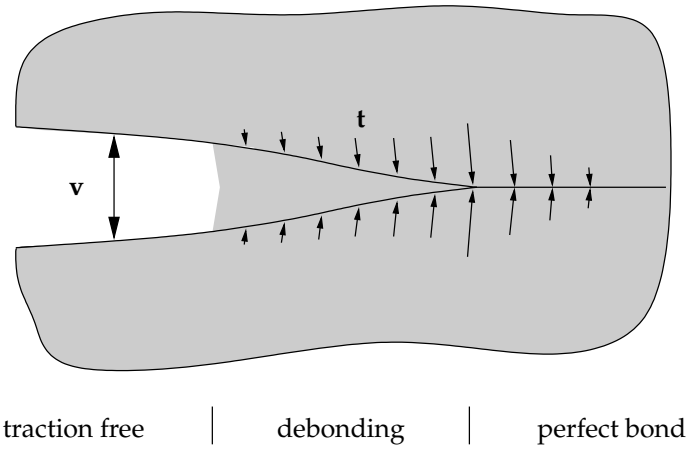

Figure 1.3 Schematic representation of the cohesive surface approach to fracture. The opening of the surface is denoted as **v**. The interface tractions that describe the perfect bond and the debonding process are represented by **t**.

is available: the *discrete fracture models*. The most prominent in this class is the cohesive zone approach, pioneered independently as a continuation of LEFM by Dugdale (1960) in the United Kingdom and Barenblatt (1962) in the Soviet Union. Whereas the use of LEFM is confined to cases where the *length* of the process zone is small compared to the structural dimensions, the cohesive zone approach can also be used when this limitation fails to hold.

In the cohesive zone approach, the complete process zone is lumped in a single plane or line ahead of the existing crack, as shown in Figure 1.3. The relation between the work expended in this cohesive zone and that in the crack tip field is typically such that the stress singularity is cancelled and the near tip stresses in the process zone are finite. Needleman (1987) extended the approach by inserting cohesive constitutive relations at specified planes in the materials, whether or not there is a crack. Apart from the fact that this approach can capture crack nucleation, there is an additional technical advantage. By specifying the cohesive relation along a surface, there is no need to determine the length of the cohesive zone. The failure characteristics of the material are governed by an independent constitutive relation that describes the separation of the cohesive surface. This cohesive constitutive relation, together with the constitutive relation for the bulk material and the appropriate balance laws and boundary and initial conditions, completely specify the

problem. Fracture, if it takes place, emerges as a natural outcome of the deformation process without introducing any additional failure criterion.

The simplest cohesive constitutive relation is one where the cohesive surface traction is a function of the displacement jump across this surface. For ductile fracture, the most important parameters appear to be the (tensile) strength and the work of separation or fracture energy (Hutchinson and Evans 2000). From dimensional considerations, this introduces a characteristic length in the model. For more brittle decohesion relations, i.e. when the decohesion law stems from micro-cracking as in concrete or ceramics, the *shape* of the stress-separation relation plays a much larger role and is sometimes even more important than the value of the tensile strength (Rots 1986).

Conventionally, the cohesive surfaces have been incorporated in the finite element mesh beforehand by means of interface elements that are placed between the standard continuum elements (Allix and Ladevèze 1992, Schellekens and de Borst 1994, Alfano and Crisfield 2001). These elements consist of two surfaces that are connected to the adjacent continuum elements. A perfect bond prior to cracking can be simulated by applying a high dummy stiffness to the interface elements.

In cases when fracture takes place along well defined interfaces as, for example in a lamellar solid (Schellekens and de Borst 1994), the placement of interface elements in the finite element mesh is clear. When the crack path is known in advance from experiments, the interface elements can be placed in the finite mesh along the known crack path (Rots 1991). However, for a solid that is homogeneous on the scale modelled, the crack path is often not known and the placement of cohesive surfaces can be problematic. In (Xu and Needleman 1993) interface elements are placed between all continuum elements in the mesh. This approach allowed the simulation of complex fracture phenomena such as crack branching (Xu and Needleman 1994) and crack initiation away from the crack tip, see Figure 1.4. Alternatively, Tijssens *et al.* (2001) have been using the method to simulate nucleation and coalescence of micro-cracks in the micro-structure of heterogeneous materials.

Nevertheless, the approach of placing interfaces between all continuum elements is not completely mesh independent. In fact, since the interface elements are aligned with element boundaries, the orientation of cracks is restricted to a limited number of angles. In addition, if, as in (Xu and Needleman

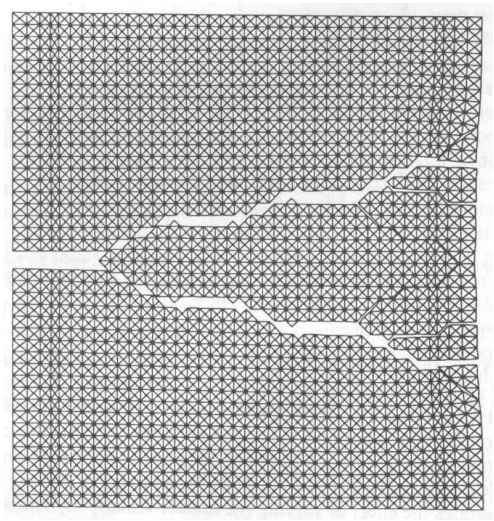

Figure 1.4 Simulation of crack branching in Polymethyl Methacrylate (PMMA) using inter-element cohesive surface models (Xu and Needleman 1994). Note that although the crack can only propagate in the 0°, $\pm 45^\circ$ and 90° directions, the propagation in other directions is captured relatively well.

1993) the initial compliances are taken to be non-zero, the presence of the interfaces contributes to the overall compliance of the body and an ill-posed problem results. The magnitude of this error can be reduced by increasing the dummy stiffness that describes the elastic behaviour of the cohesive zone prior to fracture. Unfortunately, this can cause numerical problems. High dummy stiffnesses in combination with a standard Gaussian integration scheme give rise to traction oscillations at the cohesive surfaces (Schellekens and de Borst 1993). And for dynamic simulations, large differences in compliances can lead to spurious stress wave reflections (Papoulia *et al.* 2003).

§ 1.3 The partition of unity method

Clearly, the application of both the smeared and discrete fracture models is restricted due to mesh dependency. This can vary from practical problems, such as the placement of the interface elements in the finite element mesh to numerical anomalies caused by large deformation gradients and localisation in smeared crack models or spurious traction oscillation in the cohesive sur-

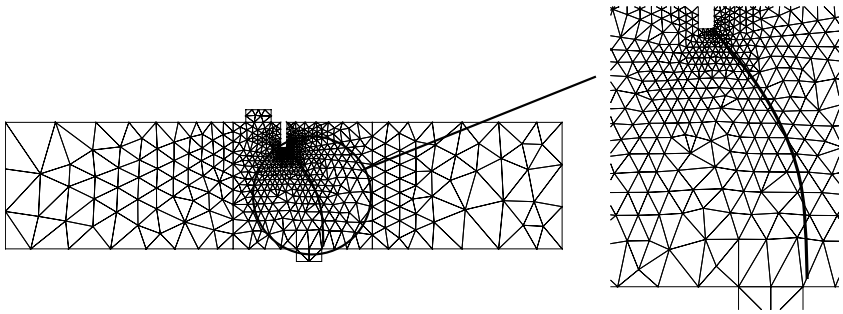

Figure 1.5 Crack growth in a single edge notched beam, simulated with the partition of unity approach to cohesive fracture. The cohesive surface (the bold line) crosses the continuum elements (Wells and Sluys 2001).

face approach. In order to avoid these deficiencies, recent developments in the field of numerical fracture mechanics have focused on new techniques to avoid mesh dependencies.*

In order to avoid finite element mesh related problems in cohesive surface models, Camacho and Ortiz (1996) used initially rigid cohesive surfaces in conjunction with adaptive mesh refinement. When the stress state in the material exceeds the maximum ultimate stress, a new, initially rigid interface element is inserted in the finite element mesh. The intersected continuum elements are replaced by means of a remeshing algorithm. In principle, this approach is based on the procedure that is commonly used in LEFM (Ingraffea and Saouma 1985), where the simulation is stopped each time a crack is propagated in order to reconstruct a new finite element mesh. Especially in the case of a finite deformation formulation or nonlinear material model for the bulk material, this requires a laborious operation of reallocating local stresses and other variables to the new material points in the finite element mesh.

*Smeared fracture models suffer from a mesh bias as well. These problems have been solved using techniques, which are rather similar to the methods used for discrete fracture models. In order to overcome numerical anomalies in the process zone due to high deformation gradients, the finite element mesh can be refined using a number of mesh refinement techniques. An overview can be found in (Askes and Rodríguez-Ferran 2001). Alternatively, meshless methods such as the element free Galerkin (EFG) have been used in combination with smeared models in order to develop a true mesh-independent method (Klein *et al.* 2001, Belytschko *et al.* 1996, Askes 2000).

In a more elegant approach, the cohesive surface is incorporated in the continuum elements by using the partition-of-unity property of finite element shape functions (Babuška and Melenk 1997) in conjunction with a discontinuous mode incorporated at the element level (Moës *et al.* 1999). Here, the cohesive zone is represented by a jump in the displacement field of the continuum elements (Wells and Sluys 2001a, Wells *et al.* 2002, Moës and Belytschko 2002). The magnitude of the displacement field is governed by additional degrees of freedom, which are added to the existing nodes of the finite element mesh. A crack (or cohesive surface) can be extended during the simulation at any time and in any direction by adding new additional degrees of freedom, see Figure 1.5. An important advantage over remeshing techniques as presented by Camacho and Ortiz (1996) is that the topology of the finite element mesh is not modified. The number of nodes and elements remains the same, as well as their mutual connectivity.*

The partition of unity approach to cohesive fracture has been used in a number of situations. Wells *et al.* (2002) extended the approach for finite strain kinematics in order to simulate delamination growth in laminated structures. Moës *et al.* (2002) applied the method for fracture in three-dimensional specimen.

§ 1.4 Levels of observation

The aforementioned numerical models can be used to simulate fracture processes on different *levels of observation*, varying from a propagating crack in a water dam (Ingraffea and Saouma 1985) to the debonding of a single fibre in a carbon fibre-epoxy prepreg (Schellekens 1992). In literature, various arrangements of levels of observation can be found. Based on the topics that will be

*The partition of unity approach to cohesive fracture is often denoted as an application of the eXtended Finite Element Method (X-FEM), for example by Belytschko and Black (1999). This name is slightly misleading since it suggests that the method is an extension of the finite element method. In fact, the approach exploits a property of the standard finite element shape functions that has not been acknowledged until the seminal publication of Babuška and Melenk (1997). Nevertheless, this partition-of-unity property has been used unintentionally before in a number of publications, e.g. (Goto *et al.* 1992).

dealt with in this thesis, the following arrangement is used, see also Table 1.1.*

Macroscopic level: This level of observation is often denoted as the structural level. The emphasis is put on the structural behaviour rather than damage or fracture in the material. The overall dimensions of the structures under investigation are much larger than the dimensions of the fracture process zone. Due to the resolution of the finite element mesh, subtle stress gradients in the vicinity of cracks cannot be captured, not to mention the events in the process zone that lead to fracture. In practice, simulations on this level are used to check whether a structure meets its design criteria such as the maximum allowable stress. Examples of analyses on this level are the structural stability (buckling) of a stringer stiffened panel in an aerospace structure, the deflection of an off-shore structure due to wave loading or the pressure distribution in a water dam.

Mesoscopic level: The scale where both structural effects and material properties are captured is called the mesoscopic level of observation. Dimensions of the specimen are in the order of magnitude of a few centimetres, which is in general of the same order of magnitude as the dimensions of the process zone. Although the specimen under investigation is often relatively small, it is still possible to describe structural aspects in combination with the failure behaviour. The analysis of fracture in small structures or structural components is an example of a simulation on the mesoscopic level of observation.

Microscopic level: On an even smaller length scale, the microscopic scale, the structural effects are neglected. The model represents a small specimen or a representative volume element, which is generally subject to a uniform load. On this level, some phenomena in the process zone can be revealed, such as the nucleation and coalescence of small cracks in the

*A similar division can be made with respect to timescales. Failure processes can last for years, such as creep fracture in metals, down to a few microseconds in the case of dynamic fracture in brittle materials. However, a detailed overview is omitted here, since all numerical models that are presented in this thesis, apart from the ones in chapters 6 and 7, are assumed to be rate independent and inertia effects are neglected.

micro-structure of the material. An illustrative example is the simulation of crack growth in cementitious materials by Tijssens *et al.* (2001).

Nanoscopic level: On all previously mentioned levels, the material was considered to be continuum, which implies that the atomic structure is neglected. However, on the nanoscopic scale, the influence of atomic structure is taken into account, although the individual atoms are not simulated explicitly. A good example is the discrete dislocation plasticity model (van der Giessen and Needleman 1995). Here, the material is taken to be continuous, but the field is enhanced with an additional displacement field caused by imperfections (dislocations). There is a strong coupling between both mechanisms and the model has been used successfully to predict a number of fatigue related phenomena such as Paris law behaviour and the accelerated growth of short cracks (Deshpande *et al.* 2003a).

Atomic level: The atomic level of observation used to be the domain of physicists, but has gradually become of interest to the engineering community as well. On this level, the material is no longer regarded as a continuum. Each individual atom is represented by a particle with an energy potential (Daw 1990). The method is able to reveal the smallest changes in the atomic structure of the material, such as the creation and movement of dislocations near a crack tip (Farkas *et al.* 2001) or the positions of atoms near a grain boundary.

The choice for the correct level of observation depends on the context in which the fracture mechanism is studied with respect to the design of the structure. This can be illustrated by means of the following example.

Example - Delamination buckling

Recently, the application of laminated materials gained popularity in the automotive and aeroplane industries. An example of such a material is Glare, which can be used as an alternative for traditional materials such as aluminium in aeroplane structures. This hybrid material consists of alternating layers of aluminium and glass fibre reinforced epoxy and has a number of advantages, including excellent impact and fire-resistance properties. The most

Scale	**Dimensions**	**Example**
Macroscopic	> 1 cm	Deformation of a wing.
Mesoscopic	1 mm-10 cm	Fracture in structural components.
Microscopic	1 μm-10 mm	Micro-crack nucleation.
Nanoscopic	1 nm-10 μm	Discrete dislocation plasticity.
Atomic	< 1 nm	Cleavage at crack tip.

Table 1.1 Overview of the different levels of observations.

prominent advantage is the excellent fatigue resistance due to the fibres in the prepreg layers. Nevertheless, laminates, and Glare is no exception, have some disadvantages as well. Due to the combination of different materials, new failure mechanisms are introduced. One of such a mechanism is delamination, which can have serious consequences for the overall stiffness of the material, especially in those cases where compressive or shear loadings are an issue. In that case a complicated failure mechanism can arise: *delamination buckling* . In this failure mechanism, a structural mechanism (local buckling of a debonded layer) amplifies the fracture delamination process. This mechanism has been studied experimentally by de Jong *et al.* (2001), see Figure 1.6.

In order to capture both the material (debonding) and the structural effects, the *mesoscopic* level of observation is the best approach. Here, the individual layers are modelled by structural elements with higher order kinematic relations in order to capture nonlinear displacement fields, needed for the simulation of buckling. Naturally, since on this level, delamination can be observed as a discrete failure mechanism, the debonding of the layers is modelled with interface elements, which are equipped with a cohesive degradation algorithm. Eventually, damage in the layers can be described by a smeared damage model, but in this case, coupling between delamination and layer damage is not taken into account. A more detailed implementation of this approach is given in the chapters 3 and 4.

Although this approach provides a good understanding of the coupling between delamination growth and local buckling, it does not reveal the de-

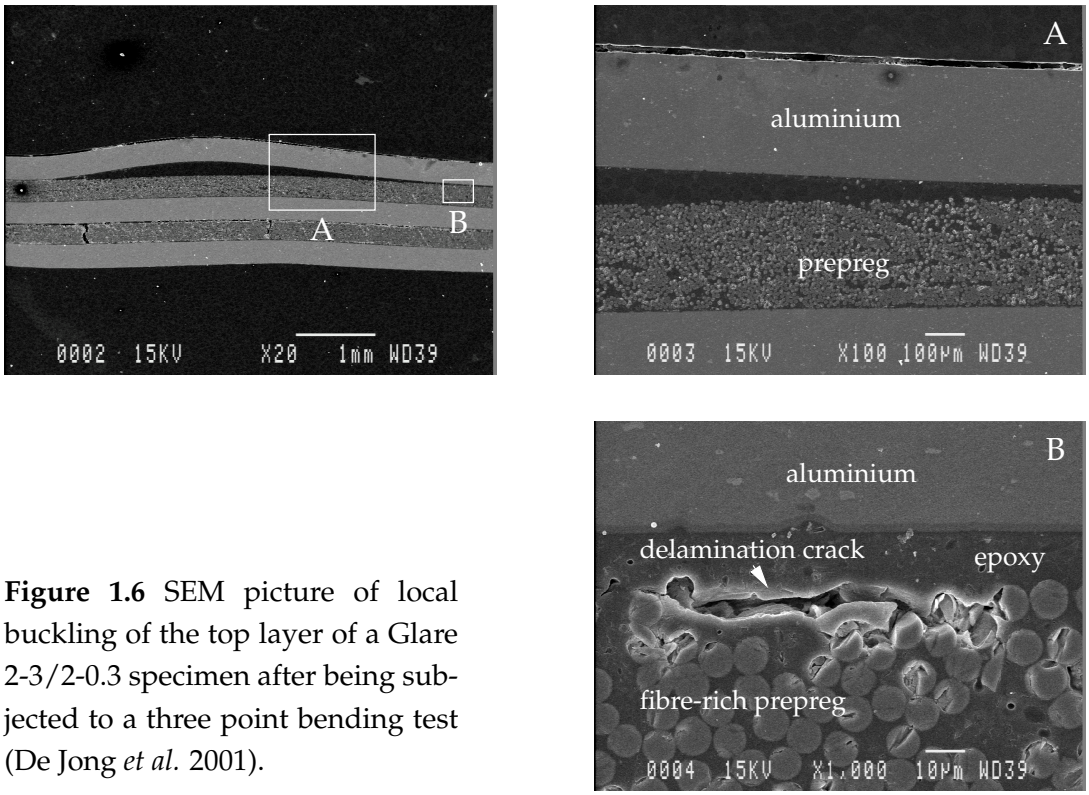

Figure 1.6 SEM picture of local buckling of the top layer of a Glare 2-3/2-0.3 specimen after being subjected to a three point bending test (De Jong *et al.* 2001).

tails of the delamination mechanism itself. Questions regarding the above-mentioned coupling between damage in the prepreg layers and delamination growth or the effect on the density of fibres in the prepreg layers remain unanswered. When zooming in on the actual delamination tip, we notice that delamination in Glare is not the failure of the bond between the aluminium and the epoxy, but adhesive debonding of the fibres and the prepreg in the transition of fibre rich and resin rich areas in the prepreg material (de Jong *et al.* 2001), detail B in Figure 1.6. Apparently, due to the treatments in the fabrication process, the bond between the aluminium and the epoxy is far stronger than the bond between epoxy and fibres.

Clearly, this phenomenon must be modelled on the *microscopic* level of observation. Both the fibres and the epoxy can be modelled with continuum elements, which in principle, can have linear kinematic relations. Since the fracture on this level of observation is a rather diffuse process, with the nucle-

ation and coalescence of many micro-separations, detail B in Figure 1.6, it can be simulated using a smeared approach (Schellekens 1992) or by a cohesive surface framework, e.g. (Tijssens *et al.* 2001). In chapter 5 we will discuss a new technique based on the partition of unity method to solve this problem in a true mesh independent way.

This example demonstrates that when zooming in to lower levels of observation, the kinematic relations that govern the (nonlinear) deformation fields in the finite element model become less complicated. On the macroscopic level, the behaviour of a structure is often simulated using *structural* elements such as shell or thin-plate elements. These elements are based on a higher order shell theory, which incorporates additional features to capture secondary effects such as bending in thin-walled structures. On smaller length scales, the structural elements are replaced by *continuum* elements with a straightforward kinematic model. Here, the material model (and especially the part that describes the phenomena in the process zone) is more important. On the smallest level of interest, the atomic level, the notion of a kinematic model has completely disappeared. The behaviour of the material follows from the cohesive relation only (the energy potential), which describes the relative movement of the rigid atoms.

Over the years, the interests of researchers in numerical fracture mechanics have moved towards lower levels of observation, for two reasons. Although the numerical simulations do not increase in complexity, the number of degrees of freedom expand when zooming in to lower levels of observation. Only recently, computers or clusters of computers are capable of handling such large numbers of equations in a reasonable amount of time. Secondly, due to miniaturising and sophistication of mechanical devices, there is a strong need for the analysis of mechanical behaviour on small length-scales. A good example in this case is the development of Micro-Electro-Mechanical Systems (MEMS). The specific dimensions of such systems approach a few microns, a length-scale where the position of individual atoms starts to play a role in the fracture process and cannot be neglected.

For completeness, an additional remark is made for studies that combine analyses on different length-scales by incorporating the deformations and fracture processes in the micro-structure of a material on a higher level of obser-

vation. A good example is the work of Kouznetsova *et al.* (2002). Here, the deformation gradient of a material point on the mesoscopic scale is imposed on a microstructural representative volume element (RVE). The solution of the corresponding boundary value problem is translated into a constitutive relation and inserted in the material point of the mesoscopic model. A promising technique to merge the atomic and the nanoscopic levels of observation has been proposed by Shilkrot *et al.* (2004). In this method, the region of interest is modelled by discrete atoms, whereas the surrounding material, which is of less interest, is modelled with a discrete dislocation model. The emphasis here is put on the transfer of defects in the atomistic structure, in particular edge dislocations, into the enhanced continuum model. Recently, Guidault *et al.* (2006) suggested a multiscale approach for the simulation of fracture. Here, the active crack tips in the macroscopic model are replaced by microscopic models in which crack propagation is governed by the aforementioned partition of unity approach.

§ 1.5 The objective and lay-out of this thesis

The partition of unity approach to cohesive fracture has proven to be a promising tool for modelling fracture mechanisms (Wells and Sluys 2001a, Moës and Belytschko 2002). However, so far, the application of the method has been limited to rather academic studies. The objective of this research is to extend this approach to developing new techniques to simulate realistic situations of fracture in the engineering practice on different levels of observation. A concise overview of the partition of unity approach to cohesive fracture is given in the next chapter. For reasons of clarity, the implementation is restricted to the most simple case, a two-dimensional quasi-static model with a small strain kinematic relation. Besides that, some remarks are made on the implementation in a finite element code. The chapter concludes with a number of numerical examples to demonstrate the performance of the method compared to traditional interface elements.

The remainder of the thesis can be divided into three parts. The first part discusses the application of the method for the simulation of delamination growth in thin-walled laminated structures on a macroscopic level of observation. Chapter 3 deals with the implementation into a three-dimensional solid-

like shell element (Remmers *et al.* 2003b). This geometrically nonlinear element, which has originally been derived by Parisch (1995), can be used to simulate the mechanical behaviour of thin-walled structures such as aeroplane fuselages. In chapter 4 the new model is used to analyse a topical subject: delamination buckling in fibre-metal laminates (Remmers and de Borst 2001b).

All aforementioned implementations of the partition of unity method have one thing in common; they do not allow for nucleation of (multiple) cracks or discontinuities. In the second part of this thesis, a new model is introduced, which can be used to simulate the nucleation, growth and coalescence of micro-separation on a microscopic level, the cohesive segments method (Remmers *et al.* 2003a). The derivation of this method and the implementation into a finite element framework are discussed in chapter 5. The extension of the method for the simulation of fast crack growth is given in chapter 6.

The final part of the thesis deals with discontinuities at an even smaller level of observation. The finite strain dislocation glide model as derived by Deshpande *et al.* (2003b) describes the creation of slip systems due to the collective motion of dislocations in a finite strain framework. However, the current implementation of this model suffers from numerical problems since the displacement jumps at the slip-systems are smeared out in the finite element mesh. In chapter 7, an alternative approach, inspired by the partition of unity method, is suggested that does not experience this shortcoming. The thesis concludes with a number of final remarks.

Chapter 2

The partition of unity approach to cohesive fracture

The cohesive surface methodology (Dugdale 1960, Barenblatt 1962, Hillerborg *et al.* 1976) is a versatile technique to simulate fracture processes in engineering materials. All the events in the process zone that eventually result in the creation of a crack are lumped into a single surface ahead of the crack tip. The separation of this cohesive surface is governed by an independent constitutive relation which characterises the fracture process of the material. A generalisation of the methodology (Needleman 1987) even allows the nucleation of new cracks, away from an existing crack tip or void, to be modelled.

Strictly speaking, the cohesive surface can be considered as a discontinuity in the displacement field of the body. This is in direct conflict with the classical formulation of solid mechanics, where the state of a body is described by continuous and smooth displacement, strain and stress fields. The spatial discretisation of the domain in finite elements offers an appropriate possibility to introduce discontinuities. By simply disconnecting the junction between two adjacent elements, a jump in the displacement field is created (Ngo and Scordelis 1967). The relative displacement of the elements is a measure for the separation of the cohesive zone. The corresponding tractions that follow from the cohesive constitutive relation are extrapolated onto nodal forces at the disconnected elements.

Instead of just disconnecting elements in the finite element model, the discontinuity can be modelled with a special type of element, the interface ele-

ment (Rots 1988, Allix and Ladevèze 1992, Schellekens and de Borst 1993, Alfano and Crisfield 2001). Such an element consists of two surfaces, which are connected to the adjacent continuum elements. Apart from the relative displacement of the two surfaces, the total rotation of the cohesive zone can be obtained as well. For that reason, interface elements are preferred for the simulation of mixed-mode fracture processes and in cases where significant geometrical effects can be expected, such as delamination buckling (Allix and Corigliano 1999).

By inserting the discontinuity after the discretisation process, the trajectory of a crack is related to the finite element mesh, which gives rise to mesh dependent solutions. This can be avoided by incorporating the displacement jump in the analytical displacement field before performing the discretisation. As a result, the discontinuity is truly a part of the boundary value problem and obviously, the mechanical model is well posed. An elegant way to introduce a discontinuity in a further continuous and smooth displacement field is to add a second displacement field multiplied with a step function on top of the existing base field (Belytschko and Black 1999). This step function, or Heaviside function, is equal to zero on one side of the discontinuity and equals one on the other side. The magnitude of the displacement jump is equal to the magnitude of the additional field exactly at the discontinuity.

The discontinuous displacement field can be transformed into a discretised field by exploiting the partition-of-unity property of finite element shape functions (Babuška and Melenk 1997). The additional displacement field is represented by an extra set of degrees of freedom, which is added to the existing nodes of the finite element mesh. Initially, this approach was applied for the simulation of fracture in a linear elastic fracture mechanics framework by Moës *et al.* (1999). Later, the method was extended in a cohesive surface formulation by Wells and Sluys (2001a) and Moës and Belytschko (2002).

The partition of unity approach to cohesive fracture has a number of advantages over the conventional models. The cohesive surface can be placed as a discontinuity anywhere in the model, irrespective of the structure of the underlying finite element mesh. Moreover, it is possible to extend a cohesive surface during the simulation by adding additional degrees of freedom. This avoids the use of high dummy stiffnesses to model a perfect bond prior to cracking and prevents numerical problems such as spurious stress oscilla-

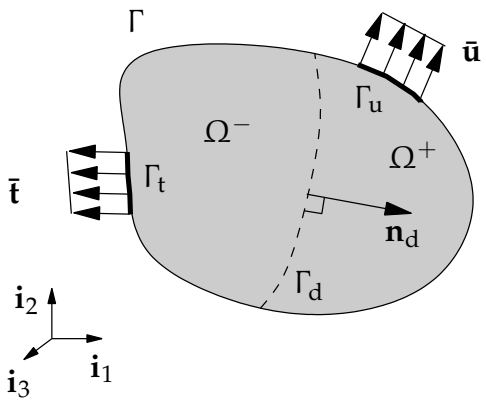

Figure 2.1 A domain Ω is crossed by a discontinuity Γ_d (denoted by the dashed line).

tions (Schellekens and de Borst 1993) or stress wave reflections in dynamic simulations. Since degrees of freedom are only added when a cohesive surface is extended, the total number of degrees of freedom can also be smaller. Finally, since the method is based on an existing cohesive surface formulation, existing cohesive constitutive models can still be used.

In this chapter, a concise overview of the partition of unity approach to cohesive fracture is given, following the work by Wells *et al.* (2001-2002). In the first sections, the kinematic relations and the derivation of the equilibrium equations in the weak form are derived. Next, the discretisation of the governing equation by means of shape functions is discussed. The largest part of the chapter is dedicated to the implementation in a two-dimensional finite element model. Important aspects are illustrated by means of a number of numerical examples. The chapter is concluded with an overview of recent applications of the partition of unity approach to fracture.

§ 2.1 Kinematic relations

Consider the domain Ω with external boundary Γ as shown in Figure 2.1. The domain is crossed by a discontinuity Γ_d. The two resulting parts of the domain are denoted as Ω^+ and Ω^-. The total displacement field $\mathbf{u}$ consists of a continuous regular field $\hat{\mathbf{u}}$ and a continuous additional displacement field $\tilde{\mathbf{u}}$

Jump function	$\mathcal{H}^+$	$\mathcal{H}^-$	h
Heaviside	1	0	1
Symmetric	1/2	-1/2	1
Unit Symmetric	1	-1	2

Table 2.1 An overview of different step functions that can be used to create a jump in the displacement field, see equations (2.2) and (2.3).

(Wells and Sluys 2001a):*

$$\mathbf{u}(\mathbf{x},t) = \hat{\mathbf{u}}(\mathbf{x},t) + \mathcal{H}_{\Gamma_\mathrm{d}}(\mathbf{x})\,\tilde{\mathbf{u}}(\mathbf{x},t)\,, \tag{2.1}$$

where $\mathbf{x}$ denotes the position of the material point in the body expressed in a Cartesian coordinate system $\mathbf{x} = x\mathbf{i}_1 + y\mathbf{i}_2 + z\mathbf{i}_3$; t is time and $\mathcal{H}_{\Gamma_\mathrm{d}}(\mathbf{x})$ is a step function which is constant on either side of the discontinuity:

$$\mathcal{H}_{\Gamma_\mathrm{d}} = \begin{cases} \mathcal{H}^+ & \text{if} \quad \mathbf{x} \in \Omega^+, \\ \mathcal{H}^- & \text{if} \quad \mathbf{x} \in \Omega^-\,. \end{cases} \tag{2.2}$$

The magnitude of the step h in this function is defined as:

$$h = \mathcal{H}^+ - \mathcal{H}^-\,. \tag{2.3}$$

Wells and Sluys (2001a) used a standard Heaviside step function to describe the jump:

$$\mathcal{H}_{\Gamma_\mathrm{d}}(\mathbf{x}) = \begin{cases} 1 & \text{if} \quad \mathbf{x} \in \Omega^+\,; \\ 0 & \text{if} \quad \mathbf{x} \in \Omega^-\,, \end{cases} \tag{2.4}$$

but as we will see in chapter 6, alternative functions can have certain advantages, (Réthoré *et al.* 2005). An overview of step functions that will be discussed in the scope of this thesis is given in Table 2.1.

*In this thesis, all variables related to the regular part of a field are denoted with a hat ($\hat{}$). All variables related to the additional part are denoted with a tilde ($\tilde{}$).

Assuming a small strain formulation, the strain field is found by taking the derivative of the displacement field (2.1) with respect to the position in the body $\mathbf{x}$:

$$\boldsymbol{\epsilon}(\mathbf{x},t) = \nabla^{\mathrm{s}}\hat{\mathbf{u}}(\mathbf{x},t) + \mathcal{H}_{\Gamma_{\mathrm{d}}}\nabla^{\mathrm{s}}\tilde{\mathbf{u}}(\mathbf{x},t) \qquad \mathbf{x} \notin \Gamma_{\mathrm{d}}\,, \tag{2.5}$$

where ∇^{s} denotes the symmetric differential operator:

$$(\nabla^{\mathrm{s}}\square)_{ij} = \frac{1}{2}\left(\frac{\partial}{\partial x_i}\square_j + \frac{\partial}{\partial x_j}\square_i\right)\,; \qquad i = 1,2,3\,. \tag{2.6}$$

Since the jump function is not uniquely defined at the discontinuity, the corresponding strain field is unbounded. Here, we use the magnitude of the displacement jump $\mathbf{v}$ as the relevant kinematic quantity:

$$\mathbf{v}(\mathbf{x},t) = h\tilde{\mathbf{u}}(\mathbf{x},t) \qquad \mathbf{x} \in \Gamma_{\mathrm{d}}\,, \tag{2.7}$$

where h is the magnitude of the jump in the step function $\mathcal{H}_{\Gamma_{\mathrm{d}}}$, see equation (2.3).

§ 2.2 Equilibrium equations

The equilibrium of the body can be expressed in the following quasi-static equilibrium equation without body forces:

$$\nabla \cdot \boldsymbol{\sigma} = \mathbf{0} \qquad \mathbf{x} \in \Omega\,; \tag{2.8}$$

with the following boundary conditions:

$$\mathbf{n}_t \cdot \boldsymbol{\sigma} = \bar{\mathbf{t}} \qquad \mathbf{x} \in \Gamma_t\,; \tag{2.9}$$

$$\mathbf{u} = \bar{\mathbf{u}} \qquad \mathbf{x} \in \Gamma_u\,, \tag{2.10}$$

where $\boldsymbol{\sigma}$ is the Cauchy stress in the bulk material, $\bar{\mathbf{t}}$ are the prescribed tractions on the external boundary Γ_t with outward normal vector $\mathbf{n}_t$ and $\bar{\mathbf{u}}$ are the prescribed displacements on Γ_u. Since the discontinuity Γ_{d} can be considered as an internal boundary, the following relation can be added:

$$\mathbf{n}_{\mathrm{d}} \cdot \boldsymbol{\sigma} = \mathbf{t} \qquad \mathbf{x} \in \Gamma_{\mathrm{d}}\,, \tag{2.11}$$

where $\mathbf{t}$ are the tractions at the internal boundary Γ_d with normal vector $\mathbf{n}_\mathrm{d}$ pointing into Ω^+. The equilibrium equation (2.8) can be expressed in a weak form by multiplication with an admissible variational displacement field $\delta\mathbf{u}$:

$$\int_\Omega \delta\mathbf{u} \cdot (\nabla\cdot\boldsymbol{\sigma})\mathrm{d}\Omega = 0\,. \tag{2.12}$$

Taking the space of the admissible variations to be the same as the actual displacement field (2.1), the variations of the displacements can be decomposed in a regular and an additional field:

$$\delta\mathbf{u} = \delta\hat{\mathbf{u}} + \mathcal{H}_{\Gamma_\mathrm{d}}\delta\tilde{\mathbf{u}}\,. \tag{2.13}$$

Similarly, the admissible displacement jump $\delta\mathbf{v}$ at the internal boundary Γ_d can be written as, see equation (2.7):

$$\delta\mathbf{v} = h\delta\tilde{\mathbf{u}}\,. \tag{2.14}$$

Substituting the variations into equation (2.12) gives:

$$\int_\Omega \delta\hat{\mathbf{u}} \cdot (\nabla\cdot\boldsymbol{\sigma})\mathrm{d}\Omega + \int_\Omega \mathcal{H}_{\Gamma_\mathrm{d}}\delta\tilde{\mathbf{u}} \cdot (\nabla\cdot\boldsymbol{\sigma})\mathrm{d}\Omega = 0\,. \tag{2.15}$$

Applying Gauss' theorem, using the symmetry of the Cauchy stress tensor, introducing the internal boundary Γ_d and the corresponding admissible displacement jump and using the boundary conditions at the external boundary Γ_t gives:

$$\begin{aligned}\int_\Omega \nabla^s\delta\hat{\mathbf{u}} : \boldsymbol{\sigma}\mathrm{d}\Omega + \int_\Omega \mathcal{H}_{\Gamma_\mathrm{d}}\nabla^s\delta\tilde{\mathbf{u}} : \boldsymbol{\sigma}\mathrm{d}\Omega + \int_{\Gamma_\mathrm{d}} h\delta\tilde{\mathbf{u}} \cdot \mathbf{t}\mathrm{d}\Gamma = \\ \int_{\Gamma_t} \delta\hat{\mathbf{u}} \cdot \bar{\mathbf{t}}\mathrm{d}\Gamma + \int_{\Gamma_t} \mathcal{H}_{\Gamma_\mathrm{d}}\delta\tilde{\mathbf{u}} \cdot \bar{\mathbf{t}}\mathrm{d}\Gamma\,.\end{aligned} \tag{2.16}$$

The first term on the left hand side of this equation describes the internal forces in the body due to the regular displacement field, whereas the second term represent the internal forces due to the additional displacement field. The third term describes the internal forces due to the tractions at the discontinuity. The right hand side of the equation contains terms related to prescribed tractions imposed on the external boundary of the domain.

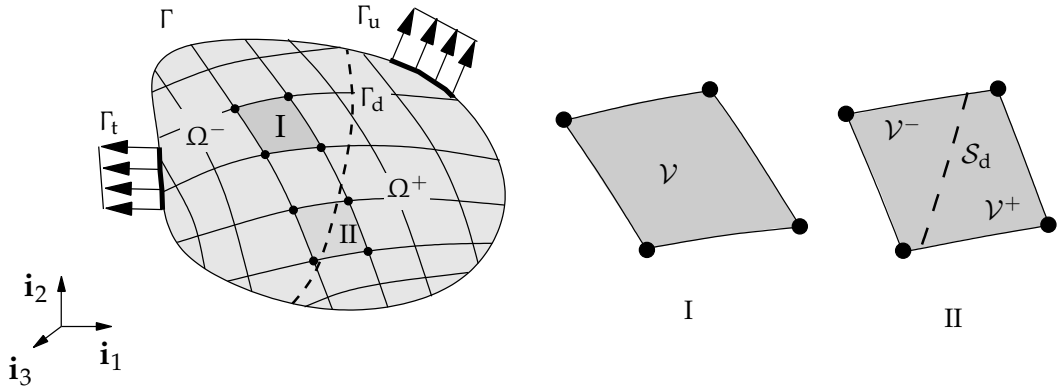

Figure 2.2 Discretisation of the domain Ω into n_{elm} finite elements supported by n_{nod} nodes. Element I is a regular element with integration volume $\mathcal{V}$. Element II is crossed by the discontinuity, which can be considered as an internal boundary $\mathcal{S}_\mathrm{d}$. The integration domain is split into two parts $\mathcal{V}^+$ and $\mathcal{V}^-$.

§ 2.3 Finite element formulation

In order to arrive at a versatile model, the equations will be solved using the finite element method. In this method, the domain Ω is divided into a number of elements with finite volume $\mathcal{V}$, which are supported by nodes, see Figure 2.2. A continuous scalar field $f(\mathbf{x}, t)$ in the domain can be represented by discrete values which are assigned to the nodes and their corresponding shape functions:

$$f(\mathbf{x}, t) = \sum_{i=1}^{n_{nod}} \phi_i(\mathbf{x}) a_i(t)\,, \tag{2.17}$$

where $\phi_i(\mathbf{x})$ is the shape function associated to node i and $a_i(t)$ is the discrete value of the scalar field f in that node. The shape function $\phi_i(\mathbf{x})$ is equal to 1 in node i and 0 in all other nodes, see Figure 2.3. Additionally, the set of shape functions possesses the so-called partition-of-unity property, which implies that the sum of all shape functions in an arbitrary point $\mathbf{x}$ in the domain is equal to 1:

$$\sum_{i=1}^{n_{nod}} \phi_i(\mathbf{x}) = 1 \qquad \forall\ \mathbf{x} \in \Omega\,. \tag{2.18}$$

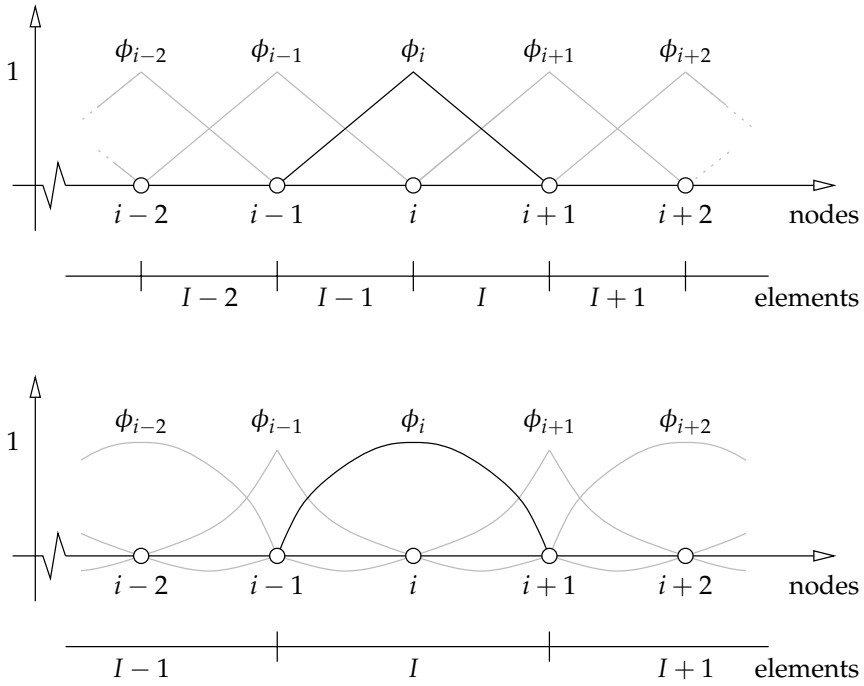

Figure 2.3 Shape functions ϕ_i for linear element (top) and quadratic (bottom) finite elements. Note that the sum of the shape functions is equal to one everywhere.

The part of the domain Ω for which the magnitude of the shape function of node i is non-zero is called the support of the node. In the case of standard iso-parametric shape functions, the support of the node is identical to the elements that are attached to this node.

It was shown by Babuška and Melenk (1997) that when the field $f(\mathbf{x}, t)$ is not continuous, it can still be discretised using the finite element shape functions in combination with an enhanced basis function, according to:

$$f(\mathbf{x}, t) = \sum_{i=1}^{n_{nod}} \phi_i(\mathbf{x}) \left(a_i(t) + \sum_{j=1}^{m} \gamma_j(\mathbf{x}) b_{ij}(t) \right), \tag{2.19}$$

where $\gamma_j(\mathbf{x}, t)$ is an enhanced basis with m orthogonal terms and b_{ij} are the additional nodal degrees of freedom that support the enhanced basis functions. The number m of enhanced base functions may be different for each node i in the model. However, in order to avoid linear dependency, the enhanced

basis γ_j and the shape functions ϕ_i may not originate from the same span of functions.

Discrete kinematic relations

In case of a three-dimensional displacement field with a single discontinuity as given in equation (2.1), the enhanced basis term γ_j in (2.19) can be replaced by the step function $\mathcal{H}_{\Gamma_\mathrm{d}}$ to give:

$$\mathbf{u}(\mathbf{x},t) = \sum_{i=1}^{n_{nod}} \phi_i(\mathbf{x}) \left(\mathbf{a}_i(t) + \mathcal{H}_{\Gamma_\mathrm{d}}(\mathbf{x}) \mathbf{b}_i(t) \right) , \tag{2.20}$$

where $\mathbf{a}_i$ and $\mathbf{b}_i$ contain the regular and additional nodal degrees of freedom of node i, respectively:

$$\mathbf{a}_i = [a_x, a_y, a_z]_i \, ; \qquad \mathbf{b}_i = [b_x, b_y, b_z]_i \, . \tag{2.21}$$

Alternatively, the discrete displacement field in (2.20) can be cast in the following form for a single element:

$$\mathbf{u} = \mathbf{N}\mathbf{a} + \mathcal{H}_{\Gamma_\mathrm{d}} \mathbf{N}\mathbf{b} \, , \tag{2.22}$$

where the matrix $\mathbf{N}$ contains the shape functions for all the nodes that support this element. The strain field can be obtained by differentiating the discrete displacement field with respect to $\mathbf{x}$, see also equation (2.5):

$$\boldsymbol{\epsilon} = \mathbf{B}\mathbf{a} + \mathcal{H}_{\Gamma_\mathrm{d}} \mathbf{B}\mathbf{b} \qquad \mathbf{x} \notin \mathcal{S}_\mathrm{d} \, , \tag{2.23}$$

where $\mathcal{S}_\mathrm{d}$ is the discontinuity in the element and matrix $\mathbf{B}$ contains the derivatives of the finite element shape functions, according to:

$$\mathbf{B} = \nabla^s \mathbf{N} \, . \tag{2.24}$$

Finally, the discrete displacement jump at the discontinuity $\mathcal{S}_\mathrm{d}$ as presented in equation (2.7) is equal to:

$$\mathbf{v} = \mathbf{H}\mathbf{b} = h\mathbf{N}\mathbf{b} \, . \tag{2.25}$$

Equilibrium equations

In the spirit of a Bubnov-Galerkin approach, the variations of the displacement fields and their derivatives with respect to position vector $\mathbf{x}$ are discretised accordingly:

$$\begin{aligned} \delta\hat{\mathbf{u}} &= \mathbf{N}\delta\mathbf{a}\,; & \delta\tilde{\mathbf{u}} &= \mathbf{N}\delta\mathbf{b}\,; \\ \nabla^s\delta\hat{\mathbf{u}} &= \mathbf{B}\,\delta\mathbf{a}\,; & \nabla^s\delta\tilde{\mathbf{u}} &= \mathbf{B}\,\delta\mathbf{b}\,. \end{aligned} \tag{2.26}$$

Inserting these relations into the equilibrium equation (2.16) yields the discretised equilibrium equation in weak form for a single element:

$$\begin{aligned} \int_{\mathcal{V}}(\mathbf{B}\delta\mathbf{a})^{\mathrm{T}}\boldsymbol{\sigma}\mathrm{d}\mathcal{V} + \int_{\mathcal{V}}\mathcal{H}_{\Gamma_\mathrm{d}}(\mathbf{B}\delta\mathbf{b})^{\mathrm{T}}\boldsymbol{\sigma}\mathrm{d}\mathcal{V} + \int_{\mathcal{S}_\mathrm{d}}(\mathbf{H}\delta\mathbf{b})^{\mathrm{T}}\mathbf{t}\mathrm{d}\mathcal{S} = \\ \int_{\mathcal{S}_t}(\mathbf{N}\delta\mathbf{a})^{\mathrm{T}}\bar{\mathbf{t}}\mathrm{d}\mathcal{S} + \int_{\mathcal{S}_t}\mathcal{H}_{\Gamma_\mathrm{d}}(\mathbf{N}\delta\mathbf{b})^{\mathrm{T}}\bar{\mathbf{t}}\mathrm{d}\mathcal{S}\,. \end{aligned} \tag{2.27}$$

By taking one of the admissible variations $\delta\mathbf{a}$ and $\delta\mathbf{b}$ at the time, the weak form of equilibrium can be separated into two sets of equations:

$$\begin{aligned} \int_{\mathcal{V}}\mathbf{B}^{\mathrm{T}}\boldsymbol{\sigma}\mathrm{d}\mathcal{V} &= \int_{\mathcal{S}_t}\mathbf{N}^{\mathrm{T}}\bar{\mathbf{t}}\mathrm{d}\mathcal{S}\,; \\ \int_{\mathcal{V}}\mathcal{H}_{\Gamma_\mathrm{d}}\mathbf{B}^{\mathrm{T}}\boldsymbol{\sigma}\mathrm{d}\mathcal{V} + \int_{\mathcal{S}_\mathrm{d}}\mathbf{H}^{\mathrm{T}}\mathbf{t}\mathrm{d}\mathcal{S} &= \int_{\mathcal{S}_t}\mathcal{H}_{\Gamma_\mathrm{d}}\mathbf{N}^{\mathrm{T}}\bar{\mathbf{t}}\mathrm{d}\mathcal{S}\,. \end{aligned} \tag{2.28}$$

The first equation is related to the regular degrees of freedom of the element, which is identical to the equilibrium equation for an element without a discontinuity. As a result, it is possible to add a discontinuity to an element during the calculations with a minimal effort by adding the additional equilibrium relations and the corresponding degrees of freedom $\mathbf{b}$.

Constitutive relations

We assume that the stress rate in the bulk material $\dot{\boldsymbol{\sigma}}$ is a function of the strain rate $\dot{\boldsymbol{\epsilon}}$ and can be expressed in terms of the nodal velocities written as:

$$\dot{\boldsymbol{\sigma}} = \mathbf{C}\dot{\boldsymbol{\epsilon}} = \mathbf{C}\left(\mathbf{B}\dot{\mathbf{a}} + \mathcal{H}_{\Gamma_\mathrm{d}}\mathbf{B}\dot{\mathbf{b}}\right), \tag{2.29}$$

where $\dot{(\,)}$ denotes the partial derivative with respect to time $\partial(\,)/\partial t$; $\dot{\mathbf{a}}$ and $\dot{\mathbf{b}}$ denote the regular and additional nodal velocities, respectively, and $\mathbf{C}$ is

the tangent stiffness matrix of the bulk material.* The traction rates at the discontinuity $\mathcal{S}_\mathrm{d}$ can be expressed in terms of the corresponding enhanced nodal velocities:

$$\dot{\mathbf{t}}_\mathrm{d} = \mathbf{T}_\mathrm{d}\dot{\mathbf{v}}_\mathrm{d}\,, \tag{2.30}$$

where $\mathbf{t}_\mathrm{d}$ denote the tractions defined in a frame of reference which is aligned with the orientation of the discontinuity in the element, see Figure 2.4. The tractions can be written as: $\mathbf{t}_\mathrm{d} = t_n\mathbf{n} + t_{s_2}\mathbf{s}_2 + t_{s_3}\mathbf{s}_3$, where t_n is the normal traction and t_{s_2} and t_{s_3} are the shear tractions in the plane of the discontinuity. The displacement jump in this local frame of reference is denoted accordingly as $\mathbf{v}_\mathrm{d} = v_n\mathbf{n} + v_{s_2}\mathbf{s}_2 + v_{s_3}\mathbf{s}_3$ and $\mathbf{T}_\mathrm{d}$ is the tangent stiffness of the traction-separation law. Transformation of the cohesive constitutive relation, equation (2.30), into the global frame of reference gives:

$$\dot{\mathbf{t}} = \mathbf{Q}^\mathrm{T}\dot{\mathbf{t}}_\mathrm{d} = \mathbf{Q}^\mathrm{T}\mathbf{T}_\mathrm{d}\dot{\mathbf{v}}_\mathrm{d} = \mathbf{Q}^\mathrm{T}\mathbf{T}_\mathrm{d}\mathbf{Q}\dot{\mathbf{v}} = \mathbf{Q}^\mathrm{T}\mathbf{T}_\mathrm{d}\mathbf{Q}h\mathbf{N}\dot{\mathbf{b}}\,, \tag{2.31}$$

so that the tangent stiffness matrix in the element local frame of reference is equal to:

$$\mathbf{T} = \mathbf{Q}^\mathrm{T}\mathbf{T}_\mathrm{d}\mathbf{Q}\,. \tag{2.32}$$

The orthogonal transformation matrix $\mathbf{Q}$ performs the transformation of the orientation of the discontinuity to the global coordinate system. Following the standard procedures, this matrix can be constructed using the triad $(\mathbf{n}, \mathbf{s}_2, \mathbf{s}_3)$ which is attached to the discontinuity (Bathe 1996):

$$\mathbf{Q} = \begin{bmatrix} \cos(\mathbf{i}_1, \mathbf{n}) & \cos(\mathbf{i}_1, \mathbf{s}_2) & \cos(\mathbf{i}_1, \mathbf{s}_3) \\ \cos(\mathbf{i}_2, \mathbf{n}) & \cos(\mathbf{i}_2, \mathbf{s}_2) & \cos(\mathbf{i}_2, \mathbf{s}_3) \\ \cos(\mathbf{i}_3, \mathbf{n}) & \cos(\mathbf{i}_3, \mathbf{s}_2) & \cos(\mathbf{i}_3, \mathbf{s}_3) \end{bmatrix}. \tag{2.33}$$

*In this derivation, it is assumed that the constitutive relation for the bulk material is both linear elastic and rate independent, but this is not a limitation of the formulation. In general, any material law can be used to model the behaviour of the bulk material, as demonstrated by Wells *et al.* (2002) and Simone and Sluys (2004).

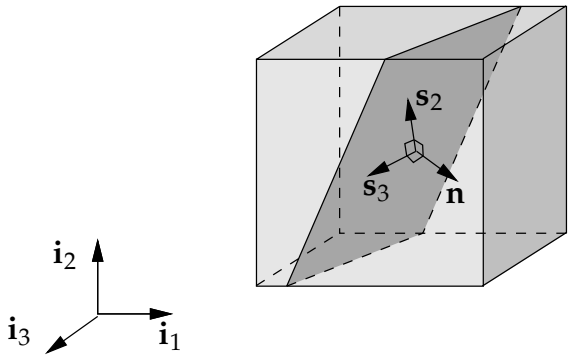

Figure 2.4 Orientation of the discontinuity within an element.

Linearisation of the equilibrium equations

In order to calculate the deformation history in an incremental fashion, the nonlinear system (2.28) is differentiated with respect to the displacement variables **a** and **b**. In the small strain formulation elaborated here, only the stress field in the bulk material $\boldsymbol{\sigma}$ and the tractions at the discontinuity **t** are functions of the discrete displacement terms **a** and **b**, according to:

$$\frac{\partial \boldsymbol{\sigma}}{\partial \mathbf{a}} = \mathbf{CB}\,; \qquad \frac{\partial \boldsymbol{\sigma}}{\partial \mathbf{b}} = \mathcal{H}_{\Gamma_\mathrm{d}}\mathbf{CB}\,; \qquad \frac{\partial \mathbf{t}}{\partial \mathbf{b}} = \mathbf{Q}^\mathrm{T}\mathbf{T}_\mathrm{d}\mathbf{QN}\,. \tag{2.34}$$

Using these relations, the linearised system of equations reads:

$$\begin{bmatrix} \mathbf{K}_{aa} & \mathbf{K}_{ab} \\ \\ \mathbf{K}_{ba} & \mathbf{K}_{bb} \end{bmatrix} \begin{bmatrix} \dot{\mathbf{a}} \\ \\ \dot{\mathbf{b}} \end{bmatrix} = \begin{bmatrix} \mathbf{f}_a^{\mathrm{ext}} \\ \\ \mathbf{f}_b^{\mathrm{ext}} \end{bmatrix} - \begin{bmatrix} \mathbf{f}_a^{\mathrm{int}} \\ \\ \mathbf{f}_b^{\mathrm{int}} \end{bmatrix}, \tag{2.35}$$

where the terms in the stiffness matrix are:

$$\begin{aligned} \mathbf{K}_{aa} &= \int_{\mathcal{V}} \mathbf{B}^\mathrm{T}\mathbf{CB}\mathrm{d}\mathcal{V}\,; \\ \mathbf{K}_{ab} = \mathbf{K}_{ba} &= \int_{\mathcal{V}} \mathcal{H}_{\Gamma_\mathrm{d}}\mathbf{B}^\mathrm{T}\mathbf{CB}\mathrm{d}\mathcal{V}\,; \\ \mathbf{K}_{bb} &= \int_{\mathcal{V}} \mathcal{H}_{\Gamma_\mathrm{d}}\mathcal{H}_{\Gamma_\mathrm{d}}\mathbf{B}^\mathrm{T}\mathbf{CB}\mathrm{d}\mathcal{V} + \int_{\mathcal{S}_\mathrm{d}} \mathbf{H}^\mathrm{T}\mathbf{Q}^\mathrm{T}\mathbf{T}_\mathrm{d}\mathbf{QH}\mathrm{d}\mathcal{S}\,. \end{aligned} \tag{2.36}$$

The internal forces are given by:

$$\begin{aligned} \mathbf{f}_a^{\text{int}} &= \int_{\mathcal{V}} \mathbf{B}^{\mathrm{T}} \boldsymbol{\sigma} \mathrm{d}\mathcal{V} \,; \\ \mathbf{f}_b^{\text{int}} &= \int_{\mathcal{V}} \mathcal{H}_{\Gamma_{\mathrm{d}}} \mathbf{B}^{\mathrm{T}} \boldsymbol{\sigma} \mathrm{d}\mathcal{V} + \int_{\mathcal{S}_{\mathrm{d}}} \mathbf{H}^{\mathrm{T}} \mathbf{Q}^{\mathrm{T}} \mathbf{t}_{\mathrm{d}} \mathrm{d}\mathcal{S} \,. \end{aligned} \tag{2.37}$$

Finally, the expression for the external forces is:

$$\begin{aligned} \mathbf{f}_a^{\text{ext}} &= \int_{\mathcal{S}_t} \mathbf{N}^{\mathrm{T}} \bar{\mathbf{t}} \mathrm{d}\mathcal{S} \,; \\ \mathbf{f}_b^{\text{ext}} &= \int_{\mathcal{S}_t} \mathcal{H}_{\Gamma_{\mathrm{d}}} \mathbf{N}^{\mathrm{T}} \bar{\mathbf{t}} \mathrm{d}\mathcal{S} \,. \end{aligned} \tag{2.38}$$

Note that if the tangent matrices $\mathbf{C}$ and $\mathbf{T}_{\mathrm{d}}$ are symmetric, symmetry of the sub-matrices $\mathbf{K}_{aa}$, $\mathbf{K}_{ab}$ and $\mathbf{K}_{bb}$ is preserved. Consequently, the total stiffness matrix also remains symmetric.

§ 2.4 Implementation aspects and examples

The governing equations have been derived in the most general way and can be implemented in any kind of continuum element as long as the underlying shape functions obey the partition-of-unity property. In the remainder of this chapter, the attention is confined to the implementation of the method in two-dimensional continuum elements with a linear elastic plane strain or plane stress constitutive relation for the bulk material.

The most important aspects of the implementation will be illustrated by means of examples with increasing complexity. First, the incorporation of a discontinuity as a static interface in a domain is discussed. Here, the emphasis is put on the enhancement of individual nodes and the numerical integration of the elements that are crossed by a discontinuity. In addition, the numerical performance of this implementation is compared with traditional interface elements (Simone *et al.* 2001, Remmers *et al.* 2001).

Next, the implementation of a discontinuity with a crack tip and the propagation of this discontinuity in a predefined direction is presented. A number of ways to model a crack tip are discussed as well as criteria for the extension of the discontinuity into a new element. The simulation of such a propagating

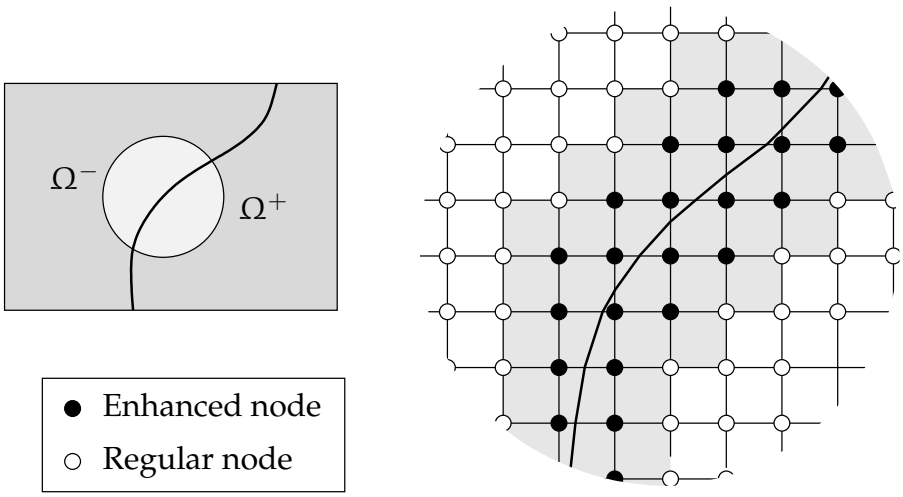

Figure 2.5 Two-dimensional finite element mesh with a discontinuity denoted by the bold line. The grey elements contain additional terms in the stiffness matrix and the internal force vector.

crack is illustrated with a peel test of a double cantilever beam (Remmers *et al.* 2001, Wells *et al.* 2002).

In the final part of the section, the modelling of a propagating crack in a direction that is not set beforehand is discussed. This requires an algorithm that predicts the correct direction in which the cohesive zone should be extended. In the accompanying example, the performance of this model is demonstrated by means of a classical example, the single-edge nodged beam (Wells and Sluys 2001a).

Static discontinuity

Consider the specimen with a static interface as shown in Figure 2.5. In the finite element model, the interface is modelled as a discontinuity in a structured mesh composed of four node elements. In principle, the additional displacement field $\tilde{\mathbf{u}}$ must be constructed by enhancing all shape functions ϕ_i in the domain by the enhancement function $\mathcal{H}_{\Gamma_d}$. This enhanced basis is then supported by additional degrees of freedom $\mathbf{b}_i$ in each node i. However, when the support of a node is not crossed by the discontinuity, the enhancement function is constant and belongs to the same span of functions as the finite

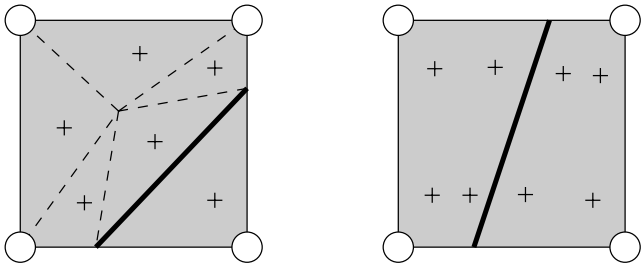

Figure 2.6 Numerical integration of quadrilateral elements crossed by a discontinuity (bold line). The sample points are denoted by a $+$. The element on the left is split into a sub-element with five vertices and one with three vertices. The first part must be triangulated into five smaller areas, denoted by the dashed lines. Each of these areas is integrated using a standard 1 point Gauss integration scheme. The element on the right is split into two quadrilateral sub-elements. Each of these parts can be integrated with a standard 2×2 Gauss integration scheme.

element shape functions. This is in violation with the requirement of the partition of unity method that the shape function and the enhanced base must be linear independent (Babuška and Melenk 1997). Therefore, only the shape functions whose supports are crossed by the discontinuity will be enriched. In the figure, these nodes are marked by black circles. The other nodes (the white circles in the figure) remain unchanged. Since only the nodes of elements that are crossed by the discontinuity have additional degrees of freedom $\mathbf{b}_i$, the total number of degrees of freedom of the system is slightly larger than for the case without a discontinuity.

When an element is supported by one or more enriched nodes, its stiffness matrix and force vector will obtain the additional coupling terms as derived in equations (2.36) to (2.38). The elements that contain a discontinuity as well, will be augmented with the surface integrals that govern the cohesive behaviour. It is assumed that the discontinuity within an element is a straight line, Figure 2.5. As a result, the transformation matrix $\mathbf{Q}$ that maps the discontinuity local frame of reference to the global $x - y$ coordinate system, see (2.33) is constant throughout the element. It was demonstrated by Wells and Sluys (2001a) that the error introduced is negligible.

The various integrals in the equilibrium equations (2.35)-(2.38) can be integrated numerically, e.g. using a Newton-Cotes or the Gauss-Seidel scheme.

The latter one is often preferred since an optimal accuracy is achieved by using only a small number of sample points. A prerequisite for the use of the Gauss-Seidel scheme is that the field that is integrated is continuous and smooth. In this case however, the stress field in the elements that are crossed by a discontinuity is only piecewise continuous. Although the accuracy will increase when more sample points are being used, the result of the numerical procedure will never be exact.

The stress field is continuous and smooth on either side of a discontinuity in an element. And since the position of the discontinuity in the element is known exactly, the terms in the equilibrium equation can be integrated in parts (Wells and Sluys 2001a). The element is divided into a number of triangular or quadrilateral sub-elements which are integrated in a conventional way, using a Gauss integration scheme, and a minimum number of integration points, see Figure 2.6.

The integration of the discontinuity terms over $\mathcal{S}_\mathrm{d}$ in the equilibrium equations is rather straightforward. In the case of a two-dimensional implementation, the discontinuity is represented by a straight line and can be integrated using a one-dimensional integration scheme.

The introduction of enhanced basis terms to the conventional finite element shape functions has an effect on the condition number of the stiffness matrix of the problem. When the discontinuity crosses an element close to one of the nodes, as shown in Figure 2.7, the contributions of the various terms in the stiffness matrix is unbalanced. This will give rise to an ill-conditioned stiffness matrix, that cannot be solved, even when a direct solver is used (Wells and Sluys 2001a).

This problem can be circumvented by only enhancing the shape function of a node when it has a significant contribution to the global stiffness matrix. In order to determine which nodes should not be enhanced, Wells and Sluys (2001a) proposed the following criterion: When the discontinuity splits the element in such a way that one part of the element is much smaller than the other part, the node that supports the smallest part is not enhanced. Or, to put it in a more general way, all nodes of the element are enhanced, when the following condition is satisfied:

$$\frac{\min(\mathcal{V}^+, \mathcal{V}^-)}{\mathcal{V}} > \epsilon_\mathrm{tol}\,, \tag{2.39}$$

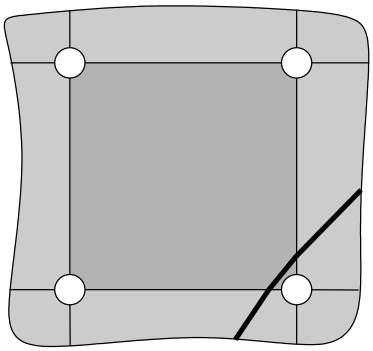

Figure 2.7 An element is crossed by a discontinuity near one of the nodes.

where ϵ_{tol} is a specific tolerance value which can be chosen between zero and one. When equation (2.39) is not met, only the nodes that support the larger of the two parts are enhanced. Clearly, omitting a support of the additional displacement field will affect the numerical results, but for reasonable low tolerance values, e.g. $\epsilon_{\text{tol}} = 0.05$, these effects are negligible.*

At this point, it is interesting to investigate the accuracy and the robustness of the partition of unity method with respect to conventional interface elements. In the following comparative numerical experiment, the effect of different schemes for the integration of the discontinuity term is studied (Schellekens and de Borst 1993, Remmers *et al.* 2001) .

Consider the beam shown in Figure 2.8. The beam is supported on both sides and has a notch in the centre. The dimensions are $w = 125\,\text{mm}$ and $h = 100\,\text{mm}$. The length of the notch is $a = 20\,\text{mm}$. The beam is made of an elastic, isotropic material with Young's modulus $E = 20\,000\,\text{MPa}$ and a Poisson's ratio $\nu = 0.2$. The applied load is equal to $P = 1000\,\text{N}$.

The finite element model consists of a structured grid of 51×20 four node elements or 25×10 eight node elements. The interface and the notch are represented by a discontinuity. In the notch, $0 < y < 20\,\text{mm}$, a traction-free constitutive relation is used, i.e. the tractions and the consistent tangent are identical to zero, irrespective of the magnitude of the displacement jump. At

*Due to the fact that the incorporation of a discontinuity affects the condition of a stiffness matrix, the use of an iterative solver is limited. For systems of equations with a high condition number, the number of iterations to obtain the correct solution increases significantly.

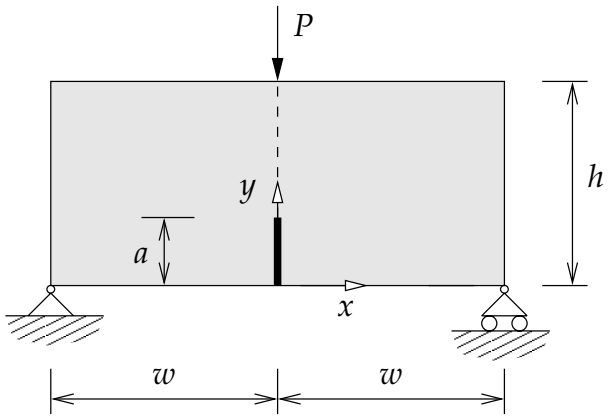

Figure 2.8 Geometry and boundary conditions of a notched beam in a three point bending test.

the interface, when $y > 20\,\text{mm}$, a linear-elastic constitutive relation is applied:

$$\mathbf{t}_\text{d} = \mathbf{T}_\text{d}\mathbf{v}_\text{d}\,; \qquad \text{where } \mathbf{T}_\text{d} = \begin{bmatrix} D & 0 \\ 0 & D \end{bmatrix}, \tag{2.40}$$

where D is the elastic dummy stiffness. Calculations have been carried out for different magnitudes of the dummy stiffness. The discontinuity is integrated using either a Gauss-Seidel or a lumped Newton-Cotes integration scheme. Since both the kinematic and the constitutive relations are linear, the equilibrium of the beam for the given load can be calculated in just a single iteration. The traction profiles at the interface are shown in Figures 2.9 to 2.11.
The most striking result from the experiments are the traction oscillations in the discontinuity when a Gauss-Seidel integration scheme is used. Moreover, it can be seen that the amplitude of the oscillations increases when the dummy stiffness D is increased. These phenomena are also observed in traditional interface elements (Schellekens and de Borst 1993). As with these elements, the oscillations disappear when a lumped integration scheme is used, see Figure 2.10. In Figure 2.11 it is shown that over-integration with this scheme again results in stress oscillations.

It can be demonstrated that the partition of unity approach to cohesive fracture is mathematically identical to the traditional interface element formulation (Simone *et al.* 2001). And apparently, as can be concluded from the

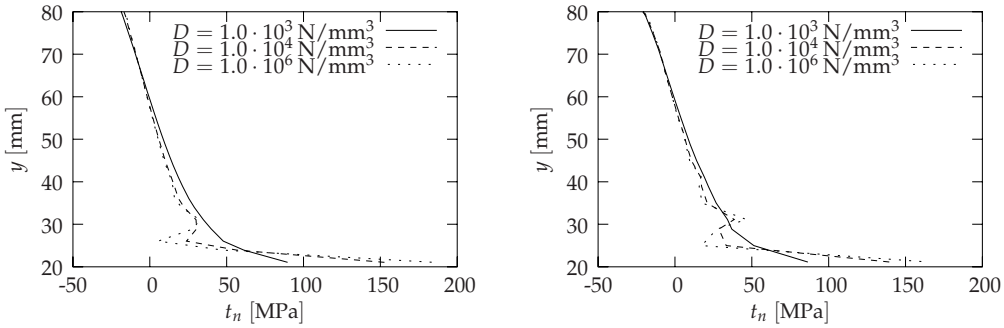

(a) Four node elements (b) Eight node elements

Figure 2.9 Normal traction t_n vs the location at the interface for different magnitudes of the dummy stiffness D using a Gauss-Seidel integration scheme to integrate the tractions at the discontinuity. Note that the amplitude of the traction oscillations increases with an increasing dummy stiffness (Remmers *et al*. 2001).

simulations, the partition of unity elements have inherited exactly the same numerical anomaly of traction oscillations when a relatively high dummy stiffness is utilised. In order to avoid possible numerical problems, in the remainder of this thesis, a lumped integration scheme is used for the numerical integration of the internal boundary $\mathcal{S}_\mathrm{d}$.

In principle, since the discontinuity can be extended during a simulation, it is no longer required to model a perfect bond prior to cracking using a high dummy stiffness. Nevertheless, the partition of unity method can also be used to model predefined interfaces in structures, as demonstrated in this example. The true advantage of this approach is that there is no longer a need to align the structure of the mesh with the geometry of the interface. A good example can be found in (Moës *et al.* 2003), where the complex geometry of a woven composite is efficiently modelled in three dimensions using the partition of unity approach. In chapter 5 an alternative application in combination with discontinuous crack growth will be presented.

Propagating discontinuity in a predetermined direction

The most important advantage of the partition of unity approach over conventional techniques is the possibility to extend a cohesive zone during a sim-

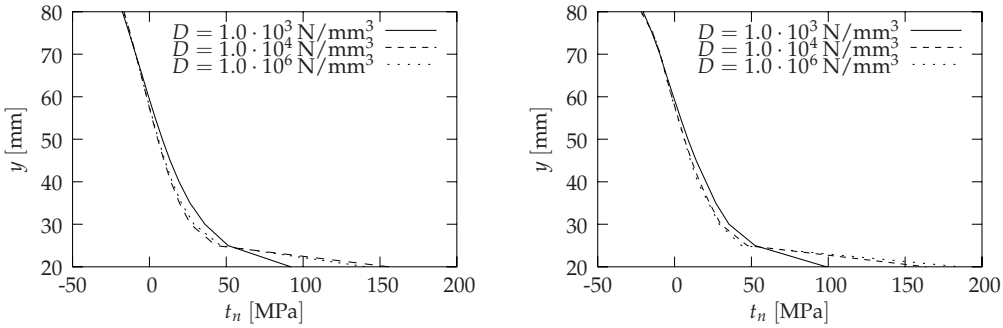

(a) Four node elements

(b) Eight node elements

Figure 2.10 Normal traction t_{n} vs. the location at the interface for different magnitudes of the dummy stiffness D using a lumped integration scheme (Remmers *et al*. 2001).

ulation. Apart from the fact that the number of additional degrees of freedom remains small, the use of a high dummy stiffness to mimic a perfect bond prior to cracking is then avoided. As a result, the chance of having traction oscillations due to large differences in stiffnesses of the interface and the bulk material is reduced to a minimum.*

Consider the domain with an initial crack or cohesive zone as shown in Figure 2.12. In contrast to the previous situation, the discontinuity does not cross the entire specimen but has a tip instead. When the tip is the terminus of a traction free discontinuity, it will give rise to a singular displacement field (Inglis 1913). In order to model such a situation adequately, two approaches can be found in literature.

The most accurate approach is to model the singular displacement fields exactly by incorporating a second additional enhanced basis in the elements around the tip (Moës and Belytschko 2002). The origin of this approach dates back from the days that the partition of unity method was used as a mesh independent way to represent a traction free discontinuity within a linear elastic fracture model (Belytschko and Black 1999). In this model, the exact instance

*Since the problem of traction oscillations is inherent in the cohesive zone approach to fracture, it will not completely disappear when the use of dummy stiffnesses is avoided. As noted by Simone *et al.* (2001), in the case of unloading right after debonding, the stiffness at the discontinuity can still be very large with respect to the stiffness of the surrounding bulk material. Nevertheless, this would be a rare event.

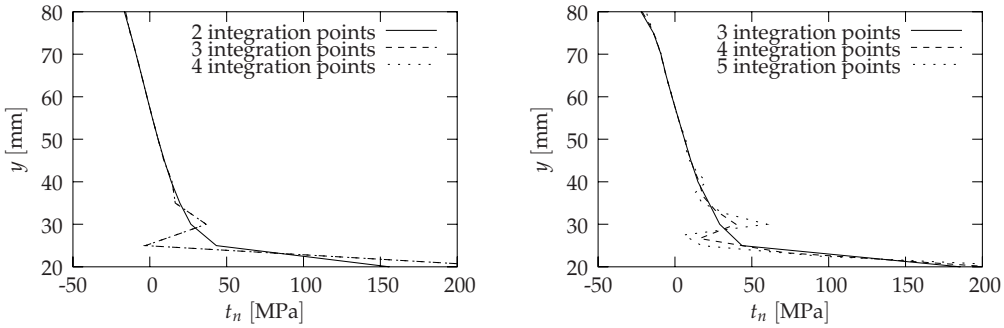

(a) Four node elements (b) Eight node elements

Figure 2.11 Normal traction t_{n} vs. the location at the interface for different number of integration points. The effect of over-integration on the normal traction is clearly visible. All simulations are performed using a Newton-Cotes integration scheme for the discontinuity terms (Remmers *et al.* 2001).

at which the crack should be extended, a stress criterion based on the full singular displacement field around the tip, is used. Indeed, the approach is accurate, also in combination with a cohesive approach to fracture, but loses generality as soon as a non-linear constitutive relation for the bulk material is used. Moreover, there is a serious overhead in the computational costs, because the approach requires a significant number of temporary additional degrees of freedom on top of the additional degrees of freedom that model the displacement jump.

An alternative approach, which will be pursued in the remainder of this thesis, was suggested by Wells and Sluys (2001a). In their model, a discontinuity is always extended across a complete element such that the tip touches the next element boundary. In order to enforce a zero displacement jump at the tip, the nodes that support this boundary are not enhanced, as can be seen in Figure 2.5. In contrast with the previous approach, the displacement field around the tip is represented by the standard, linear or quadratic, finite element shape functions. Nevertheless, by virtue of the fact that in the cohesive approach, the process zone is smeared out onto a single plane ahead of the crack tip, the displacement field in this region is relatively smooth. As a result, neglecting the higher order terms in the displacement field will hardly influence the accuracy, robustness and stability of the finite element calculations.

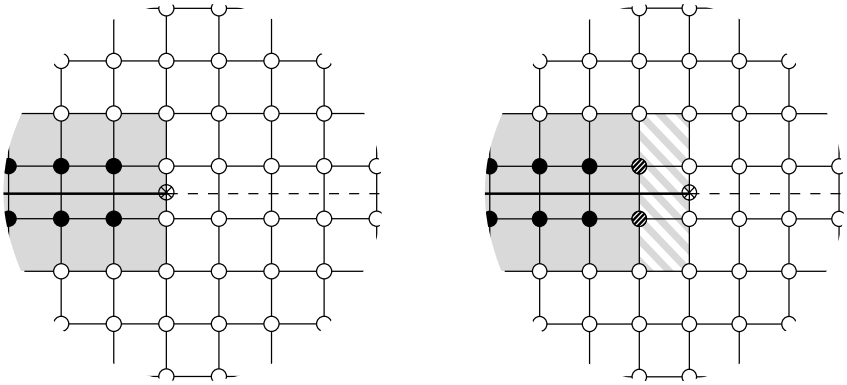

Figure 2.12 Extension of a discontinuity. Left: When the tractions in the additional sample point, denoted by $\otimes$, exceed the threshold value, the discontinuity is extend into the next element along the project weak interface (dashed line). Right: The hashed nodes and elements have just been enhanced. Note that in both pictures, the nodes that support the current crack tip are not enhanced in order to enforce a zero opening at the crack tip.

Crack growth (or strictly speaking: the extension of a discontinuity) is governed by the stress state at the tip. In the current example, the direction in which the discontinuity is extended is determined by the original problem. After all, the crack will propagate along the weak interface between the two layers of the double cantilever beam.

When the stress state in the tip exceeds the value of the ultimate traction of the adhesive material, the discontinuity is extended into the next element. All nodes of this element are enhanced, except for the ones that support the new tip, see Figure 2.12. The opening of the discontinuity is governed by the cohesive constitutive relation. The tractions, which are initially identical to the ultimate tractions, are decreased to zero according to a damage or softening relation.

The performance of the method is demonstrated in the following test. Consider a laminate as shown in Figure 2.13. The laminate with length $l = 10\,\mathrm{mm}$ consists of two layers with the same thickness $h = 0.5\,\mathrm{mm}$ and with identical isotropic material properties, Young's modulus $E = 100.0\,\mathrm{MPa}$ and Poisson's ratio $\nu = 0.3$. The two layers are connected with an adhesive with a normal strength $t_{\max} = 1.0\,\mathrm{MPa}$ and a fracture toughness of $\mathcal{G}_c = 0.1\,\mathrm{N/mm}$. The

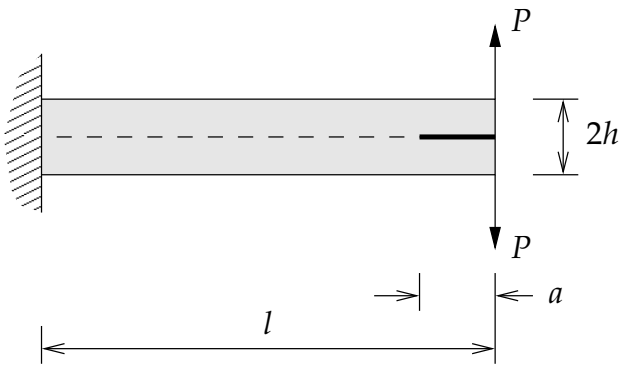

Figure 2.13 Geometry and boundary conditions of a double cantilever beam with an initial delamination.

initial delamination measures $a = 1.0\,\text{mm}$. An external load P is applied at the tips of both layers.

Delamination growth in a laminate with a symmetric lay-up can be modelled with a mode-I delamination model (Wells and Sluys 2001b) where the shear traction is assumed to remain zero. In this model, a loading function f is defined as:

$$f(v_n, \kappa) = v_n - \kappa\,, \tag{2.41}$$

where v_n is the normal separation of the crack and κ a history parameter. This history parameter is equal to the largest value of v_n reached hitherto. When $f = 0$, loading occurs and when $f < 0$ there is unloading. The normal traction force t_n at the crack edges decreases exponentially, according to the following equation:

$$t_\text{n} = t_\text{max} \exp\left(-\frac{t_\text{max}}{\mathcal{G}_c}\kappa\right). \tag{2.42}$$

In order to have quadratic convergence in a Newton-Raphson procedure for obtaining equilibrium at a structural level, a consistently linearised tangent matrix $\mathbf{T}_\text{d}$ has been derived:

$$\mathbf{T}_\text{d} = \begin{bmatrix} T_{11} & 0 \\ 0 & 0 \end{bmatrix} \qquad \text{where } T_{11} = -\frac{t_\text{max}^2}{\mathcal{G}_c} \exp\left(-\frac{t_\text{max}}{\mathcal{G}_c}\kappa\right). \tag{2.43}$$

Note that the cohesive constitutive relation consists of a debonding part only. Obviously, since the cohesive surface is only created upon crack propagation,

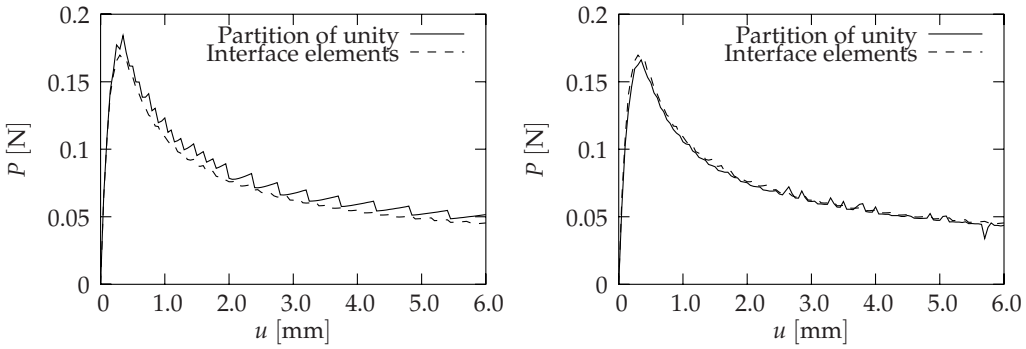

(a) Four node elements (b) Eight node elements

Figure 2.14 Applied load P vs. the tip displacement u of the double cantilever beam using the partition of unity approach and with traditional interface elements. (Remmers *et al.* 2001).

the cohesive relation does not need an elastic part to model a perfect bond prior to cracking. Due to the pure mode-I fracture conditions, the discontinuity is extended when the maximum stress in tip in the direction perpendicular to the weak interface (i.e. the y-direction) exceeds the normal strength $t_{\max}$.

The specimen has been analysed with both four node and eight node quadrilateral elements, as well with structured as with unstructured meshes. The results are compared to a model with conventional interface elements which are placed in the finite element mesh beforehand. The debonding part of the constitutive relation for these elements is described by equation (2.42). The behaviour of the interface prior to cracking is modelled with a linear elastic constitutive model with a dummy stiffness $D = 1.0{\cdot}10^6$ N/mm^3.

The load displacement curves of the analyses with the various models are given in Figure 2.14. The load-displacement curves obtained using the partition of unity approach are globally identical to the traditional method with interface elements. The small jumps in the load-displacement curve are related to the coarseness of the finite element mesh. Since a discontinuity is extended across an entire element, a significant part of the interface, i.e. the length of the element, is suddenly softening. In conventional interface elements, this transition from a perfect bond into softening behaviour occurs on the integration point level. By virtue of the fact that an integration point covers a smaller part of the interface, the overshoot is considerably smaller.

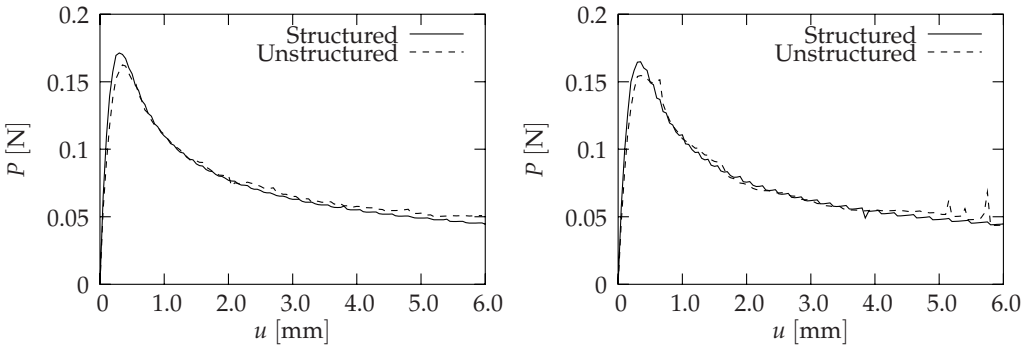

(a) Four node elements (b) Eight node elements

Figure 2.15 Applied load P vs. the tip displacement of the double cantilever beam using the partition of unity approach and with structured and unstructured meshes (Remmers *et al.* 2001).

Figure 2.15 shows the load-displacement curves of the model with unstructured meshes. Clearly, results are insensitive to the structure of the underlying finite element mesh. Figure 2.16 shows the deformed specimen with a structured and an unstructured mesh. The elements that appear to be extremely distorted actually contain the discontinuity.

Propagating discontinuity in an arbitrary direction

In the previous example, the direction of the crack was known beforehand. In most cases however, the trajectory of a crack depends on the boundary and/or the loading conditions of the specimen.* In this situation, an additional criterion must be used to predict the direction of the extension of the crack. The most efficient choice is to combine this with the criterion that determines the onset of a crack extension. Wells and Sluys (2001a) used the magnitude and the directions of the principal stress states at the current tip of the discontinuity. When the maximum principal stress exceeds a specific yield criterion, the discontinuity is extended into the next element in the direction normal to the

*Clearly, the micro-structure of the material has an important influence on the trajectory of the crack as well. In this chapter, the bulk material is considered to be homogeneous. The effect of heterogeneities in the micro-structure will be discussed in chapter 5.

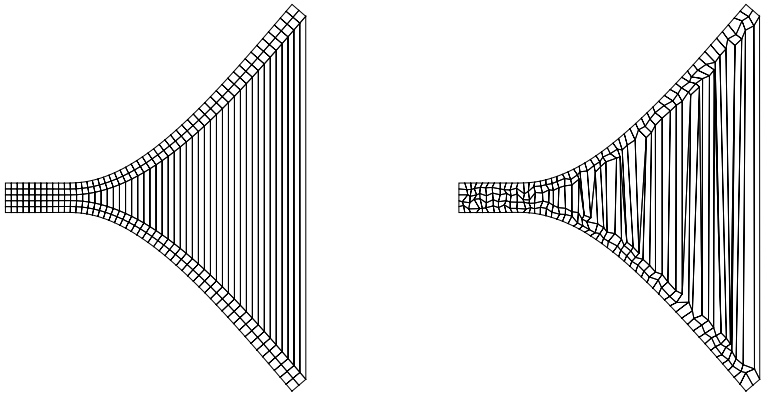

(a) Structured mesh (b) Unstructured mesh

Figure 2.16 Deformed mesh of the double cantilever beam peel test (Remmers *et al.* 2001). The deformations in this picture are not scaled up.

corresponding principal axis.*

However, the stress state obtained from a temporary sample point at the tip of the discontinuity gives inaccurate results. A better approach to determine the stress state in the tip is by using a non-local approach using a Gaussian weight function. This approach has been used successfully to determine the direction of fracture in an incompatible modes type model by Jirásek (1998). The stresses in the tip are a weighted sum of local stresses in the Gauss integration points in the model:

$$\boldsymbol{\sigma}_{\text{tip}} = \sum_{i=1}^{n_{int}} \frac{w_i}{w_{\text{tot}}} \boldsymbol{\sigma}_i \,; \qquad \text{using} \quad w_{\text{tot}} = \sum_{j=1}^{n_{int}} w_j \,, \tag{2.44}$$

where n_{int} is the total number of integration points in the domain, $\boldsymbol{\sigma}_i$ the current stress state in that integration point i and w_i a weight factor, defined as

$$w_i = \frac{(2\pi)^{2/3}}{l_a^3} \exp\left(-\frac{r_i^2}{2l_a^2}\right). \tag{2.45}$$

*In an alternative approach the direction of the extension of the cohesive zone in the finite element mesh is calculated by means of a *level set functions* (Moës *et al.* 2002). Especially in those situations when the determination of the trajectory of a crack is rather laborious, e.g. in three-dimensional models, this method has certain advantages. However, it requires the solution of an additional numerical problem and will not be discussed within the scope of this thesis.

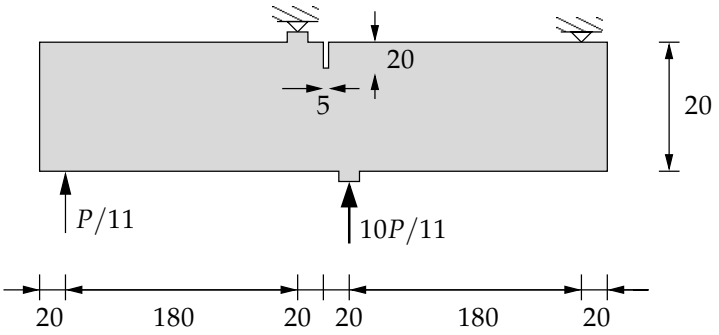

Figure 2.17 Geometry and loading conditions of the single-edge notched beam. All dimensions are in millimetres.

In this relation, r_i is the distance between integration point i and the tip of the discontinuity and l_a is a length scale parameter which determines how quickly the influence of a sample point decays away from the tip. Wells and Sluys (2001a) have taken this parameter l as approximately three times the typical element length l_e. A disadvantage of the approach is that the average stress is significantly smaller than the actual stress at the tip. As a result, the discontinuity will be extended slightly late.

One of the most illustrative examples to demonstrate the advantages of the partition of unity method is the single-edge notched beam experiment. Consider the specimen in Figure 2.17. It is made of concrete with Young's modulus $E = 35.0\,\text{GPa}$ and Poisson's ratio $\nu = 0.15$. The tensile strength and the fracture toughness are $t_{\max} = 2.8\,\text{MPa}$ and $\mathcal{G}_c = 0.1\,\text{N/mm}$, respectively. The beam has been analysed under plane strain conditions. Mesh consists of 1184 six node triangular elements. The response of the structure is determined under a crack mouth opening displacement control (de Borst 1987).

The trajectory of the discontinuity at the end of the analysis is projected onto the finite element mesh in Figure 2.18. The position of the crack is in agreement with experimental results (Schlangen 1993) and numerical simulations by Rots (1991) and Peerlings *et al.* (1998). Note that the position of the discontinuity is completely independent of the structure of the underlying finite element mesh. Figure 2.19 shows the σ_{xx} stresses in the deformed specimen. In this figure, a new post-processing technique has been used to visualise the crack. A detailed description can be found in Appendix A.

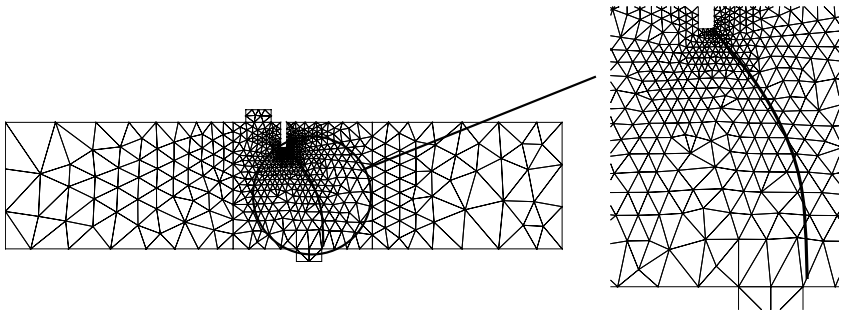

Figure 2.18 Position of the discontinuity in the single edge notched beam (Wells and Sluys 2001).

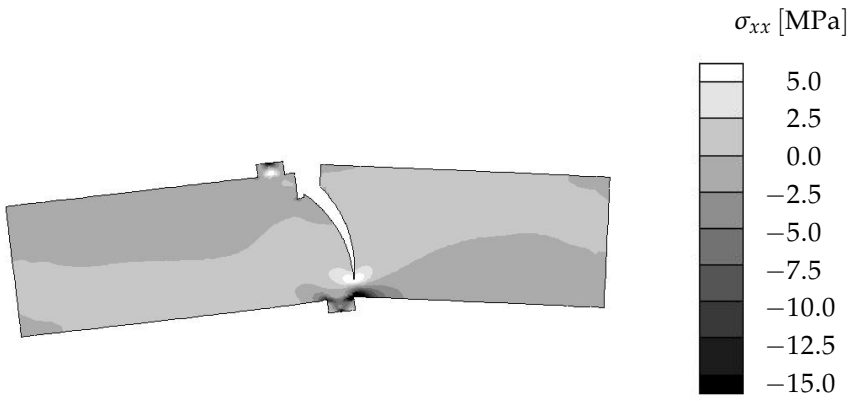

Figure 2.19 Deformation of the single edge notched beam and σ_{xx} stresses. The displacements are amplified by a factor 100.

§ 2.5 Other applications

The partition of unity approach to fracture, as presented here in the most elementary way, has been a starting point for the development of a large number of numerical techniques. Simone and Sluys (2004) used the partition of unity method in combination with a continuum damage model to simulate crack propagation in a regularised strain softening medium.

In order to arrive at a model that is able to handle large deformations, the method has been implemented in a finite strain continuum model (Wells *et al.* 2002). The discontinuous displacement field (2.1) can be used to set up a position vector of a material point in the deformed configuration, according

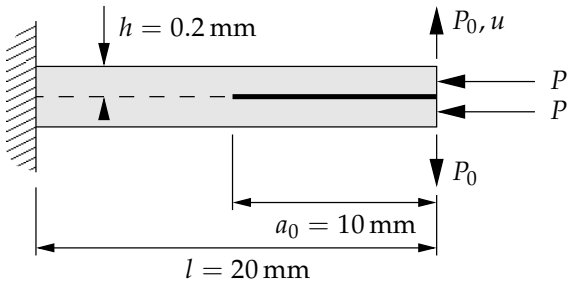

Figure 2.20 Double cantilever beam with an initial delamination a_0 under compression. The small perturbation forces P_0 are applied to trigger the buckling mode (Wells *et al*. 2003).

to:

$$\mathbf{x} = \mathbf{X} + \hat{\mathbf{u}} + \mathcal{H}_{\Gamma_{\text{d},0}}\tilde{\mathbf{u}}\,, \tag{2.46}$$

where $\mathbf{x}$ and $\mathbf{X}$ are the position vectors of a material point in deformed and undeformed (reference) configuration, respectively, and $\mathcal{H}_{\Gamma_{\text{d},0}}$ is the step function with respect to the undeformed configuration. The deformation gradient $\mathbf{F}$ is obtained by taking the gradient of (2.46) with respect to the reference configuration:

$$\mathbf{F} = \mathbf{I} + \nabla_{\mathbf{X}}\hat{\mathbf{u}} + \mathcal{H}_{\Gamma_{\text{d},0}}\nabla_{\mathbf{X}}\tilde{\mathbf{u}}\,; \qquad \mathbf{X} \notin \Gamma_{\text{d},0}\,. \tag{2.47}$$

The vector that represents the displacement jump remains identical to the displacement jump in the small strain formulation (2.7). The kinematic relations can be used to construct the equilibrium equations in weak form. This procedure is to a certain extent identical to the derivation of the governing equation in the small strain case. The update of the orientation of the discontinuity in the deformed configuration requires some extra attention.

The fact that the deformation gradient on either side of the discontinuity can be completely different, the model is able to capture geometric instabilities at the interface. This can be simulated by the following delamination buckling test. Figure 2.20 shows a double cantilever beam with an initial delamination $a_0 = 10.0\,\text{mm}$ (Wells *et al.* 2003). The beam is subjected to an axial compressive force $2P$. Two perturbation forces $P_0 = 0.001\,\text{N}$ are applied to trigger the correct buckling mode. Both layers are made of the same material with Young's modulus $E = 135\,\text{GPa}$ and Poisson's ratio 0.18. The ultimate strength of the interlaminar bonding in mode I is $t_{\max} = 50.0\,\text{N/mm}^2$. The

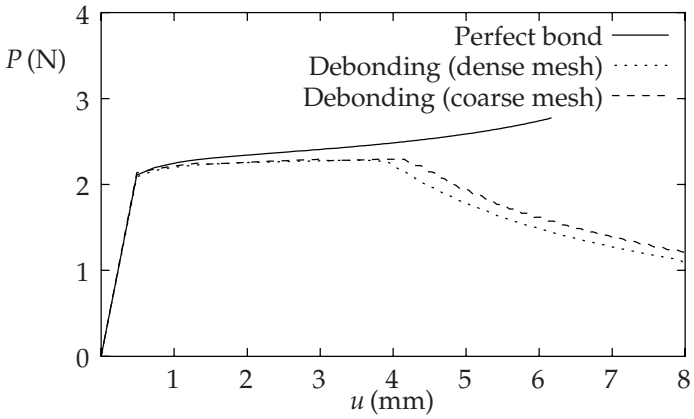

Figure 2.21 Tip displacement u of the double cantilever beam vs. the compressive load P. The load-displacement curves of two different finite element meshes are compared with the case where delamination growth is prevented (Wells *et al* 2003).

shear stiffness is equal to zero; the fracture toughness is set to $\mathcal{G}_c = 0.8\,\mathrm{N/mm}$. The critical load for local buckling (without delamination propagation) can be calculated analytically using the equation for a single cantilever beam with length a_0 and height h. For the configuration in Figure 2.20 and the adopted elastic material parameters, the analytical buckling load is equal to:

$$P_{\mathrm{cr}} = \frac{\pi^2 E h^3}{48 a_0^2} = 2.22\,\mathrm{N}\,. \tag{2.48}$$

The finite element mesh consists of 750 eight node quadrilateral elements, three elements through the thickness and 250 elements in the length. In order to emphasise the performance of the model with respect to spatial discretisation, the calculations have also been performed with a much coarser mesh that consists of just one element through the thickness and 100 in length direction. Note that in the latter case, both layers of the double cantilever beam are modelled with just one element.

Figure 2.21 shows the lateral displacement u of the beam as a function of the external force P. The load-displacement curve for a specimen with a perfect bond is given as a reference. The buckling load is in agreement with the analytical calculation in (2.48). Delamination propagation is initiated at a lateral displacement $u = 4\,\mathrm{mm}$. From this point on, the equilibrium is unstable.

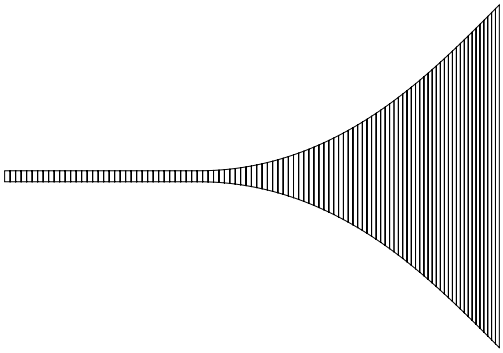

Figure 2.22 Deformation of the coarse mesh after buckling and delamination growth, tip displacement 6 mm (Wells *et al*. 2003).

The small difference between the curves for the dense and the coarse meshes can be attributed to the different densities of these meshes. Figure 2.22 shows the final deformation of the two models at a tip displacement $u = 6\,\text{mm}$.

Chapter 3

A solid-like shell element allowing for arbitrary delaminations

In the previous chapter, a general framework has been provided for the incorporation of a cohesive surface in a continuum finite element by means of the partition of unity method. It was demonstrated in the final example, that the method can be applied to elements that are based on a geometrically nonlinear kinematic formulation, without indulging on the special performances of the element (Wells *et al.* 2003). In this chapter, the method is applied to a solid-like shell element for the simulation of delamination growth in thin walled structures on a mesoscopic level of observation.

§ 3.1 The simulation of delamination

Traditionally, the numerical analysis of thin-walled structures on a macroscopic level of observation is performed by means of a special class of finite elements, commonly denoted as shell elements (Naghdi 1972, Simo and Fox 1989). These structural elements take optimal advantage of the fact that the through-the-thickness dimension of the structure is relatively small compared to the other, span-wise, dimensions. The kinematic relations and balance equations that describe the mechanical behaviour of the shell in the through-the-thickness direction are lumped into a single plane, the mid-surface of the structure. The rotation of the element's local frame of reference, which is attached to the mid-surface, is described by an additional set of rotational degrees of freedom that is added to all the nodes of the element.

Over the years, this numerical approach has resulted in a large number of different plate and shell elements, e.g. (Bathe and Dvorkin 1986, Rebel 1998), which have been used in a variety of applications, such as the analysis of the structural stability of aerospace structures (Riks and Rankin 1997). Unfortunately, due to the aforementioned approximations, the simulation of material degradation in the structure on a smaller level of observation, i.e. the mesoscopic level, appears to be problematic. The correct modelling of plasticity or damage due to bending or shear deformations requires an exact representation of the strains in all material points in the trough-the-thickness direction of the shell. Moreover, the simulation of delamination growth by stacking multiple shell elements and interface elements is not straightforward either. Apart from the lack of a physical thickness of a shell element, the coupling of the rotational degrees of freedom and the kinematic relation of the interface elements is still a point of discussion.

The mesocopic analysis of failure mechanisms in thin-walled structures requires a full three-dimensional numerical model. However, due to the slender nature of the structure, a manageable model will automatically consist of volume elements with an extremely high aspect ratio between the spanwise dimensions and the through-the-thickness dimension. Under such circumstances, conventional volume elements show an overly stiff behaviour (Bisschoff and Ramm 1997). This effect, which is often denoted as *Poisson-thickness locking*, can be avoided when the spatial dimensions of the elements in all three directions are of the same order of magnitude. This will result in very accurate but large numerical models, which are too expensive to be used in engineering applications.

Alternatively, Poisson-thickness locking can be avoided by the incorporation of a higher order strain field in the through-the-thickness direction of volume elements. This can be achieved in several ways, for example by using the enhanced assumed strain method (Klinkel *et al.* 1999). In the solid-like shell element by Parisch (1995), an additional set of internal degrees of freedom is used to add a quadratic term to the displacement field in the through-the-thickness direction, the internal 'stretch' of the element. As a result, the corresponding strain field varies linearly over the thickness instead of being constant and Poisson-thickness locking is avoided. The internal degrees of freedom are condensed on the element level and the element can be used in a

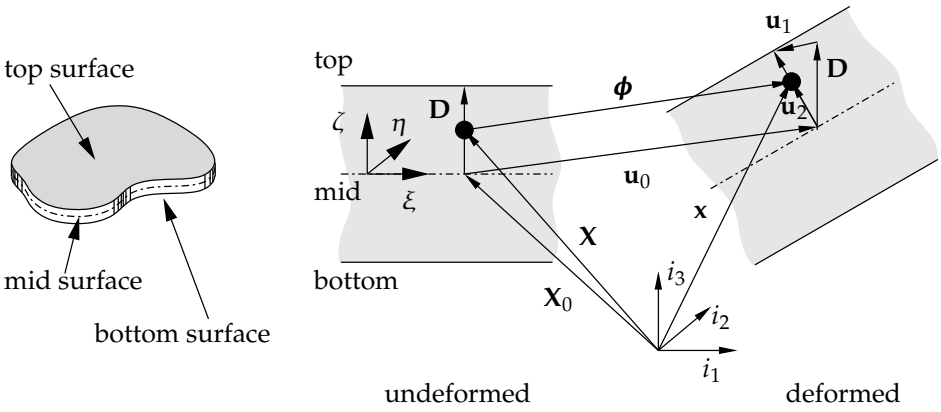

Figure 3.1 Geometry and kinematics of the thick shell in undeformed and deformed position. The dash-dotted line denotes the mid-surface of the shell.

finite element model as a regular volume element with only three translational degrees of freedom per node.

The solid-like shell element has been used successfully in combination with regular interface elements to model delamination growth in laminated structures (Hashagen *et al.* 1999). Plasticity or damage in the layers can be modelled with regular continuum material models (Hashagen and de Borst 2001). The kinematic relations of the element are described with a geometrical nonlinear theory, which allows the analysis of structural stability, even in combination with delamination growth (Remmers and de Borst 2001b).

It is possible to model a complete laminate with just one solid-like shell element in the through-the-thickness direction. In such a situation, the element is divided into a number of sub-domains, each with its own material model. In this chapter, we will extend this model with the possibility to initiate and propagate delaminations at arbitrary locations within the shell during the loading process. The new model allows for the simulating of the complete mechanical behaviour of laminated structures with just one element in the thickness direction.

§ 3.2 Kinematic relations

Consider a shell with constant thickness as shown in Figure 3.1. The position of a material point in the shell in the undeformed configuration can be written as a function of the three curvilinear coordinates $[\xi, \eta, \zeta]$:

$$\mathbf{X}(\xi, \eta, \zeta) = \mathbf{X}_0(\xi, \eta) + \zeta \mathbf{D}(\xi, \eta)\,, \tag{3.1}$$

where $\mathbf{X}_0(\xi, \eta)$ is the projection of the point on the mid-surface of the shell and $\mathbf{D}(\xi, \eta)$ is the thickness director in this point:

$$\begin{aligned} \mathbf{X}_0(\xi, \eta) &= \frac{1}{2}\big[\mathbf{X}_t(\xi, \eta) + \mathbf{X}_b(\xi, \eta)\big]\,, \\ \mathbf{D}(\xi, \eta) &= \frac{1}{2}\big[\mathbf{X}_t(\xi, \eta) - \mathbf{X}_b(\xi, \eta)\big]\,. \end{aligned} \tag{3.2}$$

The subscripts $(\cdot)_t$ and $(\cdot)_b$ denote the projections of the variable onto the top and bottom surface, respectively. The position of the material point in the deformed configuration $\mathbf{x}(\xi, \eta, \zeta)$ is related to $\mathbf{X}(\xi, \eta, \zeta)$ via the displacement field $\boldsymbol{\phi}(\xi, \eta, \zeta)$ according to:

$$\mathbf{x}(\xi, \eta, \zeta) = \mathbf{X}(\xi, \eta, \zeta) + \boldsymbol{\phi}(\xi, \eta, \zeta)\,, \tag{3.3}$$

where:

$$\boldsymbol{\phi}(\xi, \eta, \zeta) = \mathbf{u}_0(\xi, \eta) + \zeta \mathbf{u}_1(\xi, \eta) + (1 - \zeta^2)\mathbf{u}_2(\xi, \eta)\,. \tag{3.4}$$

In this relation, $\mathbf{u}_0$ and $\mathbf{u}_1$ are the displacements of $\mathbf{X}_0$ on the shell mid-surface, and the thickness director $\mathbf{D}$, respectively:

$$\begin{aligned} \mathbf{u}_0(\xi, \eta) &= \frac{1}{2}\big[\mathbf{u}_t(\xi, \eta) + \mathbf{u}_b(\xi, \eta)\big]\,, \\ \mathbf{u}_1(\xi, \eta) &= \frac{1}{2}\big[\mathbf{u}_t(\xi, \eta) - \mathbf{u}_b(\xi, \eta)\big]\,, \end{aligned} \tag{3.5}$$

and $\mathbf{u}_2(\xi, \eta)$ denotes the internal stretching of the element, which is co-linear with the thickness director in the deformed configuration and is a function of an additional 'stretch' parameter w:

$$\mathbf{u}_2(\xi, \eta) = w(\xi, \eta)[\mathbf{D}(\xi, \eta) + \mathbf{u}_1(\xi, \eta)]\,. \tag{3.6}$$

In the remainder, the displacement field $\boldsymbol{\phi}$ will be considered as a function of two kinds of variables; the ordinary displacement field $\mathbf{u}$, which will be split

in a displacement of the top and bottom surfaces $\mathbf{u}_t$ and $\mathbf{u}_b$, respectively, and the internal stretch parameter w:

$$\boldsymbol{\phi} = \boldsymbol{\phi}(\mathbf{u}_t, \mathbf{u}_b, w)\,. \tag{3.7}$$

Discontinuous displacement field

Next, we assume that the thick shell is crossed by a discontinuity surface $\Gamma_{d,0}$ which divides the domain into two parts, Ω_0^+ and Ω_0^-, see Figure 3.2. It is assumed that the discontinuity surface is parallel to the mid-surface of the thick shell. The displacement field $\boldsymbol{\phi}(\xi, \eta, \zeta)$ can now be regarded as a continuous regular field $\hat{\boldsymbol{\phi}}$ with an additional continuous field $\tilde{\boldsymbol{\phi}}$ that determines the magnitude of the displacement jump, see also (2.1). The position of a material point in the deformed configuration can then be written as:

$$\mathbf{x} = \mathbf{X} + \hat{\boldsymbol{\phi}} + \mathcal{H}_{\Gamma_{d,0}}\tilde{\boldsymbol{\phi}}\,, \tag{3.8}$$

where $\mathcal{H}_{\Gamma_{d,0}}$ represents the step function, defined as:*

$$\mathcal{H}_{\Gamma_{d,0}}(\mathbf{X}) = \begin{cases} 1 & \text{if} \quad \mathbf{X} \in \Omega_0^+\,, \\ 0 & \text{if} \quad \mathbf{X} \in \Omega_0^-\,. \end{cases} \tag{3.9}$$

Since the displacement field $\boldsymbol{\phi}$ is a function of the variables $\mathbf{u}_t$, $\mathbf{u}_b$ and w, these three terms must be split in a regular and additional part accordingly:

$$\begin{aligned} \mathbf{u}_t &= \hat{\mathbf{u}}_t + \mathcal{H}_{\Gamma_{d,0}}\tilde{\mathbf{u}}_t; \\ \mathbf{u}_b &= \hat{\mathbf{u}}_b + \mathcal{H}_{\Gamma_{d,0}}\tilde{\mathbf{u}}_b; \\ w &= \hat{w} + \mathcal{H}_{\Gamma_{d,0}}\tilde{w}\,. \end{aligned} \tag{3.10}$$

Inserting equation (3.10) into (3.5) and (3.6) gives:

$$\begin{aligned} \mathbf{u}_0 &= \hat{\mathbf{u}}_0 + \mathcal{H}_{\Gamma_{d,0}}\tilde{\mathbf{u}}_0; \\ \mathbf{u}_1 &= \hat{\mathbf{u}}_1 + \mathcal{H}_{\Gamma_{d,0}}\tilde{\mathbf{u}}_1; \\ \mathbf{u}_2 &= \hat{\mathbf{u}}_2 + \mathcal{H}_{\Gamma_{d,0}}\tilde{\mathbf{u}}_2\,, \end{aligned} \tag{3.11}$$

*Note that in this chapter, the displacement jump is represented by the standard Heaviside step function as defined in Table 2.1.

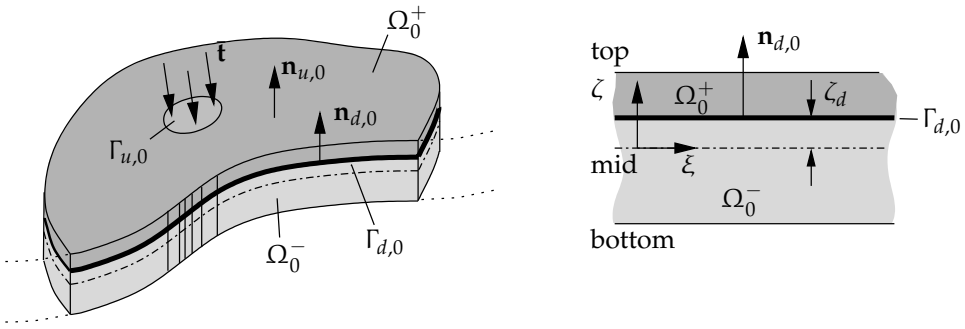

Figure 3.2 Thick shell crossed by a discontinuity $\Gamma_{d,0}$ (heavy line). The vectors $\mathbf{n}_{t,0}$ and $\mathbf{u}_{d,0}$ are perpendicular to the shell surface and the discontinuity surface, respectively.

where:

$$\begin{aligned}
\hat{\mathbf{u}}_0 &= \frac{1}{2}\big[\hat{\mathbf{u}}_t + \hat{\mathbf{u}}_b\big]\,; & \tilde{\mathbf{u}}_0 &= \frac{1}{2}\big[\tilde{\mathbf{u}}_t + \tilde{\mathbf{u}}_b\big]\,; \\
\hat{\mathbf{u}}_1 &= \frac{1}{2}\big[\hat{\mathbf{u}}_t - \hat{\mathbf{u}}_b\big]\,; & \tilde{\mathbf{u}}_1 &= \frac{1}{2}\big[\tilde{\mathbf{u}}_t - \tilde{\mathbf{u}}_b\big]\,; \\
\hat{\mathbf{u}}_2 &= \hat{w}\big[\mathbf{D} + \hat{\mathbf{u}}_1\big]\,; & \tilde{\mathbf{u}}_2 &= \tilde{w}\big[\mathbf{D} + \hat{\mathbf{u}}_1 + \tilde{\mathbf{u}}_1\big] + \hat{w}\tilde{\mathbf{u}}_1\,.
\end{aligned} \tag{3.12}$$

Note that the enhanced part of the internal stretch parameter $\mathbf{u}_2$, i.e. $\tilde{\mathbf{u}}_2$, contains regular variables and additional variables. The base vectors at the material point in undeformed configuration $\mathbf{G}_i$ can be found by differentiating the position vector $\mathbf{X}$ with respect to the iso-parametric coordinates $\Theta^i = [\xi, \eta, \zeta]$:

$$\begin{aligned}
\mathbf{G}_\alpha &= \frac{\partial \mathbf{X}}{\partial \Theta^\alpha} = \mathbf{E}_\alpha + \zeta \mathbf{D}_{,\alpha} \qquad \alpha = 1, 2\,; \\
\mathbf{G}_3 &= \frac{\partial \mathbf{X}}{\partial \Theta^3} = \mathbf{D} \quad ,
\end{aligned} \tag{3.13}$$

where $(\cdot)_{,\alpha}$ denotes the partial derivative with respect to Θ^α. $\mathbf{E}_\alpha$ is the covariant surface vector, which is the projection of the base vector $\mathbf{G}_\alpha$ on the mid-surface and is defined as:

$$\mathbf{E}_\alpha = \frac{\partial \mathbf{X}_0}{\partial \Theta^\alpha}\,. \tag{3.14}$$

The base vectors of the shell in the deformed configuration $\mathbf{g}_i$ are found in a similar fashion:

$$\begin{aligned}\mathbf{g}_\alpha =& \frac{\partial \mathbf{x}}{\partial \Theta^\alpha} = \mathbf{E}_\alpha + \hat{\mathbf{u}}_{0,\alpha} + \zeta \mathbf{D}_{,\alpha} + \zeta \hat{\mathbf{u}}_{1,\alpha} + \mathcal{H}_{\Gamma_{d,0}}\left[\tilde{\mathbf{u}}_{0,\alpha} + \zeta \tilde{\mathbf{u}}_{1,\alpha}\right] + \text{h.o.t.}\,, \\ \mathbf{g}_3 =& \frac{\partial \mathbf{x}}{\partial \Theta^3} = \mathbf{D} + \hat{\mathbf{u}}_1 - 2\zeta \hat{\mathbf{u}}_2 + \mathcal{H}_{\Gamma_{d,0}}\left[\tilde{\mathbf{u}}_1 - 2\zeta \tilde{\mathbf{u}}_2\right] + \text{h.o.t.}\end{aligned} \tag{3.15}$$

Due to the displacement jump, the base vectors in the deformed configuration $\mathbf{g}_i$ are not defined at the discontinuity $\Gamma_{d,0}$. The higher order terms (h.o.t.) in (3.15) contain terms up to the fourth order in the thickness coordinate ζ and the derivatives of the stretch parameter $\mathbf{u}_2$ with respect to the span-wise coordinates ξ and η. In the remainder, these terms will be neglected without a significant loss of accuracy of the kinematic model (Parisch 1995). The metric tensors $\mathbf{G}$ and $\mathbf{g}$ can be determined by using the base vectors $\mathbf{G}_i$ and $\mathbf{g}_i$ in equations (3.13) and (3.15):

$$G_{ij} = \mathbf{G}_i \cdot \mathbf{G}_j\,; \qquad g_{ij} = \mathbf{g}_i \cdot \mathbf{g}_j\,; \qquad i = 1,2,3\,; \tag{3.16}$$

Elaboration of the expressions yields the following components of the metric tensor in the undeformed configuration:

$$\begin{aligned} G_{\alpha\beta} &= \mathbf{E}_\alpha \cdot \mathbf{E}_\beta + \zeta\left[\mathbf{E}_\alpha \cdot \mathbf{D}_{,\beta} + \mathbf{E}_\beta \cdot \mathbf{D}_{,\alpha}\right]; \\ G_{\alpha 3} &= \mathbf{E}_\alpha \cdot \mathbf{D} + \zeta \mathbf{D}_{,\alpha} \cdot \mathbf{D}\,; \\ G_{33} &= \mathbf{D} \cdot \mathbf{D}\,, \end{aligned} \tag{3.17}$$

and in the deformed configuration (again neglecting the terms which are quadratic in thickness direction):

$$\begin{aligned} g_{\alpha\beta} =& (\mathbf{E}_\alpha + \hat{\mathbf{u}}_{0,\alpha} + \mathcal{H}_{\Gamma_{d,0}}\tilde{\mathbf{u}}_{0,\alpha}) \cdot (\mathbf{E}_\beta + \hat{\mathbf{u}}_{0,\beta} + \mathcal{H}_{\Gamma_{d,0}}\tilde{\mathbf{u}}_{0,\beta}) \\ &+ \zeta\big[(\mathbf{E}_\alpha + \hat{\mathbf{u}}_{0,\alpha} + \mathcal{H}_{\Gamma_{d,0}}\tilde{\mathbf{u}}_{0,\alpha}) \cdot (\mathbf{D}_{,\beta} + \hat{\mathbf{u}}_{1,\beta} + \mathcal{H}_{\Gamma_{d,0}}\tilde{\mathbf{u}}_{1,\beta}) \\ &\quad + (\mathbf{E}_\beta + \hat{\mathbf{u}}_{0,\beta} + \mathcal{H}_{\Gamma_{d,0}}\tilde{\mathbf{u}}_{0,\beta}) \cdot (\mathbf{D}_{,\alpha} + \hat{\mathbf{u}}_{1,\alpha} + \mathcal{H}_{\Gamma_{d,0}}\tilde{\mathbf{u}}_{1,\alpha})\big]\,; \\ g_{\alpha 3} =& (\mathbf{E}_\alpha + \hat{\mathbf{u}}_{0,\alpha} + \mathcal{H}_{\Gamma_{d,0}}\tilde{\mathbf{u}}_{0,\alpha}) \cdot (\mathbf{D} + \hat{\mathbf{u}}_1 + \mathcal{H}_{\Gamma_{d,0}}\tilde{\mathbf{u}}_1) \\ &+ \zeta\big[(\mathbf{D} + \hat{\mathbf{u}}_1 + \mathcal{H}_{\Gamma_{d,0}}\tilde{\mathbf{u}}_1) \cdot (\mathbf{D}_{,\alpha} + \hat{\mathbf{u}}_{1,\alpha} + \mathcal{H}_{\Gamma_{d,0}}\tilde{\mathbf{u}}_{1,\alpha}) \\ &\quad - 2(\mathbf{E}_\alpha + \hat{\mathbf{u}}_{0,\alpha} + \mathcal{H}_{\Gamma_{d,0}}\tilde{\mathbf{u}}_{0,\alpha}) \cdot (\hat{\mathbf{u}}_2 + \mathcal{H}_{\Gamma_{d,0}}\tilde{\mathbf{u}}_2)\big]\,; \\ g_{33} =& (\mathbf{D} + \hat{\mathbf{u}}_1 + \mathcal{H}_{\Gamma_{d,0}}\tilde{\mathbf{u}}_1) \cdot (\mathbf{D} + \hat{\mathbf{u}}_1 + \mathcal{H}_{\Gamma_{d,0}}\tilde{\mathbf{u}}_1) \\ &- \zeta 4(\mathbf{D} + \hat{\mathbf{u}}_1 + \mathcal{H}_{\Gamma_{d,0}}\tilde{\mathbf{u}}_1) \cdot (\hat{\mathbf{u}}_2 + \mathcal{H}_{\Gamma_{d,0}}\tilde{\mathbf{u}}_2)\,. \end{aligned} \tag{3.18}$$

We can rewrite these relations as:

$$\begin{aligned} G_{ij} &= G^0_{ij} + \zeta G^1_{ij}\,; \\ g_{ij} &= g^0_{ij} + \zeta g^1_{ij}\,. \end{aligned} \tag{3.19}$$

where G^0_{ij} and g^0_{ij} correspond to the constant terms in equations (3.17) and (3.18), whereas G^1_{ij} and g^1_{ij} correspond to the terms that vary linearly with respect to the thickness ζ. Apart from the covariant base vectors in the undeformed state, we will need the contravariant counterparts to derive the strain field later on. They can be derived as follows:

$$\mathbf{G}^j = (G_{ij})^{-1}\mathbf{G}_i\,. \tag{3.20}$$

The contravariant base vector $\mathbf{G}^j$ is related to the contravariant surface vector $\mathbf{E}^k$ via the so-called shell tensor μ^j_k (Ogden 1984):

$$\mathbf{G}^j = \mu^j_k \mathbf{E}^k; \qquad \mu^j_k = (\delta^j_k - \zeta \bar{G}^j_k)\mathbf{E}^k\,, \tag{3.21}$$

where δ^j_k is the Kronecker delta and $\bar{G}^j_k$ denotes the mixed variant metric tensor which is calculated with the contravariant and the covariant tensor components, equation (3.19):

$$\bar{G}^j_k = G^{0\ jm} G_{1\ mk} \tag{3.22}$$

It is emphasised that $\bar{G}^j_k$ is only non-zero when the undeformed shell is curved.

Green-Lagrange strain field

The Green-Lagrange strain tensor $\boldsymbol{\gamma}$ is defined conventionally in terms of the deformation gradient $\mathbf{F}$:

$$\boldsymbol{\gamma} = \frac{1}{2}(\mathbf{F}^{\mathrm{T}}\mathbf{F} - \mathbf{I})\,, \tag{3.23}$$

where $\mathbf{I}$ is the unit tensor. The deformation gradient $\mathbf{F}$ can be written as a function of the covariant base-vector in the deformed configuration $\mathbf{g}_i$ and the contravariant base-vector in the undeformed reference configuration $\mathbf{G}^i$:

$$\mathbf{F} = \mathbf{g}_i \otimes \mathbf{G}^i\,. \tag{3.24}$$

Inserting this relation in equation (3.23) we can write the Green-Lagrange strain tensor in terms of the contravariant basis $\mathbf{G}^j$:

$$\boldsymbol{\gamma} = \gamma_{ij}\mathbf{G}^i \otimes \mathbf{G}^j; \qquad \text{where:} \quad \gamma_{ij} = \frac{1}{2}(g_{ij} - G_{ij})\,. \tag{3.25}$$

Substituting equation (3.21) in this relation yields:

$$2\gamma_{ij} = (g_{ij} - G_{ij})(\delta^i_k - \zeta\bar{G}^i_k)(\delta^j_l - \zeta\bar{G}^j_l)\mathbf{E}^k \otimes \mathbf{E}^l \tag{3.26}$$

After some manipulations, the strain tensor can be written in terms of the membrane mid-surface strain ϵ_{ij} and the bending strain ρ_{ij} according to:

$$2\boldsymbol{\gamma} = (\epsilon_{ij} + \zeta\rho_{ij})\mathbf{E}^i \otimes \mathbf{E}^j\,, \tag{3.27}$$

where:

$$\begin{aligned}
2\epsilon_{\alpha\beta} &= \mathbf{E}_\alpha\cdot(\hat{\mathbf{u}}_{0,\beta}+\mathcal{H}_{\Gamma_{d,0}}\tilde{\mathbf{u}}_{0,\beta}) + \mathbf{E}_\beta\cdot(\hat{\mathbf{u}}_{0,\alpha}+\mathcal{H}_{\Gamma_{d,0}}\tilde{\mathbf{u}}_{0,\alpha}) \\
&\quad + (\hat{\mathbf{u}}_{0,\alpha}+\mathcal{H}_{\Gamma_{d,0}}\tilde{\mathbf{u}}_{0,\alpha})\cdot(\hat{\mathbf{u}}_{0,\beta}+\mathcal{H}_{\Gamma_{d,0}}\tilde{\mathbf{u}}_{0,\beta})\,; \\
2\epsilon_{\alpha 3} &= \mathbf{E}_\alpha\cdot(\hat{\mathbf{u}}_1+\mathcal{H}_{\Gamma_{d,0}}\tilde{\mathbf{u}}_1) + \mathbf{D}\cdot(\hat{\mathbf{u}}_{0,\alpha}+\mathcal{H}_{\Gamma_{d,0}}\tilde{\mathbf{u}}_{0,\alpha}) \\
&\quad + (\hat{\mathbf{u}}_{0,\alpha}+\mathcal{H}_{\Gamma_{d,0}}\tilde{\mathbf{u}}_{0,\alpha})\cdot(\hat{\mathbf{u}}_1+\mathcal{H}_{\Gamma_{d,0}}\tilde{\mathbf{u}}_1)\,; \\
2\epsilon_{33} &= 2\mathbf{D}\cdot(\hat{\mathbf{u}}_1+\mathcal{H}_{\Gamma_{d,0}}\tilde{\mathbf{u}}_1) + (\hat{\mathbf{u}}_1+\mathcal{H}_{\Gamma_{d,0}}\tilde{\mathbf{u}}_1)\cdot(\hat{\mathbf{u}}_1+\mathcal{H}_{\Gamma_{d,0}}\tilde{\mathbf{u}}_1)\,; \\
2\rho_{\alpha\beta} &= \mathbf{E}_\beta\cdot(\hat{\mathbf{u}}_{1,\alpha}+\mathcal{H}_{\Gamma_{d,0}}\tilde{\mathbf{u}}_{1,\alpha}) + \mathbf{E}_\alpha\cdot(\hat{\mathbf{u}}_{1,\beta}+\mathcal{H}_{\Gamma_{d,0}}\tilde{\mathbf{u}}_{1,\beta}) \\
&\quad + \mathbf{D}_{,\alpha}\cdot(\hat{\mathbf{u}}_{0,\beta}+\mathcal{H}_{\Gamma_{d,0}}\tilde{\mathbf{u}}_{0,\beta}) + \mathbf{D}_{,\beta}\cdot(\hat{\mathbf{u}}_{0,\alpha}+\mathcal{H}_{\Gamma_{d,0}}\tilde{\mathbf{u}}_{0,\alpha}) \\
&\quad + (\hat{\mathbf{u}}_{1,\alpha}+\mathcal{H}_{\Gamma_{d,0}}\tilde{\mathbf{u}}_{1,\alpha})\cdot(\hat{\mathbf{u}}_{0,\beta}+\mathcal{H}_{\Gamma_{d,0}}\tilde{\mathbf{u}}_{0,\beta}) \\
&\quad + (\hat{\mathbf{u}}_{1,\beta}+\mathcal{H}_{\Gamma_{d,0}}\tilde{\mathbf{u}}_{1,\beta})\cdot(\hat{\mathbf{u}}_{0,\alpha}+\mathcal{H}_{\Gamma_{d,0}}\tilde{\mathbf{u}}_{0,\alpha}) \\
&\quad - \bar{G}^\lambda_\alpha[\mathbf{E}_\beta\cdot(\hat{\mathbf{u}}_{0,\lambda}+\mathcal{H}_{\Gamma_{d,0}}\tilde{\mathbf{u}}_{0,\lambda}) + \mathbf{E}_\lambda\cdot(\hat{\mathbf{u}}_{0,\beta}+\mathcal{H}_{\Gamma_{d,0}}\tilde{\mathbf{u}}_{0,\beta}) \\
&\qquad + (\hat{\mathbf{u}}_{0,\lambda}+\mathcal{H}_{\Gamma_{d,0}}\tilde{\mathbf{u}}_{0,\lambda})\cdot(\hat{\mathbf{u}}_{0,\beta}+\mathcal{H}_{\Gamma_{d,0}}\tilde{\mathbf{u}}_{1,\beta})] \\
&\quad - \bar{G}^\lambda_\beta[\mathbf{E}_\alpha\cdot(\hat{\mathbf{u}}_{0,\lambda}+\mathcal{H}_{\Gamma_{d,0}}\tilde{\mathbf{u}}_{0,\lambda}) + \mathbf{E}_\lambda\cdot(\hat{\mathbf{u}}_{0,\alpha}+\mathcal{H}_{\Gamma_{d,0}}\tilde{\mathbf{u}}_{0,\alpha}) \\
&\qquad + (\hat{\mathbf{u}}_{0,\lambda}+\mathcal{H}_{\Gamma_{d,0}}\tilde{\mathbf{u}}_{0,\lambda})\cdot(\hat{\mathbf{u}}_{0,\alpha}+\mathcal{H}_{\Gamma_{d,0}}\tilde{\mathbf{u}}_{1,\alpha})]\,; \\
2\rho_{\alpha 3} &= \mathbf{D}_{,\alpha}\cdot(\hat{\mathbf{u}}_1+\mathcal{H}_{\Gamma_{d,0}}\tilde{\mathbf{u}}_1) + \mathbf{D}\cdot(\hat{\mathbf{u}}_{1,\alpha}+\mathcal{H}_{\Gamma_{d,0}}\tilde{\mathbf{u}}_{1,\alpha}) \\
&\quad + (\hat{\mathbf{u}}_1+\mathcal{H}_{\Gamma_{d,0}}\tilde{\mathbf{u}}_1)\cdot(\hat{\mathbf{u}}_{1,\alpha}+\mathcal{H}_{\Gamma_{d,0}}\tilde{\mathbf{u}}_{1,\alpha})\,; \\
2\rho_{33} &= -4(\mathbf{D}+\hat{\mathbf{u}}_1+\mathcal{H}_{\Gamma_{d,0}}\tilde{\mathbf{u}}_1)\cdot(\hat{\mathbf{u}}_2+\mathcal{H}_{\Gamma_{d,0}}\tilde{\mathbf{u}}_2)\,.
\end{aligned} \tag{3.28}$$

Note that the strain fields on either side of the discontinuity $\Gamma_{d,0}$ are not necessarily equal. This implies that it is possible to capture phenomena which are

restricted to just one layer of the laminate such as delamination buckling as demonstrated by Wells *et al.* (2003).

The strain field is still defined in the iso-parametric frame of axes $\mathbf{E}^i$. In order to obtain the strains in the element local frame of reference $\mathbf{l}_j$, they must be transformed using:

$$\gamma_{ij} = (\epsilon_{ij} + \zeta\rho_{ij})T_i^k T_j^l; \qquad T_i^k = \mathbf{E}^k\mathbf{l}_i\,. \tag{3.29}$$

The magnitude of the displacement jump $\mathbf{v}$ at the internal discontinuity $\Gamma_{d,0}$ is equal to the magnitude of the additional displacement field at the discontinuity ζ_{d}, cf. equation (2.7). In the spirit of previous assumptions, we neglect the terms that vary quadratically in the thickness direction, so that:

$$\mathbf{v} = \tilde{\mathbf{u}}_0 + \zeta_{\mathrm{d}}\tilde{\mathbf{u}}_1\,. \tag{3.30}$$

Since we have used the Heaviside function (3.9), the multiplication factor h is equal to 1 and may be omitted from the equation.

§ 3.3 Equilibrium equations

The static equilibrium equation for the body Ω with respect to the undeformed configuration can be written as:

$$\nabla_0 \cdot \mathbf{P} = 0 \qquad \text{in} \quad \Omega_0\,; \tag{3.31}$$

where $\mathbf{P}$ is the nominal stress tensor. The corresponding boundary conditions are:

$$\begin{aligned} \mathbf{n}_{t,0} \cdot \mathbf{P} &= \bar{\mathbf{t}} \qquad \text{on} \quad \Gamma_{t,0}\,; \\ \mathbf{n}_{d,0} \cdot \mathbf{P} &= \mathbf{t} \qquad \text{on} \quad \Gamma_{d,0}\,, \end{aligned} \tag{3.32}$$

where $\bar{\mathbf{t}}$ is the applied external load in the reference configuration; $\mathbf{n}_{t,0}$ is the outward unit normal vector to the body and $\mathbf{n}_{d,0}$ is the inward unit normal to Ω_0^+, see also Figure 3.2. The governing equations can be written in weak form by multiplying equation (3.31) by an admissible displacement variation $\delta\boldsymbol{\phi}$ and integrating the result over the domain Ω_0:

$$\int_{\Omega_0} \delta\boldsymbol{\phi} \cdot (\nabla_0 \cdot \mathbf{P})\mathrm{d}\Omega_0 = 0\,, \tag{3.33}$$

which must hold for all admissible variation of the displacement field $\delta\boldsymbol{\phi}$. Following a standard Bubnov-Galerkin approach, the space of admissible displacement variations is taken the same as the field of actual displacements, see also equation (2.13). Referring to equation (3.8), we can therefore write:

$$\delta\boldsymbol{\phi} = \delta\hat{\boldsymbol{\phi}} + \mathcal{H}_{\Gamma_{d,0}}\delta\tilde{\boldsymbol{\phi}}\,. \tag{3.34}$$

Substituting this relation into equation (3.33) gives:

$$\int_{\Omega_0} \delta\hat{\boldsymbol{\phi}} \cdot (\nabla_0 \cdot \mathbf{P}) \mathrm{d}\Omega_0 + \int_{\Omega_0} \mathcal{H}_{\Gamma_{d,0}}\delta\tilde{\boldsymbol{\phi}} \cdot (\nabla_0 \cdot \mathbf{P}) \mathrm{d}\Omega_0 = 0\,, \tag{3.35}$$

which must hold for all admissible variations $\delta\hat{\boldsymbol{\phi}}$ and $\delta\tilde{\boldsymbol{\phi}}$. The equation can be expanded using Gauss' theorem. The Heaviside function can be eliminated by changing the integration domain Ω_0 into Ω_0^+ (Wells and Sluys 2001a):

$$\begin{aligned}\int_{\Omega_0} \nabla_0 \cdot (\mathbf{P} \cdot \delta\hat{\boldsymbol{\phi}}) \mathrm{d}\Omega_0 - \int_{\Omega_0} \nabla_0 \delta\hat{\boldsymbol{\phi}} : \mathbf{P} \mathrm{d}\Omega_0 + \\ \int_{\Omega_0^+} \nabla_0 \cdot (\mathbf{P} \cdot \delta\tilde{\boldsymbol{\phi}}) \mathrm{d}\Omega_0 - \int_{\Omega_0^+} \nabla_0 \delta\tilde{\boldsymbol{\phi}} : \mathbf{P} \mathrm{d}\Omega_0 = 0\,.\end{aligned} \tag{3.36}$$

In this equation, $\nabla_0\delta\hat{\boldsymbol{\phi}}$ and $\nabla_0\delta\tilde{\boldsymbol{\phi}}$ are the deformation gradients of the regular and the additional parts of the admissible displacement variations (Wells *et al.* 2002). Applying the boundary conditions and the traction at the discontinuity, equation (3.32), the equation above can be written as:

$$\begin{aligned}\int_{\Omega_0} \nabla_0 \delta\hat{\boldsymbol{\phi}} : \mathbf{P}\, \mathrm{d}\Omega_0 + \int_{\Omega_0^+} \nabla_0 \delta\tilde{\boldsymbol{\phi}} : \mathbf{P}\, \mathrm{d}\Omega_0 + \int_{\Gamma_{d,0}} \delta\tilde{\mathbf{v}} \cdot \mathbf{t}\, \mathrm{d}\Gamma_0 = \\ \int_{\Gamma_{t,0}} \delta\hat{\boldsymbol{\phi}} \cdot \bar{\mathbf{t}}\, \mathrm{d}\Gamma_0 + \mathcal{H}_{\Gamma_{d,0}} \int_{\Gamma_{t,0}} \delta\tilde{\boldsymbol{\phi}} \cdot \bar{\mathbf{t}}\, \mathrm{d}\Gamma_0\,.\end{aligned} \tag{3.37}$$

The terms $\nabla_0\delta\hat{\boldsymbol{\phi}} : \mathbf{P}$ and $\nabla_0\delta\tilde{\boldsymbol{\phi}} : \mathbf{P}$ can be replaced by the work-conjugate terms $\delta\hat{\boldsymbol{\gamma}} : \boldsymbol{\sigma}$ and $\delta\tilde{\boldsymbol{\gamma}} : \boldsymbol{\sigma}$ (Belytschko *et al.* 2000), where $\delta\hat{\boldsymbol{\gamma}}$ and $\delta\tilde{\boldsymbol{\gamma}}$ are the regular and additional parts of the variation of the Green-Lagrange strain field and $\boldsymbol{\sigma}$ is the second Piola-Kirchhoff stress tensor:

$$\begin{aligned}\int_{\Omega_0} \delta\hat{\boldsymbol{\gamma}} : \boldsymbol{\sigma}\, \mathrm{d}\Omega_0 + \int_{\Omega_0^+} \delta\tilde{\boldsymbol{\gamma}} : \boldsymbol{\sigma}\, \mathrm{d}\Omega_0 + \int_{\Gamma_{d,0}} \delta\tilde{\mathbf{v}} \cdot \mathbf{t}\, \mathrm{d}\Gamma_0 = \\ \int_{\Gamma_{t,0}} \delta\hat{\boldsymbol{\phi}} \cdot \bar{\mathbf{t}}\, \mathrm{d}\Gamma_0 + \mathcal{H}_{\Gamma_{d,0}} \int_{\Gamma_{t,0}} \delta\tilde{\boldsymbol{\phi}} \cdot \bar{\mathbf{t}}\, \mathrm{d}\Gamma_0\,.\end{aligned} \tag{3.38}$$

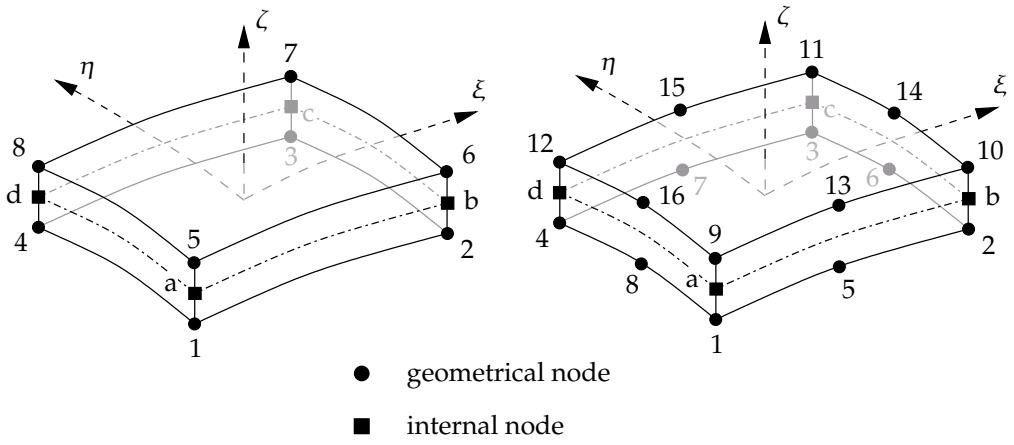

Figure 3.3 Geometry and location of the nodes for the eight-node (left) and the sixteen-node solid-like shell element. Each geometrical node contains a regular set of three degrees of freedom $[a_x, a_y, a_z]_i$ and an additional set of three degrees of freedom $[b_x, b_y, b_z]_i$. The internal nodes contain one regular and one additional degree-of-freedom (p_j and q_j respectively).

The regular and additional variational strain fields $\delta\hat{\boldsymbol{\gamma}}$ and $\delta\tilde{\boldsymbol{\gamma}}$ can be expressed in terms of the variational displacement components $\delta\hat{\mathbf{u}}$ and $\delta\tilde{\mathbf{u}}$ and the variational stretch terms $\delta\hat{w}$ and $\delta\tilde{w}$. This derivation can be found in section B.1.

§ 3.4 Finite element formulation

The solid-like shell element can be formulated as an eight-node or as a sixteen-node element, see Figure 3.3. In both cases, a linear distribution of the internal stretch is assumed, so that only four internal degrees of freedom, situated at the four corners of the mid-surface of the element, are necessary (Parisch 1995). Each geometrical node i contains three degrees of freedom $[a_x, a_y, a_z]_i$ that set up the regular displacement field $\hat{\mathbf{u}}$ and a set of three additional degrees of freedom $[b_x, b_y, b_z]_i$ that describes the enhanced displacement field $\tilde{\mathbf{u}}$. Likewise, there are two sets of internal degrees of freedom: p_j that constructs the regular stretch term $\hat{w}$ and q_j that constructs the additional stretch term $\tilde{w}$.

The projected displacement at the bottom surfaces of the element $\mathbf{u}_b$ is constructed using the degrees of freedom at the bottom nodes of the element only.

Likewise, the projected displacement at the top surface $\mathbf{u}_t$ is constructed using the degrees of freedom of the top nodes. For example, the sixteen-node element has eight bottom and eight top nodes. Hence, the continuous value $\mathbf{u}_b$ can be constructed from the eight bottom nodes, using the eight bi-quadratic shape functions Ψ_i. In the case of an eight-node element, $\mathbf{u}_b$ is constructed using the four bottom nodes in combination with the four bi-linear shape functions for a quadrilateral element. Since the internal stretch w is constructed with four internal degrees of freedom in both elements, we use the four bi-linear shape functions Φ_j. Comparing equation (2.22), the projection of the displacement vector can be constructed by interpolating the regular and enhanced degrees of freedom at the bottom nodes of the element:

$$\mathbf{u}_b = \hat{\mathbf{u}}_b + \mathcal{H}_{\Gamma_{d,0}}\tilde{\mathbf{u}}_b \;=\; \sum_{i=1}^{n_\mathrm{s}} \mathbf{\Psi}_i \mathbf{a}_i + \mathcal{H}_{\Gamma_{d,0}} \sum_{i=1}^{n_\mathrm{s}} \mathbf{\Psi}_i \mathbf{b}_i \,, \tag{3.39}$$

where i denotes the element node number, n_s is the number of nodes at the bottom or top surface of the element, $\mathbf{\Psi}$ represents the conventional matrix which contains the element shape functions for node i in three directions ξ, η, ζ:

$$\mathbf{\Psi}_i = \Psi_i \mathbf{I}_3 \,. \tag{3.40}$$

$\mathbf{I}_3$ is the 3×3 identity matrix. The projected displacements on the top surface $\mathbf{u}_t$ can be interpolated using the degrees of freedom at the top nodes of the element:

$$\mathbf{u}_t = \hat{\mathbf{u}}_t + \mathcal{H}_{\Gamma_{d,0}}\tilde{\mathbf{u}}_t \;=\; \sum_{i=1}^{n_\mathrm{s}} \mathbf{\Psi}_i \mathbf{a}_{i+n_\mathrm{s}} + \mathcal{H}_{\Gamma_{d,0}} \sum_{i=1}^{n_\mathrm{s}} \mathbf{\Psi}_i \mathbf{b}_{i+n_\mathrm{s}} \,, \tag{3.41}$$

Similarly, the internal degrees of freedom are calculated according to:

$$w = \hat{w} + \mathcal{H}_{\Gamma_{d,0}}\tilde{w} \;=\; \sum_{j=1}^{4} \Phi_j p_j + \mathcal{H}_{\Gamma_{d,0}} \sum_{j=1}^{4} \Phi_j q_j \,. \tag{3.42}$$

The discretised displacement of the shell mid-surface and the displacement of the thickness director, $\mathbf{u}_0$ and $\mathbf{u}_1$ respectively, can be found using relations (3.12), (3.39) and (3.41):

$$\begin{aligned} \hat{\mathbf{u}}_0 &= \mathbf{N}_0 \mathbf{a} \,; \qquad \tilde{\mathbf{u}}_0 = \mathbf{N}_0 \mathbf{b} \,; \\ \hat{\mathbf{u}}_1 &= \mathbf{N}_1 \mathbf{a} \,; \qquad \tilde{\mathbf{u}}_1 = \mathbf{N}_1 \mathbf{b} \,, \end{aligned} \tag{3.43}$$

where $\mathbf{N}_0$ and $\mathbf{N}_1$ are defined as:

$$\begin{aligned}\mathbf{N}_0 &= \frac{1}{2}\left[\boldsymbol{\Psi}_1, \boldsymbol{\Psi}_2, \ldots, \boldsymbol{\Psi}_{n_\mathrm{s}}, \boldsymbol{\Psi}_1, \boldsymbol{\Psi}_2, \ldots, \boldsymbol{\Psi}_{n_\mathrm{s}}\right]^\mathrm{T};\\ \mathbf{N}_1 &= \frac{1}{2}\left[-\boldsymbol{\Psi}_1, -\boldsymbol{\Psi}_2, \ldots, -\boldsymbol{\Psi}_{n_\mathrm{s}}, \boldsymbol{\Psi}_1, \boldsymbol{\Psi}_2, \ldots, \boldsymbol{\Psi}_{n_\mathrm{s}}\right]^\mathrm{T}.\end{aligned} \tag{3.44}$$

From equation (3.42) the interpolation matrix for the internal degrees of freedom can be defined:

$$\mathbf{N}_w = \left[\Phi_1, \Phi_2, \Phi_3, \Phi_4\right]^\mathrm{T}. \tag{3.45}$$

Trivially, the derivatives of the displacement vectors $\mathbf{u}_0$ and $\mathbf{u}_1$ with respect to the iso-parametric coordinates ξ and η can be written as:

$$\begin{aligned}\hat{\mathbf{u}}_{0,\alpha} &= \mathbf{N}_{0,\alpha}\mathbf{a}; \qquad & \tilde{\mathbf{u}}_{0,\alpha} &= \mathbf{N}_{0,\alpha}\mathbf{b};\\ \hat{\mathbf{u}}_{1,\alpha} &= \mathbf{N}_{1,\alpha}\mathbf{a}; \qquad & \tilde{\mathbf{u}}_{1,\alpha} &= \mathbf{N}_{1,\alpha}\mathbf{b},\end{aligned} \tag{3.46}$$

where the matrices $\mathbf{N}_{0,\alpha}$ and $\mathbf{N}_{1,\alpha}$ contain the derivatives of the shape functions:

$$\begin{aligned}\mathbf{N}_{0,\alpha} &= \frac{1}{2}\left[\boldsymbol{\Psi}_{1,\alpha}, \boldsymbol{\Psi}_{2,\alpha}, \ldots, \boldsymbol{\Psi}_{n_\mathrm{s},\alpha}, \boldsymbol{\Psi}_{1,\alpha}, \boldsymbol{\Psi}_{2,\alpha}, \ldots, \boldsymbol{\Psi}_{n_\mathrm{s},\alpha}\right]^\mathrm{T};\\ \mathbf{N}_{1,\alpha} &= \frac{1}{2}\left[-\boldsymbol{\Psi}_{1,\alpha}, -\boldsymbol{\Psi}_{2,\alpha}, \ldots, -\boldsymbol{\Psi}_{n_\mathrm{s},\alpha}, \boldsymbol{\Psi}_{1,\alpha}, \boldsymbol{\Psi}_{2,\alpha}, \ldots, \boldsymbol{\Psi}_{n_\mathrm{s},\alpha}\right]^\mathrm{T},\end{aligned} \tag{3.47}$$

with:

$$\boldsymbol{\Psi}_{i,\alpha} = \frac{\partial \Psi_i}{\partial \alpha}\,\mathbf{I}_3\,. \tag{3.48}$$

There are three kinds of admissible variations that need to be discretised, namely those of the Green-Lagrange strain tensor $\delta\hat{\boldsymbol{\gamma}}$ and $\delta\tilde{\boldsymbol{\gamma}}$, that of the displacement jump , $\delta\tilde{\mathbf{v}}$, and that of the displacement field itself, $\delta\hat{\boldsymbol{\phi}}$ and $\delta\tilde{\boldsymbol{\phi}}$. The variations of the Green-Lagrange strain field can be written as:

$$\begin{aligned}\delta\hat{\boldsymbol{\gamma}} &= \mathbf{B}_u\delta\mathbf{a} + \mathbf{B}_w\delta\mathbf{p};\\ \delta\tilde{\boldsymbol{\gamma}} &= \mathbf{B}_u\delta\mathbf{b} + \mathbf{B}_w\delta\mathbf{q},\end{aligned} \tag{3.49}$$

with $\mathbf{B}_u$ and $\mathbf{B}_w$ as defined in section B.1. From equation (3.30) one obtains the discrete variation displacement jump:

$$\delta\tilde{\mathbf{v}} = \mathbf{N}_0\delta\mathbf{b} + \zeta_\mathrm{d}\mathbf{N}_1\delta\mathbf{b} = \mathbf{H}\delta\mathbf{b}\,, \tag{3.50}$$

Since the load can only be applied to the geometrical nodes (Parisch 1995), the admissible displacement terms in the external load parts of the equilibrium equations can be replaced by a modified admissible displacement field $\delta\boldsymbol{\phi}^*$ which is defined as:

$$\delta\boldsymbol{\phi}^* = \delta\hat{\boldsymbol{\phi}}^* + \delta\tilde{\boldsymbol{\phi}}^* = \delta\hat{\mathbf{u}}_0 + \zeta\delta\hat{\mathbf{u}}_1 + \mathcal{H}_{\Gamma_{d,0}}\left(\delta\tilde{\mathbf{u}}_0 + \zeta\delta\tilde{\mathbf{u}}_1\right), \tag{3.51}$$

or in discrete form:

$$\delta\hat{\boldsymbol{\phi}}^* = \mathbf{N}^*\delta\mathbf{a}\,; \qquad \delta\tilde{\boldsymbol{\phi}}^* = \mathbf{N}^*\delta\mathbf{b}\,, \qquad \text{where } \mathbf{N}^* = (\mathbf{N}_0 + \zeta\mathbf{N}_1)\,. \tag{3.52}$$

Substituting equations (3.49), (3.50) and (3.52) into the equilibrium equation (3.38) gives:

$$\begin{aligned}
&\int_{\mathcal{V}_0}(\mathbf{B}_u\delta\mathbf{a} + \mathbf{B}_w\delta\mathbf{p})^{\mathrm{T}}\boldsymbol{\sigma}\,\mathrm{d}\mathcal{V}_0 + \int_{\mathcal{V}_0^+}(\mathbf{B}_u\delta\mathbf{b} + \mathbf{B}_w\delta\mathbf{q})^{\mathrm{T}}\boldsymbol{\sigma}\,\mathrm{d}\mathcal{V}_0 + \\
&\qquad\int_{\mathcal{S}_{\mathrm{d},0}}(\mathbf{H}\delta\mathbf{b})^{\mathrm{T}}\mathbf{t}\,\mathrm{d}\mathcal{S}_0 = \\
&\qquad\qquad\int_{\mathcal{S}_t}(\mathbf{N}^*\delta\mathbf{a})^{\mathrm{T}}\bar{\mathbf{t}}\,\mathrm{d}\mathcal{S}_0 + \int_{\mathcal{S}_t}\mathcal{H}_{\Gamma_{d,0}}(\mathbf{N}^*\delta\mathbf{b})^{\mathrm{T}}\bar{\mathbf{t}}\,\mathrm{d}\mathcal{S}_0\,.
\end{aligned} \tag{3.53}$$

By taking the variation of one admissible variation $\delta\mathbf{a}$, $\delta\mathbf{b}$,$\delta\mathbf{p}$ or $\delta\mathbf{q}$ at the time and setting the others to zero, the following four systems of equations can be derived:

$$\begin{aligned}
\int_{\mathcal{V}_0}\mathbf{B}_u^{\mathrm{T}}\boldsymbol{\sigma}\,\mathrm{d}\mathcal{V}_0 &= \int_{\mathcal{S}_t}\mathbf{N}^{*\mathrm{T}}\bar{\mathbf{t}}\,\mathrm{d}\mathcal{S}_0\,;\\
\int_{\mathcal{V}_0^+}\mathbf{B}_u^{\mathrm{T}}\boldsymbol{\sigma}\,\mathrm{d}\mathcal{V}_0 + \int_{\mathcal{S}_{\mathrm{d},0}}\mathbf{H}^{\mathrm{T}}\mathbf{t}\,\mathrm{d}\mathcal{S}_0 &= \int_{\mathcal{S}_t}\mathcal{H}_{\Gamma_{d,0}}\mathbf{N}^{*\mathrm{T}}\bar{\mathbf{t}}\,\mathrm{d}\mathcal{S}_0\,;\\
\int_{\mathcal{V}_0}\mathbf{B}_w^{\mathrm{T}}\boldsymbol{\sigma}\,\mathrm{d}\mathcal{V}_0 &= \mathbf{0}\,;\\
\int_{\mathcal{V}_0^+}\mathbf{B}_w^{\mathrm{T}}\boldsymbol{\sigma}\,\mathrm{d}\mathcal{V}_0 &= \mathbf{0}\,.
\end{aligned} \tag{3.54}$$

The left hand sides of these equations constitute the internal force vectors:

$$\begin{aligned}
\mathbf{f}_a^{\text{int}} &= \int_{\mathcal{V}_0} \mathbf{B}_u^{\mathrm{T}} \boldsymbol{\sigma} \, \mathrm{d}\mathcal{V}_0 \,; \\
\mathbf{f}_b^{\text{int}} &= \int_{\mathcal{V}_0^+} \mathbf{B}_u^{\mathrm{T}} \boldsymbol{\sigma} \, \mathrm{d}\mathcal{V}_0 + \int_{\mathcal{S}_\mathrm{d}} \mathbf{H}^{\mathrm{T}} \mathbf{t} \, \mathrm{d}\mathcal{S}_0 \,; \\
\mathbf{f}_p^{\text{int}} &= \int_{\mathcal{V}_0} \mathbf{B}_w^{\mathrm{T}} \boldsymbol{\sigma} \, \mathrm{d}\mathcal{V}_0 \,; \\
\mathbf{f}_q^{\text{int}} &= \int_{\mathcal{V}_0^+} \mathbf{B}_w^{\mathrm{T}} \boldsymbol{\sigma} \, \mathrm{d}\mathcal{V}_0 \,,
\end{aligned} \tag{3.55}$$

while the right-hand-sides represent the external force vectors:

$$\begin{aligned}
\mathbf{f}_a^{\text{ext}} &= \int_{\mathcal{S}_t} \mathbf{N}^{*\mathrm{T}} \bar{\mathbf{t}} \, \mathrm{d}\mathcal{S}_0 \,; \\
\mathbf{f}_b^{\text{ext}} &= \int_{\mathcal{S}_t} \mathcal{H}_{\Gamma_{d,0}} \mathbf{N}^{*\mathrm{T}} \bar{\mathbf{t}} \, \mathrm{d}\mathcal{S}_0 \,; \\
\mathbf{f}_p^{\text{ext}} &= \mathbf{0} \,; \\
\mathbf{f}_q^{\text{ext}} &= \mathbf{0} \,.
\end{aligned} \tag{3.56}$$

Constitutive relations

For the bulk material and for the interface standard constitutive relations can be used. At this stage, the treatment is restricted to small strains, but allows for arbitrarily large displacement gradients. Consequently, a linear relation can be postulated between the increments of the second Piola-Kirchhoff stress $\Delta\boldsymbol{\sigma}$, and the Green-Lagrange strain, $\Delta\boldsymbol{\gamma}$, see equation (B.3):

$$\Delta\boldsymbol{\sigma} = \mathbf{C}\Delta\boldsymbol{\gamma} \,, \tag{3.57}$$

where $\mathbf{C}$ is the tangent stiffness matrix of the bulk material. For the discontinuity, the constitutive relation reads:

$$\Delta\mathbf{t}_\mathrm{d} = \mathbf{T}_\mathrm{d}\Delta\mathbf{v}_\mathrm{d} \,, \tag{3.58}$$

where $\Delta\mathbf{v}_\mathrm{d}$ is the incremental displacement jump at the discontinuity in the current orientation of the discontinuity, denoted by the subscript 'd'. Transformation into the element local frame of reference in the undeformed configuration gives, see (2.31):

$$\Delta\mathbf{t} = \mathbf{Q}^{\mathrm{T}}\Delta\mathbf{t}_\mathrm{d} = \mathbf{Q}^{\mathrm{T}}\mathbf{T}_\mathrm{d}\Delta\mathbf{v}_\mathrm{d} = \mathbf{Q}^{\mathrm{T}}\mathbf{T}_\mathrm{d}\mathbf{Q}\Delta\mathbf{v} \,, \tag{3.59}$$

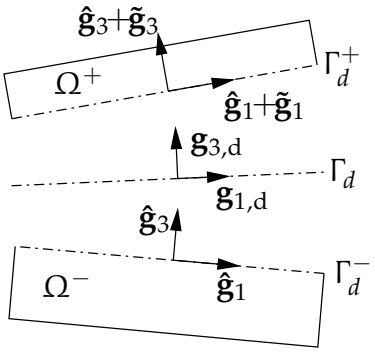

Figure 3.4 The orientation of the discontinuity in the element in the deformed configuration.

so that in the undeformed configuration, the tangent stiffness matrix is equal to:

$$\mathbf{T} = \mathbf{Q}^{\mathrm{T}}\mathbf{T}_{\mathrm{d}}\mathbf{Q}\,. \tag{3.60}$$

The orthogonal transformation matrix $\mathbf{Q}$ performs the transformation of the orientation of the discontinuity in the current configuration into the undeformed configuration and can be composed using the base vectors in the deformed configuration, equation (3.15). However, since the triads $\mathbf{g}_i$ at both sides of the discontinuity are normally different, see Figure 3.4, it is not possible to assign a unique direction for the discontinuity in the deformed position. Therefore, the average direction is taken (Wells *et al.* 2002). The base vectors in deformed position are then equal to:

$$\begin{aligned}
\mathbf{g}_{\alpha,\mathrm{d}} &= \hat{\mathbf{g}}_\alpha + \frac{1}{2}\tilde{\mathbf{g}}_\alpha = \mathbf{E}_\alpha + \hat{\mathbf{u}}_{0,\alpha} + \frac{1}{2}\tilde{\mathbf{u}}_{0,\alpha} + \zeta\mathbf{D}_{,\alpha} + \zeta\hat{\mathbf{u}}_{1,\alpha} + \frac{1}{2}\zeta\tilde{\mathbf{u}}_{1,\alpha}\,; \\
\mathbf{g}_{3,\mathrm{d}} &= \hat{\mathbf{g}}_3 + \frac{1}{2}\tilde{\mathbf{g}}_3 = \mathbf{D} + \hat{\mathbf{u}}_1 + \frac{1}{2}\tilde{\mathbf{u}}_1 - 2\zeta\hat{\mathbf{u}}_2 - \zeta\tilde{\mathbf{u}}_2\,.
\end{aligned} \tag{3.61}$$

The base vectors that describe the orientation of the discontinuity can be used to construct the transformation matrix $\mathbf{Q}$:

$$Q_{ij} = \cos(\mathbf{g}_{i,\mathrm{d}}, \mathbf{G}_j)\,. \tag{3.62}$$

Note that in this situation, the transformation matrix $\mathbf{Q}$ is a function of the deformation of the element. This is in contrast with the constant transformation matrix for the element based on a small strain deformation gradient as presented in the previous chapter.

Linearisation of the governing equations

The stiffness matrix which is needed for the solution of the nonlinear system of equations can be found by differentiating the internal forces vector, equation (3.55) with respect to the displacement field. Since both the stresses and tractions ($\boldsymbol{\sigma}$ and $\mathbf{t}$) as well as the geometric matrices $\mathbf{B}_u$ and $\mathbf{B}_w$ are a function of the displacements, the stiffness matrix can be decomposed in two parts, the so-called *material* part and the *geometric* part.

The first part, which is denoted as $\mathbf{K}^{\mathrm{m}}$, involves the rate of stresses and tractions and depends on the response of the constitutive relations of the bulk material, equation (3.57), and the cohesive surface, equation (3.58). Since:

$$\frac{\partial \boldsymbol{\sigma}}{\partial \mathbf{a}} = \frac{\partial \boldsymbol{\sigma}}{\partial \mathbf{b}} = \mathbf{C}\mathbf{B}_u \,; \qquad \frac{\partial \boldsymbol{\sigma}}{\partial \mathbf{p}} = \frac{\partial \boldsymbol{\sigma}}{\partial \mathbf{q}} = \mathbf{C}\mathbf{B}_w \,, \tag{3.63}$$

we obtain for the material part of the bulk material:

$$\mathbf{K}^{\mathrm{m}} = \begin{bmatrix} \int_{\mathcal{V}_0} \mathbf{A}^{\mathrm{m}}_{uu} \mathrm{d}\mathcal{V}_0 & \int_{\mathcal{V}_0^+} \mathbf{A}^{\mathrm{m}}_{uu} \mathrm{d}\mathcal{V}_0 & \int_{\mathcal{V}_0} \mathbf{A}^{\mathrm{m}}_{uw} \mathrm{d}\mathcal{V}_0 & \int_{\mathcal{V}_0^+} \mathbf{A}^{\mathrm{m}}_{uw} \mathrm{d}\mathcal{V}_0 \\ \int_{\mathcal{V}_0^+} \mathbf{A}^{\mathrm{m}}_{uu} \mathrm{d}\mathcal{V}_0 & \int_{\mathcal{V}_0^+} \mathbf{A}^{\mathrm{m}}_{uu} \mathrm{d}\mathcal{V}_0 & \int_{\mathcal{V}_0^+} \mathbf{A}^{\mathrm{m}}_{uw} \mathrm{d}\mathcal{V}_0 & \int_{\mathcal{V}_0^+} \mathbf{A}^{\mathrm{m}}_{uw} \mathrm{d}\mathcal{V}_0 \\ \int_{\mathcal{V}_0} \mathbf{A}^{\mathrm{m}}_{wu} \mathrm{d}\mathcal{V}_0 & \int_{\mathcal{V}_0^+} \mathbf{A}^{\mathrm{m}}_{wu} \mathrm{d}\mathcal{V}_0 & \int_{\mathcal{V}_0} \mathbf{A}^{\mathrm{m}}_{ww} \mathrm{d}\mathcal{V}_0 & \int_{\mathcal{V}_0^+} \mathbf{A}^{\mathrm{m}}_{ww} \mathrm{d}\mathcal{V}_0 \\ \int_{\mathcal{V}_0^+} \mathbf{A}^{\mathrm{m}}_{wu} \mathrm{d}\mathcal{V}_0 & \int_{\mathcal{V}_0^+} \mathbf{A}^{\mathrm{m}}_{wu} \mathrm{d}\mathcal{V}_0 & \int_{\mathcal{V}_0^+} \mathbf{A}^{\mathrm{m}}_{ww} \mathrm{d}\mathcal{V}_0 & \int_{\mathcal{V}_0^+} \mathbf{A}^{\mathrm{m}}_{ww} \mathrm{d}\mathcal{V}_0 \end{bmatrix}, \tag{3.64}$$

where

$$\begin{aligned} \mathbf{A}^{\mathrm{m}}_{uu} &= \mathbf{B}_u^{\mathrm{T}} \mathbf{C}\mathbf{B}_u \,; \qquad & \mathbf{A}^{\mathrm{m}}_{uu} &= \mathbf{B}_u^{\mathrm{T}} \mathbf{C}\mathbf{B}_w \,; \\ \mathbf{A}^{\mathrm{m}}_{wu} &= \mathbf{B}_w^{\mathrm{T}} \mathbf{C}\mathbf{B}_u \,; \qquad & \mathbf{A}^{\mathrm{m}}_{ww} &= \mathbf{B}_w^{\mathrm{T}} \mathbf{C}\mathbf{B}_w \,. \end{aligned} \tag{3.65}$$

For the discontinuity, the following relation holds:

$$\frac{\partial \mathbf{t}}{\partial \mathbf{b}} = \mathbf{Q}^{\mathrm{T}} \mathbf{T}_{\mathrm{d}} \mathbf{Q}\mathbf{H} \,. \tag{3.66}$$

Substitution there gives the contribution of the discontinuity to the material part of the stiffness matrix:

$$\mathbf{K}_d^{\mathrm{m}} = \begin{bmatrix} \mathbf{0} & \mathbf{0} & \mathbf{0} & \mathbf{0} \\ \mathbf{0} & \int_{\mathcal{S}_{\mathrm{d},0}} \mathbf{A}_d^{\mathrm{m}} \mathrm{d}\mathcal{S}_0 & \mathbf{0} & \mathbf{0} \\ \mathbf{0} & \mathbf{0} & \mathbf{0} & \mathbf{0} \\ \mathbf{0} & \mathbf{0} & \mathbf{0} & \mathbf{0} \end{bmatrix}. \tag{3.67}$$

where

$$\mathbf{A}_d^{\mathrm{m}} = \mathbf{H}^{\mathrm{T}} \mathbf{Q}^{\mathrm{T}} \mathbf{T}_{\mathrm{d}} \mathbf{Q} \mathbf{H} \,. \tag{3.68}$$

The geometric part of the stiffness matrix, denoted as $\mathbf{K}^{\mathrm{g}}$, accounts for the geometric effects of the deformation, such as bending. This contribution to the stiffness matrix is essential for the analysis of structural stability. It is obtained by differentiating the incremental change of the variational strains, see section B.1, with respect to the displacements. Multiplication of the result with the current stresses yield:

$$\mathbf{K}^{\mathrm{g}} = \begin{bmatrix} \int_{\mathcal{V}_0} \mathbf{A}_{uu}^{\mathrm{g}} \mathrm{d}\mathcal{V}_0 & \int_{\mathcal{V}_0^+} \mathbf{A}_{uu}^{\mathrm{g}} \mathrm{d}\mathcal{V}_0 & \int_{\mathcal{V}_0} \mathbf{A}_{uw}^{\mathrm{g}} \mathrm{d}\mathcal{V}_0 & \int_{\mathcal{V}_0^+} \mathbf{A}_{uw}^{\mathrm{g}} \mathrm{d}\mathcal{V}_0 \\ \int_{\mathcal{V}_0^+} \mathbf{A}_{uu}^{\mathrm{g}} \mathrm{d}\mathcal{V}_0 & \int_{\mathcal{V}_0^+} \mathbf{A}_{uu}^{\mathrm{g}} \mathrm{d}\mathcal{V}_0 & \int_{\mathcal{V}_0^+} \mathbf{A}_{uw}^{\mathrm{g}} \mathrm{d}\mathcal{V}_0 & \int_{\mathcal{V}_0^+} \mathbf{A}_{uw}^{\mathrm{g}} \mathrm{d}\mathcal{V}_0 \\ \int_{\mathcal{V}_0} \mathbf{A}_{wu}^{\mathrm{g}} \mathrm{d}\mathcal{V}_0 & \int_{\mathcal{V}_0^+} \mathbf{A}_{wu}^{\mathrm{g}} \mathrm{d}\mathcal{V}_0 & \mathbf{0} & \mathbf{0} \\ \int_{\mathcal{V}_0^+} \mathbf{A}_{wu}^{\mathrm{g}} \mathrm{d}\mathcal{V}_0 & \int_{\mathcal{V}_0^+} \mathbf{A}_{wu}^{\mathrm{g}} \mathrm{d}\mathcal{V}_0 & \mathbf{0} & \mathbf{0} \end{bmatrix}, \tag{3.69}$$

where $\mathbf{A}_{uu}^{\mathrm{g}}$, $\mathbf{A}_{uw}^{\mathrm{g}}$ and $\mathbf{A}_{wu}^{\mathrm{g}}$ are defined in section B.3. Consistent linearisation of the surface integrals related to the tractions at the discontinuity, as pre-

sented in equation (3.55), will result in additional, non-symmetric, terms in the geometric part of the stiffness matrix due to the transformation matrix $\mathbf{Q}$, equation (3.59). However, since these contributions are relatively small, they have only a minor impact on the iteration process (Wells *et al.* 2002). Due to the additional computational effort required to solve a non-symmetric system, these terms are neglected. The total stiffness matrix can be composed from the three parts as given in equations (3.64), (3.67) and (3.69):

$$\mathbf{K} = \mathbf{K}^{\mathrm{m}} + \mathbf{K}^{\mathrm{m}}_{\mathrm{d}} + \mathbf{K}^{\mathrm{g}} \,. \tag{3.70}$$

§ 3.5 Implementation aspects

The implementation of the model in a finite element code roughly follows the description in chapter 2. Nevertheless, due to the presence of the internal degrees of freedom, the geometry of the element and the fact that the direction of delamination growth is fixed, some differences are worth mentioning.

Adding degrees of freedom

The enhancement of both the geometrical nodes and the internal nodes can be demonstrated by means of a practical situation. Consider the laminated panel as depicted in Figure 3.5. The panel has an initial circular delamination and is locally stiffened by a set of doublers. The finite element model consists of eight-node solid-like shell elements. The initial delamination is modelled as a traction free discontinuity. The doubler is modelled by stacking additional layers of solid-like shell elements.

Figure 3.6 shows a detail of the finite element model near the delamination front. When an element is crossed by a discontinuity, both the corresponding geometric nodes as well as the internal degrees of freedom are enhanced. This implies that each geometrical node contains three additional degrees of freedom giving six degrees of freedom in total. The internal node has one extra degree of freedom added to the single regular degree of freedom. As demonstrated in the previous chapter, the displacement jump at the delamination front must be equal to zero. For this specific element, this implies that both the geometric nodes and the corresponding internal degrees of freedom on the edges that are touched by the delamination front are not enhanced.

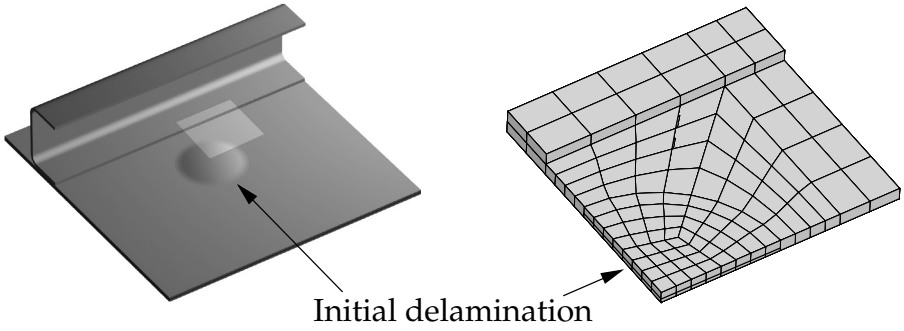

Figure 3.5 A cut-out of a stringer stiffened panel made of a laminate material with a small initial circular delamination. On the right-hand side, a fragment of the corresponding finite element model is shown (the highlighted area). The delamination is modelled as a traction free discontinuity.

The discontinuity is extended when the stress state at the delamination front exceeds a threshold level. Although the direction of this cohesive surface is known beforehand (remember that the delamination path is constrained by the lay-up of laminae in the elements) in a three dimensional model, matters are slightly more complicated. In order to have a proper discontinuity, it is required that at most two out of the four edges of a solid-like shell element form a delamination front. An additional requirement is that these two edges must be neighbours, as shown in Figure 3.7. In all the other cases, the discontinuity is never allowed to open since none of the geometric and internal nodes of the element is enhanced. In order to avoid such situations, the stress state at the delamination front is only monitored at the corner edges of an element. When the delamination criterion is violated, the discontinuity is expanded in those elements that are connected to this corner. As a result, situations as sketched in Figure 3.7 (a) and (b) are avoided.

An additional remark must be made for the situation where solid-like shell elements are stacked. Generally, the enhancement of a node affects all surrounding elements. However, the internal nodes that contain the extra degree of freedom to construct the quadratic displacement field of the element, is an element local node and the corresponding stiffness and force terms can be condensed from the global system of equations (this will be discussed in the next paragraph). As a result, the internal nodes of stacked elements directly on top

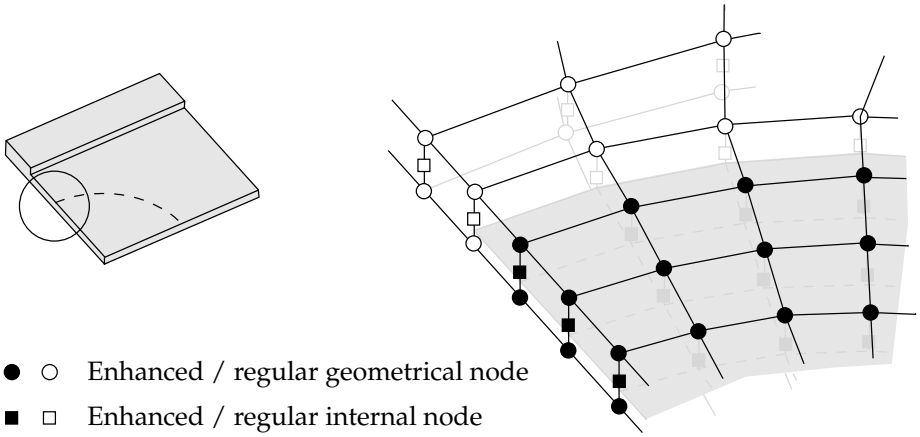

Figure 3.6 Detail of the finite element model. The discontinuity is shown as grey surface. The nodes on the edge of the discontinuity are not enhanced in order to assure a zero delamination opening at this location.

or below an enhanced element does not need to be enhanced, see Figure 3.8.

Condensation of the internal degrees of freedom

Since the internal degrees of freedom are not able to support an external loading, it was suggested by Parisch (1995) to eliminate them on element level by condensation. The complete set of the linearised equilibrium equations for a single element can be written as:

$$\begin{bmatrix} \mathbf{K}_{aa} & \mathbf{K}_{ab} & \mathbf{K}_{ap} & \mathbf{K}_{aq} \\ \mathbf{K}_{ba} & \mathbf{K}_{bb} & \mathbf{K}_{bp} & \mathbf{K}_{bq} \\ \mathbf{K}_{pa} & \mathbf{K}_{pb} & \mathbf{K}_{pp} & \mathbf{K}_{pq} \\ \mathbf{K}_{qa} & \mathbf{K}_{qb} & \mathbf{K}_{qp} & \mathbf{K}_{qq} \end{bmatrix} \begin{bmatrix} \mathrm{d}\mathbf{a} \\ \mathrm{d}\mathbf{b} \\ \mathrm{d}\mathbf{p} \\ \mathrm{d}\mathbf{q} \end{bmatrix} = \begin{bmatrix} \mathbf{f}_a^{\mathrm{ext}} \\ \mathbf{f}_b^{\mathrm{ext}} \\ \mathbf{0} \\ \mathbf{0} \end{bmatrix} - \begin{bmatrix} \mathbf{f}_a^{\mathrm{int}} \\ \mathbf{f}_b^{\mathrm{int}} \\ \mathbf{f}_p^{\mathrm{int}} \\ \mathbf{f}_q^{\mathrm{int}} \end{bmatrix}, \tag{3.71}$$

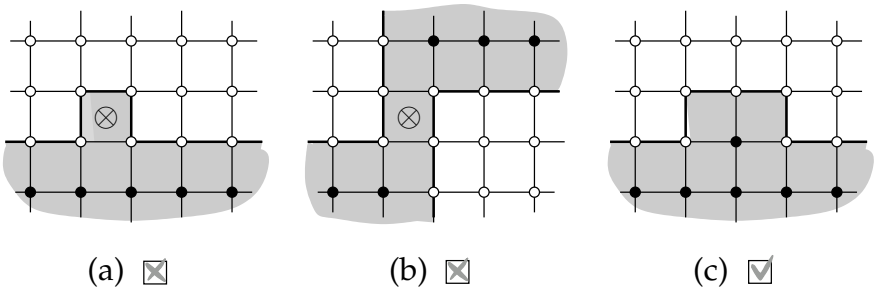

Figure 3.7 Examples of configuration of eight node solid-like shell elements with a discontinuity (top view). The black nodes represent the enhanced geometric and internal nodes, the grey shade the elements with a discontinuity and the bold line the current delamination front. The configurations in (a) and (b) are ill-posed. Since none of the nodes that construct the displacement fields in the element marked with a $\otimes$ is enhanced, the discontinuity is not able to open. Configuration (c) is a correct example.

where vector $[\mathrm{d}\mathbf{a}, \mathrm{d}\mathbf{b}, \mathrm{d}\mathbf{p}, \mathrm{d}\mathbf{q}]^{\mathrm{T}}$ denotes the incremental degrees of freedom. Since the applied force at the internal degrees of freedom are equal to zero, we can write the incremental internal degrees of freedom $\mathrm{d}\mathbf{p}$ and $\mathrm{d}\mathbf{q}$ as follows:

$$\begin{bmatrix} \mathrm{d}\mathbf{p} \\ \mathrm{d}\mathbf{q} \end{bmatrix} = - \begin{bmatrix} \mathbf{K}_{pp} & \mathbf{K}_{pq} \\ \mathbf{K}_{qp} & \mathbf{K}_{qq} \end{bmatrix}^{-1} \left(\begin{bmatrix} \mathbf{K}_{pa} & \mathbf{K}_{pb} \\ \mathbf{K}_{qa} & \mathbf{K}_{qb} \end{bmatrix} \begin{bmatrix} \mathrm{d}\mathbf{a} \\ \mathrm{d}\mathbf{b} \end{bmatrix} + \begin{bmatrix} \mathbf{f}_p^{\mathrm{int}} \\ \mathbf{f}_q^{\mathrm{int}} \end{bmatrix} \right) . \tag{3.72}$$

The internal degrees of freedom can be eliminated by substituting this relation into equation 3.71. Further derivation yields the condensed stiffness matrix:

$$\bar{\mathbf{K}} = \begin{bmatrix} \mathbf{K}_{aa} & \mathbf{K}_{ab} \\ \mathbf{K}_{ba} & \mathbf{K}_{bb} \end{bmatrix} - \begin{bmatrix} \mathbf{K}_{ap} & \mathbf{K}_{aq} \\ \mathbf{K}_{bp} & \mathbf{K}_{bq} \end{bmatrix} \begin{bmatrix} \mathbf{K}_{pp} & \mathbf{K}_{pq} \\ \mathbf{K}_{qp} & \mathbf{K}_{qq} \end{bmatrix}^{-1} \begin{bmatrix} \mathbf{K}_{pa} & \mathbf{K}_{pb} \\ \mathbf{K}_{qa} & \mathbf{K}_{qb} \end{bmatrix} , \tag{3.73}$$

and the condensed internal forces vector:

$$\bar{\mathbf{f}}^{\mathrm{int}} = \begin{bmatrix} \mathbf{f}_a^{\mathrm{int}} \\ \mathbf{f}_b^{\mathrm{int}} \end{bmatrix} - \begin{bmatrix} \mathbf{K}_{ap} & \mathbf{K}_{aq} \\ \mathbf{K}_{bp} & \mathbf{K}_{bq} \end{bmatrix} \begin{bmatrix} \mathbf{K}_{pp} & \mathbf{K}_{pq} \\ \mathbf{K}_{qp} & \mathbf{K}_{qq} \end{bmatrix}^{-1} \begin{bmatrix} \mathbf{f}_p^{\mathrm{int}} \\ \mathbf{f}_q^{\mathrm{int}} \end{bmatrix} . \tag{3.74}$$

It is emphasised that the additional degrees of freedom at geometrical nodes that describe the displacement jump cannot be condensed. The magnitude of

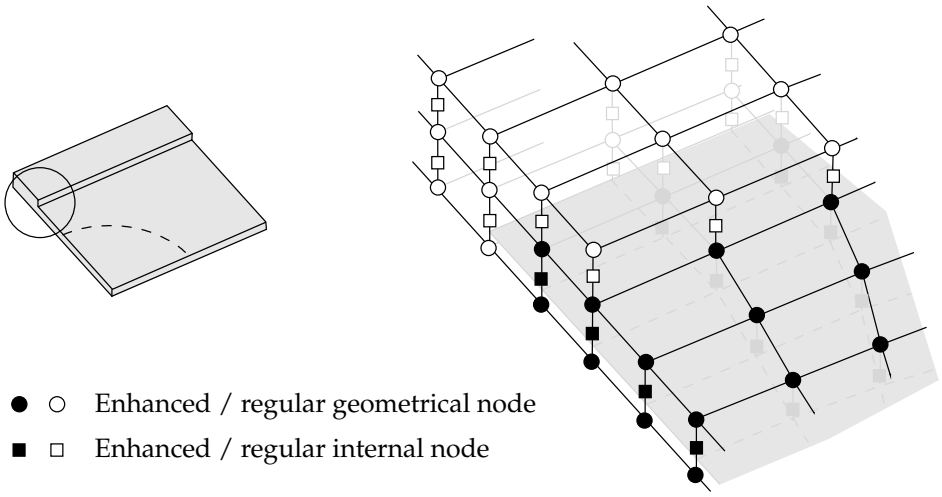

Figure 3.8 In case of stacked solid-like shell elements, the internal degrees of freedom in the neighbouring elements are not enhanced.

the displacement jump must be continuous across element boundaries. The degrees of freedom that describe this jump are therefore global and cannot be solved on the element local level. An exception is made for the additional internal degrees of freedom $\mathbf{q}$. Since the regular internal degrees of freedom $\mathbf{p}$ are already discontinuous across element boundaries, there is no need for the additional internal degrees of freedom to be continuous. In practice, an enhanced eight-node solid-like shell element has a total of 56 degrees of freedom; two times three in each geometrical node plus two times four internal degrees of freedom. These last two sets are eliminated by condensation reducing the contribution of the element to the global solution vector to 48 degrees of freedom.

Shear locking

It was observed by Parisch (1995) that the eight-node element suffers from the same shear locking phenomenon as general four node shell elements. A remedy to this problem is the assumed natural strain approach (Bathe and Dvorkin 1986). Here, the transverse shear strains ϵ_{23} and ϵ_{13} in (3.28b) are composed of alternative strain formulations $\bar{\epsilon}_{23}$ and $\bar{\epsilon}_{13}$ which are evaluated at four alternative positions along the edges of the elements, the tying points

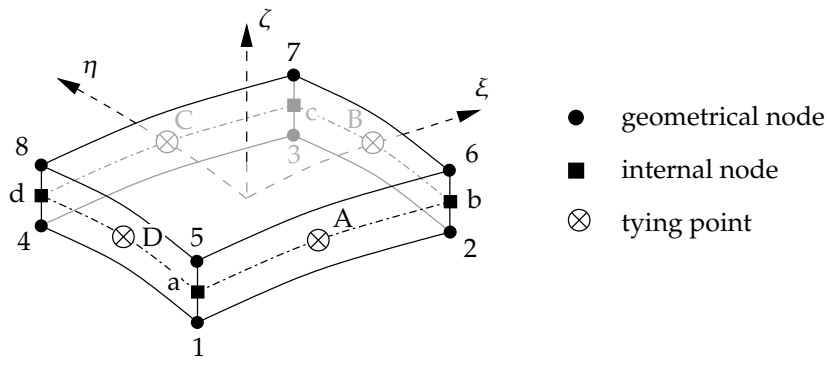

Figure 3.9 Location of tying points in eight-node solid-like shell element.

A-D in Figure 3.9. The corresponding strain terms in the Gauss integration points are obtained by straightforward interpolation:

$$\begin{aligned} \epsilon_{23}^{\text{ANS}} &= \chi_A \bar{\epsilon}_{23}^{A} + \chi_C \bar{\epsilon}_{23}^{C} \,; \\ \epsilon_{13}^{\text{ANS}} &= \chi_B \bar{\epsilon}_{13}^{B} + \chi_D \bar{\epsilon}_{13}^{D} \,. \end{aligned} \tag{3.75}$$

In this equation χ_S denote the corresponding linear shape functions. The contributions of the assumed natural strain terms to the discretised variational strain and the geometric part of the stiffness matrix can be found in section B.4.

Numerical integration

The construction of the element internal force vector and stiffness matrix requires a proper integration of three domains; $\mathcal{V}_0$, $\mathcal{V}_0^+$ and $\mathcal{S}_0$. In this case, all three domains are standard geometrical entities (two six-sided volumes and a rectangular surface) and can therefore be integrated numerically with standard Gauss integration schemes.

§ 3.6 Numerical examples

Two examples are presented to demonstrate the performance of the element. In the first example, attention is focused on the accuracy of the element for a decreasing thickness in geometrically linear applications. In the second example, the performance of the element in a geometrically and physically

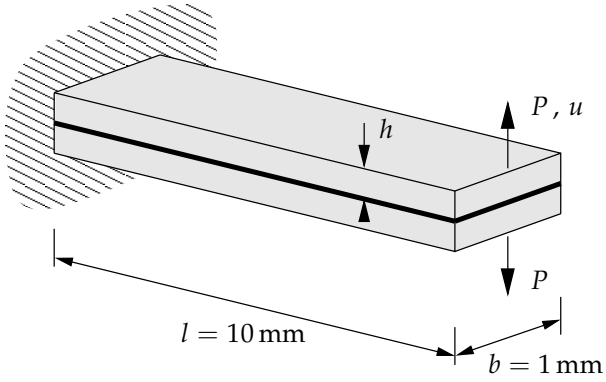

Figure 3.10 Geometry of a delaminated double cantilever beam under peel loading.

nonlinear analysis is illustrated by means of the simulation of a delamination buckling test.

A peel test

To test the performance of the new element for a decreasing thickness, a peel test has been performed. The double cantilever beam shown in Figure 3.10 consists of two layers of the same material with Young's modulus $E = 100.0$ N/mm^2 and Poisson's ratio $\nu = 0.0$. The beam has delaminated over its entire length. The test is performed for two different models. The first model contains ten eight-node enhanced solid-like shell elements (SLS+8); the second model is built with just five sixteen-node enhanced solid-like shell elements (SLS+16). In both cases, only one element in thickness direction is used. The delamination is modelled by a traction free discontinuity.

The linear out-of-plane displacements are given as functions of the ratio of layer thickness and beam length in Figure 3.11. The results are normalised by the exact solution that follows from the theory of beam deflections. The eight-node enhanced solid-like shell element gives nearly exact results for aspect ratios up to 2000. The performance of the sixteen-node solid-like shell element is even better. Indeed, it appears that the bending properties of the enhanced element are not affected by the enhancement and give the same performance as the underlying element (Parisch 1995). The enhanced element effectively acts as two elements.

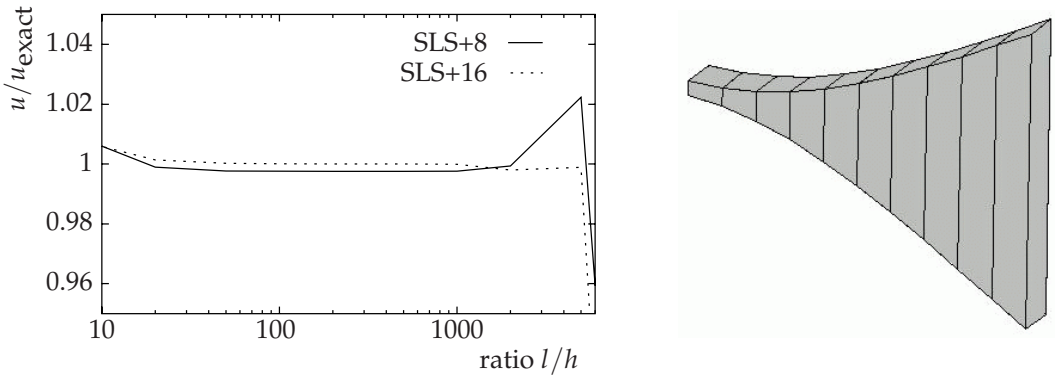

Figure 3.11 Double cantilever beam loaded by a peel force. Left: the normalised linear solution u/u_{exact} as a function of the length over layer thickness ratio l/h. Right: the deformed mesh.

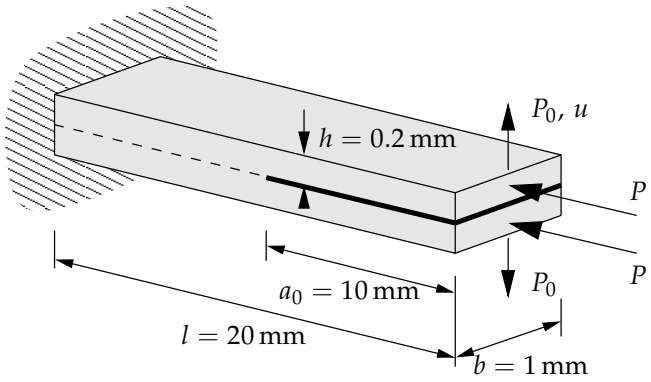

Figure 3.12 Geometry of double cantilever beam with initial delamination a_0 under compression.

Delamination buckling of a cantilever beam

Next, a combination of delamination growth and structural instability is considered (Allix and Corigliano 1999, Wells *et al.* 2003). The double cantilever beam in Figure 3.12 has an initial delamination length of $a_0 = 10\,\text{mm}$ and is subjected to an axial compressive load $2P$. Two small perturbation forces P_0 are applied to trigger the desired buckling mode. Both layers are made of the same material with Young's modulus $E = 135\,000\,\text{N/mm}^2$ and Poisson's ratio $\nu = 0.18$. The ultimate strength of the bond in mode-I is equal to $t_{I,ult} = 50\,\text{N/mm}^2$, the fracture toughness is $G_c = 0.8\,\text{N/mm}$. The critical load for local buckling of the beam, prior to delamination growth can be

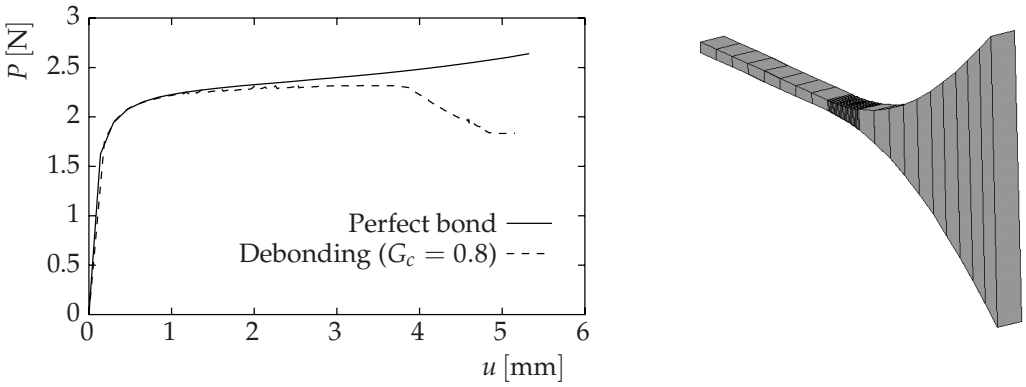

Figure 3.13 Delamination buckling test. Left: tip displacement as a function of the applied axial load P. Right: final deformation.

calculated analytically using the equation for a single cantilever beam with length a_0 and thickness h. For the given material parameters, the buckling load P_{cr} is equal to:

$$P_{\text{cr}} = \frac{\pi^2 E h^3}{48 a_0^2} = 2.22\,\text{N}\,. \tag{3.76}$$

The finite element mesh used for the analysis is composed of eight-node enhanced solid-like shell elements and is shown in Figure 3.13. Again, it consists of only one element in thickness direction. In order to capture delamination growth correctly, the mesh is locally refined.

Figure 3.13 shows the lateral displacement u of the beam as a function of the external force P. The load-displacement response for a specimen with a perfect bond (no delamination) is given as a reference. The numerically calculated buckling load is in agreement with the analytical solution. Steady delamination growth starts at a lateral displacement $u = 4\,\text{mm}$, which is in agreement with previous simulations (Allix and Corigliano 1999).

§ 3.7 Conclusions

In this chapter, the partition of unity approach to cohesive fracture is incorporated in a structural element, the solid-like shell element (Parisch 1995, Remmers *et al.* 2003b). The new element can be used for the simulation of de-

lamination growth in thin-walled composite structures. This new approach has a number of advantages. First, the displacement jump is only activated as the delamination propagates, which already results in a reduction of the total number of degrees of freedom. Moreover, it is possible to model a laminate and capture delamination, with just one element in the thickness direction. With conventional techniques, at least double the number of elements is needed. These properties allow the use of coarse meshes and to analyse delamination phenomena on a mesoscopic level of observation.

The two examples clearly demonstrate that the discontinuous solid-like shell elements possess the same properties as the original element. The delamination buckling example underlines the excellent performance of the element in combined geometrically and physically nonlinear analyses.

A solid-like shell element allowing for arbitrary delaminations

Chapter 4

Delamination buckling of fibre-metal laminates

Over the last decades, there has been a search for new materials with improved properties that can replace the traditional aluminium alloys in aerospace structures. At the Faculty of Aerospace Engineering at Delft University of Technology, these activities resulted in the development of fibre-metal laminates, a hybrid material made of alternating layers of light-weight metal alloys and fibre-reinforced prepreg (Vlot 2001).

The history of the development of fibre-metal laminates can be traced back to the early 1950s when the Dutch aerospace manufacturer Fokker started to use alternative techniques to bond structural components. Instead of riveting aluminium stringers and doublers to the aluminium skin panels, these structural parts were literally glued using adhesives in combination with autoclave cycles. Due to the absence of rivet holes, the resulting structure appeared to possess an increased residual strength.

Inspired by these results, the search for new materials focused on the development of aluminium based laminates. One of the initial designs consisted of aluminium and aramid reinforced prepreg, which became known under the acronym Arall. The material showed a significant increase in the fatigue resistance (Marissen 1988). Further improvements led to the development of Glare in which the aramid fibres were replaced by glass fibres, see Figure 4.1. This material has even superior fatigue performance in aircraft structures (Vogelesang *et al.* 1995). Moreover, it also appeared to possess excellent impact and fire resistance properties (Roebroeks 1997). As opposed to tradi-

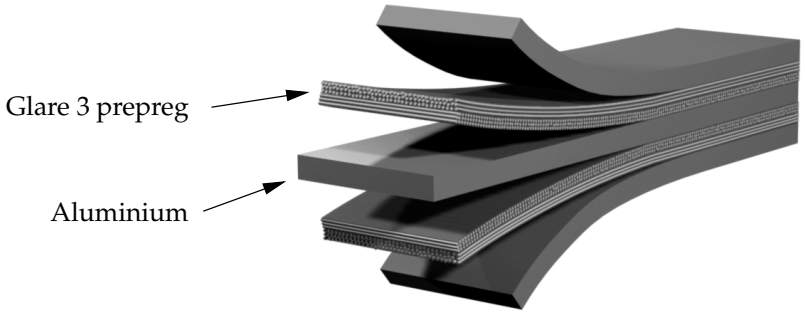

Figure 4.1 Schematic overview of Glare 3. The first, third and fifth layer consist of aluminium. The intermediate layers are $0/90^\circ$ glass fibre reinforced cross plies.

tional composite materials such as carbon fibre-reinforced epoxies, durability of the material seems of less concern, since the prepreg is protected from the environment by the relatively durable outer aluminium layer. Even more important, the material can be applied in the structure in the same way as traditional aluminium panels, whereas in general, for composite materials, special methods for fixation are required. In 2001, after a long period of extensive research, Glare was selected as the main material for the skin in the Airbus A380.

Despite this success, there are a number of unanswered questions regarding the physical and mechanical properties of fibre-metal laminates such as Glare. One of these concerns the behaviour of panels with initial delaminations that are subjected to compressive and / or shear loadings, as shown in Figure 4.2. Upon loading, the delaminated layer may buckle locally. The out-of-plane displacement of this layer will cause high interlaminar stresses at the delamination front. When these stresses exceed a yield limit, the delaminated area will extend, which in turn will lead to a decrease of post-buckling stiffness, progressive delamination growth and eventually, failure of the panel. Because of these concerns, so far, Glare will only be applied to those parts of the structure of the A380 that are loaded in pure tension: the crown section of the fuselage.

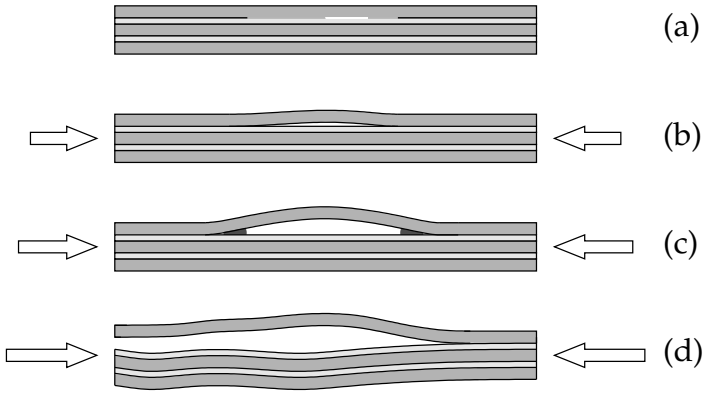

Figure 4.2 Schematic representation of the delamination buckling failure mechanism; (a) initial delamination, (b) local buckling, (c) delamination growth, (d) failure.

Fortunately, the delamination buckling scenario has never been observed in laboratory experiments with panels with an initial delamination under *axial compressive loadings* (Vlot 1991, Bosker 1998). It was found that the outer layer buckled locally with a small reduction of the global stiffness of the specimen as a result. Even when the applied load was increased up to 200 MPa, no delamination growth was observed (Vlot 1991, Bosker 1998). The same conclusion could be drawn from fatigue tests (Hooijmeijer and Bosker 2000) and experiments where the specimen was exposed to extreme environmental conditions that may degenerate the quality of the adhesive material (Bosker 2000). Apparently, the interlaminar bond is strong enough to withstand the tractions in the interface and therefore, delamination buckling due to axial compression is not a major concern for this kind of material.

Numerical simulations have shown that the shear tractions in the interface between the aluminium and the prepreg layer play an important role in the initiation of delamination growth (Remmers and de Borst 2001a). This is most likely the explanation why delamination growth is not observed in axial compression tests, but it also suggests that delamination buckling may be a point of concern when a delaminated panel is subjected to a *shear loading*.

In this chapter, the discontinuous solid-like shell element as described in chapter 3 will be used to simulate the mechanical behaviour of Glare panels under compression.

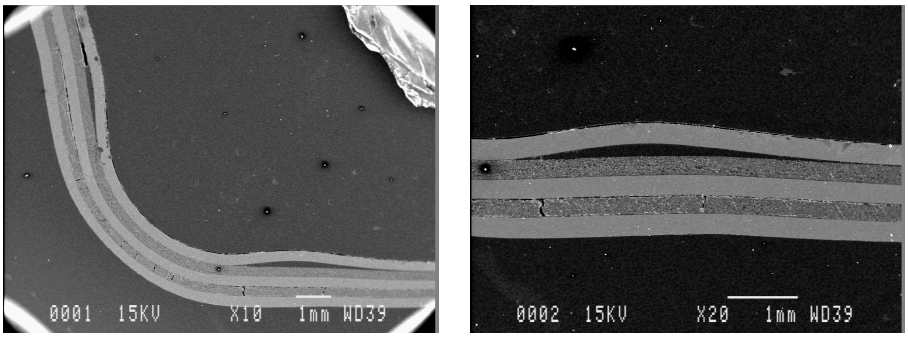

(a) Overview. (b) Detail.

Figure 4.3 SEM picture of local buckling of the top layer of a Glare 2-3/2-0.3 specimen after being subjected to a three-point bending test (de Jong *et al.* 2001).

§ 4.1 Experimental observations

Figure 4.3 (a) shows a small specimen of Glare 2-3/2-0.3, which has been subjected to a three-point bending test in order to determine the ultimate shear traction of the interface between the aluminium and the prepreg layer (de Jong *et al.* 2001). In this specific case - most likely due to a production error - the outer layer has buckled and delaminated, as shown in Figure 4.3 (b). The prepreg layer has remained undamaged, apart from some single fibres that seemingly have left the prepreg, see Figure 4.4 (a).

When we take a closer look at the crack front, Figure 4.4 (b), we notice that the actual interface between the two layers -the adhesive bond of aluminium and epoxy- has remained intact and that the crack starts near a fibre inside the prepreg layer. This observation can be explained as follows. Before fabrication, the aluminium panels are extensively treated. First, the existing oxidised surface is removed by an etching process. Then, the aluminium is anodised to create an oxide layer with a good morphology. After this, the surface is treated with a primer in order to enhance the durability of the bond. Finally, several hours after application of the primer, the laminate is stacked and put in the autoclave.

Consequently, the adhesive bonding between the aluminium and the prepreg layer is of excellent quality. In fact, the ultimate interface strength is

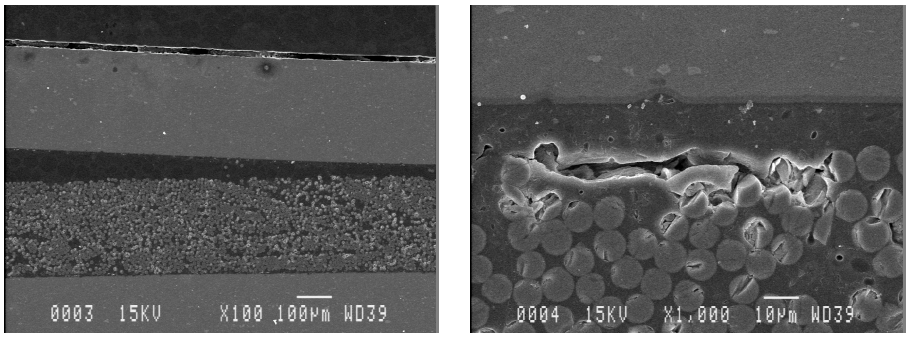

(a) Overview. (b) Crack tip.

Figure 4.4 SEM picture of delamination front of a Glare 2-3/2-0.3 specimen due to delamination buckling (de Jong *et al.* 2001).

much higher than the strength in the transition zone between fibre rich and resin rich prepreg. A crack will therefore initiate in this area.

§ 4.2 Numerical model

Delamination buckling is a combination of structural effects (instability) and material nonlinearities. In order to take both mechanisms into account, we will investigate the phenomena on a mesoscopic level. This means that the aluminium and the fibre-reinforced prepreg layers will be considered as homogeneous, orthotropic materials, with given constitutive parameters. The laminate will be modelled by a single solid-like shell element.

The crack growth in the transition zone between the fibre rich and resin rich prepreg is simulated by a discontinuity inside the elements. In order to avoid numerical problems with progressing delamination fronts, the discontinuity is present at the beginning of the analysis, even in the case of a perfect bond. The delamination characteristics of the transition zone are lumped in an orthotropic cohesive constitutive relation that governs the opening of the discontinuity. The perfect bond prior to cracking is simulated by a dummy stiffness. The initial delamination is modelled by an traction free discontinuity. Self contact in the initial delamination is avoided by a frictionless contact algorithm.

Delamination model

From the three-point bending test (Figure 4.4) it appeared that delamination is a combination of two damage mechanisms on a microscopic scale: an adhesive debonding of the interface between the fibres and the matrix material and a cohesive matrix crack. In order to capture both mechanisms, a damage model is used at a mesoscopic scale. In this model, the stiffness of the interface between the aluminium and the prepreg layers is reduced by means of damage parameters, which are initially equal to zero and equal one when the material is completely damaged (Lemaitre and Chaboche 1990). An equivalent relative displacement of the interface is taken as the controlling parameter for damage growth. As soon as the equivalent relative displacement exceeds an initial or threshold value, the damage parameter starts to increase according to a damage growth relation.

Delamination growth in composite materials depends on the angle between the fibre orientation and the delamination front. Therefore, a single scalar damage parameter cannot be used. Furthermore, the delamination crack is a combination of mode I and mode II. Moreover, a difference can be observed between tension and compression in the mode-I direction. In the latter case, the material is not damaged, but behaves perfectly plastic. A model that incorporates these aspects has been derived by Schipperen (2000) and is based on the constitutive assumptions in the plasticity-based delamination models by Schellekens and de Borst (1994) and Hashagen (1998).

The constitutive relation of the discontinuity can then be written as:

$$\mathbf{t}_\mathrm{d} = (\mathbf{I} - \mathbf{d})\mathbf{D}\mathbf{v}_\mathrm{d}\,, \tag{4.1}$$

where $\mathbf{D}$ the initial elastic 'dummy' stiffness, $\mathbf{I}$ is the unit tensor and $\mathbf{d}$ a second-order damage tensor. We consider the case that only the diagonal terms of this tensor are non-zero. Damage occurs when the current equivalent relative displacement κ exceeds all previously attained values:

$$\kappa(\mathbf{v}, t) = \max[\kappa(\mathbf{v}, \tau)|\tau < t\,,\, \kappa_\mathrm{init}]\,, \tag{4.2}$$

with κ_init the initial or threshold value of κ. The equivalent relative displacement is a function of the relative displacements in the three directions:

$$\kappa = \sqrt{\frac{1}{2}\mathbf{v}_\mathrm{d}^\mathrm{T}\mathbf{P}\mathbf{v}_\mathrm{d} + \mathbf{q}^\mathrm{T}\mathbf{v}_\mathrm{d}}\,, \tag{4.3}$$

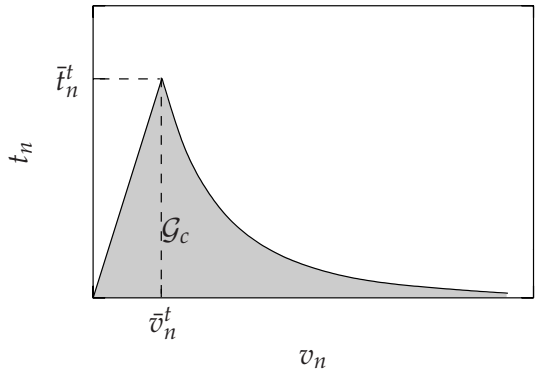

Figure 4.5 Traction-relative displacement relation in mode-I direction for the orthotropic delamination model.

where,

$$\mathbf{P} = \text{diag}\left[2\frac{\bar{v}_n^t}{\bar{v}_n^c}, 2\left(\frac{\bar{v}_n^t}{\bar{v}_{s1}}\right)^2, 2\left(\frac{\bar{v}_n^t}{\bar{v}_{s2}}\right)^2\right], \tag{4.4}$$

and:

$$\mathbf{q} = \text{diag}\left[\bar{v}_n^t\left(1 - \frac{\bar{v}_n^t}{\bar{v}_n^c}\right)^2, 0, 0\right]^{\text{T}}, \tag{4.5}$$

where $\bar{v}_n^t$ and $\bar{v}_c^t$ are the relative displacement equivalents for the yield traction in the normal direction (respectively tension and compression); $\bar{v}_{s1}$ and $\bar{v}_{s2}$ are the relative displacement equivalents under shear loadings.

Softening is governed by the fracture toughness G_c. Experiments with Glare show a softening behaviour of the interface that resembles an exponential curve, see Figure 4.5. Inspired by this, the following relation is used for the diagonal components of damage parameter $\mathbf{d}$:

$$d_{ii} = 1 - \frac{\kappa}{|\mathbf{v}_\text{d}|}\exp\left(-\frac{2D_{ii}\bar{v}_n^t}{G_c}(\kappa - \bar{v}_n^t)\right), \tag{4.6}$$

where $|\mathbf{v}_\text{d}|$ is the magnitude of the displacement jump $\mathbf{v}_\text{d}$. The damage parameters d_{ii} in this model will approach the limit value 1.0 asymptotically. This improves the numerical stability of the model, which is important, since we can expect large relative velocities in the case of delamination buckling. The use of a tangent stiffness matrix guarantees quadratic convergence in the nonlinear analysis.

Frictionless contact model

As a result of delamination growth, the local buckling mode of the delaminated layer will change. Consequently, some areas of this layer will move inwards and penetrate the underlying prepreg layers. A contact algorithm is needed in order to prevent this in the numerical simulation.

In the current model, the traction free discontinuity that represents the initial delamination is equipped with a penalty contact algorithm. Initially, the stiffness terms in the constitutive relation are equal to zero. As soon as the normal component of the relative displacement v_n of the two adjacent surfaces in the element is negative, a penalty stiffness D_{pen} is applied, according to:

$$\mathbf{t}_{\text{d}} = \mathbf{D}\mathbf{v}_{\text{d}} \,, \tag{4.7}$$

where

$$\begin{cases} \mathbf{D} = \text{diag}[D_{\text{pen}}, 0, 0] & \text{if } v_n < 0, \\ \mathbf{D} = \text{diag}[0, 0, 0] & \text{if } v_n > 0. \end{cases} \tag{4.8}$$

Note that for reasons of simplicity, the additional stiffnesses in the transverse directions of the element due to friction are neglected, assuming that this will not have a large effect on the global behaviour of the structure.

§ 4.3 Small Arall strip with initial delamination

One of the earliest investigations on the behaviour of delaminated fibre-metal laminates was done by Vlot (1991). Consider a thin strip as shown in Figure 4.6. The strip is made of Arall, a predecessor of Glare, and consists of two layers: an aluminium layer with thickness $h_1 = 0.3\,\text{mm}$ and an aramid reinforced prepreg layer, thickness $h_2 = 0.2$. The adhesive between these layers has initially delaminated over a length of $l = 18\,\text{mm}$. The strip is attached to a thick aluminium substrate in order to prevent global buckling of the structure.

Since the specimen is symmetric along both the x-axis and the y-axis, only one quarter is modelled, see Figure 4.7. Symmetrical boundary conditions are applied to the cutting edges. In order to decrease the size of the model further, the thick substrate is not modelled either. Instead, the displacements in the z-direction of the lower bound of the Arall prepreg layer are constrained. The

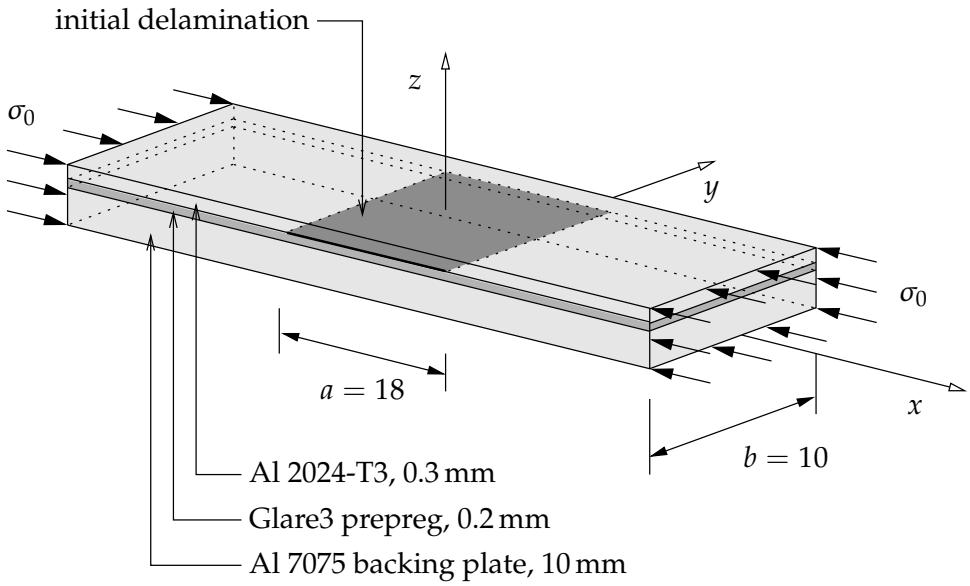

Figure 4.6 Geometry of the Arall strip with initial delamination subjected to a compressive force. All dimensions in [mm].

two remaining layers are modelled with just one element in thickness direction with a total thickness of 0.5 mm. The discontinuity is placed 0.3 mm from the top. The correct local buckling mode is triggered by a small perturbating force.

In order to be able to increase the applied load to extreme high levels, the aluminium is assumed to be linear elastic with Young's modulus $E = 72\,000$ MPa and Poisson's ratio 0.3. The aramid fibre-reinforced prepreg is modelled as a linear elastic orthotropic material. The homogeneous material properties are obtained from (Verbruggen 1986) and are listed in Table 4.1.

The tractions at the onset of fracture of the interface between the aluminium layer and the prepreg layer are obtained from previous simulations with similar materials (Hashagen 1998). The ultimate traction in normal direction in tension and compression are assumed to be $\bar{t}_n^t = 50.0$ MPa and $\bar{t}_n^c = 150.0$ MPa respectively, and the ultimate traction in the two transverse directions equals $\bar{t}_{s1} = \bar{t}_{s2} = 25.0$ MPa. The fracture toughness is $G_c = 1.1\,\mathrm{N/mm}$. An initial 'dummy' stiffness of the interface elements of $D_{ii} = 50\,000\,\mathrm{N/mm^3}$ is assumed.

An analytical solution for the local buckling load of a clamped panel with

E_{11}	57 700 MPa	G_{12}	5 500 MPa	ν_{12}	0.195
E_{22}	5 022 MPa	G_{23}	5 500 MPa	ν_{23}	0.032
E_{33}	5 022 MPa	G_{13}	5 500 MPa	ν_{13}	0.032

Table 4.1 Material parameters for a uni-directional Arall prepreg.

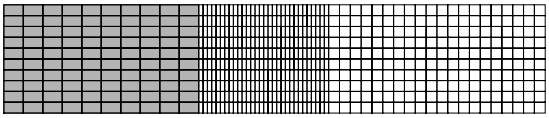

Figure 4.7 Top view of the finite element mesh used for the simulation of delamination growth in the Arall strip. The initial delamination is located at the grey elements.

thickness $h_1 = 0.3\,\text{mm}$ and length $l = 18\,\text{mm}$ was formulated by Kachanov (1988). In this specific case, the critical buckling load is equal to:

$$\sigma_{0,\text{K}} = \frac{\pi^2 E}{3(1-\nu^2)}\left(\frac{h_1}{l}\right)^2 = 72.3\,\text{MPa}\,. \tag{4.9}$$

First, the critical buckling load of the model is determined by means of an eigenvalue analysis. Since it is not possible to use nonlinear material models in this type of analysis, the interface elements are assumed to be linear elastic with a stiffness $D_{ii} = 50\,000\,\text{MPa}$. The lowest eigenvalue is found at $\sigma_0 = 62.96\,\text{MPa}$. This is not completely in agreement with the analytical estimation, since in the finite element model, the outer aluminium layer is supported by a relatively flexible Arall layer, whereas in the analytical estimation, a rigid support was assumed. The buckling load in the laboratory experiments varied from 40 to 45 MPa (Vlot 1991).

Next, the deformation of the model is calculated in a quasi-static analysis. The load-displacement curve is shown in Figure 4.8. Due to the small initial imperfection, it is not possible to pinpoint an unambiguous value for the buckling load. When the post-buckling path is extrapolated, a buckling load $\sigma_0 \approx 60.0\,\text{MPa}$ is found, which is in agreement with the eigenvalue analysis.

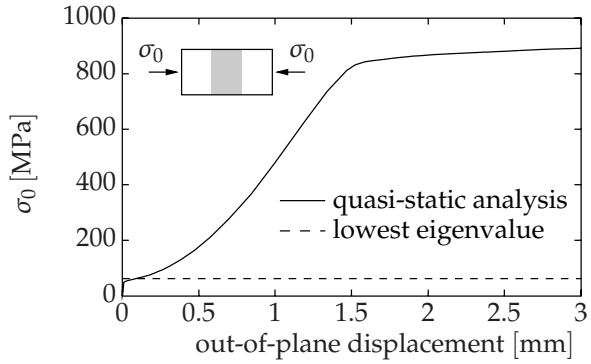

Figure 4.8 Out-of-plane displacement of the delaminated Arall strip versus applied axial load σ_0. The dashed line corresponds to the critical buckling load obtained by the eigenvalue analysis.

Progressive delamination growth starts at an axial load level $\sigma_0 = 750\,\text{MPa}$. This delamination growth is triggered by the shear tractions in the interface exceeding the ultimate level of 25.0 MPa. The calculations are continued up to the point that both layers have separated completely.

§ 4.4 Glare panel with circular delamination

In the next example, the behaviour of a Glare panel with a circular initial delamination under both a compressive and a shear loading is examined. The failure mechanism is now somewhat more complicated, since the direction in which the delaminated zone will propagate is not evident. Similar studies with carbon fibre-reinforced epoxies (Rinderknecht 1994) show that the delamination grows in a direction perpendicular to the main loading direction. As a result, the delaminated area transforms from a circular area into an ellipsoidal one. Consequently, the buckling mode will change as well, and some parts of the top layer will tend to move inwards. We consider the possibility of self-contact and apply the contact algorithm.

Consider the specimen as shown in Figure 4.9. The panel consists of an aluminium layer with thickness $h_1 = 0.2\,\text{mm}$ and a Glare3 $0/90^\circ$ prepreg layer with a thickness $h_2 = 0.25\,\text{mm}$. A circular delamination with radius 8 mm is assumed. The layers are attached to a thick backing plate in order to prevent global buckling. In the first simulation a uni-axial compressive

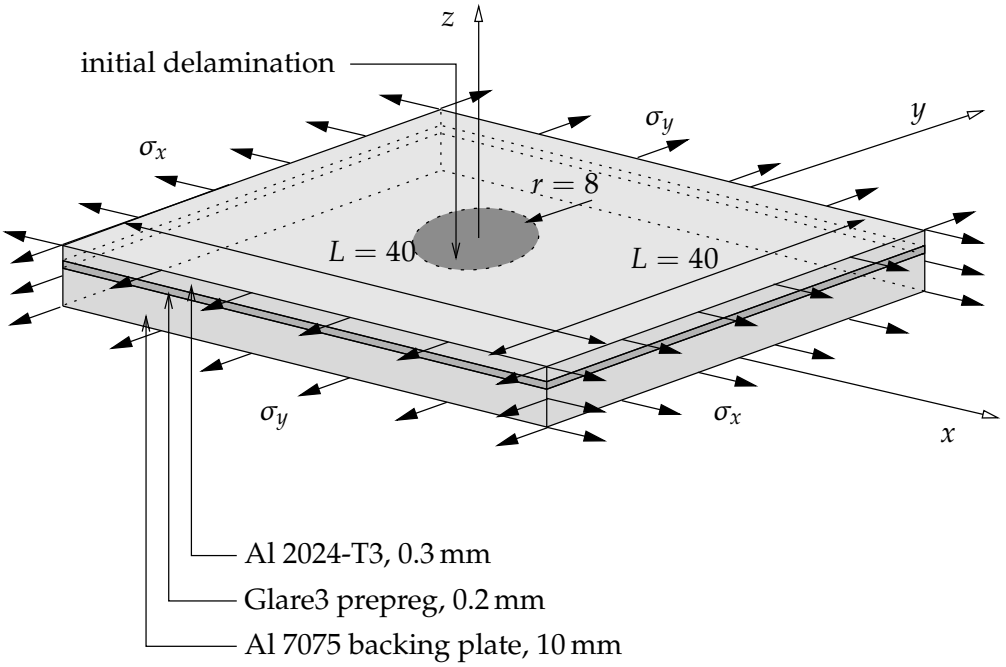

Figure 4.9 Geometry of the Glare panel with a circular initial delamination, which is located between the top aluminium layer and the Glare prepreg layer. All dimensions in [mm].

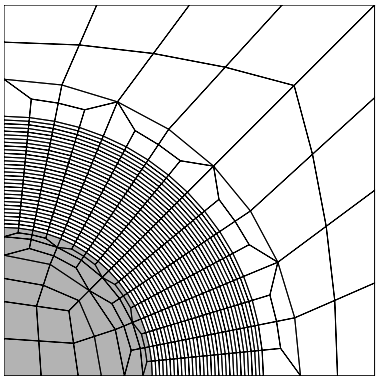

Figure 4.10 Top view of the finite element mesh used for the simulation of delamination growth in the Glare panel. The initial delamination located at the grey elements. Note that just one quarter of the panel ($x > 0$, $y > 0$) is modelled.

E_{11}	33 170 MPa	G_{12}	5 500 MPa	ν_{12}	0.195
E_{22}	33 170 MPa	G_{23}	5 500 MPa	ν_{23}	0.032
E_{33}	9 400 MPa	G_{13}	5 500 MPa	ν_{13}	0.032

Table 4.2 Material parameters for $0/90^\circ$ Glare3 prepreg.

loading in x-direction is considered ($\sigma_x = -\sigma_0$, $\sigma_y = 0.0$).

The analytical estimation for the local buckling load of a clamped unidirectional panel with thickness h_1 subjected to an axial compressive load σ_0 was derived by Shivakumar and Whitcomb (1985). For the given configuration, the lowest critical buckling load is equal to $\sigma_0 = 113.2\,\text{MPa}$.

The finite element mesh is built with the same assumptions as in the previous example and is shown in Figure 4.10. The material parameters for the Glare3 layer are obtained from (Hashagen 1998) and are listed in Table 4.2. The material constants for the delamination damage model are identical to the parameters in the previous example.

The critical buckling load is determined by means of an eigenvalue analysis. The contact algorithm and the interface damage model are not included in this analysis yet, for the reasons mentioned before. The lowest buckling mode was found to be $\sigma_0 = 82.03\,\text{MPa}$. The corresponding eigenmode is shown in Figure 4.11. The buckling load is significantly lower than the analytical estimation. Again, this difference can be attributed to the relatively soft support of the Glare3 prepreg layer.

The contact algorithm is included in the quasi-static analysis. The penalty stiffness is set equal to the dummy stiffness of the interface elements with the delamination model: $D_{pen} = 50\,000\,\text{MPa}$. The out-of-plane displacement of the centre point of the panel, $(x, y) = (0, 0)$, is shown in Figure 4.12. The local buckling load is in agreement with the eigenvalue analysis. Initial delamination growth does not start before a load $\sigma_0 = 300\,\text{MPa}$. Progressive delamination starts at an external load $\sigma_0 \approx 950\,\text{MPa}$. As expected, the delamination expands in a direction perpendicular to the loading direction, see Figures 4.13. Figure 4.14 shows the delaminated interface. Here, it is assumed that the cohesive surface has lost its load carrying capability when $d_{11} > 0.95$.

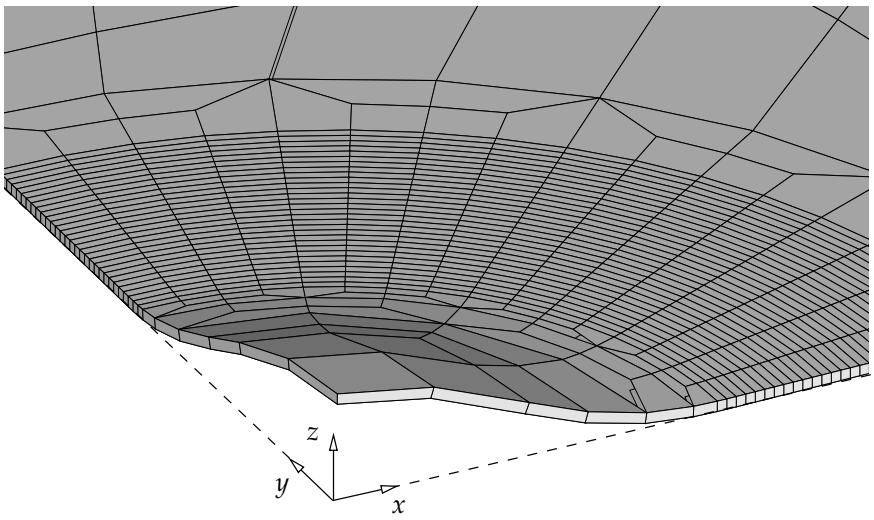

Figure 4.11 Buckling mode that corresponds to the critical buckling load $\sigma_0 = 82.03\,\text{MPa}$ of the Glare panel under uni-axial loading. Note that only the part of the solid-like shell element that represents the aluminium top layer is shown.

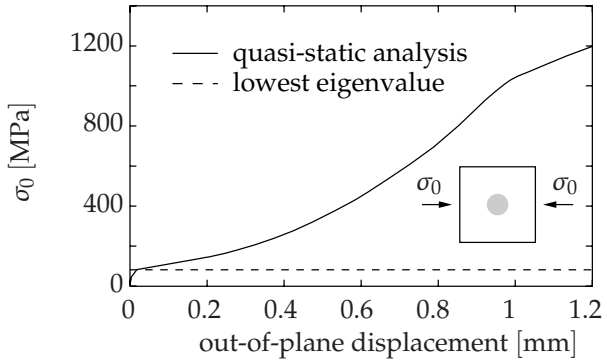

Figure 4.12 Out-of-plane displacement of top layer versus applied axial compressive load σ_0. The dashed line corresponds to the critical buckling load obtained by the eigenvalue analysis.

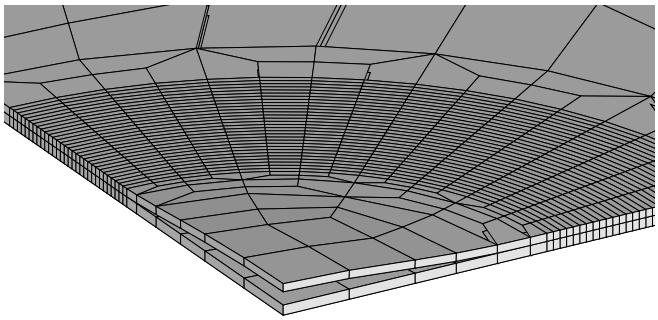

(a) Post buckling, $\sigma_0 = 238\,\text{MPa}$.

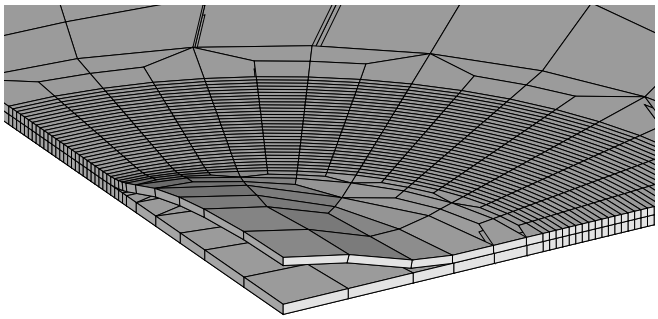

(b) First delamination, $\sigma_0 = 1009\,\text{MPa}$.

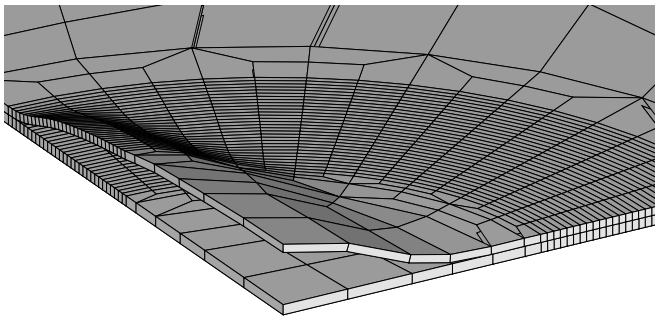

(c) Progressive delamination, $\sigma_0 = 1248\,\text{MPa}$.

Figure 4.13 Deformation of the Glare laminate under uni-axial loading. Note that in (c) a large part of the initial delamination is closed.

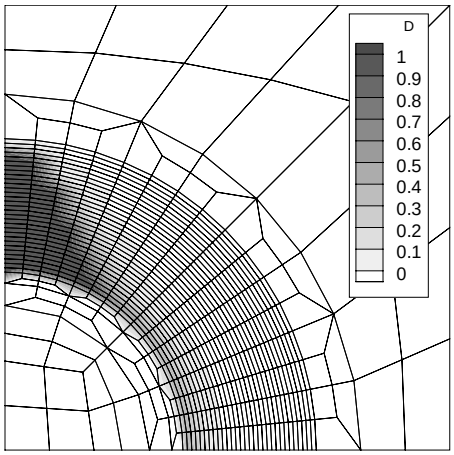

Figure 4.14 Damage in the interface at the final step of the simulation of the panel under the uni-axial loading condition.

The panel has also been subjected to a bi-axial stress state: a compressive stress in x-direction and a tension in the y direction ($\sigma_x = -\sigma_0; \sigma_y = \sigma_0$). At an angle of 45° ($x = y$), this stress state can be regarded as a pure shear stress $\tau = \frac{1}{2}(\sigma_y - \sigma_x) = \sigma_0$.

The lowest eigenvalue load for this loading case is determined by an eigenvalue analysis and is equal to $\tau = 154.8$ MPa. The corresponding eigenmode is shown in Figure 4.15. Note that this mode has three half waves in the x-direction: some parts of the delaminated aluminium tend to move inwards.

Figure 4.16 shows the load-displacement curve of the panel in the quasi-static simulation. The buckling load in this simulation is much higher ($\tau \approx 250$ MPa) than the lowest eigenvalue. This is due to the fact that in this case, the aluminium layer cannot buckle in the eigenmode that corresponds to the critical load, since the frictionless contact algorithm prevents the aluminium layer to move inwards.

Consequently, the onset of delamination growth is found at a higher load level too. Progressive delamination is observed at a load level $\tau \approx 1300$ MPa. Figure 4.17 shows the delaminated area at the end of the quasi-static analysis. It can be seen that this zone is less wide than the delaminated area in the sim-

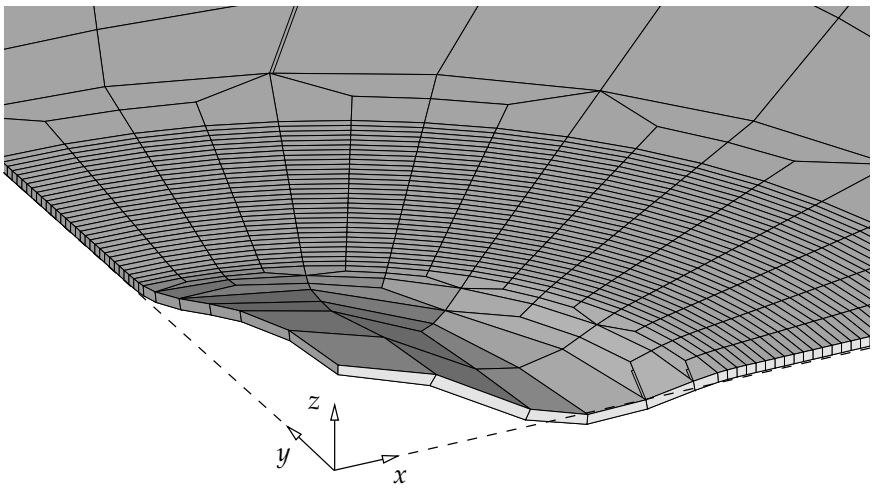

Figure 4.15 Buckling mode that corresponds to the critical buckling load $\tau = 154.8\,\text{MPa}$ under bi-axial loading. Just the aluminium top layer is shown in this figure. Note that large parts of this layer tend to move in the negative z-direction.

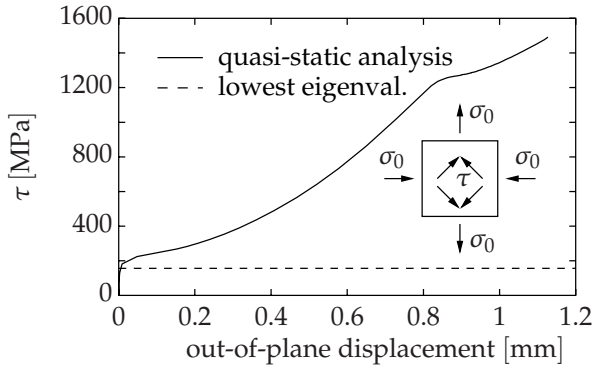

Figure 4.16 Out-of-plane displacement of top layer versus applied axial effective shear loading τ. The dashed line corresponds to the critical buckling load obtained by the eigenvalue analysis.

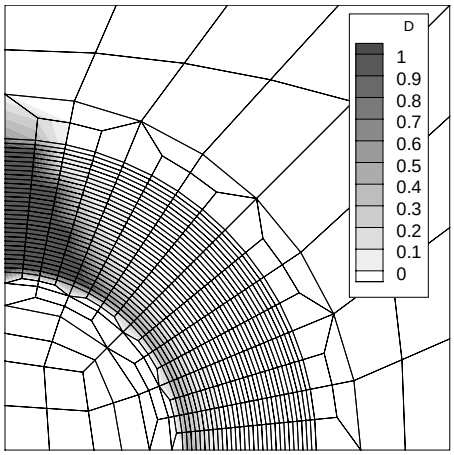

Figure 4.17 Damage in the interface at the final step of the simulation of the panel under the bi-axial loading condition.

ulation of uni-axial loading, which is an effect of the slightly different initial buckling mode.

§ 4.5 Conclusions

In this chapter, the discontinuous solid-like shell element has been used to simulate delamination buckling of fibre-metal laminates on a mesoscopic level. Experimental observations are used to capture the failure mechanisms at the interface and to translate these mechanisms in the delamination model.

The numerical tools have been applied to the simulation of three experiments: a small Arall strip under an axial compressive loading and a Glare panel with a circular initial delamination under both an axial compressive and a shear loading. In all simulations, delamination growth did not occur within the ranges of stresses that are usual in aerospace structures. Nevertheless, in our simulations, we could raise the stresses to much higher (but also less realistic levels) in order to determine the load level at which delamination growth would start and monitor the accompanying failure mechanisms.

Suggestions that delamination buckling of fibre-metal laminates can be a

point of concern when the panel is loaded in shear do not hold. Even in these cases, the load level at which progressive delamination growth is observed is far beyond the stresses that can be expected in the engineering practice.

Chapter 5

The cohesive segments method

It has been demonstrated in the previous chapters that the partition of unity approach to cohesive fracture is a flexible tool to simulate crack growth in structures on a macro- or mesoscopic level of observation. On these levels, the material is assumed to be homogeneous and the complex interaction of multiple micro-separations in the process zone can altogether be lumped in a cohesive zone which is incorporated in the finite element mesh by a single discontinuity.

On smaller levels of observation, the assumption that the material is homogeneous loses validity. Different constituents and imperfections in the material lead to inhomogeneous stress distributions, which in turn give rise to the nucleation of many microscopic cracks. The specific length at which these events happen, i.e. the length of the process zone, is now of the same order of magnitude as the dimensions of the specimen under investigation. When these phenomena are lumped into a single dominant crack some crucial features of the fracture process will be lost. In an accurate numerical analysis at this level of observation, the nucleation and growth of individual microcracks as well as their coalescence must be simulated.

The cohesive zone formulation, which proved to be capable of simulating crack nucleation (Needleman 1987), can be used to perform such detailed analyses. By placing cohesive interfaces at all interelement boundaries in the finite element mesh, crack branching and crack nucleation away from the crack tip can be captured (Xu and Needleman 1994). By equipping these cohesive interfaces with different constitutive relations, both fracture at the interfaces between constituents as well as cohesive fracture in the bulk ma-

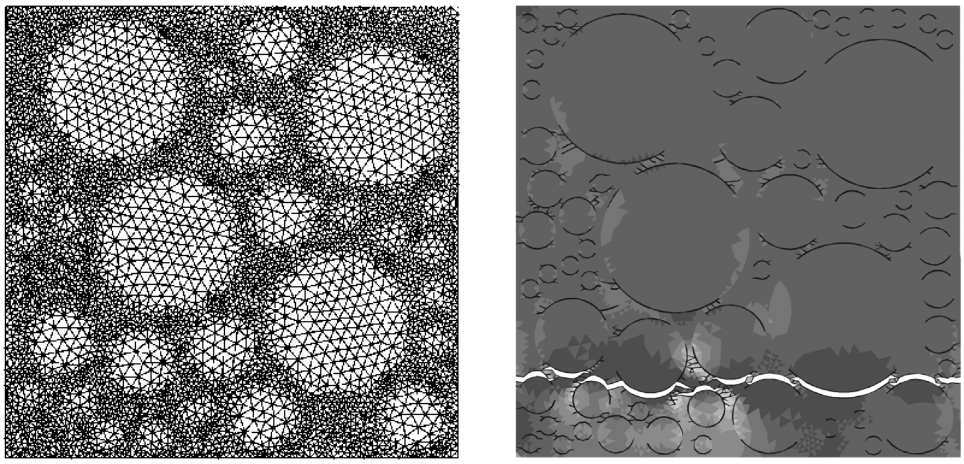

Figure 5.1 Simulation of fracture in a cementitious material. The figure on the left shows the finite element mesh of a specimen with circular aggregates. The figure on the right shows the hydrostatic stress and the deformed geometry after total fracture. The displacements are magnified by a factor 10.0 (Tijssens *et al.* 2001).

terial can be modelled. Examples of the simulation of complex crack growth in heterogeneous materials can be found in (Tijssens *et al.* 2001, Arata *et al.* 2001, Coker *et al.* 2003), see also Figure 5.1.

In the aforementioned contributions, the cohesive constitutive relations are equipped with a non-zero initial compliance to model a perfect bond prior to cracking. When the tractions exceed a limit value, also when this occurs in virgin material away from the crack tip, the stiffness of the interface is decreased according to a softening law. Since the interfaces form a web that covers the complete specimen, the nucleation, growth, branching and coalescence of multiple cracks is captured anywhere in the domain, without using additional requirements.

Notwithstanding the success of the method, it suffers from a small mesh bias since cracks are forced to propagate in prescribed directions, along the interelement boundaries. However, when the mesh is dense enough, any direction of crack growth is captured automatically by the composition of different angles. A more serious problem is related to the fact that the interfaces have a non-zero compliance prior to cracking. As a result, the overall stiffness of the

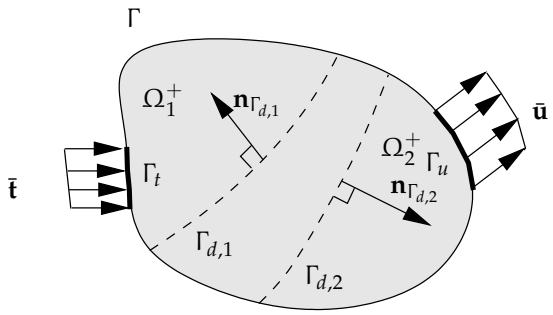

Figure 5.2 Domain Ω with two discontinuities, $\Gamma_{d,1}$ and $\Gamma_{d,2}$ (dashed lines). It is assumed that the discontinuities do not cross.

material is reduced, which may influence the accuracy of the results, at least in a quantitative sense.

These problems can be avoided when the interfaces are only introduced in the finite element mesh when needed. Camacho and Ortiz (1996) used the cohesive zone approach in conjunction with an adaptive mesh refinement technique. When the traction in a material point exceeds a threshold value, an interface is inserted in the mesh in the correct direction. An important disadvantage is that since the surrounding elements are modified, the material history in the corresponding integration points needs to be remapped onto the new integration points in the modified elements. Apart from the computational overhead, such a procedure will inevitably lead to the introduction of small errors.

The next logical step in the development of a truly mesh independent tool to simulate complex fracture phenomena in a discrete manner is the use of the partition of unity approach. In this chapter, the original formulation is extended to the *cohesive segments method* , which is able to describe multiple interacting cracks in a domain. Apart from a number of small modifications to the kinematic relations and equilibrium equations, additional implementation rules are presented in order to simulate the nucleation of a new crack, the coalescence of multiple cracks and crack branching.

§ 5.1 Kinematic relations

The key feature of the cohesive segments approach is the possible emergence of *multiple* cohesive zones in a domain. Consider the domain Ω with boundary Γ as shown in Figure 5.2. The domain contains m discontinuities $\Gamma_{\mathrm{d},j}$, where $j = 1...m$. It is assumed that the discontinuities do not cross. Each discontinuity splits the domain into two parts, which are denoted accordingly as Ω_j^- and Ω_j^+. For all discontinuities j in the domain, the following relation must hold:

$$\Omega_j^- \cup \Omega_j^+ = \Omega \qquad \forall \quad j = 1...m\,. \tag{5.1}$$

The displacement field in the domain Ω consists of a continuous regular displacement field $\hat{\mathbf{u}}$ plus m additional continuous displacement fields $\tilde{\mathbf{u}}_j$, cf. (Daux *et al.* 2000):

$$\mathbf{u}(\mathbf{x},t) = \hat{\mathbf{u}}(\mathbf{x},t) + \sum_{j=1}^{m} \mathcal{H}_{\Gamma_{\mathrm{d},j}}(\mathbf{x})\tilde{\mathbf{u}}_j(\mathbf{x},t)\,, \tag{5.2}$$

where $\mathbf{x}$ denotes the position of a material point, t is time and $\mathcal{H}_{\Gamma_{\mathrm{d},j}}$ is a step function, associated to the discontinuity $\Gamma_{\mathrm{d},j}$, see equation (2.2). As in the original implementation of the partition of unity method, different step functions can be used, see Table 2.1. The strain field in the bulk material is obtained by taking the derivative of the displacement field (5.2) with respect to the position of the material point:

$$\epsilon(\mathbf{x},t) = \nabla^s\hat{\mathbf{u}}(\mathbf{x},t) + \sum_{j=1}^{m} \mathcal{H}_{\Gamma_{\mathrm{d},j}}(\mathbf{x})\nabla^s\tilde{\mathbf{u}}_j(\mathbf{x},t) \qquad \mathbf{x} \notin \Gamma_{\mathrm{d},j}\,, \tag{5.3}$$

where a superscript s denotes the symmetric part of a differential operator. Note that at the discontinuities $\Gamma_{\mathrm{d},j}$, the strains are not defined. There, the magnitude of the displacement jump

$$\mathbf{v}_j(\mathbf{x},t) = h\tilde{\mathbf{u}}_j(\mathbf{x},t)\,, \tag{5.4}$$

is the relevant kinematic quantity with h defined in (2.3).

§ 5.2 Equilibrium equations

Consider the quasi-static equilibrium equations without body forces and the corresponding boundary conditions:

$$\nabla \cdot \boldsymbol{\sigma} = \mathbf{0} \qquad \mathbf{x} \in \Omega\,, \tag{5.5}$$

$$\mathbf{n}_t \cdot \boldsymbol{\sigma} = \bar{\mathbf{t}} \qquad \mathbf{x} \in \Gamma_t\,, \tag{5.6}$$

$$\mathbf{u} = \bar{\mathbf{u}} \qquad \mathbf{x} \in \Gamma_u\,, \tag{5.7}$$

$$\mathbf{n}_{d,j} \cdot \boldsymbol{\sigma} = \mathbf{t}_j \qquad \mathbf{x} \in \Gamma_{\mathrm{d},j}\,, \tag{5.8}$$

where $\boldsymbol{\sigma}$ is the Cauchy stress in the bulk material, $\bar{\mathbf{t}}$ are the prescribed tractions on Γ_t with outward normal vector $\mathbf{n}_t$, $\bar{\mathbf{u}}$ are the prescribed displacements on Γ_u and $\mathbf{t}_j$ are the tractions at discontinuity $\Gamma_{\mathrm{d},j}$. The normal $\mathbf{n}_{d,j}$ at discontinuity $\Gamma_{\mathrm{d},j}$ points into Ω_j^+. Equilibrium can be expressed in a weak form by multiplication with an admissible variational displacement field $\delta\mathbf{u}$:

$$\int_\Omega \delta\mathbf{u} \cdot (\nabla \cdot \boldsymbol{\sigma}) \mathrm{d}\Omega = 0\,. \tag{5.9}$$

Taking the space of the admissible variations to be the same as the actual displacement field, equation (5.2), the variations of the displacements can be decomposed as:

$$\delta\mathbf{u} = \delta\hat{\mathbf{u}} + \sum_{j=1}^{m} \mathcal{H}_{\Gamma_{\mathrm{d},j}} \delta\tilde{\mathbf{u}}_j\,. \tag{5.10}$$

Substituting the variations into equation (5.9) gives:

$$\int_\Omega \delta\hat{\mathbf{u}} \cdot (\nabla \cdot \boldsymbol{\sigma}) \mathrm{d}\Omega + \sum_{j=1}^{m} \int_\Omega \mathcal{H}_{\Gamma_{\mathrm{d},j}} \delta\tilde{\mathbf{u}}_j \cdot (\nabla \cdot \boldsymbol{\sigma}) \mathrm{d}\Omega = 0\,. \tag{5.11}$$

Applying Gauss' theorem, using the symmetry of the Cauchy stress tensor and using the boundary conditions at the external boundary Γ_t and at the discontinuity planes $\Gamma_{\mathrm{d},j}$ gives:

$$\begin{aligned} \int_\Omega \nabla^s \delta\hat{\mathbf{u}} : \boldsymbol{\sigma} \mathrm{d}\Omega + \sum_{j=1}^{m} \int_\Omega \mathcal{H}_{\Gamma_{\mathrm{d},j}} \nabla^s \delta\tilde{\mathbf{u}}_j : \boldsymbol{\sigma} \mathrm{d}\Omega + \sum_{j=1}^{m} \int_{\Gamma_{\mathrm{d},j}} \delta\tilde{\mathbf{u}}_j \cdot \mathbf{t}_j \mathrm{d}\Gamma = \\ \int_{\Gamma_t} \delta\hat{\mathbf{u}} \cdot \bar{\mathbf{t}} \mathrm{d}\Gamma + \sum_{j=1}^{m} \int_{\Gamma_t} \mathcal{H}_{\Gamma_{\mathrm{d},j}} \delta\tilde{\mathbf{u}}_j \cdot \bar{\mathbf{t}} \mathrm{d}\Gamma\,. \end{aligned} \tag{5.12}$$

Note that the only difference in this equation with respect to the original equation with just a single discontinuity (2.16) is the appearance of the summation symbol in front of the terms that contain the additional admissible displacement field $\delta\tilde{\mathbf{u}}_j$ or derivations thereof.

§ 5.3 Finite element formulation

The interpolation scheme according to Babuška and Melenk (1997), allows for the existence of multiple enhanced base functions. When the enhanced basis terms $\gamma_j(\mathbf{x})$ in equation (2.19) are substituted by the step functions $\mathcal{H}_{\Gamma_{\mathrm{d},j}}(\mathbf{x})$, the displacement field in equation (5.2) can be written in the following discrete form:

$$\mathbf{u} = \mathbf{N}\mathbf{a} + \sum_{j=1}^{m} \mathcal{H}_{\Gamma_{\mathrm{d},j}} \mathbf{N}\mathbf{b}_j \,. \tag{5.13}$$

Here, the vector $\mathbf{a}$ contains the regular nodal degrees of freedom of the element and $\mathbf{b}_j$ contains the additional nodal degrees of freedom associated with discontinuity $\Gamma_{\mathrm{d},j}$. Note that the magnitude of each displacement jump is supported by a unique set of degrees of freedom $\mathbf{b}_j$. As a result, multiple discontinuities in the same element can be simulated, which is necessary for the correct implementation of coalescing cracks. The matrix $\mathbf{N}$ contains the conventional element shape functions.

The discretised strain field can be derived by straightforward differentiation:

$$\boldsymbol{\epsilon} = \mathbf{B}\mathbf{a} + \sum_{j=1}^{m} \mathcal{H}_{\Gamma_{\mathrm{d},j}} \mathbf{B}\mathbf{b}_j \,, \tag{5.14}$$

where $\mathbf{B}$ contains the spatial derivatives of the element shape functions. The discrete displacement jump at discontinuity $\Gamma_{\mathrm{d},j}$, see equation (5.4), is equal to:

$$\mathbf{v}_j = \mathbf{H}\mathbf{b}_j \,, \tag{5.15}$$

where $\mathbf{H}$ is defined in equation (2.25). Finally the variations of the displacement fields and their spatial derivatives can be discretised as:

$$\begin{aligned} \delta\hat{\mathbf{u}} &= \mathbf{N}\delta\mathbf{a}\,; & \delta\tilde{\mathbf{u}}_j &= \mathbf{N}\delta\mathbf{b}_j\,; \\ \nabla^s\delta\hat{\mathbf{u}} &= \mathbf{B}\delta\mathbf{a}\,; & \nabla^s\delta\tilde{\mathbf{u}}_j &= \mathbf{B}\delta\mathbf{b}_j\,, \end{aligned} \tag{5.16}$$

Inserting these relations into the weak form of the equilibrium equation (5.12) yields the equilibrium equation for a single element with volume $\mathcal{V}$ and discontinuities $\mathcal{S}$:

$$\begin{aligned}\int_{\mathcal{V}}(\mathbf{B}\delta\mathbf{a})^{\mathrm{T}}\boldsymbol{\sigma}\mathrm{d}\mathcal{V}+\sum_{j=1}^{m}\int_{\mathcal{V}}\mathcal{H}_{\Gamma_{\mathrm{d},j}}(\mathbf{B}\delta\mathbf{b}_j)^{\mathrm{T}}\boldsymbol{\sigma}\mathrm{d}\mathcal{V}+\sum_{j=1}^{m}\int_{\mathcal{S}_{\mathrm{d},j}}(\mathbf{N}\delta\mathbf{b}_j)^{\mathrm{T}}\mathbf{t}_j\mathrm{d}\mathcal{S}=\\ \int_{\mathcal{S}_t}(\mathbf{N}\delta\mathbf{a})^{\mathrm{T}}\bar{\mathbf{t}}\mathrm{d}\mathcal{S}+\sum_{j=1}^{m}\int_{\mathcal{S}_t}\mathcal{H}_{\Gamma_{\mathrm{d},j}}(\mathbf{N}\delta\mathbf{b}_j)^{\mathrm{T}}\bar{\mathbf{t}}\mathrm{d}\mathcal{S}\,.\end{aligned} \tag{5.17}$$

By taking all the variations $\delta\mathbf{a}$ and $\delta\mathbf{b}_j$ respectively, the weak equilibrium equations can be separated in a set of $m+1$ equilibrium equations:

$$\begin{aligned}\int_{\mathcal{V}}\mathbf{B}^{\mathrm{T}}\boldsymbol{\sigma}\mathrm{d}\mathcal{V} &= \int_{\mathcal{S}_t}\mathbf{N}^{\mathrm{T}}\bar{\mathbf{t}}\mathrm{d}\mathcal{S}\,;\\ \int_{\mathcal{V}}\mathcal{H}_{\Gamma_{\mathrm{d},1}}\mathbf{B}^{\mathrm{T}}\boldsymbol{\sigma}\mathrm{d}\mathcal{V}+\int_{\mathcal{S}_{\mathrm{d},1}}\mathbf{N}^{\mathrm{T}}\mathbf{t}_1\mathrm{d}\mathcal{S} &= \int_{\mathcal{S}_t}\mathcal{H}_{\Gamma_{\mathrm{d},1}}\mathbf{N}^{\mathrm{T}}\bar{\mathbf{t}}\mathrm{d}\mathcal{S}\,;\\ \int_{\mathcal{V}}\mathcal{H}_{\Gamma_{\mathrm{d},2}}\mathbf{B}^{\mathrm{T}}\boldsymbol{\sigma}\mathrm{d}\mathcal{V}+\int_{\mathcal{S}_{\mathrm{d},2}}\mathbf{N}^{\mathrm{T}}\mathbf{t}_2\mathrm{d}\mathcal{S} &= \int_{\mathcal{S}_t}\mathcal{H}_{\Gamma_{\mathrm{d},2}}\mathbf{N}^{\mathrm{T}}\bar{\mathbf{t}}\mathrm{d}\mathcal{S}\,;\\ &\vdots\\ \int_{\mathcal{V}}\mathcal{H}_{\Gamma_{\mathrm{d},m}}\mathbf{B}^{\mathrm{T}}\boldsymbol{\sigma}\mathrm{d}\mathcal{V}+\int_{\mathcal{S}_{\mathrm{d},m}}\mathbf{N}^{\mathrm{T}}\mathbf{t}_m\mathrm{d}\mathcal{S} &= \int_{\mathcal{S}_t}\mathcal{H}_{\Gamma_{\mathrm{d},m}}\mathbf{N}^{\mathrm{T}}\bar{\mathbf{t}}\mathrm{d}\mathcal{S}\,.\end{aligned} \tag{5.18}$$

The equilibrium equation that is related to the regular degrees of freedom is identical to the equilibrium equation for an element without a discontinuity. Therefore, it is possible to add a discontinuity to an element during the calculations with a minimal effort by adding the additional equilibrium relations and the corresponding degrees of freedom $\mathbf{b}_j$.

After inserting the cohesive relations for the bulk material (2.29) and the various cohesive surfaces (2.31), the discretised equilibrium equation (5.18)

can be linearised in a standard manner, giving:

$$\begin{bmatrix} \mathbf{K}_{aa} & \mathbf{K}_{ab_1} & \dots & \mathbf{K}_{ab_m} \\ \mathbf{K}_{ab_1} & \mathbf{K}_{b_1b_1} & \dots & \mathbf{K}_{b_1b_m} \\ \vdots & \vdots & \ddots & \vdots \\ \mathbf{K}_{ab_m} & \mathbf{K}_{b_1b_m} & \dots & \mathbf{K}_{b_mb_m} \end{bmatrix} \begin{bmatrix} \dot{\mathbf{a}} \\ \dot{\mathbf{b}}_1 \\ \vdots \\ \dot{\mathbf{b}}_m \end{bmatrix} = \begin{bmatrix} \mathbf{f}_a^{\text{ext}} \\ \mathbf{f}_{b_1}^{\text{ext}} \\ \vdots \\ \mathbf{f}_{b_m}^{\text{ext}} \end{bmatrix} - \begin{bmatrix} \mathbf{f}_a^{\text{int}} \\ \mathbf{f}_{b_1}^{\text{int}} \\ \vdots \\ \mathbf{f}_{b_m}^{\text{int}} \end{bmatrix}, \tag{5.19}$$

where the terms in the stiffness matrix are:

$$\begin{aligned} \mathbf{K}_{aa} &= \int_{\mathcal{V}} \mathbf{B}^{\mathrm{T}}\mathbf{C}\mathbf{B}\mathrm{d}\mathcal{V}\,; \\ \mathbf{K}_{ab_j} &= \int_{\mathcal{V}} \mathcal{H}_{\Gamma_{\mathrm{d},j}}\mathbf{B}^{\mathrm{T}}\mathbf{C}\mathbf{B}\mathrm{d}\mathcal{V}\,; \\ \mathbf{K}_{b_jb_j} &= \int_{\mathcal{V}} \mathcal{H}^2_{\Gamma_{\mathrm{d},j}}\mathbf{B}^{\mathrm{T}}\mathbf{C}\mathbf{B}\mathrm{d}\mathcal{V} + \int_{\mathcal{S}_{\mathrm{d},j}} \mathbf{H}^{\mathrm{T}}\mathbf{Q}^{\mathrm{T}}\mathbf{T}_{\mathrm{d}}\mathbf{Q}\mathbf{H}\mathrm{d}\mathcal{S}\,; \\ \mathbf{K}_{b_jb_k} &= \int_{\mathcal{V}} \mathcal{H}_{\Gamma_{\mathrm{d},j}}\mathcal{H}_{\Gamma_{\mathrm{d},k}}\mathbf{B}^{\mathrm{T}}\mathbf{C}\mathbf{B}\mathrm{d}\mathcal{V}\,; \qquad \text{if } \; j \neq k\,. \end{aligned} \tag{5.20}$$

The internal forces are given by:

$$\begin{aligned} \mathbf{f}_a^{\text{int}} &= \int_{\mathcal{V}} \mathbf{B}^{\mathrm{T}}\boldsymbol{\sigma}\mathrm{d}\mathcal{V}\,; \\ \mathbf{f}_{b_j}^{\text{int}} &= \int_{\mathcal{V}} \mathcal{H}_{\Gamma_{\mathrm{d},j}}\mathbf{B}^{\mathrm{T}}\boldsymbol{\sigma}\mathrm{d}\mathcal{V} + \int_{\mathcal{S}_{\mathrm{d},j}} \mathbf{H}^{\mathrm{T}}\mathbf{Q}^{\mathrm{T}}\mathbf{t}_{\mathrm{d},j}\mathrm{d}\mathcal{S}\,. \end{aligned} \tag{5.21}$$

Finally, the expression for the external forces is:

$$\begin{aligned} \mathbf{f}_a^{\text{ext}} &= \int_{\mathcal{S}_t} \mathbf{N}^{\mathrm{T}}\bar{\mathbf{t}}\mathrm{d}\mathcal{S}\,; \\ \mathbf{f}_{b_j}^{\text{ext}} &= \int_{\mathcal{S}_t} \mathcal{H}_{\Gamma_{\mathrm{d},j}}\mathbf{N}^{\mathrm{T}}\bar{\mathbf{t}}\mathrm{d}\mathcal{S}\,. \end{aligned} \tag{5.22}$$

Note that if the tangent matrices $\mathbf{C}$ and $\mathbf{T}_{\mathrm{d}}$ are symmetric, symmetry of the sub-matrices $\mathbf{K}_{aa}$, $\mathbf{K}_{ab_j}$ and $\mathbf{K}_{b_jb_k}$ is preserved. Consequently, the total stiffness matrix also remains symmetric.

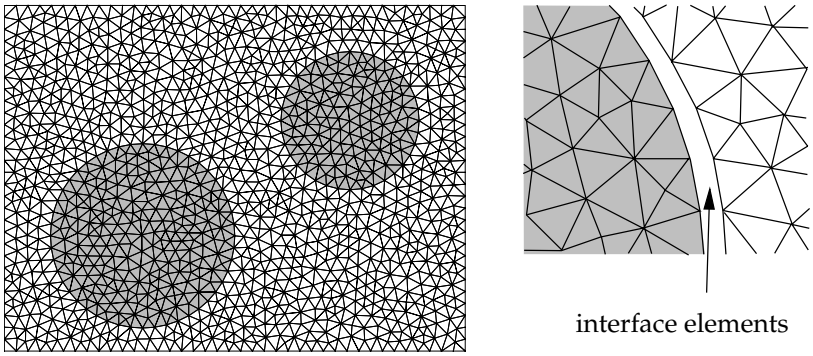

Figure 5.3 Conventional finite element mesh of a specimen with two aggregates (grey continuum elements) in a matrix material. To visualise the interface elements in the detail on the right, the continuum elements that represent the matrix material have a small offset.

§ 5.4 Implementation and constitutive relations

Cohesive segments can be used in two ways. First, they can be applied to model the interfaces between different constituents in the material. Secondly, cohesive segments can be employed to model the nucleation, propagation and coalescence of micro-cracks in the bulk material. In both applications, the same kinematic model is used, but the implementation is different, as well as the corresponding cohesive constitutive relations. In the remainder of this chapter, both cases are discussed separately.

Material interfaces

In general, an interface between two constituents can be regarded as a weak discontinuity in the kinematic relation. That is, as long as the interface is intact, the displacement field across the interface is continuous. But due to the stiffness mismatch on either side of the interface, the strain field is discontinuous. In a classical finite element model, such an interface can be modelled using C^0 continuum elements, where, by definition, the strain field is discontinuous at the interelement boundaries. When the structure of the finite

element mesh is aligned with the internal structure of the material, the requirement of having a weak discontinuity at the interfaces is automatically satisfied, see Figure 5.3.

Debonding of the interface or delamination can be simulated by placing interface elements at the element boundaries that represent the material interface. The weak discontinuity in the strain field is now replaced by a strong discontinuity in the displacement field. The opening of the interface elements is governed by a cohesive constitutive relation that specifies the debonding process (Schellekens and de Borst 1993).

In the cohesive segments method, a strong discontinuity is introduced in the displacement field by means of an additional displacement field in combination with a step function. Obviously, the corresponding strain field, which is the spatial derivative of the displacement field, is locally unbounded. From a kinematic point of view, the cohesive segments method is identical to the classical interface element approach and can be used to model material interfaces (Moës *et al.* 2003).

A cohesive segment that models a material interface is inserted in the finite element mesh at the start of a simulation, see Figure 5.4. The procedure to insert these segments is identical to the procedure used in the original formulation as presented in section 2.4. The nodes that support an element that is crossed by the discontinuity are enhanced by a set of additional degrees of freedom. In order to perform a correct numerical integration of the domain of the element, the element is divided into two parts, each with the appropriate positions of Gauss points. The constitutive laws for the bulk material on either side of the discontinuity can be different. An important characteristic of this application of a cohesive segment is that it does not have a tip: the segment is either a closed loop or ends at the boundary of the specimen. As a result, the segment is not able to propagate.

Obviously, modelling material interfaces in this way has certain advantages. First, the finite element mesh does not have to coincide with the positions of the interfaces in the domain. As demonstrated in Figure 5.4, even a structured mesh consisting of quadrilateral elements can be used to model relatively complex structures. Moreover, since the structure of the mesh is not related to the position of interfaces, the same mesh can be used multiple times to perform analyses of specimens with identical dimensions and boundary

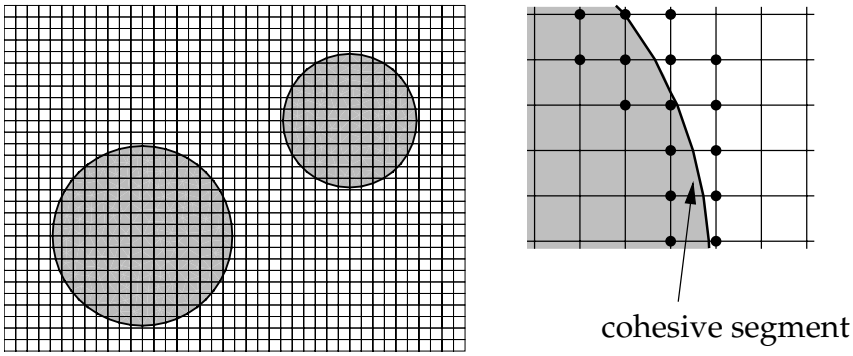

Figure 5.4 Finite element mesh of a specimen with two aggregates (grey areas) that are represented by cohesive segments. The nodes that support the elements that are crossed by the cohesive segment are enhanced with an additional set of degrees of freedom.

conditions, but with different topologies of the internal structure. This is in contrast to the classical interface element approach, where each distribution of material interfaces in the domain requires a new finite element mesh, as demonstrated in (Tijssens *et al.* 2001).

Since the cohesive segment must represent a perfect bond at the beginning of the simulation, the corresponding cohesive constitutive relation must contain an elastic part to model the initial bond. Of course, this is in contradiction with one of the advantages of partition of unity based methods: to avoid the use of cohesive zones with dummy stiffnesses to model a perfect bond. However, in the case of interfaces between materials, there is a good physical reason to use initial stiffnesses. In reality, the interface between two constituents is hardly ever a perfect bond. Incomplete adhesion and cavities will locally result in a reduction of the stiffness. Even though it is difficult to determine the magnitude of this stiffness reduction, the use of a dummy stiffness can take that reduction into account, at least in a qualitative sense. To avoid traction oscillations due to the relatively large dummy stiffness, the interface terms in the internal force vector and the stiffness matrix (5.19) are integrated using a Newton-Cotes integration scheme (Schellekens and de Borst 1993, Remmers *et al.* 2001, Simone *et al.* 2001).

The constitutive relation that governs the opening of these cohesive segments can be chosen from a long list of interface constitutive relations (Allix and Ladevèze 1992, Schipperen and de Borst 2001, Camanho *et al.* 2003). In this context, we prefer to use a mixed-mode relation that has been suggested by Xu and Needleman (1993). Here, the work of separation of the interface $\mathcal{G}$ as a function of the displacement jump is described by the following relation:

$$\begin{aligned}\mathcal{G} =& \mathcal{G}_c + \mathcal{G}_c \exp\left(-\frac{v_n}{\delta_n}\right) \\ &\times \left\{\left[1 - r + \frac{v_n}{\delta_n}\right]\frac{1-q}{r-1} - \left[q + \left(\frac{r-q}{r-1}\right)\frac{v_n}{\delta_n}\right]\exp\left(-\frac{v_t^2}{\delta_t^2}\right)\right\},\end{aligned} \tag{5.23}$$

where $\mathcal{G}_c$ is the fracture toughness of the interface, v_n and v_s are the normal and shear components of the displacement jump in the discontinuity frame of reference: $\mathbf{v}_\mathrm{d}$, respectively and δ_n and δ_s are the corresponding characteristic lengths. These characteristic lengths in turn are related to the normal and shear cohesive strengths of the interface, $t_{n,\max}$ and $t_{s,\max}$ and the normal and shear works of separation $\mathcal{G}_{c,n}$ and $\mathcal{G}_{c,s}$

$$\mathcal{G}_{c,n} = e\, t_{n,\max}\delta_n\,; \qquad \mathcal{G}_{c,s} = \sqrt{\frac{1}{2}e}\, t_{s,\max}\delta_s\,, \qquad \text{where} \quad e = \exp(1)\,. \tag{5.24}$$

The mode-mixity of the model is controlled by the parameters q and r. The first parameter denotes the ratio of the fracture energy in the normal and shear direction $q = \mathcal{G}_s/\mathcal{G}_n$, the second parameter controls the magnitude of the normal opening v_n^* in case of a complete pure shear separation when the normal traction is zero: $r = v_n^*/\delta_n$.

The interface tractions are obtained by taking the first derivative of (5.23) with respect to the displacement jump $\mathbf{v}$:

$$\begin{aligned} t_n &= -\frac{\mathcal{G}_c}{\delta_n}\exp\left(\frac{-v_n}{\delta_n}\right) \\ &\quad\times\left\{\left[-r + \frac{v_n}{\delta_n}\right]\frac{1-q}{r-1} - \left[q - \frac{(r-q)(v_n-\delta_n)}{(r-1)\delta_n}\exp\left(-\frac{v_t^2}{\delta_t^2}\right)\right]\right\}\,; \\ t_s &= \frac{2\mathcal{G}_c}{\delta_t^2}\exp\left(\frac{-v_n}{\delta_n}\right)\left[q + \left(\frac{r-q}{r-1}\right)\frac{v_n}{\delta_n}\right] v_s \exp\left(-\frac{v_t^2}{\delta_t^2}\right). \end{aligned} \tag{5.25}$$

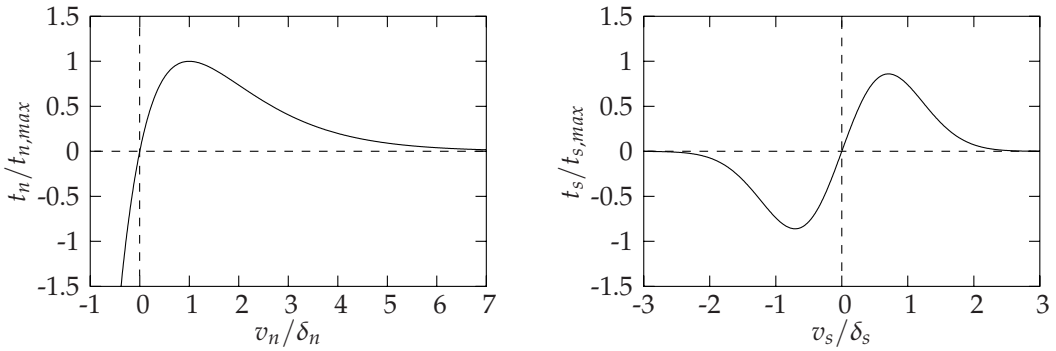

(a) Normal traction (b) Shear traction

Figure 5.5 The normalised tractions across the discontinuity as a function of the corresponding component of the displacement jump when $q = 1$ and $r = 0$. (a) Normal traction versus the normal component of the displacement jump v_n with $v_s = 0$. (b) Shear traction versus the shear component of the displacement jump v_s with $v_n = 0$ (Xu and Needleman, 1994).

The load displacement curves for the normal and shear traction as a function of the normal and shear opening of the cohesive segment are given in Figure 5.5. The maximum value of t_n in pure mode-I fracture is attained when the normal opening v_n is equal to δ_n. The maximum value of the shear traction in a pure mode-II opening t_s is reached when $|v_s| = \sqrt{2}\delta_s/2$.

The consistent tangent matrix $\mathbf{T}_{\mathrm{d}}$ is obtained by taking the second derivative of the energy potential (5.23) with respect to the displacement jump $\mathbf{v}$. Unfortunately, this tangent matrix is not symmetric, hence destroying the symmetry in the element stiffness matrix $\mathbf{K}$, see equation (5.19).

In most situations, the parameters that characterise the mode-mixity of the model q and r are set to 1 and 0 respectively. Hence, the complete debonding behaviour of the interface can be described with only two parameters $\mathcal{G}_c$ and $t_{n,\max}$. In addition, the complete pre- and post-failure behaviour is described by a single continuous function and derivatives thereof. As a result, this nonlinear constitutive relation has proven to be extremely robust.

Cohesive cracks

The other application of cohesive segments is to model the nucleation, growth and coalesce of micro-cracks in the virgin material. In this case, the segments

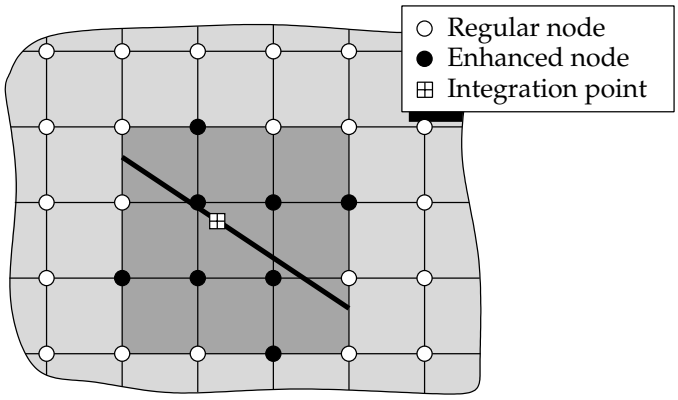

Figure 5.6 Creation of a new cohesive segment (bold line) in virgin material. The segment crosses the integration point in the bulk material in which the criterion was violated. The segment is stretched until it touches the boundary of the patch of elements (grey area) that share the nodes of the element in which the yield criterion was violated.

are not present in the material at the onset of the analysis, but are created and extended during the course of a simulation.

The evolution of micro-cracks can be divided into three stages: the nucleation, the growth and finally the coalescence with other segments. In all cases, the same criterion is used to determine when and in which direction a segment is created or extended. In order to arrive at a consistent numerical model, this fracture criterion is narrowly connected to the cohesive constitutive relation that governs the debonding process of a cohesive segment. This fracture criterion and the constitutive relation are discussed at the end of this section.

When the stress state in a specific integration point in the bulk material violates the yield criterion of the material, a new cohesive segment is added. The segment, which is assumed to be straight, crosses this integration point and is extended into the neighbouring elements until it touches the outer boundaries of these elements, see Figure 5.6. The patch of neighbouring elements consists of all elements that share one of the nodes of the central element that contains the integration point in which the criterion was violated. The nodes that support these outer boundaries are not enhanced in order to guarantee a zero crack opening at the tips of the new segments.

The reason to create a micro-crack by extending a cohesive segment over multiple elements is based on practical considerations. Since the nodes that construct the tip of an element are not enhanced, a segment that only crosses one element would be kinematically impossible since, at least in bi-linear elements, *all* nodes support the tips of the segment.

Creating a new segment will not immediately reduce the high stresses in the bulk material. Depending on the fracture toughness of the material and the magnitude of the load step, the stresses in the vicinity of the centre of the new segment will only slowly fade away. Even so, especially in dynamic simulations, it can occur that the stress state locally increases for a small period of time. To prevent new segments from being nucleated in the same position in a short period of time, an element and its neighbours can only be the source of a new segment once in a simulation.

The extension of a cohesive segment is modelled in the same way as in the original formulation by Wells and Sluys (2001a). When the stress state in the tip violates the fracture criterion for a specific angle, the segment is extended into the next element in that direction, until it touches the boundary of that element. As reported in chapter 2, the stress state at the tip is not known exactly. Therefore, the stresses are estimated by calculating the average stress state in the vicinity using a Gauss averaging criterion (2.45). The most accurate prediction of the direction of the crack was obtained when the specific averaging length l_a was chosen to be three times the specific element length in the mesh around the tip. As a result, the stress state is underestimated and in general, the cohesive segment is extended slightly too late. In the original formulation by Wells and Sluys (2001a), this did not appear to be a serious problem, but in the cohesive segments method, a discrepancy is created since the fracture criterion is used to determine both the nucleation of a segment as well as its extension. The nucleation is based on the stress state in a single integration point instead of an average stress state that is too low by definition. Hence, the nucleation of a new segment is biased over the extension of an existing segment, which will hamper quantitative analysis of diffuse fracture problems. In transient simulations, which will be discussed in the next chapter, these problems will be even more pronounced.

In order to solve this discrepancy, two alternative approaches have been examined. In the first approach, different stress states are used to determine

(i) *when* a segment should be extended and (ii) *in which direction* the segment should be extended. In practice, the method works as follows. At the tip of a segment, the stress state in the nearest integration point, which is in general a good representative of the peak stress, is monitored. When this stress state violates the criterion for extension, a second, averaged stress state is determined, based on a number of integration point within a certain radius of the tip, according to equation (2.45). The direction of the extension is then based on this averaged stress state. Note that the averaged stress state is significantly smaller than the peak stress.

The advantages of this approach are evident. The segment is extended at the correct load step and in the correct direction. However, this method is unreliable in situations where mode transitions become an important factor. A good example of the mode transition phenomenon is observed in dynamic shear failure experiments (Kalthoff and Winkler 1988). Here, the direction of crack propagation depends on the magnitude of the applied load. For low impact velocities, the crack propagates as a cleavage crack at an angle of 70° with respect to the initial crack, at high impact velocities, the crack propagates nearly straight ahead as an adiabatic shear band. In numerical simulations, it appears that the proposed method is able to capture both mechanisms, but the exact impact velocity for which mode transition occurs cannot be found, since the criterion is based on inconsistent stress states.

In an alternative approach, both the creation as well as the extension of a cohesive segment are based on averaged stress states. A single average length l_a is used for all cases. In order to reduce the computational effort, a new segment can only be nucleated at one point for each element, e.g. the geometric centre of the element. In both situations, the average stress state is used to determine both the instance as well as the direction of creation or extension. Obviously, failure will occur with some delay, the creation of a new segment is no longer biased over the extension of an existing one.

Since it is not clear which of the two approaches is preferred, both techniques will be used in the remainder of this thesis.

A key feature of the method is the possibility to have multiple, interacting cohesive segments. To accommodate this, each cohesive segment is supported by a unique set of additional degrees of freedom. When two segments meet

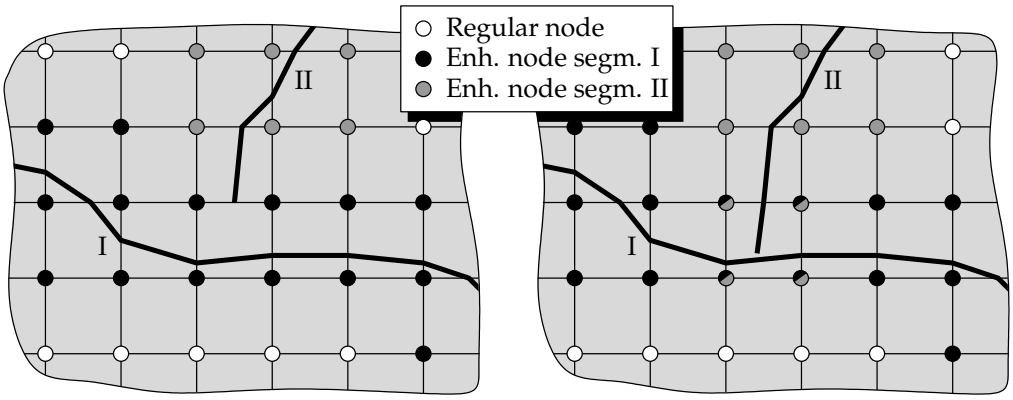

Figure 5.7 Merging of two cohesive segments (bold lines). Segment II is extended until it touches segment I (right picture). Segment I can be regarded as a free edge so that segment II will not have a tip in this case. Consequently, all nodes of the element will be enhanced in order to support displacement discontinuity of segment II. Note that the nodes of these elements are enhanced twice.

within a single element, the nodes that support the elements are enhanced twice. Consider the situation depicted in Figure 5.7 (a), in which segment II is approaching another segment (I), which can either be a material interface or a previously created cohesive crack. When the fracture criterion at the tip of segment II is violated, the segment is extended accordingly. The position of segment I marks a discontinuity and can therefore be considered as a free edge in the material. Hence, segment two is only extended until it touches segment I, see Figure 5.7 (b). Since this segments forms a free edge, there is no new tip for segment II and all nodes of the corresponding element are enhanced.

Taking into account all previously mentioned rules, crack branching is taken care of automatically. When the fracture criterion in an integration point in the vicinity of an existing segment is violated, a new segment is created which may cross the existing one, see Figure 5.8. In that case, the new segment only contains a single tip.

In previous implementations, the orientation of the extension of a discontinuity is taken perpendicular to the direction of the major axis of the principal stress. Although this method has proven to be efficient (Wells and Sluys 2001a), there are two important drawbacks. First, in a principal stress

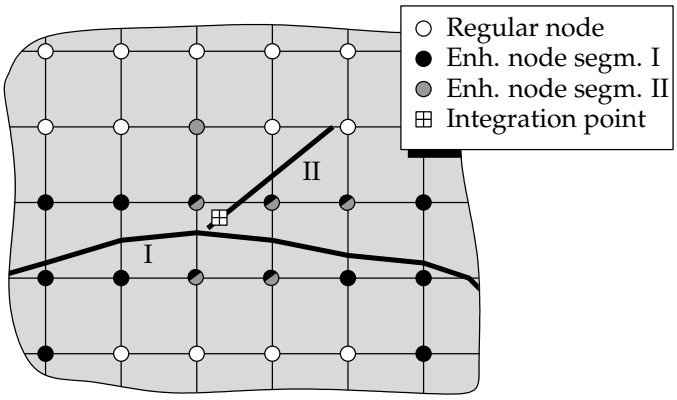

Figure 5.8 Crack branching. When the equivalent stress in an integration point near an existing segment (I) exceeds the strength of the bulk material, a new segment (II) is created. This new segment is extended until it touches either the boundary of its neighbour elements or the existing segment (I). In the situation depicted in the figure, the new segment only has one tip.

formulation, no distinction is made between compressive and tensile stresses. Hence, a violation can be triggered by a combination of compressive stresses, whereas in reality, such a state is not likely to lead to crack growth. Moreover, the contribution of the normal and shear stresses in the criterion is of equal importance, whereas in many cohesive models, the influence of the shear traction is reduced by applying a weight factor.

Here, a different approach is pursued. In order to arrive at an unbiased stress-based fracture model, the failure criterion is closely related to the cohesive constitutive relation (Camacho and Ortiz 1996). A stress state $\boldsymbol{\sigma}$ in a point can be transformed into normal and shear tractions t_n and t_s along an imaginary axis η, which is rotated by an angle θ with respect to the x-axis, see Figure 5.9:

$$t_n = \mathbf{n}^{\mathrm{T}}\boldsymbol{\sigma}\mathbf{n}\,; \qquad t_s = \mathbf{s}^{\mathrm{T}}\boldsymbol{\sigma}\mathbf{n}\,, \tag{5.26}$$

where $\mathbf{n}$ and $\mathbf{s}$ are the unit normal and tangent vectors to the η-axis respectively:

$$\mathbf{n} = [-\sin\theta, \cos\theta]^{\mathrm{T}}\,; \qquad \mathbf{s} = [\cos\theta, \sin\theta]^{\mathrm{T}}\,. \tag{5.27}$$

The normal and shear tractions $\mathbf{t}_n$ and $\mathbf{t}_s$ can be used to construct an equivalent

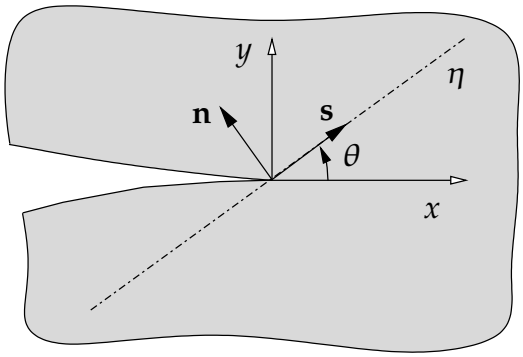

Figure 5.9 Calculation of the equivalent traction t_{eq} along an imaginary axis η at an angle θ with respect to the x-axis.

traction t_{eq} which is a function of the angle θ of the η-axis:

$$t_{\text{eq}}(\theta) = \sqrt{< t_n >^2 + \frac{1}{\beta} t_s^2}\,, \tag{5.28}$$

where $<\cdot>$ are the McCauley brackets:

$$< x >= \begin{cases} 0 & \text{if} \quad x \leq 0, \\ x & \text{if} \quad x > 0\,, \end{cases} \tag{5.29}$$

and β is a scaling factor that is typically set to 2.3 (Camacho and Ortiz 1996). For a given stress state $\boldsymbol{\sigma}$, the equivalent stress state t_{eq} can be determined for all orientations θ of the imaginary axis η. Because of the periodic nature of trigonometric functions, it is sufficient to determine the tractions in the range $0 < \theta < \pi$. An example is presented in Figure 5.10.

The angle for which the equivalent traction exceeds the maximum allowable traction first is the direction in which the crack will propagate. This angle θ_{max} can be found by solving the corresponding minimisation problem. Since the equivalent traction t_{eq} is a function of quadratic trigonometry functions, it can be demonstrated that the function contains two local maxima within the region $0 < \theta < \pi$. Each of these maxima resides in one of the two quadrants. In order to determine the global maximum equivalent traction it is necessary to obtain the local maxima first. This can be done by a minimisation algorithm, such as a one-dimensional bisection algorithm (Press *et al.* 1988). Out

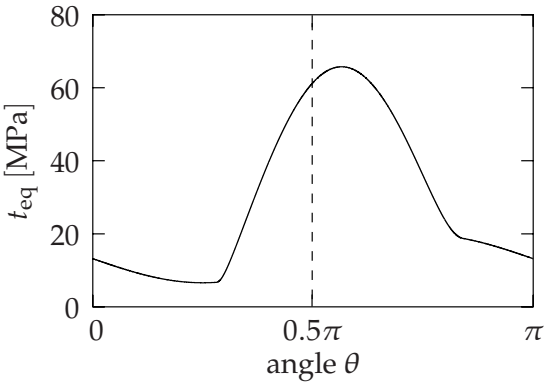

Figure 5.10 The equivalent stress t_{eq} versus the angle θ with respect to the x-axis for the stress state $\boldsymbol{\sigma} = [\sigma_{11}, \sigma_{22}, \sigma_{12}]^T = [60, -40, 20]^T$ MPa. The scaling factor β is taken to be 2.3.

of the two local maxima, it is easy to determine the absolute maximum in the domain $t_{eq,max}$. When this maximum equivalent traction exceeds the strength of the material t_{max}, a new segment is inserted, or an existing one is extended in the direction of the corresponding angle θ_{max}.

To avoid sudden jumps in stresses when a discontinuity is inserted, the constitutive behaviour of the cohesive segment is related to the stress state in the bulk material that violates the fracture criterion. The initial tractions in this irreversible model are taken to be equal to the normal and shear tractions in the bulk material at the exact moment of nucleation, see equation (5.26), see also (Camacho and Ortiz 1996).

For the debonding behaviour, a distinction is made between normal and shear behaviour. When the normal traction component $t_{n,0}$ is positive, the cohesive segment is assumed to open as a cleavage crack. The cohesive tractions in both normal and shear directions t_n and t_s decrease monotonically from their initial values $t_{n,0}$ and $t_{s,0}$ to zero as a function of the normal displacement jump, see Figure 5.11 (a):

$$t_n = t_{n,0}\left(1 - \frac{v_n}{v_{n,cr}}\right); \qquad t_s = t_{s,0}\left(1 - \frac{v_n}{v_{n,cr}}\right)\mathrm{sgn}(v_s), \tag{5.30}$$

where v_n and v_s are the normal and sliding displacement respectively, $\mathrm{sgn}(\square)$ is the signum function:

$$\mathrm{sgn}(x) = \frac{x}{|x|}. \tag{5.31}$$

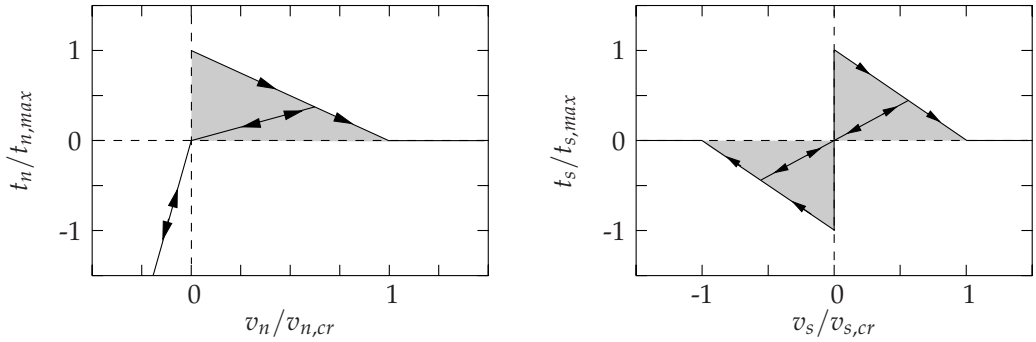

(a) Cleavage crack (b) Shear crack

Figure 5.11 The normalised tractions across the discontinuity as a function of the corresponding component of the displacement jump for a pure mode-I cleavage crack and a shear crack (Camacho and Ortiz, 1996).

The characteristic length of the cohesive law is determined by the critical normal opening displacement $v_{\mathrm{n,cr}}$ at which the crack has fully developed and the tractions have reduced to zero. This parameter is related to the fracture toughness $\mathcal{G}_c$, or the area under the softening curve and can be determined as follows:

$$v_{\mathrm{n,cr}} = \frac{2\mathcal{G}_c}{t_{\mathrm{n},0}}\,. \tag{5.32}$$

When after some opening displacement $v_{\mathrm{n},1}$, the crack starts to close due to local unloading, the following relation is applied:

$$t_{\mathrm{n}} = t_{\mathrm{n},0}\left(1 - \frac{v_{\mathrm{n},1}}{v_{\mathrm{n,cr}}}\right)\frac{v_{\mathrm{n}}}{v_{\mathrm{n},1}}\,; \qquad t_{\mathrm{s}} = t_{\mathrm{s},0}\left(1 - \frac{v_{\mathrm{n},1}}{v_{\mathrm{n,cr}}}\right)\frac{v_{\mathrm{n}}}{v_{\mathrm{n},1}}\mathrm{sgn}(v_{\mathrm{s}})\,. \tag{5.33}$$

Once the normal displacement jump exceeds the critical opening $v_{\mathrm{n,cr}}$, the tractions in both normal and shear directions are set to zero.

When the initial normal traction $t_{0,\mathrm{n}}$ is negative, the discontinuity is assumed to open in a shear mode. The shear tractions decay in a linear fashion from the initial value $t_{\mathrm{s},0}$ to zero according to, see Figure 5.11 (b):

$$t_{\mathrm{s}} = t_{\mathrm{s},0}\left(1 - \frac{|v_s|}{v_{\mathrm{s,cr}}}\right)\mathrm{sgn}(v_{\mathrm{s}})\,. \tag{5.34}$$

As in the tensile case, a linear relation is assumed for the reloading curve:

$$t_{\mathrm{s}} = t_{\mathrm{s},0}\left(1 - \frac{|v_s|}{v_{\mathrm{s,cr}}}\right)\frac{v_{\mathrm{s}}}{|v_{\mathrm{s},1}|}\,. \tag{5.35}$$

§ 5.5 Solution procedure

The possibility of having a number of active crack tips in various locations in the domain gives rise to new problems related to the robustness of the solution technique. Traditionally, nonlinear algebraic systems are solved in an incremental iterative manner. The external vector $\mathbf{f}^{\mathrm{ext}}$ is represented by a unit load $\bar{\mathbf{f}}$, which is multiplied by a loading parameter λ:

$$\mathbf{f}^{\mathrm{ext}} = \lambda\bar{\mathbf{f}}\,. \tag{5.36}$$

This loading parameter λ is increased monotonically and for each intermediate value λ_i the current equilibrium of the system is calculated. This process is repeated until the final load factor is reached.

When the behaviour of a structure is dominated by structural instabilities or fracture, the complete deformation envelop is not governed by a monotonically increasing external load. Instead, the load-displacement curve is characterised by a limit point, as shown in Figure 5.12. The alternative approach where the magnitude of a set of degrees of freedom is monotonically increased (prescribed displacement) fails when this load-displacement curve shows a snap-back behaviour.

The arc-length or path-following method developed by Riks (1979) is a technique that allows to solve the complete solution of a system, irrespective of the presence of limit and snap-back points. Here, the loading parameter λ is regarded as an additional unknown variable of the system, which brings the total sum of unknowns of the model to $N+1$, where N is the total number of degrees of freedom of the displacement field $\mathbf{u}$. Since the number of governing equations is still equal to N, the system is undetermined and an additional equation needs to be introduced. This *constraint equation* defines an additional relation between the (incremental) load parameter λ and the displacement field $\mathbf{u}$. In the procedure suggested by Riks (1979) the constraint equation defines an auxiliary plane in the solution space that is perpendicular to the load-displacement path in the current equilibrium point. The new

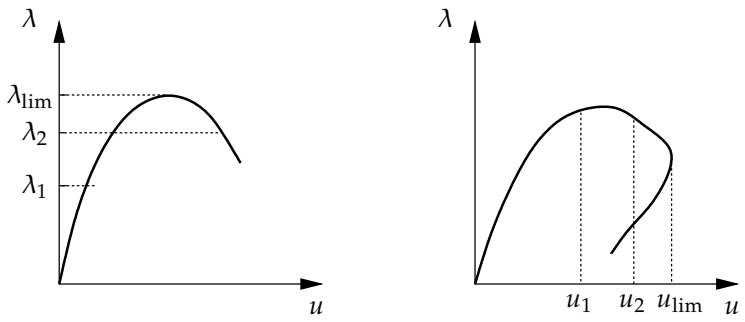

Figure 5.12 Load vs displacement curves. The figure on the left shows a limit point situation. The complete path cannot be followed using a monotonically increasing load factor λ. Moreover, the solution for λ_2 is not unique. The maximum attainable load is marked by λ_{lim}. The figure on the right depicts a snap-back point. The solution cannot be found with a monotonically increasing prescribed displacement u and the solution at u_2 is not unique. The maximum prescribed displacement is denoted by u_{lim}.

equilibrium-state $(\mathbf{u}, \lambda)$ is confined to this plane. It can be observed from Figure 5.13 that this procedure allows to cross a limit point or a snap back point. In an attempt to improve the convergence speed and robustness of the method under more severe circumstances, a number of authors have suggested alternative constraint equations (Ramm 1981, Crisfield 1982), which basically adopt the original idea from Riks (1979).

These methods perform well as long as the non-linearity in the system of equations is of a global nature, which is the case in structural stability or buckling analyses, for example. When the non-linearity is confined to a small portion of the system, the procedure often fails to find the new equilibrium state. Examples of such behaviour can be found in fracture mechanics. The onset and propagation of fracture is generally governed by a nonlinear constitutive behaviour in only a few integration points, which are the numerical representation of the process zone. Typically, this only affects the degrees of freedom that are located in the nodes that support the elements that contain these integration points. The overall mechanical behaviour remains almost linear and the constraint equation will not guide the solution into the right direction. Consequently, the new equilibrium state will not be found.

In order to increase the sensitivity in cases where the non-linearity is con-

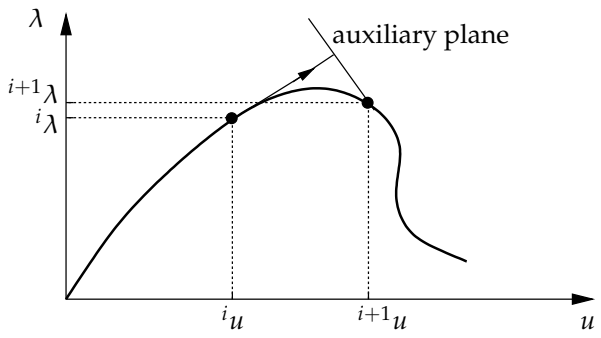

Figure 5.13 Load factor λ vs. an arbitrary displacement u using Riks' path-following method. The new solution $^{i+1}(\mathbf{u}, \lambda)$ is confined to the auxiliary plane.

fined to a small area, the constraint equation can be constructed by using a selected group of degrees of freedom. In the crack mouth opening displacement control method (CMOD), weight factors are applied in such a way that only the degrees of freedom that reside in the process zone contribute to the constraint equation (de Borst 1987). Unfortunately, these weight factors need to be assigned manually, which requires knowledge of the direction of the crack in advance. If this information is not available, the simulation must be stopped to apply new weight factors each time the process zone has propagated over a considerable distance in the finite element mesh. Alternatively, Geers (1999a) introduced algorithms to determine the weight factors automatically. This approach, in combination with problem specific constraint equations has resulted in a standard framework that allows for the efficient and robust analysis of various nonlinear problems (Geers 1999b).

Recently, an alternative approach has been suggested by Gutiérrez (2004). Instead of projecting a surface based on the current equilibrium position in order to confine the next solution, the constraint equation is based on an energy criterion, in such a way that the amount of energy that is dissipated in the deformation process is always a maximum for a given displacement and load increment. Obviously, this approach is much more appealing from a physical point of view in a sense that it actually obeys the most important rule for fracture mechanics, which is that a system always prefers to go to an energetic minimum.

The energy release during the fracture process in a mechanical system can

be obtained from the first principle of thermodynamics and can be written in rate form as:

$$\dot{V} = P - \mathcal{G}\,, \tag{5.37}$$

where $\dot{V}$ is the rate of the elastic potential, P is the power of the applied forces and $\mathcal{G}$ is the energy release rate. The elastic potential energy V stored in an equilibrium configuration is equal to the energy stored in the bulk material plus the energy stored in the cohesive segments:

$$V = \frac{1}{2}\int_{\Omega} \boldsymbol{\epsilon}\cdot\boldsymbol{\sigma}\mathrm{d}\Omega + \sum_{j=1}^{m}\frac{1}{2}\int_{\Gamma_{\mathrm{d},j}} \mathbf{v}_j\cdot\mathbf{t}_j\mathrm{d}\Gamma\,. \tag{5.38}$$

Casting this relation in a discrete form by substituting equations (5.14) and (5.15) gives:

$$V = \frac{1}{2}\int_{\mathcal{V}} \left(\mathbf{a}^{\mathrm{T}}\mathbf{B}^{\mathrm{T}} + \sum_{j=1}^{m}\mathcal{H}_{\Gamma_{\mathrm{d},j}}\mathbf{b}_j^{\mathrm{T}}\mathbf{B}^{\mathrm{T}}\right)\boldsymbol{\sigma}\mathrm{d}\mathcal{V} + \frac{1}{2}\sum_{j=1}^{m}\int_{\mathcal{S}_{\mathrm{d},j}} \mathbf{b}_j^{\mathrm{T}}\mathbf{N}^{\mathrm{T}}\mathbf{t}_j\mathrm{d}\mathcal{S}\,, \tag{5.39}$$

which, according to the global equilibrium equations (5.18) - (5.22) can be written as:

$$V = \frac{1}{2}\mathbf{a}^{\mathrm{T}}\mathbf{f}_a^{\mathrm{int}} + \frac{1}{2}\sum_{j=1}^{m}\mathbf{b}_j^{\mathrm{T}}\mathbf{f}_{b_j}^{\mathrm{int}}\,, \tag{5.40}$$

where $\mathbf{f}_a^{\mathrm{int}}$ and $\mathbf{f}_{b_j}^{\mathrm{int}}$ are the total internal force vectors associated to the regular and enhanced degrees of freedom $\mathbf{a}$ and $\mathbf{b}_j$, respectively. This relation should hold for any converged equilibrium state, where the internal force vectors are equal to the external force vectors. Hence, equation (5.40) can be written as:

$$V = \frac{1}{2}\mathbf{a}^{\mathrm{T}}\mathbf{f}_a^{\mathrm{ext}} + \sum_{j=1}^{m}\mathbf{b}_j^{\mathrm{T}}\mathbf{f}_{b_j}^{\mathrm{ext}}\,. \tag{5.41}$$

We now assume that the total solution space is described by a global vector $\mathbf{d}$ that contains the regular and the enhanced degrees of freedom, i.e. $\mathbf{d} = [\mathbf{a}, \mathbf{b}_1, ..., \mathbf{b}_m]^{\mathrm{T}}$. When the applied external force is formulated as a constant unit force vector $\bar{\mathbf{f}}$ times a multiplication factor λ (5.36), the expression for the internal energy can finally be stated as:

$$V = \frac{1}{2}\mathbf{d}^{\mathrm{T}}\lambda\bar{\mathbf{f}}\,. \tag{5.42}$$

The rate form of this equation can be found by differentiating this equation with respect to a quasi time:

$$\dot{V} = \frac{1}{2}\dot{\mathbf{d}}^{\mathrm{T}}\lambda\bar{\mathbf{f}} + \frac{1}{2}\mathbf{d}^{\mathrm{T}}\dot{\lambda}\bar{\mathbf{f}}\,. \tag{5.43}$$

The power of the external forces is equal to the product of the external force vector and the displacement rate at the current load increment:

$$P = \dot{\mathbf{d}}^{\mathrm{T}}\lambda\bar{\mathbf{f}}\,. \tag{5.44}$$

By substituting equations (5.43) and (5.44) into (5.37), the amount of energy that has been dissipated from the system $\mathcal{G}$ can be written as:

$$\mathcal{G} = \frac{1}{2}\left(\lambda\dot{\mathbf{d}}^{\mathrm{T}} - \dot{\lambda}\mathbf{d}^{\mathrm{T}}\right)\bar{\mathbf{f}}\,. \tag{5.45}$$

By the second law of thermodynamics, the amount of energy that has dissipated in a system is increasing monotonically. Hence, equation (5.45), which consists of the displacement degrees of freedom $\mathbf{d}$ and the load factor λ, is an ideal candidate to construct the additional constraint equation. Replacing the dissipated energy $\mathcal{G}$ by the rate of the path parameter τ, the constraint equation in rate form reads:

$$\frac{1}{2}\left(\lambda\dot{\mathbf{d}} - \dot{\lambda}\mathbf{d}^{\mathrm{T}}\right)\bar{\mathbf{f}} - \dot{\tau} = 0\,. \tag{5.46}$$

This parametrisation can be written in a discrete form by applying an Euler-forward scheme:

$$\frac{1}{2}\left({}^{i}\lambda\Delta\mathbf{d}^{\mathrm{T}} - \Delta\lambda({}^{i}\mathbf{d})^{\mathrm{T}}\right)\bar{\mathbf{f}} - \Delta\tau = 0\,, \tag{5.47}$$

where i is the time step number and $\Delta(\,) = {}^{i+1}(\,) - {}^{i}(\,)$. The incremental path parameter $\Delta\tau$ represents the amount of energy that is dissipated in one load step. A graphical representation is given in figure 5.14.

The augmented system of equation $\mathbf{r}(\mathbf{d}, \lambda)$ consists of the set of N equilibrium equations (5.18) and the constraint equation in discrete form (5.47):

$$\mathbf{r}(\mathbf{d}, \Delta\lambda) = \begin{bmatrix} \mathbf{f}^{\mathrm{int}}({}^{i+1}\mathbf{d}) - (\Delta\lambda + {}^{i}\lambda)\bar{\mathbf{f}}^{\mathrm{ext}} \\ \frac{1}{2}\left({}^{i}\lambda({}^{i+1}\mathbf{d} - {}^{i}\mathbf{d}) - \Delta\lambda\,{}^{i}\mathbf{d}^{\mathrm{T}}\right)\bar{\mathbf{f}} - \Delta\tau \end{bmatrix} = \mathbf{0} \tag{5.48}$$

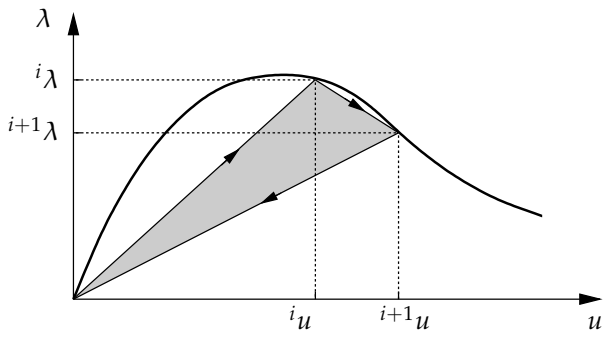

Figure 5.14 The load factor λ vs. a specific displacement u of a system under energy constraint control. The shaded area is a measure for the additionally dissipated energy between two load steps i and $i+1$. Note that the method will only converge when this area is positive, i.e. when the direction of the enclosed boundary is clockwise.

This system can be solved in an iterative manner by using a Newton-Raphson approach. Assuming that k is the iteration number, the new state is defined as:

$$\begin{bmatrix} {}^{i+1}\mathbf{d} \\ \Delta\lambda \end{bmatrix}^{(k+1)} = \begin{bmatrix} {}^{i+1}\mathbf{d} \\ \Delta\lambda \end{bmatrix}^{(k)} - \left(\frac{\partial \mathbf{r}}{\partial({}^{i+1}\mathbf{d}, \Delta\lambda)} \right)^{-1} \mathbf{r}^{(k)} \tag{5.49}$$

with the $(N+1) \times (N+1)$ Jacobian matrix of the form:

$$\frac{\partial \mathbf{r}}{\partial({}^{i+1}\mathbf{d}, \Delta\lambda)} = \begin{bmatrix} \mathbf{K}(\mathbf{d}) & -\bar{\mathbf{f}} \\ \frac{1}{2}{}^{i}\lambda\bar{\mathbf{f}}^{\mathrm{T}} & -\frac{1}{2}{}^{i}\mathbf{d}^{\mathrm{T}}\bar{\mathbf{f}} \end{bmatrix} \tag{5.50}$$

where $\mathbf{K}(\mathbf{d})$ is the total stiffness matrix of the system, which is obviously a function of the total set of degrees of freedom $\mathbf{d}$.

Note that the Jacobian of the system of equations is not symmetric. Moreover, due to the additional column and row vectors, the optimal band structure of this Jacobian is destroyed and cannot be recovered. In order to guarantee a relatively efficient solution, the system needs to be solved in parts. Details of this approach are given in Appendix C.

Clearly, the constraint equation can only be used when a certain amount of energy is dissipated in a single load step. In most cases however, the specimen is completely intact at the beginning of the simulation and fracture is only

initiated when a certain external load level is attained. Hence, the analysis is normally started using a standard force controlled solution method where the load factor $\Delta\lambda$ is increased monotonically. As soon as a fracture is initiated and enough energy is dissipated, the force control is switched into an energy control. In (Gutiérrez 2004), this switching point is determined by means of the number of iterations used in the Newton-Raphson procedure to obtain a new converged solution. Assuming that both the constitutive relation for the bulk material as well as the kinematic relations are linear functions, a sudden increase of the the number of iterations is a measure for the activation of the nonlinear softening relations that describe the fracture processes.

Here, an alternative procedure to switch from a force controlled to an energy controlled solution technique is used. The amount of energy that has dissipated during a force controlled step can be monitored using equation (5.45). As soon as the incremental dissipated energy exceeds a threshold value τ_{init}, the next equilibrium is determined by using an energy controlled procedure.* The initial incremental path parameter $\Delta\tau$ is assumed to be equal to the amount of energy that has been dissipated in the previous step. The magnitude of the threshold value τ_{init} can be based on the fracture toughness of the material and the equivalent length of an element.

In order to calculate the complete quasi-static behaviour of the specimen in as few steps as possible, the incremental path parameter $\Delta\tau$ is adjusted in such a way that the number of iterations per load step is equal to an optimal k_{opt} (Riks 1979). The magnitude of the new incremental path parameter is related to the previous magnitude and the number of iterations in the previous step k^{i-1}, according to:

$$\Delta\tau^i = \Delta\tau^{i-1} 0.5^n \qquad \text{where} \quad n = \frac{k^{i-1} - k_{\text{opt}}}{4}\,. \tag{5.51}$$

In general, $k_{\text{opt}} = 5$ is considered to be an efficient number of iterations in these kind of analyses (Riks 1979).

A limiting factor in the current partition of unity based implementation is the fact that a cohesive segment can only be extended or nucleated after each

*This procedure to initiate the energy constraint method is step-size dependent. When the initial loadstep is taken to large, it can occur that the energy constraint method is not initiated in time.

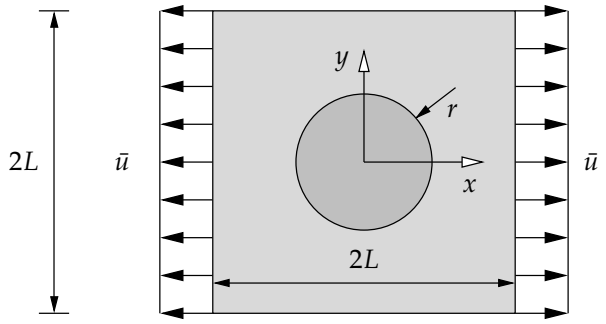

Figure 5.15 Dimensions and boundary conditions of the single fibre in an epoxy matrix.

converged time step. As a result, the maximum incremental path parameter is bounded by the fracture toughness of the material and an equivalent element length. A maximum value for the path parameter $\Delta\tau$ is chosen such that the tip of a cohesive zone will at most propagate through a single element within one load step:

$$\Delta\tau_{\text{crit}} = \alpha_s \mathcal{G}_c l_e \,. \tag{5.52}$$

In this equation, α_s is a scaling parameter which can be varied between 0.0 and 1.0. In the numerical examples presented in this chapter, α_s is chosen to be 0.5.

§ 5.6 Numerical examples

The features of the cohesive segments method are illustrated in two numerical problems with increasing complexity. In both simulations, the behaviour of the bulk material is taken to be linear elastic.

Debonding of a single fibre

Consider a single fibre in epoxy material as shown in Figure 5.15. The radius of the fibre is taken to be $r = 5\,\mu$m, which is equal to the average radius of a single fibre in the prepreg layers in Glare, as can be deduced from Figure 4.4 (b). In order to minimise the effect of the boundary of the specimen on the debonding of the fibre, L is assumed to be $15\,\mu$m. The specimen is sub-

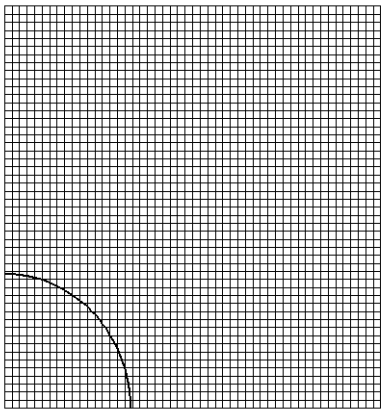

Figure 5.16 Finite element mesh of the single fibre in the epoxy material. The cohesive segment that represents the fibre-epoxy interface is denoted by the bold line. Because of symmetry in both geometry as in boundary and loading conditions, only one quarter of the specimen is modelled.

jected to a prescribed displacement $\bar{u}$ in the x-direction. The top and bottom edges, $y = \pm L$, are constrained in the y-direction.

Both the fibre as well as the epoxy are modelled as a linear elastic materials. Young's modulus and the Poisson's ratio of the fibre is taken $E = 225\,\text{GPa}$ and $\nu = 0.2$ respectively. The stiffness of the epoxy material is $E = 4.3\,\text{GPa}$ and the corresponding Poisson's ratio is set to $\nu = 0.34$. The interface is modelled by Xu-Needleman's cohesive law, equation (5.23) to (5.25). The strength of the interface is taken to be $t_{\max} = 50.0\,\text{MPa}$. The fracture toughness $\mathcal{G}_c$ of the interface will be varied. The additional parameters in this constitutive relation β, r and q are set to 2.3, 1.0 and 0.0 respectively.

The geometry of the specimen, the boundary conditions and the applied load are symmetric about both the x- and y-axes. Hence, only one quarter of the specimen is modelled. The finite element mesh consists of 50×50 quadrilateral elements of side length $0.3\,\mu\text{m}$, see Figure 5.16. The interface of the fibre is represented by a cohesive segment that is placed in the mesh at the start of the analysis.

In order to demonstrate the performance of the energy constraint arc-length method, the complete evolution of fibre debonding is simulated for different values of the fracture toughness of the interface, varying from $\mathcal{G}_c = 0.001$ to

step	$\Delta\lambda$	$\Delta\tau$	**iter.**
7	$1.67 \cdot 10^{-1}$	$5.97 \cdot 10^{-5}$	3
8	$8.71 \cdot 10^{-2}$	$8.44 \cdot 10^{-5}$	3
9	$-3.38 \cdot 10^{-2}$	$1.19 \cdot 10^{-4}$	3
10	$-1.82 \cdot 10^{-1}$	$1.69 \cdot 10^{-4}$	3

Table 5.1 Step number, load factor λ, incremental path parameter $\Delta\tau$ and the number of iterations for the simulation of fibre debonding with an interface fracture toughness $\mathcal{G}_c = 0.001\,\mathrm{N/mm}$.

$\mathcal{G}_c = 0.004\,\mathrm{N/mm}$. In all simulations, the first steps are carried out under displacement control. Here, the unit prescribed displacement is $\bar{u} = 0.025\,\mu\mathrm{m}$. The displacement control is switched into energy control when the dissipated energy in a single step exceeds the value of $1.0 \cdot 10^{-5}\,\mathrm{Nm}$. Since the position of the interface is fixed and the creation of new cohesive segments is not taken into account, there is no need to limit the incremental path-parameter $\Delta\tau$.

Figure 5.17 shows the σ_{xx} stress in the bottom right corner of the finite element mesh versus the magnitude of the prescribed displacement $\bar{u}$. In all simulations, the energy control method is initiated after load step 3. The small differences in the slopes of the three curves prior to failure can be attributed to different initial stiffnesses of the fibre-epoxy interface. This is a consequence of the fact that in Xu-Needleman's cohesive law the initial stiffness is not set explicitly but is related to the fracture toughness $\mathcal{G}_c$ and the strength of the interface $t_{\max}$.

A detail of the stress-displacement curve around the limit point in the case $\mathcal{G}_c = 0.001\,\mathrm{N/mm}$ is shown in Figure 5.18. It shows that the energy constraint method is able to capture both the limit point and the snap-back behaviour in relatively a little amount of load steps. The number of iterations in these critical steps as well as the corresponding values of the incremental path parameter and the load factor are given in Table 5.1. In all load steps around this critical point, the number of iterations never exceeds 3, which demonstrates that the energy constraint method is indeed a robust algorithm.

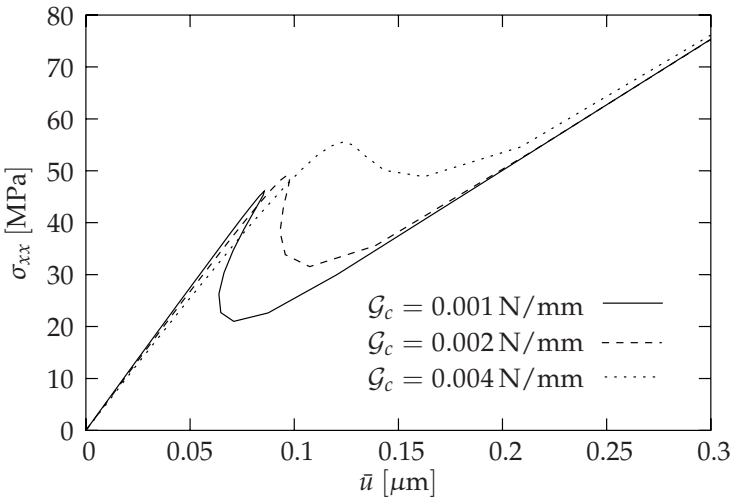

Figure 5.17 The σ_{xx} stress in point A of the specimen, at $[x, y] = [15, 0]\,\mu$m, versus the prescribed displacement of the single fibre in the epoxy with an interface fracture toughness of $\mathcal{G}_c = 0.001, 0.002$ and $0.004\,\mathrm{N/mm}$, respectively.

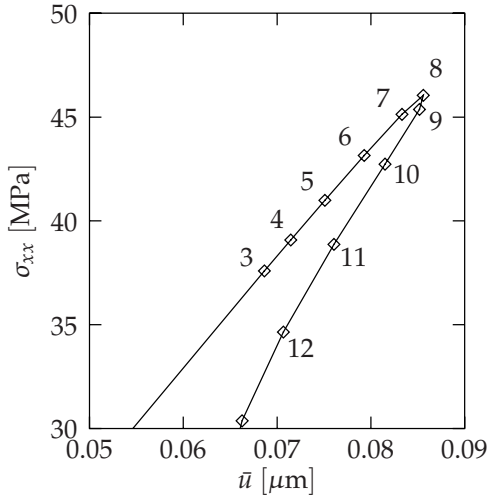

Figure 5.18 Detail of σ_{xx} stress in point A versus the prescribed displacement of the simulation with an interface fracture toughness $\mathcal{G}_c = 0.001\,\mathrm{N/mm}$. The numbers correspond to the current load step.

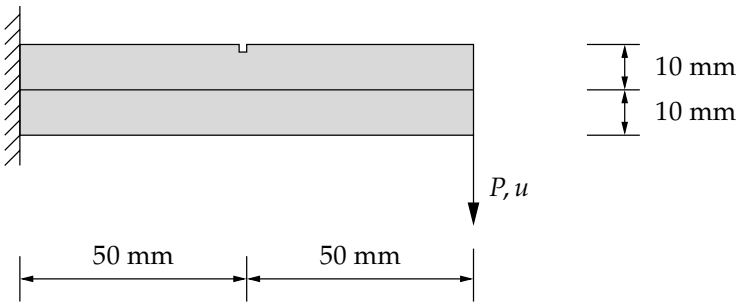

Figure 5.19 Geometry and loading conditions of a double-cantilever beam with an initial notch.

A notched double-cantilever beam

In the following example, the nucleation of a crack in virgin material is investigated, as well as the coalescence of this crack with an interface. Consider the double cantilever beam with a small notch as shown in Figure 5.19, (de Borst *et al.* 2004). The beam is subjected to bending by a point load at the tip of the lower beam. The two beams are assumed to be isotropic linear elastic and have identical properties: Young's modulus $E = 20.0$ GPa and Poisson's ratio $\nu = 0.2$. The cohesive tensile strength of this material is $t_{\max} = 2.5\,\mathrm{MPa}$, the work of separation is $\mathcal{G}_c = 40.0\ \mathrm{N/m}$. The fracture in the bulk material is modelled by the Camacho-Ortiz cohesive law (5.30). The adhesive that bonds the two layers is modelled with Xu-Needleman's delamination model with a non-zero compliance prior to cracking. In this example, we assume that $\mathcal{G}_c^{\mathrm{adh}} = 10.0\,\mathrm{N/m}$, $t_{n,\max} = t_{s,\max} = 1.0\,\mathrm{MPa}$.

The specimen is analysed with a mesh having 99×21 elements. The notch is simulated by removing a single element from the mesh. The interface between the two layers is modelled by a cohesive segment, which is added to the mesh beforehand. This implies that one part of the element that is crossed by this segment belongs to the top layer of the double-cantilever beam, the other part belongs to the bottom layer. The analysis is started under load control, with a unit load $\bar{P} = 0.1\,\mathrm{N}$. The energy control is used when the dissipated energy in a single step exceeds the value of $1.0 \cdot 10^{-6}\,\mathrm{Nm}$. The maximum incremental path parameter $\Delta\tau_{\max}$ is set to $2.0 \cdot 10^{-5}\,\mathrm{Nm}$.

The tip displacement u is plotted against the applied load in Figure 5.20. When the applied load is equal to $P \approx 2.4\,\mathrm{N}$, a crack nucleates at the notch in

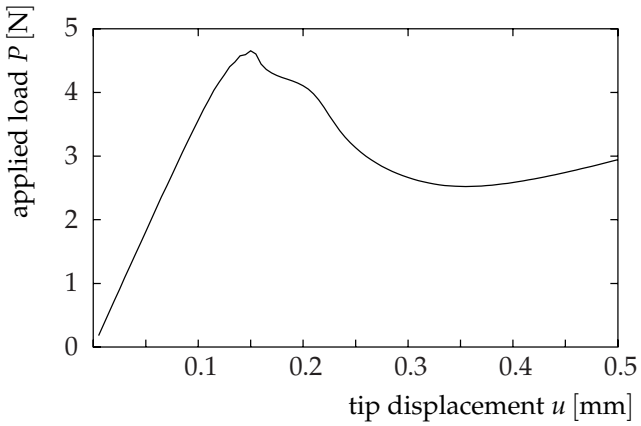

Figure 5.20 Load-displacement curve of the double-cantilever beam with an initial notch.

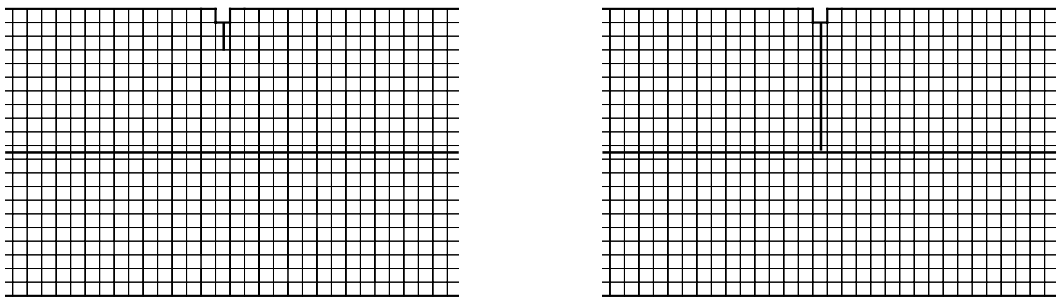

Figure 5.21 Position of cohesive segments during the simulation at crack initiation in the top layer (a) and after total failure of the top layer (b).

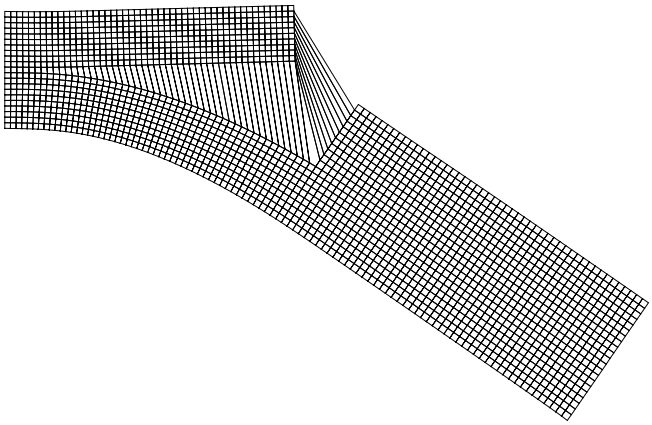

Figure 5.22 Final deformation of the specimen (amplification factor 100.0).

the top layer. A new cohesive segment is added to the finite element model as shown in Figure 5.21 (a). Upon further loading, the crack propagates towards the interface, Figure 5.21 (b). From this moment on, the interface is loaded in nearly a pure mode-II. When the shear tractions in the interface exceed the decohesion strength, the two layers start to debond. Figure 5.22 shows the deformation of the specimen at the final stage of loading, when $u = 0.5\,\text{mm}$.

§ 5.7 Conclusions

In this chapter, a method has been described in which the nucleation, growth and coalescence of multiple cracks can be simulated. Individual cracks are represented by cohesive segments, which are added to finite elements by using the partition-of-unity property of the finite element shape functions. The numerical formulation is a moderate extension to existing partition of unity approaches to cohesive fracture. Nevertheless, the actual implementation of the method can be somewhat elaborate from a bookkeeping point of view, since a single element can be crossed by multiple discontinuities, each with its own additional degrees of freedom.

The method can in principle naturally simulate distributed cracking which frequently occurs in a heterogeneous solid. Thus, the cohesive segments ap-

proach embraces both extremes, distributed cracking with crack nucleation, growth and eventual coalescence at multiple locations as well as the initiation and propagation of a single, dominant crack without needing special assumptions. What is needed is a decohesion constitutive relation which then implicitly specifies the conditions for crack nucleation and the crack propagation direction. In this fashion, the cohesive segments method can be regarded as a bridge between two historically opposing methodologies for the simulation of fracture.

Some capabilities of the cohesive segments method have been illustrated by simple two dimensional examples. The extension of the formulation to more complex bulk and cohesive constitutive relations and to three dimensions is straightforward in principle. The ability of the method to capture complex crack patterns accurately, such as shown in Figure 5.1, remains to be demonstrated. However, the initial studies here suggest that the cohesive segments method provides a promising approach for modelling complex fracture behaviour.

Chapter 6

Dynamic crack growth

Fast crack propagation in brittle solids is typically accompanied by diffuse cracking patterns such as crack branching and micro-crack nucleation away from the crack tip. These phenomena play an important role in the overall cracking behaviour and determine the attainable crack speeds of the material (Freund 1998). The prediction of these crack speeds appeared to be not straightforward. Whereas analytical models reveal that the limiting crack speed approaches the Rayleigh wave speed of the material, in reality, the crack speeds are rarely greater than half this value.

The exact path of a crack and the position of the tip may play an important role in this discrepancy. Based on experiments, Ravi-Chandar and Knauss (1984) argued that the occurrence of micro-cracks ahead of a main crack tip influences the overall speed of the main crack and plays a role in the crack branching process. Gao (1993) suggested a wavy-crack model that incorporates small deviations of the crack tip from its original crack path, hence reducing the apparent crack speed. Although the models were based on fairly idealised assumptions, they provided reasonably good explanations for the described phenomena.

To arrive at a more flexible model, Xu and Needleman (1994) simulated fast crack propagation using a modified version of the original cohesive surface framework (Needleman 1987). The method appeared to be able to address crack branching and micro-crack nucleation (Xu and Needleman 1996). Nevertheless, some fundamental numerical problems remained. Since the cohesive surfaces are aligned with element boundaries, the orientation of cracks is restricted to a number of predefined angles. When the mesh is relatively

dense, the global path of a crack can be captured by a combination of angles. But on smaller levels of observation, the model is not able to reveal very small deviations of a crack path. Another disadvantage is caused by the fact that the cohesive surfaces have an initial non-zero compliance. The presence of the cohesive surfaces reduces the overall stiffness of the body, especially in the vicinity of a crack tip. As a result, the Rayleigh wave speed in the material drops, which could possibly lead to spurious nucleation of micro-cracks or improper crack branches.

In order to compensate for the last deficiency, cohesive zones with an initial zero compliance have been used by Falk *et al.* (2001). Here, the cohesive surfaces at the inter-element boundaries are only activated when the local stress exceeds a yield limit. The problems related to the mismatch in the compliance of the material were hereby solved. Unfortunately, the model failed to predict the occurrence of branches and the attained crack speed in the different simulations reached as high as the Rayleigh wave speed.

The cohesive segments method as discussed in the previous chapter is a logical alternative to study these phenomena in more detail. Apart from the fact that a cohesive segment is only inserted when needed, cracks are allowed to propagate through the mesh in arbitrary directions, irrespective of the structure of the underlying finite element mesh. Consequently, every little detail, related to the trajectory of the mesh can be captured and the issues of the attainable crack speeds can possibly be revealed.

In this chapter, the cohesive segments method is extended to a time dependent model that can be used to address dynamic fracture problems. The corresponding equilibrium equations are presented in the next section, followed by an extensive survey into the numerical stability of the time integration technique. The application of the model is demonstrated by means of a number of examples.

§ 6.1 Linear momentum balance

The kinematic relations for a material point in a domain with m discontinuities have been derived for a quasi-static implementation in chapter 5. The displacement field can be written as a regular displacement field $\hat{\mathbf{u}}$ plus m

additional fields $\tilde{\mathbf{u}}_j$, see equation (5.2):

$$\mathbf{u}(\mathbf{x},t) = \hat{\mathbf{u}}(\mathbf{x},t) + \sum_{j=1}^{m} \mathcal{H}_{\Gamma_{\mathrm{d},j}}(\mathbf{x})\tilde{\mathbf{u}}_j(\mathbf{x},t)\,.$$

The strain field follows by taking the spatial derivative of the total displacement field, see (5.3):

$$\epsilon(\mathbf{x},t) = \nabla^s\hat{\mathbf{u}}(\mathbf{x},t) + \sum_{j=1}^{m} \mathcal{H}_{\Gamma_{\mathrm{d},j}}(\mathbf{x})\nabla^s\tilde{\mathbf{u}}_j(\mathbf{x},t) \qquad \mathbf{x} \notin \Gamma_{\mathrm{d},j}\,,$$

In addition, the acceleration of a material point can be found by differentiating the displacement field, equation (5.2) twice with respect to time: *

$$\ddot{\mathbf{u}}(\mathbf{x},t) = \ddot{\hat{\mathbf{u}}}(\mathbf{x},t) + \sum_{j=1}^{m} \mathcal{H}_{\Gamma_{\mathrm{d},j}}(\mathbf{x})\ddot{\tilde{\mathbf{u}}}_j(\mathbf{x},t)\,, \tag{6.1}$$

where $(\ddot{})$ denotes the second time derivative: $\partial^2(\,)/\partial t^2$.

The linear momentum balance equations for the domain Ω including inertia terms, but without body forces, are equal to:

$$\rho\ddot{\mathbf{u}} + \nabla\cdot\boldsymbol{\sigma} = \mathbf{0} \qquad \mathbf{x} \in \boldsymbol{\Omega}\,, \tag{6.2}$$

where ρ is the density of the material and $\boldsymbol{\sigma}$ is the Cauchy stress in the bulk material. The corresponding boundary conditions for the external boundary and the discontinuities are respectively:

$$\begin{aligned} \mathbf{n}_t\cdot\boldsymbol{\sigma} &= \bar{\mathbf{t}} \qquad & \mathbf{x} &\in \Gamma_t\,; \\ \mathbf{n}_{\mathrm{d},j}\cdot\boldsymbol{\sigma} &= \mathbf{t}_j \qquad & \mathbf{x} &\in \Gamma_{\mathrm{d},j}\,, \end{aligned} \tag{6.3}$$

where $\bar{\mathbf{t}}$ are the prescribed tractions on Γ_t with outward normal vector $\mathbf{n}_t$ and $\mathbf{t}_j$ are the tractions at discontinuity $\Gamma_{\mathrm{d},j}$. The normal vector $\mathbf{n}_{\mathrm{d},j}$ points from Ω_j^- to Ω_j^+.

*Strictly speaking, since the additional displacement field can be added during a simulation, the step functions $\mathcal{H}_{\Gamma_{\mathrm{d},j}}$ are functions of time as well. However, as we will see in section 6.3, the system of equations will be solved in a discrete manner, which allows us to omit this time derivative.

Equilibrium can be expressed in a weak form by multiplication with an admissible variational displacement field $\delta\mathbf{u}$:

$$\int_\Omega \delta\mathbf{u}\cdot(\rho\ddot{\mathbf{u}})\mathrm{d}\Omega + \int_\Omega \delta\mathbf{u}\cdot(\nabla\cdot\boldsymbol{\sigma})\mathrm{d}\Omega = 0\,, \tag{6.4}$$

In line with previous derivations, it is assumed that the space of the admissible variation $\boldsymbol{\eta}$ is the same as the field of the actual displacements, equation (5.10):

$$\delta\mathbf{u} = \hat{\delta}\mathbf{u} + \sum_{j=1}^{m} \mathcal{H}_{\Gamma_{\mathrm{d},j}}\tilde{\delta}\mathbf{u}_j\,.$$

Inserting the strain and the acceleration field (6.1), applying Gauss' theorem, eliminating some of the Heaviside functions by changing the integration domain and incorporating the boundary conditions, the momentum balance (6.4), can be written as:

$$\begin{aligned}\int_\Omega \rho\delta\hat{\mathbf{u}}\cdot\ddot{\hat{\mathbf{u}}}\mathrm{d}\Omega + \sum_{j=1}^{m}\int_\Omega \mathcal{H}_{\Gamma_{\mathrm{d},j}}\rho\left(\delta\tilde{\mathbf{u}}_j\cdot\ddot{\hat{\mathbf{u}}} + \delta\hat{\mathbf{u}}\cdot\ddot{\tilde{\mathbf{u}}}_j\right)\mathrm{d}\Omega + \sum_{j=1}^{m}\sum_{k=1}^{m}\int_\Omega \mathcal{H}_{\Gamma_{\mathrm{d},j}}\mathcal{H}_{\Gamma_{\mathrm{d},k}}\rho\delta\tilde{\mathbf{u}}_j\cdot\ddot{\tilde{\mathbf{u}}}_k\mathrm{d}\Omega \\ + \int_\Omega \nabla^s\delta\hat{\mathbf{u}} : \boldsymbol{\sigma}\mathrm{d}\Omega + \sum_{j=1}^{m}\int_\Omega \mathcal{H}_{\Gamma_{\mathrm{d},j}}\nabla^s\delta\tilde{\mathbf{u}}_j : \boldsymbol{\sigma}\mathrm{d}\Omega + \sum_{j=1}^{m}\int_{\Gamma_{\mathrm{d},j}} \delta\tilde{\mathbf{u}}_j\cdot\mathbf{t}_j\mathrm{d}\Gamma = \\ \int_{\Gamma_t}\delta\hat{\mathbf{u}}\cdot\bar{\mathbf{t}}\mathrm{d}\Gamma + \sum_{j=1}^{m}\int_{\Gamma_t}\mathcal{H}_{\Gamma_{\mathrm{d},j}}\delta\tilde{\mathbf{u}}_j\cdot\bar{\mathbf{t}}\mathrm{d}\Gamma\,.\end{aligned} \tag{6.5}$$

The first three terms in the equation represent the inertia of the body, whereas the remaining terms are related to the internal forces, the cohesive tractions and the applied external tractions, respectively, cf. equation (5.12).

§ 6.2 Finite element discretisation

The spatial discretisation of the system of equations in weak form is identical to the quasi-static formulation. The discretised acceleration can be found by differentiating the discrete displacement field, equation (5.13) twice with respect to time:

$$\ddot{\mathbf{u}} = \mathbf{N}\ddot{\mathbf{a}} + \sum_{j=1}^{m}\mathcal{H}_{\Gamma_{\mathrm{d},j}}\mathbf{N}\ddot{\mathbf{b}}_j\,. \tag{6.6}$$

Inserting this expression and the discrete admissible variation, equation (5.16) into (6.5) and taking the variations $\delta\mathbf{a}$ and $\delta\mathbf{b}_j$ respectively, gives the following set of equilibrium equations:

$$\begin{bmatrix} \mathbf{M}_{aa} & \mathbf{M}_{ab_1} & \dots & \mathbf{M}_{ab_m} \\ \mathbf{M}_{ab_1} & \mathbf{M}_{b_1b_1} & \dots & \mathbf{M}_{b_1b_m} \\ \vdots & \vdots & \ddots & \vdots \\ \mathbf{M}_{ab_m} & \mathbf{M}_{b_1b_m} & \dots & \mathbf{M}_{b_mb_m} \end{bmatrix} \begin{bmatrix} \ddot{\mathbf{a}} \\ \ddot{\mathbf{b}}_1 \\ \vdots \\ \ddot{\mathbf{b}}_m \end{bmatrix} = \begin{bmatrix} \mathbf{f}_a^{\text{ext}} \\ \mathbf{f}_{b_1}^{\text{ext}} \\ \vdots \\ \mathbf{f}_{b_m}^{\text{ext}} \end{bmatrix} - \begin{bmatrix} \mathbf{f}_a^{\text{int}} \\ \mathbf{f}_{b_1}^{\text{int}} \\ \vdots \\ \mathbf{f}_{b_m}^{\text{int}} \end{bmatrix}. \tag{6.7}$$

The internal and external force vectors have been defined in equations (5.21) and (5.22). The terms in the mass matrix $\mathbf{M}$ are:

$$\begin{aligned} \mathbf{M}_{aa} &= \int_{\mathcal{V}} \rho \mathbf{N}^{\mathrm{T}} \mathbf{N} \mathrm{d}\mathcal{V}\,; \\ \mathbf{M}_{ab_j} &= \int_{\mathcal{V}} \mathcal{H}_{\Gamma_{\mathrm{d},j}} \rho \mathbf{N}^{\mathrm{T}} \mathbf{N} \mathrm{d}\mathcal{V}\,; \\ \mathbf{M}_{b_jb_k} &= \int_{\mathcal{V}} \mathcal{H}_{\Gamma_{\mathrm{d},j}} \mathcal{H}_{\Gamma_{\mathrm{d},k}} \rho \mathbf{N}^{\mathrm{T}} \mathbf{N} \mathrm{d}\mathcal{V}\,. \end{aligned} \tag{6.8}$$

Note that this element mass matrix is completely filled.

The implementation of the method in the finite element mesh is identical to the implementation in the quasi-static case. The cohesive constitutive relations are the same as well.

§ 6.3 Solution procedure

The equilibrium equations are discretised in the time domain using a variant of the Newmark-β explicit time integration scheme with $\beta = 0$ (Belytschko *et*

al. 1976):

$$\dot{\mathbf{d}}^{t+\frac{1}{2}\Delta t} = \dot{\mathbf{d}}^{t} + \frac{1}{2}\Delta t\, \ddot{\mathbf{d}}^{t}\,; \tag{6.9a}$$

$$\mathbf{d}^{t+\Delta t} = \mathbf{d}^{t} + \Delta t\, \dot{\mathbf{d}}^{t+\frac{1}{2}\Delta t}\,; \tag{6.9b}$$

$$\ddot{\mathbf{d}}^{t+\Delta t} = \mathbf{M}^{-1}\left(\mathbf{f}^{\text{ext},t+\Delta t} - \mathbf{f}^{\text{int},t+\Delta t}\right)\,; \tag{6.9c}$$

$$\dot{\mathbf{d}}^{t+\Delta t} = \dot{\mathbf{d}}^{t+\frac{1}{2}\Delta t} + \frac{1}{2}\Delta t\, \ddot{\mathbf{d}}^{t+\Delta t}\,, \tag{6.9d}$$

In these equations Δt is the discrete time step and $\mathbf{d}$ represents the total array of degrees of freedom in the system: $\mathbf{d} = [\mathbf{a}, \mathbf{b}_1, \ldots, \mathbf{b}_m]^{\text{T}}$.

For wave equations, the time step is limited by the speed of the stress wave in the material, or the dilation speed c_{d}. In general, the simulation becomes unstable when the stress wave crosses a single element with a specific element length l_e within one time interval Δt. Hence, the critical interval is equal to:

$$\Delta t_{\text{cr}} = \frac{l_e}{c_{\text{d}}}\,. \tag{6.10}$$

Traditionally, the calculation time of an explicit time integration procedure is reduced significantly by using a diagonal mass representation $\mathbf{M}^{\text{diag}}$ in equation (6.9c). In such a matrix, all terms are zero except for the ones on the diagonal. The inverse of a diagonal matrix can easily be determined by taking the inverse of each diagonal component. As a result, the system of equations (6.9c) is no longer coupled and each degree of freedom i can be solved separately:

$$d_i^{t+\Delta t} = \frac{f_i^{\text{ext},t+\Delta t} - f_i^{\text{int},t+\Delta t}}{M_i^{\text{diag}}}\,. \tag{6.11}$$

A diagonal mass matrix can be constructed in several different ways. In the case of a standard continuum element formulation, it is possible to concentrate the mass of the element in its nodes. Each node then has a portion of the total mass of the element, which is placed on the diagonal term of the corresponding degrees of freedom in the mass matrix.

An alternative approach that is pursued here is to *lump* the mass matrix by replacing the diagonal term of the mass matrix by the total sum of the mass terms on the corresponding row. The off-diagonal terms are set to zero. In

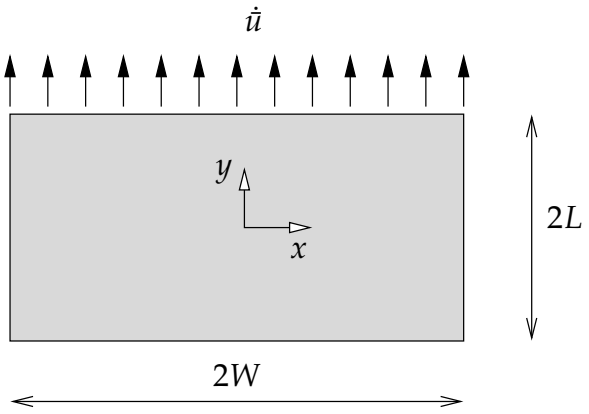

Figure 6.1 Geometry and loading condition of the block.

the case of a system with n unknowns, the diagonal mass matrix $\mathbf{M}^{\text{diag}}$ can be written as:

$$M_i^{\text{diag}} = \sum_j^n M_{ij} \,. \tag{6.12}$$

It can be seen from equation (6.7) that the mass matrix contains terms that couple the regular and additional degrees of freedom. By lumping the matrix, this information will be lost. In order to determine the effects of lumping, the different approaches are studied in the following example, which is based on a numerical test by Xu and Needleman (1994).

Consider the plane strain wave propagation block in Figure 6.1. The block has dimensions $L = 5\,\text{mm}$ and $W = 10\,\text{mm}$ and is made of PMMA with Young's modulus $E = 3.24\,\text{GPa}$, Poisson's ratio $\nu = 0.35$ and density $\rho = 1190\,\text{kg/m}^3$. The corresponding dilatational, shear and Rayleigh wave speeds can be obtained from the following relations (Freund 1998):

$$c_\text{d} = \sqrt{\frac{E(1-\nu)}{\rho(1+\nu)(1-2\nu)}}\,; \quad c_\text{s} = \sqrt{\frac{E}{2\rho(1+\nu)}}\,; \quad c_\text{R} = c_\text{s}\frac{0.862+1.14\nu}{1+\nu}\,. \tag{6.13}$$

According to these relations, the dilatational, shear and Rayleigh wave speeds for the given material are $c_\text{d} = 2090\,\text{m/s}$, $c_\text{s} = 1004\,\text{m/s}$ and $c_\text{R} = 938\,\text{m/s}$ respectively.

The block is not supported and is loaded by an impact velocity $\dot{u}$, acting in the positive y direction on the top boundary of the block (at $y = +L$). The

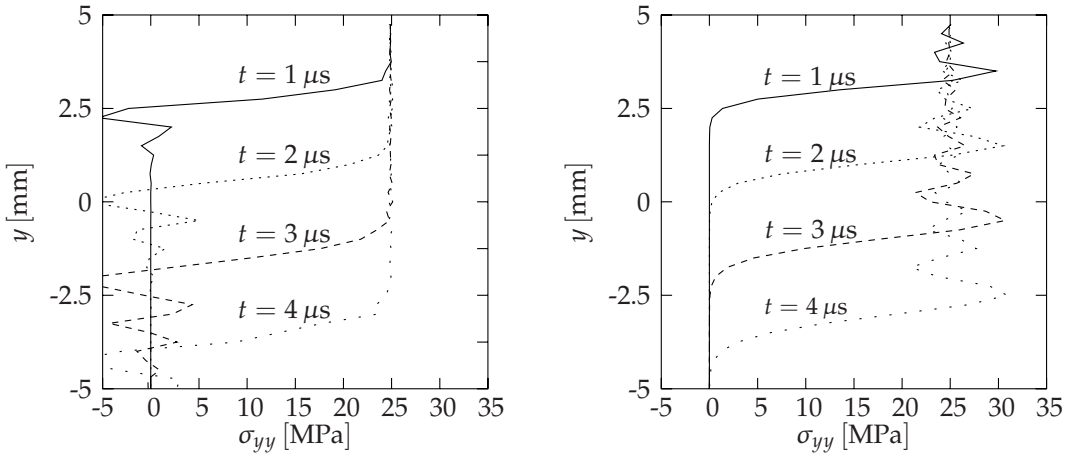

(a) Consistent mass matrix (b) Lumped mass matrix

Figure 6.2 Stress curves σ_{yy} versus vertical position y measured along the centre of the plane strain wave specimen ($x = 0.0\,\text{mm}$) at different times during the simulation.

impact velocity is increased linearly to a constant value V within a certain rise time t_r, according to:

$$\dot{\bar{u}} = \begin{cases} Vt/t_r & \text{for} \quad t < t_r\,, \\ V & \text{for} \quad t \geq t_r\,. \end{cases} \tag{6.14}$$

In this experiment, the rise time is taken to be $t_r = 1.0 \cdot 10^{-7}\,\text{s}$ and the prescribed velocity $V = 10\,\text{m/s}$. The uni-axial stress wave created by these loading conditions will propagate through the block at approximately the dilatational wave speed, $c_\text{d} = 2090\,\text{m/s}$, carrying a tensile stress of 25.0 MPa.

Since the block and the loading conditions are symmetric about the y-axis, only the part in the positive x-axis is modelled using a regular mesh with 39×39 four node elements. The specific length of each element is $l_e = 0.256\,\text{mm}$. The displacements x-direction of the nodes at $x = 0.0\,\text{mm}$ are constrained in order to enforce symmetric boundary conditions. Regarding the specific length of an element and the magnitude of the dilatational wave speed, a sufficiently small time step of $\Delta t = 1.0 \cdot 10^{-9}\,\text{s}$ has been used in the simulations, which have been performed using both a lumped and a consistent representation of the mass matrix.

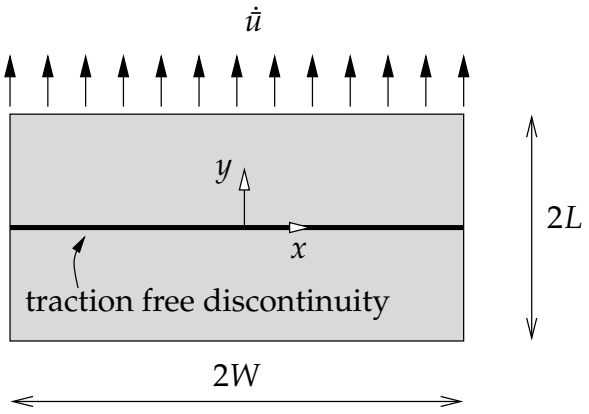

Figure 6.3 Geometry and loading condition of the block with a traction free discontinuity.

Figure 6.2 shows the profile of the σ_{yy} stress along the y-axis at $x = 0.0\,\text{mm}$ during the simulation. It can be seen that the average magnitude of the stress wave is in agreement with the analytical prediction of 25 MPa. The small stress oscillations of approximately 5.0 MPa can be contributed to the relatively coarse mesh that has been used in these simulations. The wave speed can be determined from the progression of the stress front with respect to time. Due to the numerical smoothing in the coarse mesh, the position of the stress wave cannot be determined exactly. Nevertheless, a rough estimation reveals that the wave speed is in good agreement with the analytically obtained dilatational speed $c_\text{d} = 2090\,\text{m/s}$.

A remarkable difference between the simulations with the lumped mass matrix and the simulations with the consistent mass matrix is the appearance of the stress overshoot. The lumped mass matrix gives rise to an extra overshoot of approximately 5.0 MPa on top of the wave front of 25.0 MPa, whereas in the case of a consistent mass matrix, the stress wave is proceeded by a dip of 5.0 MPa.

Subsequently, the block is divided into two parts by means of a horizontal crack at $y = 0\,\text{mm}$ crossing the entire width of the specimen, Figure 6.3. In the finite element model, this crack is represented as a traction free cohesive segment. In this particular case, the discontinuity is modelled using a standard Heaviside enhancement function, where $\mathcal{H}^+ = 1$ and $\mathcal{H}^- = 0$, see Table 2.1. The boundary conditions and material parameters of the specimen, as well as

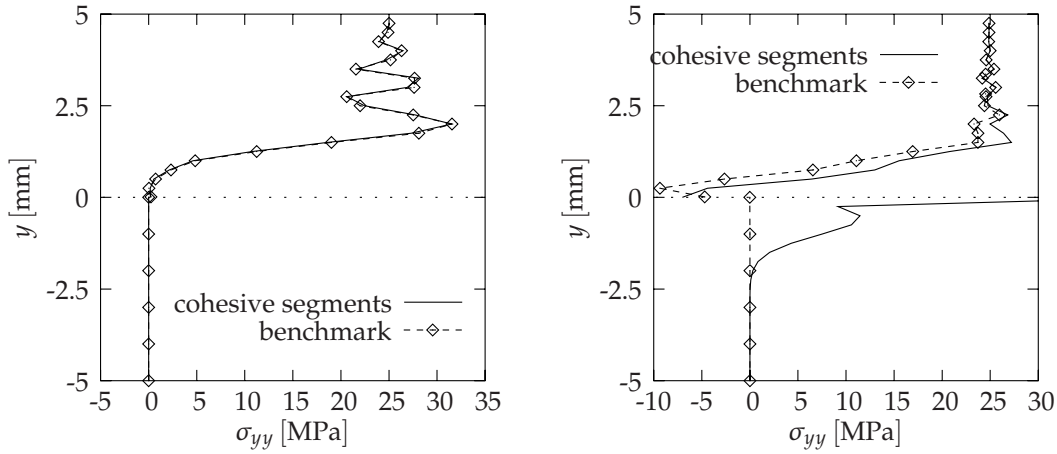

(a) Consistent mass matrix (b) Lumped mass matrix

Figure 6.4 Stress curves σ_{yy} versus vertical position y measured along the centre of the plane strain wave specimen ($x = 0.0$ mm) at $t = 3\,\mu$s. The initial crack (denoted by the dotted line) is modelled as a traction free cohesive segment which is constructed using a Heaviside jump function.

the impact velocity are not changed.

In the simulations, the stress wave carrying a tensile stress of 25 MPa will propagate from the top side of the specimen to reach the crack after approximately $t = 2\,\mu$s. Since the crack can be considered as a traction free boundary, the wave will reflect and move upwards. Obviously, the traction free crack prevents any kind of physical contact between the two parts of the specimen and the stresses in the lower part of the specimen will remain zero throughout the simulation.

Figure 6.4 shows the σ_{yy} stress curves along the y-axis in the centre of the specimen for both the model with a consistent and with a lumped representation of the mass matrix. In both graphs, the stress state at $t = 3\,\mu$s is shown. At this instance, the stress wave has been reflected by the traction free crack. Both simulations are compared with a benchmark calculation in which the slit is modelled in the traditional way: by disconnecting adjacent elements. The benchmark calculations are performed using a consistent and a lumped mass matrix, respectively.

The simulation of the specimen with the crack using the consistent mass matrix shows perfect agreement with the benchmark simulation, see Figu-

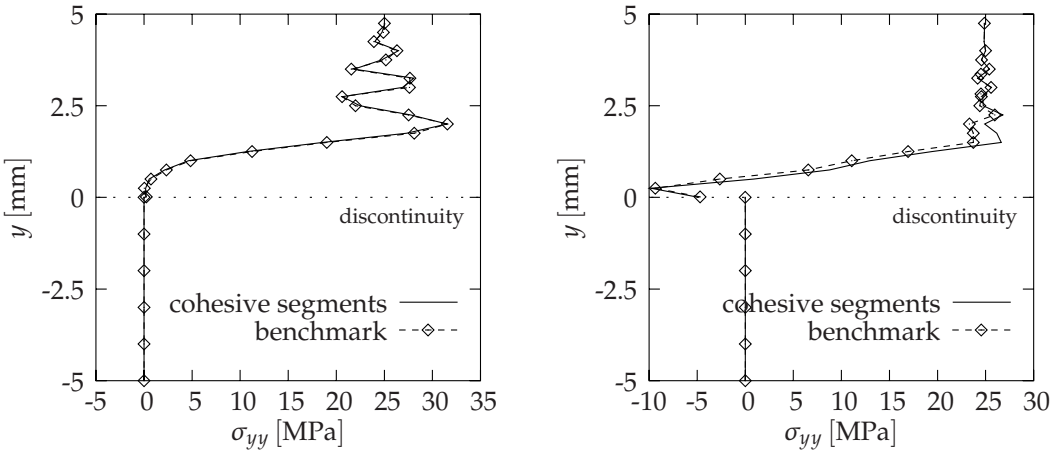

(a) Consistent mass matrix (b) Lumped mass matrix

Figure 6.5 Stress curves σ_{yy} versus vertical position y measured along the centre of the plane strain wave specimen ($x = 0.0$ mm) at $t = 3$ μs. The initial crack (denoted by the dotted line) is modelled as a traction free cohesive segment which is constructed using a unit symmetric jump function.

re 6.4 (a). The stress wave is properly reflected and, more important, the lower part of the specimen remains completely stress free. This is not the case in the simulation with a lumped mass matrix, Figure 6.4 (b). Here a considerable amount of the energy is transferred across the cohesive segment to result in a stress wave with an amplitude of 10 MPa in the lower part of the specimen. As a matter of fact, this spurious stress wave propagates with exactly the dilatation speed. Even more alarming is the extremely high stress peak of over 42 MPa in the integration points just below the discontinuity. Compared to this, the small mismatch of the stresses in the top part of the specimen, can be considered as a modest problem.

The simulations are now repeated with a different jump function. Instead of the Heaviside function a symmetric jump function is used, in which $\mathcal{H}^+ = 1$ and $\mathcal{H}^- = -1$, Table 2.1. The corresponding traction profiles are shown in Figure 6.5. Remarkably, the spurious stress wave reflections in the simulations with the lumped mass matrix representation have disappeared, Figure 6.5 (b). The stresses in the lower part of the specimen remain zero. Apparently, this can be contributed to the symmetric nature of the enhancement function. Nevertheless, the mismatch in the reflected stress wave in the top

part of the specimen did not disappear, which reveals a small inconsistency in the current lumped matrix model. The stress waves in the simulation with the consistent mass matrix again show a perfect agreement to the benchmark simulations, see Figure 6.5 (a).

An alternative way to check the accuracy of the method is to look at the energy balance of the system. Obviously, the amount of external work that is used to deform the specimen must be equal to the total internal energy, which is composed of the strain energy and the kinetic energy. The external work $\mathcal{W}$ at time $t + \Delta t$ is obtained by integration in time, according to, see (Belytschko *et al.* 2000):

$$\mathcal{W}^{t+\Delta t} = \mathcal{W}^t + \frac{1}{2}\Delta t \left(\dot{\mathbf{d}}^{t+\frac{1}{2}\Delta t}\right)^{\mathrm{T}} \left(\mathbf{f}^{\mathrm{ext},t} + \mathbf{f}^{\mathrm{ext},t+\Delta t}\right) . \tag{6.15}$$

When the specimen is loaded by a prescribed velocity instead of an external force, this relation can be written as:

$$\mathcal{W}^{t+\Delta t} = \mathcal{W}^t + \frac{1}{2}\Delta t \left(\dot{\mathbf{d}}_{\mathrm{p}}^{t+\frac{1}{2}\Delta t}\right)^{\mathrm{T}} \left(\mathbf{f}^{\mathrm{int},t} + \mathbf{f}^{\mathrm{int},t+\Delta t}\right) , \tag{6.16}$$

where $\dot{\mathbf{d}}_{\mathrm{p}}^{t+\frac{1}{2}\Delta t}$ denotes the prescribed velocity vector in which the unconstrained degrees of freedom are replaced by zeros. The internal strain energy is obtained as follows:

$$\mathcal{E}_{\mathrm{int}}^{t+\Delta t} = \mathcal{E}_{\mathrm{int}}^{t} + \frac{1}{2}\Delta t \left(\dot{\mathbf{d}}^{t+\frac{1}{2}\Delta t}\right)^{\mathrm{T}} \left(\mathbf{f}^{\mathrm{int},t} + \mathbf{f}^{\mathrm{int},t+\Delta t}\right) , \tag{6.17}$$

whereas the kinetic energy is given by:

$$\mathcal{E}_{\mathrm{kin}}^{t} = \frac{1}{2} \left(\dot{\mathbf{d}}^{t}\right)^{\mathrm{T}} \mathbf{M} \dot{\mathbf{d}}^{t} . \tag{6.18}$$

Energy conservation requires that the sum of internal and kinetic energy is equal to the total external work, or:

$$|\mathcal{E}_{\mathrm{kin}} + \mathcal{E}_{\mathrm{int}} - \mathcal{W}| < \varepsilon \max(|\mathcal{W}|, |\mathcal{E}_{\mathrm{int}}|, \mathcal{E}_{\mathrm{kin}}) , \tag{6.19}$$

where ε is a small tolerance. When this tolerance is on the order of 10^{-2} or smaller, it can be concluded that energy is conserved (Belytschko *et al.* 2000).

The energy variations as a function of time for the simulations with the traction free discontinuity are shown in Figure 6.6. Figure 6.6 (a) shows the

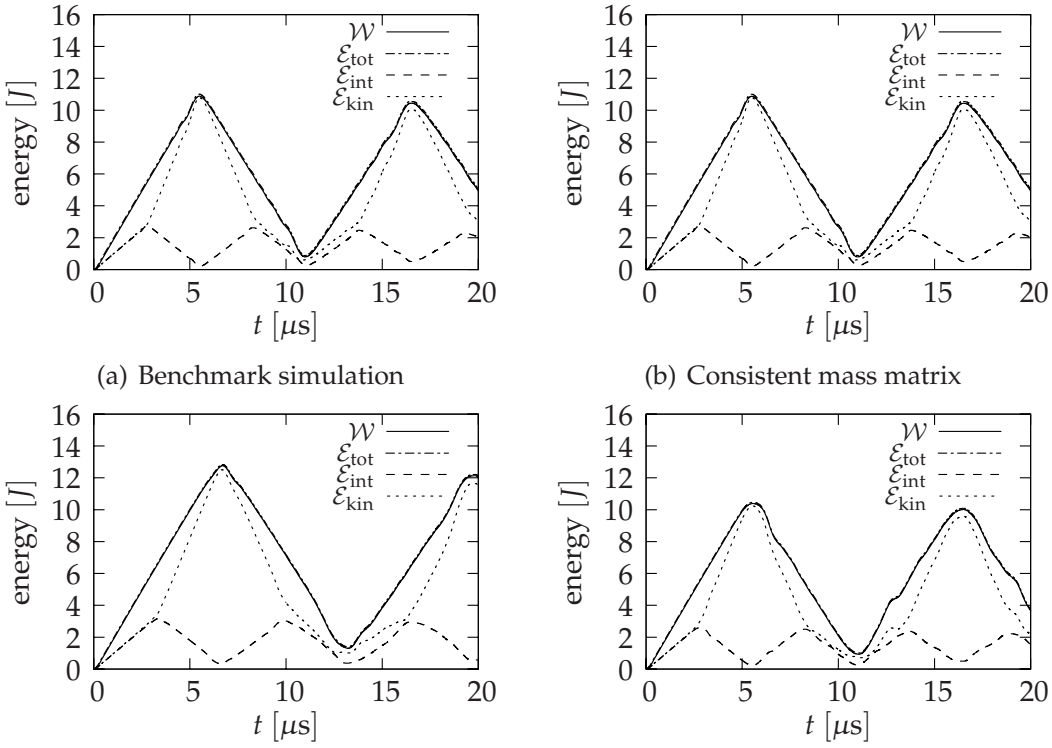

(a) Benchmark simulation

(b) Consistent mass matrix

(c) Lumped mass / Heaviside jump

(d) Lumped mass / symmetric jump

Figure 6.6 Energy variations as a function of time. Figure (a) shows the benchmark simulation with a traditional finite element mesh. The other figures show the calculations with a traction free cohesive segment with (b) a consistent mass matrix, (c) a lumped mass matrix and a Heaviside jump function and (d) a lumped mass matrix and a symmetric jump function.

variation of energy for the benchmark calculation in which the crack is modelled in the traditional way by disconnecting adjacent elements. In this particular case, a consistent mass matrix is used. The energy variations for the calculation with a lumped mass matrix are nearly identical. It can be seen that in these calculations, the kinetic and internal strain energy sum up to the external work, which indicates that energy is conserved.*

Figures 6.6 (b) to (d) show the energy variations for the simulations in which the slit is modelled by traction free discontinuity. In (b) a consistent

*The line that represents the total internal energy $\mathcal{E}_{tot}$ is hardly visible in Figures 6.6 (a) to (d) since it is overlapped by the line representing the external work $\mathcal{W}$.

mass matrix has been used, in combination with a Heaviside jump function for the discontinuity. In the calculation depicted in (c) a lumped mass matrix has been used. Here, the discontinuity has been modelled with a Heaviside step function. Finally, Figure 6.6 (d) shows the energy variation of the simulation with a lumped mass matrix in combination with a unit symmetric step function for the discontinuity.

Although in both simulations with the lumped mass matrix energy is conserved, the variation of total internal energy in time is different than the variation of total energy in the benchmark case. For the calculations with the Heaviside jump this was to be expected. It was demonstrated before that a significant amount of energy was transferred across the discontinuity. As a result, the magnitude of the stress waves reflecting back from the discontinuity is smaller, which in turn gives rise to a different behaviour at the clamped edge. The deviation of the total energy in the case of a lumped mass matrix in combination with a unit symmetric jump function, Figure 6.6 (d) may come as a surprise. In the previous tests, this combination did not give rise to spurious stress wave reflections into the lower part of the specimen. Nevertheless, the magnitude of the σ_{yy} stress carried by the reflecting stress wave is slightly different than the magnitude of this stress in the benchmark simulation, see Figure 6.5 (b). It appears that this relatively small deviation gives rise to a difference in the total energy variation.

Despite the differences in energy variations, in all cases, the total energy is well conserved. Apparently, the traction free discontinuity does not give rise to the creation or dissipation of internal energy, even when a lumped mass matrix and a Heaviside jump function are used. The magnitudes of the tolerance ε for all four cases are shown in Figure 6.7. Apart from a few peaks, the average value of the tolerance is indeed on the order of 10^{-2}. The large peak at the start of the simulation is due to the fact that at this instant the prescribed velocity $\bar{u}$ is increased to its final value V in a relatively short amount of time. The second peak after approximately $t = 10\,\mu$s is caused by the reflecting stress wave that reaches the crack of the specimen for the second time. This marks a sudden change in the direction of stress wave propagation, which results in an abrupt change of external work and therefore in an increase of the energy mismatch. In general, these boundary effects are less significant when a denser finite element mesh is used in which the amount of degrees of

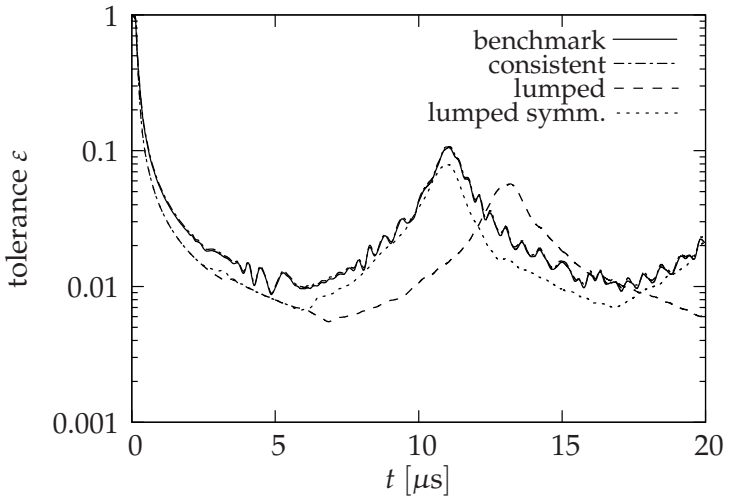

Figure 6.7 Energy tolerances as a function of time for the four simulations: the benchmark simulation, the traction free discontinuity with a consistent mass matrix, the lumped mass matrix in combination with the Heaviside jump function and the lumped mass matrix in combination with the symmetric jump function.

freedom that are constrained is relatively small.

In general, the simulations in which a consistent mass matrix is used gives results that are identical to the benchmark simulations. When a lumped mass matrix is used, different jump functions to give rise to different results. When the discontinuity is modelled by a Heaviside function, spurious reflections of stress waves are observed. This is not the case with a unit-symmetric jump function. However, in both cases, the results are not identical to the benchmark calculations, which can be seen from the energy analysis.

It goes without saying that in this case, numerical accuracy is preferred over computational efficiency. Therefore, all simulations in the remainder of this chapter are performed using a consistent mass matrix in combination with a Heaviside jump function.

§ 6.4 Stability of the time-integration algorithm

It has already been observed by Babuška and Melenk (1997) and later confirmed by Munts *et al.* (2003), that in most cases, the condition of the ma-

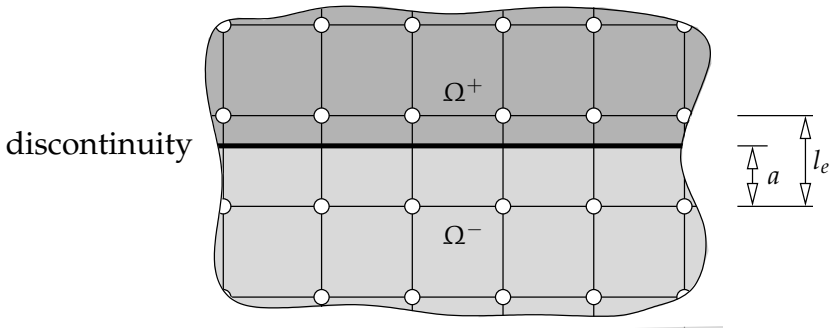

Figure 6.8 Detail of the quadrilateral finite element mesh that has been used to determine the critical time step for various positions of a discontinuity.

trix decreases significantly when base functions are added to shape functions by using the partition of unity method. In the case of creating displacement a jump, it can occur that when a discontinuity crosses an element close to a node, the matrix becomes ill-conditioned. This can be solved by enhancing only those nodes that have a significant contribution to the stiffness matrix (Wells and Sluys 2001a), see also Figure 2.7.

In dynamic crack growth simulations, where the equations of motions are discretised in the time domain by using an explicit integration method, a more or less equivalent problem occurs. It appears that when an element is crossed by a discontinuity, the two separated parts can be considered as individual elements, each with a smaller effective length l_e than the original element. In principle, an element can be crossed by a discontinuity in such a way that one of the two resulting portions of the element becomes so small that, according to relation (6.10), the critical time increment for a stable solution procedure will almost be infinitesimal. In such a situation, numerical solutions, such as the selective enhancement of nodes, do not work.

In order to determine the exact effect of the position of the discontinuity on the critical time step of the explicit time integration method, the simulation of the plane strain wave specimen with an initial slit is considered again. In this case, the specimen is modelled using a structured mesh of 40×40 quadrilateral elements with an specific element length $l_e = 0.25\,\text{mm}$. The position of the horizontal traction free cohesive segment that models the initial slit is varied between $a = 0.0\,\text{mm}$ and $a = 0.25\,\text{mm}$ so that it covers all positions within a single element, see Figure 6.8. The material parameters and the boundary

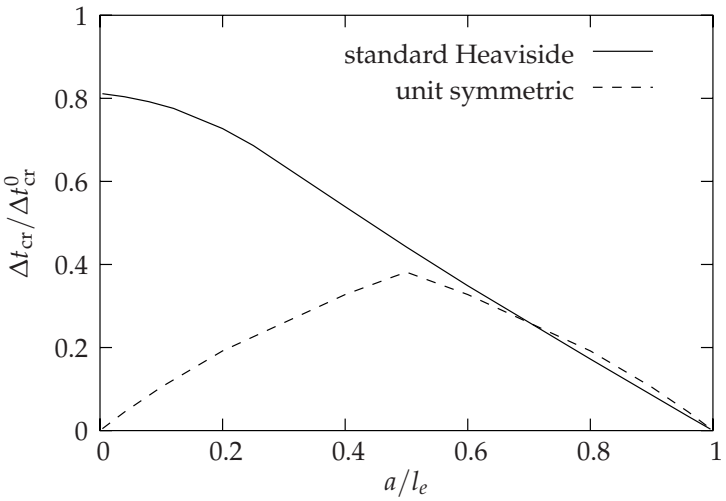

Figure 6.9 The critical time step vs. the position of the discontinuity within the element. s denotes the distance of the discontinuity with respect to the nodes in the Ω^- part of the domain.

and loading conditions remain the same. The simulations are performed using a standard Heaviside function and a unit-symmetric enhancement function.

The critical time increment Δt_{cr} is shown as a function of the position of the discontinuity within the element in Figure 6.9. The critical time increments are normalised by the critical time step in case of a simulation without a discontinuity Δt^0_{cr}. This value is found to be 0.1172 μs which is relatively close to the estimation from equation (6.10): $\Delta t^0_{\text{cr}} = 0.1196\ \mu$s.

As expected, the critical time increment decreases almost linearly to zero when the discontinuity approaches the boundary of the element. In the case of the standard Heaviside enhancement function, there is no difference whether this boundary is in the Ω^+ or the Ω^- part of the domain. When using the unit-symmetric enhancement function, this effect only occurs when the discontinuity is in the vicinity of nodes in the Ω^+ part of the domain. On the other side of the element, the critical time increment increases up to over 80% of the nominal critical increment when the discontinuity approaches the boundary in the Ω^- part of the domain.

In order to avoid an infinitesimal critical increments, a discontinuity is not allowed to cross an element boundary within a certain distance hl_e to a node,

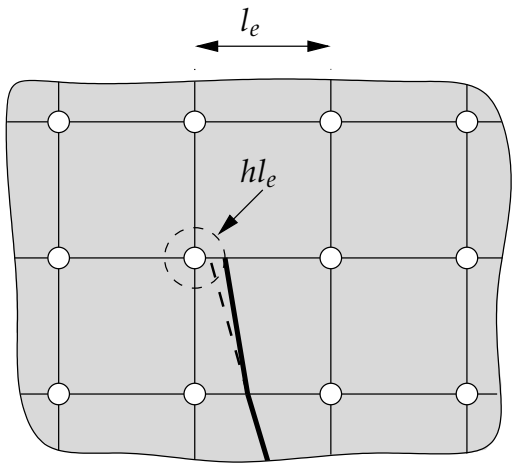

Figure 6.10 Overview of the algorithm that prevents a discontinuity to cross an element boundary in the vicinity of a supporting node. The grey dashed line denotes the original position of the discontinuity. Since it crosses the node within a distance hl_e (denoted by the dashed circle), it is moved away from the node.

where h is an offset factor between 0.0 and 0.5, see Figure 6.10. And although the exact position of a new segment is slightly modified, it can be demonstrated that for reasonably small values of h the deflection is minimal. In the remaining simulations in this chapter, an offset factor $h = 0.1$ has been used. The corresponding deflection of the crack is then in the order of a few degrees.*

Because of the nearly linear relation between the critical time step and the distance between the discontinuity, the stability requirement can be expanded as follows:

$$\Delta t = \alpha \frac{h\, l_e}{c_{\mathrm{d}}}\,, \tag{6.20}$$

where α is a factor to compensate for shock wave effects at delamination propagation (Xu and Needleman 1994). When $\alpha = 0.1$ the solution appears to be

*An alternative approach is to move the node towards the original terminus of the discontinuity. The small cut-off is then avoided and the discontinuity is allowed to propagate in its original direction. A drawback of this approach is that this small remeshing operation will change the position of the nodes and the shape of all surrounding elements, which, in turn, requires a remapping of the integration points in these elements as well.

stable.

It is worth noting that the aforementioned problem does not occur when the equations are solved using an implicit time integration scheme, such as the multi-step method (Park 1975). This method is unconditionally stable, which implies that there is no restriction to the magnitude of the time step. On the other hand, an implicit scheme requires the solution of a full nonlinear system of equations by means of a Newton-Raphson iteration scheme. Taking into account that the matrix in this system of equations contains stiffness terms that change continuously, the time needed to solve the system increases dramatically, especially when a direct solver is used.

Apart from this, an implicit time integration procedure is only an adequate alternative when the time increment can be chosen sufficiently large, e.g. in cases where high frequency effects are of secondary importance. In the simulation of dynamic crack growth, the propagation of the stress waves plays a major role in the overall fracture behaviour. Since these stress waves propagate through the mesh at the relatively high dilatational speed, the time increment must be chosen very small. In a typical simulation, time increments of the order of magnitude of $\Delta t = 1.0 \cdot 10^{-9}$ s are not uncommon so that the analysis of a specimen in the first $10.0\,\mu$s after impact requires 10 000 time steps. Clearly, under these circumstances, an explicit time integration scheme is preferred.

§ 6.5 Numerical examples

The performance of the explicit cohesive segments method is demonstrated in three numerical examples. First, the propagation of a single crack in a specimen loaded in tension is analysed. In this example, the emphasis is put on the numerical consistency of the method. The second example deals with the propagation of a crack in the classical dynamic shear failure test (Kalthoff and Winkler 1988). Finally, the ability of crack branching is investigated in a bimaterial specimen loaded in tension.

Crack propagation under tension

In the previous section, it was observed that the inclusion of a discontinuity in a finite element model can influence the robustness of the explicit time integration scheme. In the following example, the effects of *extending* a cohesive segment during a simulation is considered. Here, the attention is focused on the energy balance of the system.

Consider the square block with length sides $L = 3\,\text{mm}$ as shown in Figure 6.11. The block is made of PMMA with a Young's modulus $E = 3.24\,\text{GPa}$, Poisson's ratio $\nu = 0.35$ and density $\rho = 1190\,\text{kg/m}^3$ and contains an edge crack that penetrates $a = 0.25\,\text{mm}$ into the material. The block is loaded in tension by two pulse loads that are applied to the top and bottom edges respectively. In the finite element model, these pulses are represented by prescribed velocities with magnitudes $V = 6\,\text{m/s}$. This magnitude is reached after a rise time $t_r = 1.0 \cdot 10^{-7}\,\text{s}$, see equation (6.14). The fracture properties of the material are slightly modified to avoid a small cohesive length and therefore the necessity to use dense finite element meshes. In this simulation, the strength of the material is set to $t_{\max} = 1.0 \cdot 10^8\,\text{N/m}^2$ and the fracture toughness $\mathcal{G}_c = 700\,\text{N/m}$. Because of symmetry, it is assumed that the crack will propagate in a straight line along the x-axis. The initiation criterion is modified such that the cohesive segment is extended when the σ_{yy} stress in the crack tip exceeds the strength $t_{\max}$. The stress state in the tip is determined by using the averaging function (2.44). The averaging length l_a is taken to be two times the element length in the finite element mesh.

The block is analysed with three different finite element meshes that consist of quadrilateral elements only. In the first mesh, the specific length of an element is $l_e = 37.5\,\mu\text{m}$, in the second mesh, which is depicted in Figure 6.12, this length is $l_e = 25.0\,\mu\text{m}$ and in the third mesh $l_e = 12.5\,\mu\text{m}$. In all simulations a timestep $\Delta t = 1.0 \cdot 10^{-9}\,\text{s}$ is used. The initial edge crack is modelled as a traction free cohesive segment. When the segment is extended, its opening is governed by the Camacho-Ortiz cohesive law, see equation (5.30).

Since in this specific case, the trajectory of the crack is known beforehand, a comparative study is performed in which the crack is modelled as a weak interface. In this benchmark calculation, an cohesive segment is inserted over the full width of the specimen at the start of the analysis. The first 0.25 mm

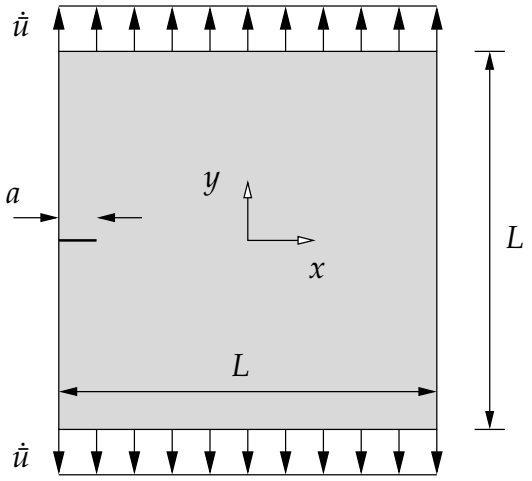

Figure 6.11 Geometry and loading conditions of a square block with an initial side crack.

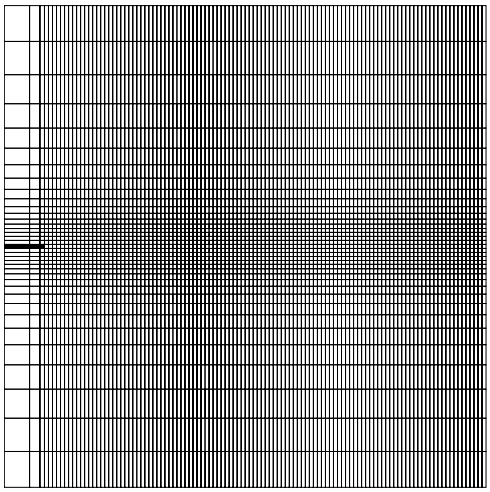

Figure 6.12 Finite element mesh of the square block with an initial side crack, indicated by the bold line. The specific length of the elements in the zone through which the crack will propagate is $l_e = 25.0\,\mu$m.

of this segment are traction free, the remaining part is equipped with Xu-Needleman's cohesive law, see equation (5.25), with the same cohesive properties as mentioned above. Apart from the fact that the cohesive zone in this case has an initial non-zero compliance, the overall behaviour of this model must be nearly identical. However, note that in contrast with the original calculations, no degrees of freedom are added during the simulation in this benchmark model.

The energy variations of the simulations are given in Figure 6.13. In these plots, a distinction is made between the contribution of the bulk material and the cohesive segments to the internal energy $\mathcal{E}_{\text{int}}$:

$$\mathcal{E}_{\text{int}} = \mathcal{E}_{\text{bulk}} + \mathcal{E}_{\text{coh}} \,, \tag{6.21}$$

where $\mathcal{E}_{\text{bulk}}$ is the internal energy of the bulk material, which is defined as:

$$\mathcal{E}_{\text{bulk}}^{t+\Delta t} = \mathcal{E}_{\text{bulk}}^{t} + \frac{1}{2}\Delta t \left(\dot{\mathbf{d}}^{t+\frac{1}{2}\Delta t}\right)^{\text{T}} \left(\mathbf{f}_{\text{bulk}}^{\text{int},t} + \mathbf{f}_{\text{bulk}}^{\text{int},t+\Delta t}\right) \,, \tag{6.22}$$

where $\mathbf{f}_{\text{bulk}}^{\text{int}}$ is the contribution of the *bulk material* to the internal forces, see equation (5.21). For the cohesive segments, a similar relation can be formulated:

$$\mathcal{E}_{\text{coh}}^{t+\Delta t} = \mathcal{E}_{\text{coh}}^{t} + \frac{1}{2}\Delta t \left(\dot{\mathbf{d}}^{t+\frac{1}{2}\Delta t}\right)^{\text{T}} \left(\mathbf{f}_{\text{coh}}^{\text{int},t} + \mathbf{f}_{\text{coh}}^{\text{int},t+\Delta t}\right) \,, \tag{6.23}$$

where $\mathbf{f}_{\text{coh}}^{\text{int}}$ is the contribution of the *cohesive segments* to the internal forces, see (5.21).

Figure 6.13 (a) shows the variations of the total work $\mathcal{W}$, the sum of internal energies $\mathcal{E}_{\text{tot}}$ and the variations of the individual terms $\mathcal{E}_{\text{bulk}}$, $\mathcal{E}_{\text{coh}}$ and $\mathcal{E}_{\text{kin}}$ for the benchmark simulation with a predefined cohesive segment in combination with Xu-Needleman's cohesive relation, i.e. the simulation in which no degrees of freedom are added during the simulation. In this particular figure, the energy variations of the simulation with the dense mesh are shown, but the results with the coarser meshes are nearly identical. Figures 6.13 (b) to (d) show the variations of the simulations with the coarse, medium and dense mesh respectively. It appears that in all four cases, the total internal energy is in good agreement with the external work of the simulations. This can also be seen in Figure 6.14 in which the error tolerances of the four simulations are plotted. In none of the cases ε exceeds the value of 0.01. It can be concluded

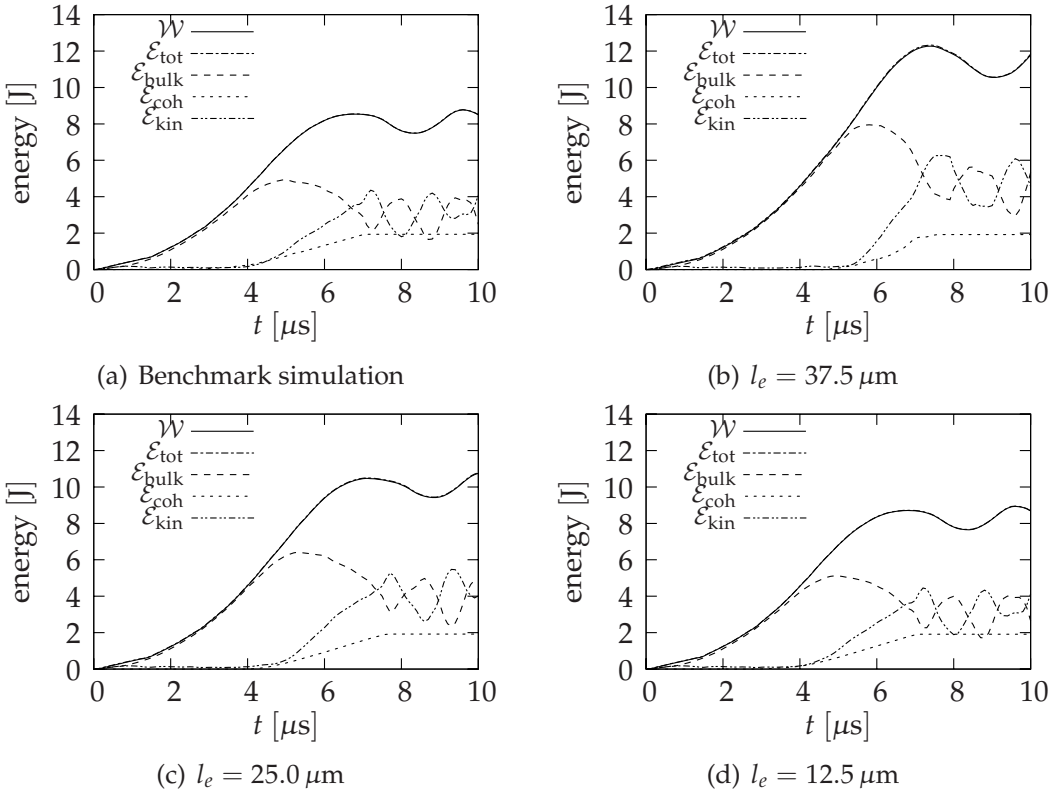

(a) Benchmark simulation

(b) $l_e = 37.5\,\mu$m

(c) $l_e = 25.0\,\mu$m

(d) $l_e = 12.5\,\mu$m

Figure 6.13 Energy variations as a function of time. Figure (a) shows the benchmark simulation with an initial cohesive segment with Xu-Needleman's cohesive relation. The other figures show the calculations with a propagating cohesive segment in meshes with different specific element lengths (b) 37.5 μm, (c) 25.0 μm and (d) 12.5 μm.

that irrespective of the coarseness of the finite element mesh, the creation of new degrees of freedom does not destroy the energy balance. This is a result of the fact that in the cohesive constitutive relation, the value of the strength $t_{\text{n},0}$ is taken to be equal to the the stress state that caused the cohesive segment to propagate. Effects of overshoot are thus cancelled and stress continuity is ensured (Papoulia *et al.* 2003).

Nevertheless, a remarkable difference in the simulations with the coarser meshes can be observed, Figure 6.13 (b) and (c). Here, the total work is significantly larger than the total work in the benchmark simulation (a) and the simulation with the dense mesh (d). This a consequence of the fact that the

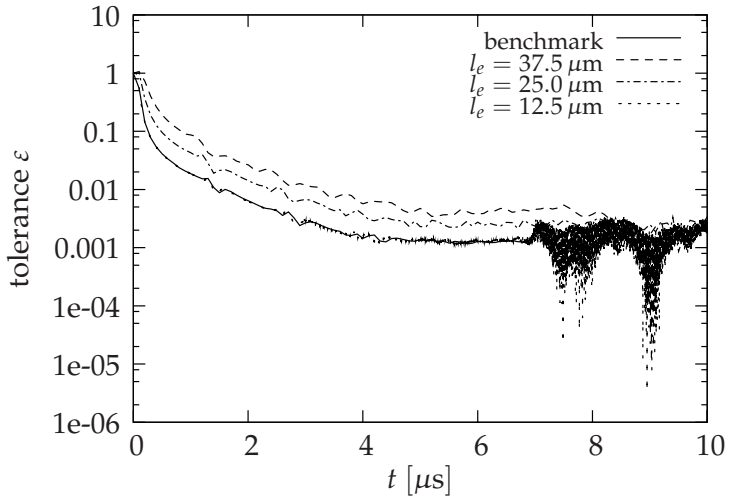

Figure 6.14 Energy tolerances as a function of time for the four simulations of a propagating straight crack through a square block.

averaging length l_a in these simulations is of the same order of magnitude, or even larger, than the cohesive length. As a result, the new segment is extended too late, allowing the bulk material to store too much internal energy prior to crack propagation. This can also be concluded from Figure 6.15 where the position of the crack tip are plotted as a function of time. Here, the position of the crack tip is defined as the first point along the cohesive segment where the tractions have reduced to 5% the value of the strength of the material. In the simulations with the coarser meshes, the crack starts to propagate slightly too late.

Figure 6.16 shows the velocity of the crack tip as a function of time. It can be seen that the crack tip quickly accelerates to arrive at the Rayleigh wave speed of the material, $c_{\mathrm{R}} = 938\,\mathrm{m/s}$, which is in agreement with analytical studies. In this figure, only the graph of the simulation with the densest finite element mesh is shown: the graphs of the simulations with the coarser meshes show extreme velocity peaks. This can be explained by the fact that the elements are too large compared to the length of the cohesive zone. In these situations, the cohesive segment is extended over a few elements in a small period of time (three extensions in three consecutive time steps is not uncommon) and subsequently remains stationary for a longer period.

The coarseness of the mesh does not have an effect on the internal energy

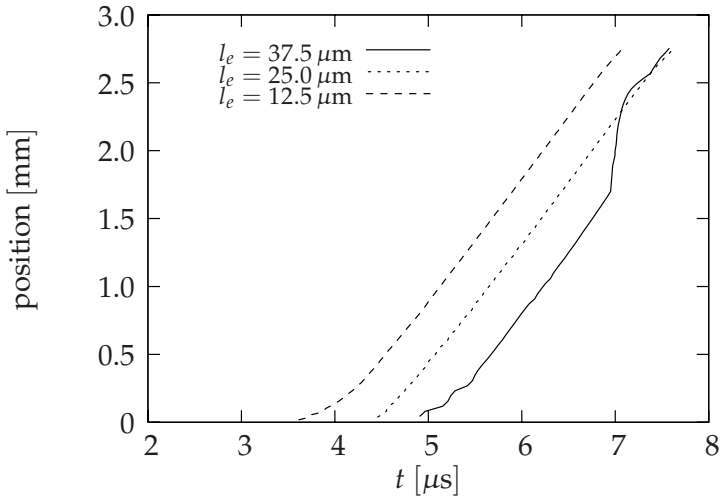

Figure 6.15 Position of the crack tip as a function of time for the four simulations of a propagating straight crack through a square block.

dissipated by the cohesive segment. In all simulations with a propagating segment, the final value of the cohesive internal energy $\mathcal{E}_{\text{coh}}$, when the crack has completely crossed the specimen is equal to $\mathcal{E}_{\text{coh}} = 1.92\,\text{J}$, which is exactly identical to the length of the crack, 2.75 mm times the fracture toughness of the material $\mathcal{G}_c = 700\,\text{N/m}$. In the benchmark simulation, with a initial cohesive segment, this value is slightly bigger, $\mathcal{E}_{\text{coh}} = 1.93\,\text{J}$, which is probably due to the fact that prior to cracking, the cohesive zone, with its initial non-zero compliance, already contributes to the internal energy.

The stress distribution and the deformed mesh are shown in Figure 6.17. In this picture, the results of the simulation with a propagating cohesive segment in a finite element mesh with $l_e = 12.5\,\mu$m are depicted.

Dynamic shear failure

An experimental set-up for subjecting edge cracks in plate specimens to high rate shear loading has been proposed by Kalthoff and Winkler (1988) and related configurations have been used subsequently in a variety of investigations, e.g. (Mason *et al.* 1994) and (Ravi-Chandar 1995). At sufficiently high rates of loading, fracture in this configuration takes place by cleavage cracking at an angle of approximately 60° to 70° with respect to the initial crack. This

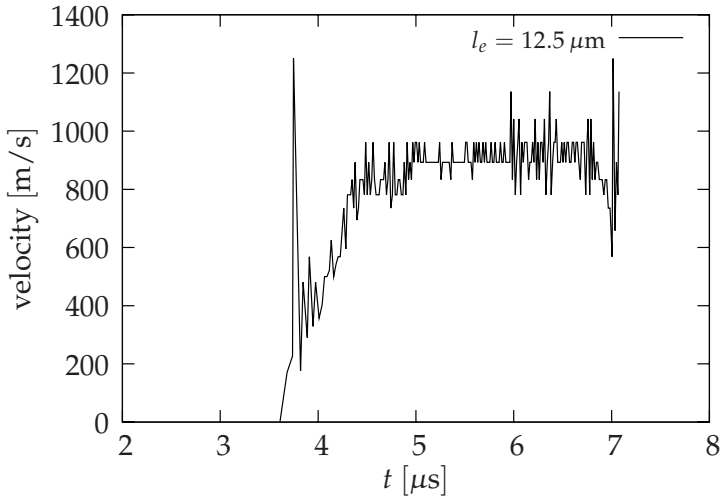

Figure 6.16 Velocity of the crack tip as a function of time for the simulation with the $l_e = 12.5\,\mu$m.

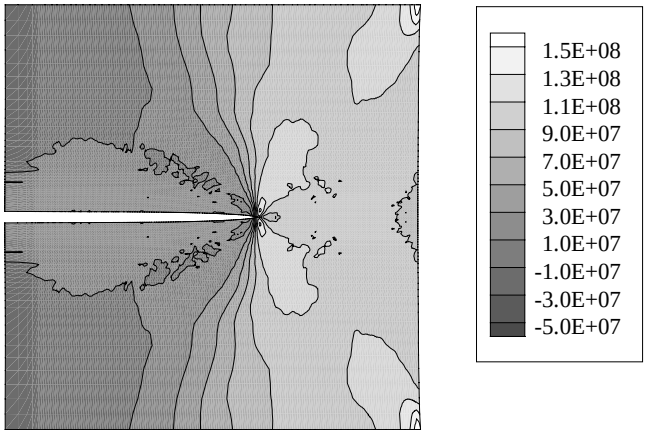

Figure 6.17 The deformed specimen and the σ_{yy} stress distribution at $t = 5.0\,\mu$s for the simulation with a propagating cohesive segment $l_e = 12.5\,\mu$m.

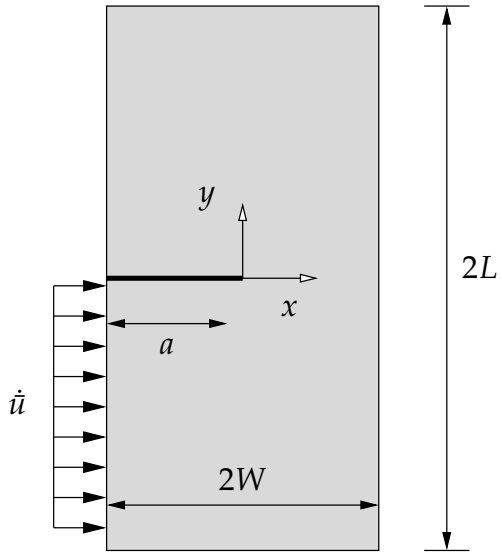

Figure 6.18 Geometry and loading conditions of the specimen for the dynamic shear failure test.

type of failure has been modelled by Needleman and Tvergaard (1995) and Li *et al.* (2002). At higher impact velocities, the crack propagates as an adiabatic shear band at an angle of approximately -5° with respect to the original crack (Kalthoff and Bürgel 2004). Here, we explore the use of the cohesive segments method to analyse the configuration shown in Figure 6.18.

The specimen in the figure has dimensions $L = 0.003\,\mathrm{m}$ and $W = 0.0015\,\mathrm{m}$ and has an initial crack with length $a = 0.0015\,\mathrm{m}$. It is made of an isotropic linear elastic material with Young's modulus $3.24 \cdot 10^9\,\mathrm{N/m^2}$, Poisson's ratio 0.35 and density $\rho = 1190.0\,\mathrm{kg/m^3}$. The corresponding dilatational, shear and Rayleigh wave speeds are $c_\mathrm{d} = 2090\,\mathrm{m/s}$, $c_\mathrm{s} = 1004\,\mathrm{m/s}$ and $c_\mathrm{R} = 938\,\mathrm{m/s}$, respectively. The ultimate normal traction of the material is set to $100.0 \cdot 10^6\,\mathrm{N/m^2}$ and the fracture toughness is $700\,\mathrm{N/m}$. The lower part of the specimen is subjected to an impulse load in the positive $x-$direction which is modelled as a prescribed velocity with magnitude V with a rise time $t_r = 0.1\,\mu\mathrm{s}$, see equation (6.14).

The specimen is discretised using quadrilateral elements. In the region around the crack tip, the mesh is locally refined such that the specific length of the elements equals $l_e = 15.0\,\mu\mathrm{m}$, see Figure 6.19. According to equation (6.20), the time increment is set to $\Delta t = 1.0 \cdot 10^{-10}\,\mathrm{s}$. At the start of the

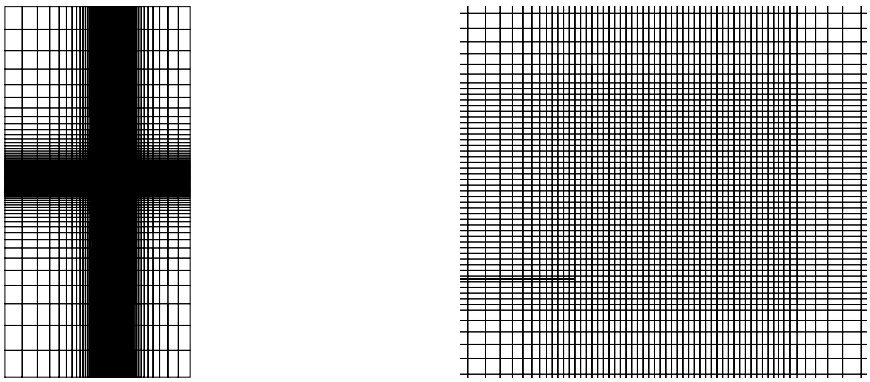

(a) Full mesh (b) Detail of crack tip region

Figure 6.19 Finite element mesh of the dynamic shear failure experiment. The initial crack is modelled as a cohesive segment, which is denoted by the bold line. The specific length of the elements ahead of the crack tip is $l_e = 15.0\mu$m.

simulation, the model contains 11587 degrees of freedom. The initial crack is modelled as a traction free discontinuity and therefore, in contrast with the simulations done by Needleman and Tvergaard (1995), the crack tip is sharp. The possibility of crack nucleation away from the main crack tip is not taken into account.

The specimen is loaded with three different impact velocities profiles $\bar{u}$, see equation (6.14), with maximum values $V = 25$, $V = 40$ and $V = 55\,\mathrm{m/s}$. In all cases, the rise time is taken $t_r = 1.0 \cdot 10^{-7}$. The trajectories of the cracks are shown in Figure 6.20. The corresponding positions of the crack tips as a function of time are shown in Figure 6.21. In this graph, the position of the crack tip is the sample point on the cohesive segment that has just become traction free. Clearly, this point is not the same as the actual tip of the cohesive segment.

In the case of the $V = 25\,\mathrm{m/s}$ impact loading, the cohesive segment is extended for the first time at $t = 3.01\,\mu$s at an angle of roughly 65°, which is in agreement with experimental observations (Kalthoff and Winkler 1988). At $t \approx 3.7\,\mu$s the propagation of the crack slows down and the orientation

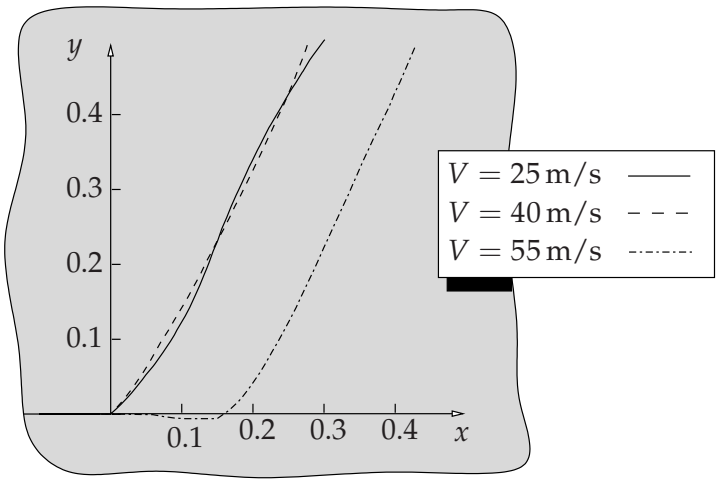

Figure 6.20 The trajectory of the cracks in the dynamic shear failure simulation for different impact velocities. The original crack tip was located at the origin of the coordinate system. All dimensions in millimetres.

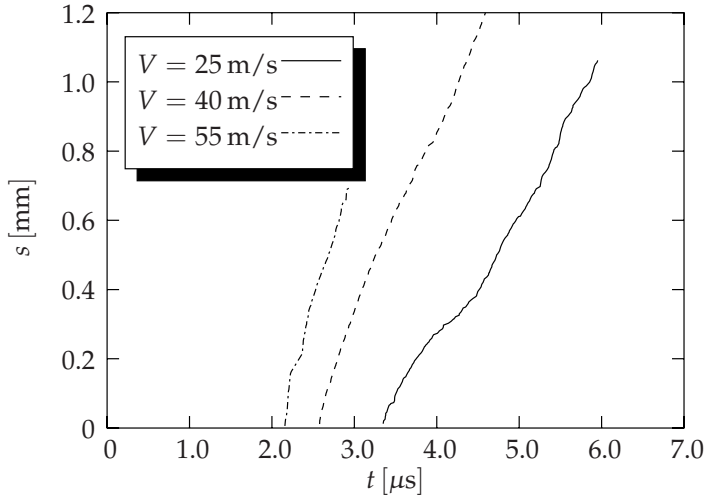

Figure 6.21 Crack length s versus time for different impact velocities. Distance s is measured with respect to the original crack tip.

of the trajectory changes to 50°. This small deviation is caused by one of the reflections of the initial compressive stress wave which travels through the specimen in the horizontal direction at the dilatational speed c_{d}. At approximately 3.7 μs after impact, this stress waves passes the region just to the right of the original crack tip for the third time. The additional compressive stress changes the stress state at the current crack tip and therefore the angle of the principal stress. Once this wave has passed, the crack trajectory continues at an angle of approximately 65°. Figure 6.22 shows the position of the crack and the corresponding stress contours at various instances during the simulation.

When the impact load is 40 m/s, the trajectory of the crack is almost a straight line. Apparently, the direction of the crack is less influenced by reflecting stress waves. When the specimen is loaded by an impact load of 55 m/s, the crack will not propagate as a cleavage crack at an angle of 70° but as an adiabatic shear crack. However, in the current model, the bulk material is assumed to be linear elastic, which means that no energy is dissipated and the adiabatic shear band is not sustained.

Figure 6.22 shows the deformed specimen and the σ_{xx} stress distribution at the end of the simulation for the three different loading cases. Note that in the simulation with an impact velocity $V = 55\,\mathrm{m/s}$, the initial crack has a negative normal normal displacement jump. This could have been avoided by extending the initial traction free discontinuity with a contact cohesive law. However, since the shear jump displacements in this region are of the order of 10 times the element length l_e, the use of such a contact algorithm is no longer correct from a physical point of view.

Crack growth along an interface

The specimen in Figure 6.23 consists of two parts with different elastic material properties that are bonded along $y = 0$ with a centre crack along the bond line. The dimensions of the specimen are $2W = 12\,\mathrm{mm}$ and $2L = 6\,\mathrm{mm}$. The centre crack measures $2a = 2\,\mathrm{mm}$. The top and bottom edges of the specimen are subjected to impact loads that are modelled as prescribed velocities that increase linearly to a value $V = 20\,\mathrm{m/s}$ with a rise time $t_r = 10^{-7}\,\mathrm{s}$.

The top part of the specimen is made of a material with Young's modulus $E = 3.24 \cdot 10^9\,\mathrm{N/m^2}$. The Poisson's ratio is $\nu = 0.3$ and the density

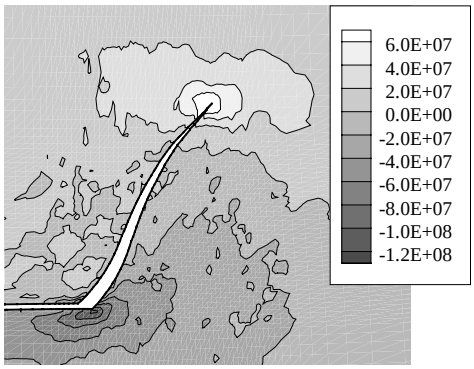

(a) $V = 25\,\mathrm{m/s},\ t = 4.8\,\mu\mathrm{s}$

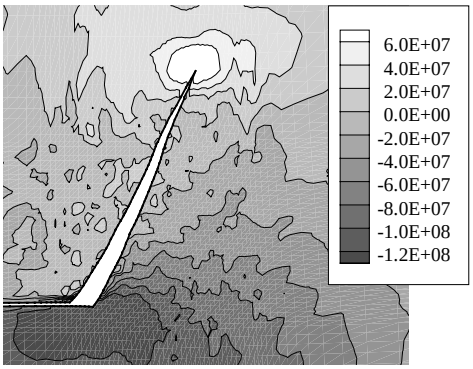

(b) $V = 40\,\mathrm{m/s},\ t = 3.6\,\mu\mathrm{s}$

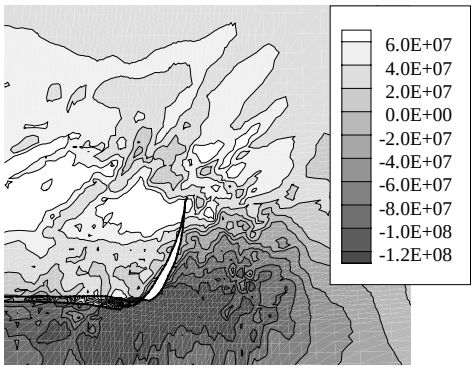

(c) $V = 55\,\mathrm{m/s},\ t = 2.56\,\mu\mathrm{s}$

Figure 6.22 Deformed specimen and σ_{xx} stresses of the dynamic shear failure experiment under different impact velocities V. All stresses in $[\mathrm{N/m^2}]$.

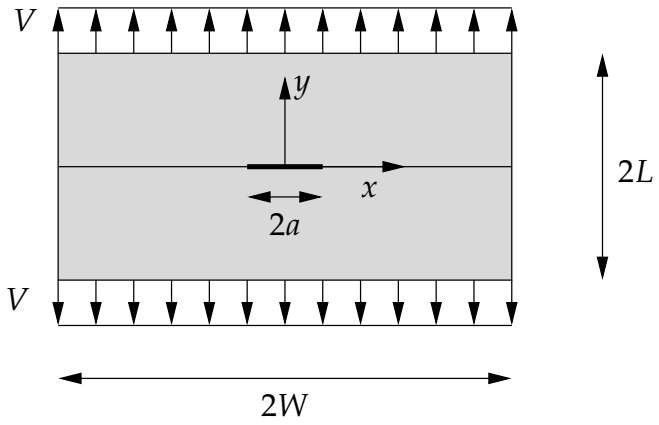

Figure 6.23 Geometry and loading conditions of the interface crack growth specimen.

is $\rho = 1190\,\mathrm{kg/m^3}$. The material properties of the lower part are: $E = 12.2 \cdot 10^9\,\mathrm{N/m^2}$, $\nu = 0.3$ and $\rho = 1190\,\mathrm{kg/m^3}$, respectively. The interface is represented by a cohesive segment with Xu-Needleman's constitutive relation with $t_{\max} = 3.24 \cdot 10^8\,\mathrm{N/m^2}$ and $\mathcal{G}_c = 700\,\mathrm{N/m}$. At the initially debonded part, a traction free constitutive relation is used. In the simulation, cracks are allowed to nucleate in the top part of the specimen. Here, the fracture properties are $t_{\max} = 410 \cdot 10^6\,\mathrm{N/m^2}$ and $\mathcal{G}_c = 700\,\mathrm{N/m}$.

Because of symmetry along the y-axis, only one half of the specimen is modelled. The relatively coarse mesh consists of 39×39 four node elements, the time step chosen to be $\Delta t = 1.0 \cdot 10^{-9}$ s.

Upon loading, after approximately $t = 2.0\,\mu$s, the interface starts to debond, see Figure 6.24 (a). The stress state around the crack tip soon builds up to a level such that a new cohesive segment nucleates in the top half of the specimen, Figure 6.24 (b). This segment crosses the interface at an angle of approximately 65° with the interface. According to the implementation as described in the previous chapter, this new segment has a finite length of two elements. During the creation and opening of this branch, the debonding of the interface arrests. However, the new cohesive segment is not extended and the branch seems to arrest. Instead, after some time, the interface starts to debond away from the branch position as a so-called daughter crack, similar to the fracture patterns in (Coker *et al.* 2003), Figure 6.24 (c). After 3.3 μs the interface has completely debonded and the specimen has lost its load carrying capability.

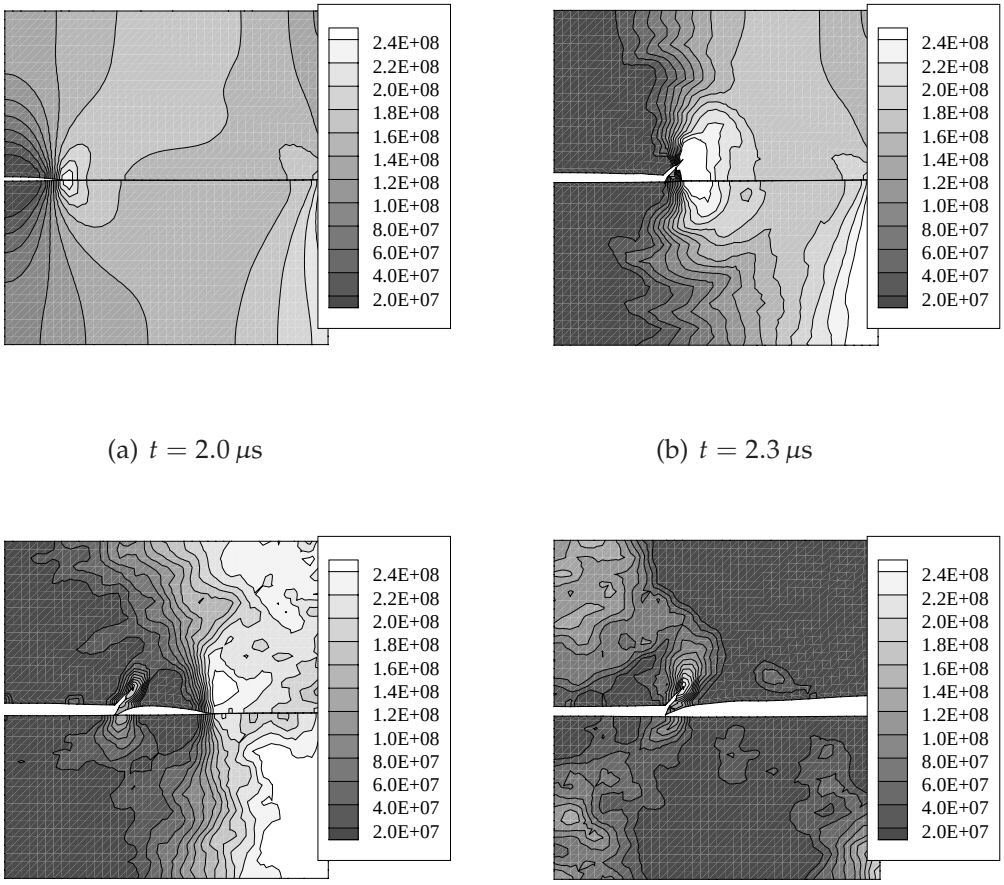

(a) $t = 2.0\,\mu$s

(b) $t = 2.3\,\mu$s

(c) $t = 2.8\,\mu$s

(d) $t = 3.3\,\mu$s

Figure 6.24 Evolution of fracture in the bi-material specimen. The colour gradient represents the σ_{yy} stresses $[\mathrm{N/m^2}]$. (a) Onset of debonding at the interface. (b) Creation of a new cohesive segment in the bulk material. This new segment is created at an angle of 68° with respect to the interface. (c) Continuation of debonding of the interface as a daughter crack ahead of the current crack tip. (d) Total failure of the specimen.

A mesh refinement study reveals that the reason that the branch arrest is not a physical one, but is related to a flaw in the numerical model. Both the nucleation of a crack, as well as its extension, are controlled by the same criterion. However, in order to arrive at a reliable stress state in the tip of a cohesive segment, the stresses are determined by averaging the stresses in the vicinity using equation (2.45). As a result, the corresponding tip stress is slightly lower than the actual local stress and a higher stress state is needed to extend a segment. The nucleation of a new cohesive segment however, is determined by the exact stress state in an integration point the bulk material.

In dynamic simulations, the instant of crack propagation appears to be an important factor. In the case of two competing cracks, as displayed in this example, the slight unbalance in propagation criterion can result in the spurious arrest of a crack that is expected to propagate.

§ 6.6 Conclusions

In this chapter, the cohesive segments method has been used to simulate fast crack propagation in brittle solids. Special attention is paid to the implementation of the method in a Newmark-β explicit time integration scheme. An important conclusion is that, in contrast to more traditional finite element models, it is not possible to lump the mass matrix to decrease the computational effort needed to solve the system of equations. When a Heaviside jump function is used, spurious transfer of tractions has been observed. This phenomenon disappears when the Heaviside function is replaced by a unit-symmetric jump function. However, from an energetic point of view, the numerical results still showed small deviations.

Additional studies showed that adding degrees of freedom during a simulation, does not affect the energy conservation. Even in the case of relatively coarse meshes, the internal and kinetic energy of the system sums up to the total external work.

The fine qualities of the cohesive segments method are demonstrated in the dynamic shear test. For modest impact velocities, the crack propagates at an angle of approximately 70° with the initial crack, which is in agreement with various experimental observations and analytical studies. Even small deviations of this trajectory due to reflecting stress waves are captured. The

adiabatic shear crack, which is observed under high impact velocities, is obtained as well.

The criterion that is used to calculate the stress state at the tip of a segment is still a point of concern. Due to stress averaging, it is not possible to determine the exact impact velocity that marks the failure mode transition in the dynamic shear test. It also hampers a quantitative analysis in the case of multiple, interacting cracks, as shown in the final example. Here, the creation of a new, deviating crack was captured well. However, it is not clear if this crack arrested for physical reasons, or because of the ill-posedness of the crack propagation algorithm.

Chapter 7

Finite strain discrete dislocation plasticity

The fracture characteristics of brittle materials are determined by the nucleation, growth and coalescence of micro-separations in the process zone. The heterogeneity of the material on the microscopic level of observation plays an important role, as well as imperfections. The cohesive segments method, which has been developed in the previous chapters, is able to simulate these different aspects in a mesh-independent way.

There is a class of materials in which an additional mechanism plays an important role in the overall fracture behaviour. In crystalline solids, a considerable amount of energy is dissipated by plastic deformation of the material. At relatively low stress levels, the collective motion of dislocations, often denoted as slip, influences the fracture process in two ways. First, due to the plastic flow, the stress intensity in the process zone is reduced significantly, slowing down the fracture process. On the other hand, when multiple dislocations leave the material at a free surface, they create small imperfections. These imperfections can give rise to local stress concentrations and become a new site for micro-crack nucleation.

In conventional continuum plasticity models, the glide of individual dislocations in materials is neglected. By smearing out the effect of the slip in the bulk material's constitutive relation, the interaction between plastic flow and the fracture process is lost. Additionally, continuum plasticity models suffer from a similar deficiency as continuum damage models: they fail to predict the exact size of the plastic zone.

Since the late 1980s considerable activity has been directed at representing plastic flow on a nanoscopic level of observation in terms of the dynamics of large numbers of interacting dislocations. In the discrete dislocation formulation by Devincre and Kubin (1994) and van der Giessen and Needleman (1995) dislocations are represented as line singularities in an elastic solid. The displacements and stresses due to dislocations are obtained by an analytical solution for an infinite medium (Hirth and Lothe 1982). In order to compensate for the finite dimensions of the specimen and the boundary and loading conditions, a complementary finite element solution is added. Additional constitutive laws that describe dislocation glide, pinning at obstacles and annihilation enable to predict the collective motion of dislocations. The framework accounts for both stress enhancement due to organised dislocation structures and stress relaxation arising from dislocation glide. Recently, the model has been used in combination with cohesive zone formulations to simulate the interaction between plastic flow and (fatigue) crack growth (Cleveringa *et al.* 2001, Deshpande *et al.* 2003a).

The discrete dislocation plasticity framework however is restricted to infinitesimal deformations. As a result, the effect of lattice reorientation on the dislocation glide and the effect of geometry changes on the momentum balance are not taken into account. Moreover, the creation of new surfaces when dislocations leave the specimen is neglected, which hampers the simulation of crack nucleation at free surfaces.

In order to solve the first problem, Deshpande *et al.* (2003b) have developed a finite strain discrete dislocation plasticity model. Here, the finite element model is based on a large displacement kinematic description. The additional dislocation stress field is determined analytically with respect to the deformed configuration and added in an incremental fashion. Due to the change of geometry, the model naturally accounts for the reorientation of the slip planes.

Because of dislocation glide, the total displacement field that is used in the updated Lagrange algorithm is only piece-wise continuous, as shown in Figure 7.1 (b). In the current finite strain dislocation model however, this jump in the displacement field is neglected and smeared out on the element level, which gives rise to deformations as shown in Figure 7.1 (c). Consequently, the deformation gradient, which is derived from the nodal displacements, is

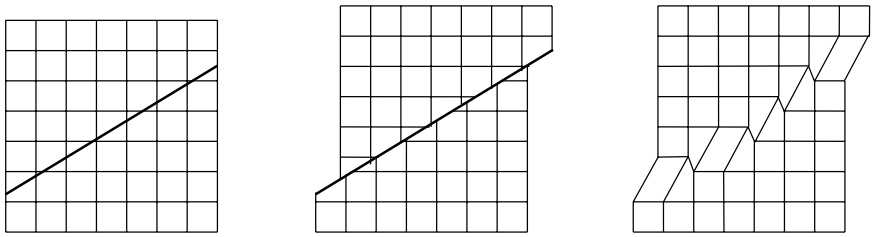

Figure 7.1 (a) Undeformed lattice with one active slip plane. (b) Geometry change due to slip discontinuity across the active slip plane. (c) Effect of smearing slip on a finite element mesh.

overestimated. Apart from the fact that this introduces a numerical error, the model fails to converge when the smeared deformation gradient becomes too large. Additionally, neglecting the displacement jumps at slip planes avoids the creation of new surfaces at the free edges when dislocations leave the material.

In the light of the previous chapters, the partition of unity property of finite element shape functions would be an ideal candidate to introduce the discontinuity in the finite element mesh. The singular displacement field generated by a line dislocation can be incorporated in the numerical displacement field by enhancing the existing nodes of the finite element mesh. In (Ventura *et al.* 2005) such an implementation is presented for a small strain discrete dislocation model. Here, the displacement and stress fields are embedded in the kinematic relations of the finite element model. By using the appropriate constitutive relations for the nucleation and glide of individual dislocations, the complete problem is specified by a single boundary value problem.

This approach has certain prospects, but in the current implementation by Ventura *et al.* (2005) there are some disadvantages. The displacement field of a single dislocation decays with the order of reciprocal distance. In other words, the influence of a dislocation is observed far away from its position in the domain. In the partition of unity framework, this implies that all nodes should be enhanced in order to represent the contribution to the displacement field of a single dislocation field exactly. Taking into account that in a typical simulation hundreds of dislocations can be active, it is obvious that the computational overhead is very large. Moreover, since dislocations con-

stantly move through the specimen, their positions, and therefore their nodal enhancement functions, must be updated after each time step. Finally, the resolution of the finite element mesh is too low to capture the large strain gradient in the vicinity of a dislocation core. In principle, these gradients can be captured by adding the correct, singular base functions, but the numerical integration of the elements remains a point of concern. No matter how many integration points are used, the strain gradients will be smeared out to a certain extend. Since the glide of a dislocation is partly a function of the stress field generated by the other dislocations, it is obvious that small deviations of these stress fields may alter the behaviour of a dislocation. When dislocations are relatively close, e.g. in the case of a pile-up near an obstacle or a grain boundary, the effect of the errors in the stress fields becomes significant.

In this chapter, an alternative approach for the simulation of discrete dislocation plasticity in a finite strain framework is presented. The approach is based on the original idea by van der Giessen and Needleman (1995). The displacement and stress fields are described by analytical relations (Nabarro 1967). A complementary boundary value problem, the finite element solution, is used to correct for the appropriate boundary and loading conditions. As opposed to the small strain formulation, both the analytical and the complementary problem are cast in a rate form and projected on the current, deformed configuration of the specimen. The key feature of the proposed model is that in the kinematic formulation, the contribution of the displacement jump due to slip in this deformed configuration is separated from the total deformation gradient in the kinematic formulation.

After a description of the kinematic relations, the equilibrium equations are presented. The chapter concludes with some remarks on the implementation of the method in a finite element code and some future prospects.

§ 7.1 Kinematic relations

The finite strain discrete dislocation model that is presented in this chapter, is based on the same kinematical framework as used in the original small strain model by van der Giessen and Needleman (1995). The total stresses and the strains of the body are written as the superposition of singular analytical fields, containing the contributions of discrete dislocations, and complemen-

tary numerical fields that enforce the boundary conditions. In a small strain formulation, the undeformed and the deformed configuration coincide and as a results, the two fields may be added.

In a finite strain formulation however, the superposition principle does no longer hold. Here, the mutual positions of the discrete dislocations depend on the total deformation of the body. The stress and strain fields that are generated by these discrete dislocations can only be expressed in rate form, related to the current configuration of the body according to an updated Lagrangian integration scheme (Deshpande *et al.* 2003b).

Consider a crystalline solid with plastic deformation taking place by glide of a collection of discrete dislocations along a specified set of crystallographic directions, the so-called slipsystems. The total deformation is composed of the summation of the singular fields of all dislocations and the complementary numerical deformation. As in continuum crystal plasticity models, a distinction is made between deformation of the lattice and deformation of the material. At each material point, a set of three orthonormal vectors define the orientation of the lattice. Stress is related to the deformation of the lattice by an elastic constitutive relation. The basic assumptions are: (i) dislocation glide is the only mechanism that gives rise to plastic deformation; (ii) the elastic properties are unaffected by dislocation glide and (iii) outside the dislocation cores, the dislocation stress, strain and displacement fields are well approximated by linear elasticity. All finite deformations arise as a consequence of the displacement jumps induced by dislocation glide. These displacement jumps lead to lattice rotations that may be finite. Hence, the finite deformation effects that the formulation aims to capture are those due to deformation-induced lattice rotations and the change in shape of the body due to slip. Additional phenomena that may be involved in finite plastic deformation, such as modified elastic properties, finite lattice strains and dislocation mobility mechanisms other than slip, are not accounted for.

Both the original undeformed state as well as the current deformed configuration are represented in the same rectangular Cartesian coordinate system. Let $\mathbf{X}$ be the position of a material point in the undeformed configuration. The position of this point in the deformed configuration $\mathbf{x}$ is then:

$$\mathbf{x}(\mathbf{X}, t) = \mathbf{X} + \hat{\mathbf{u}}(\mathbf{X}, t) + \tilde{\mathbf{u}}(\mathbf{X}, t)\,, \tag{7.1}$$

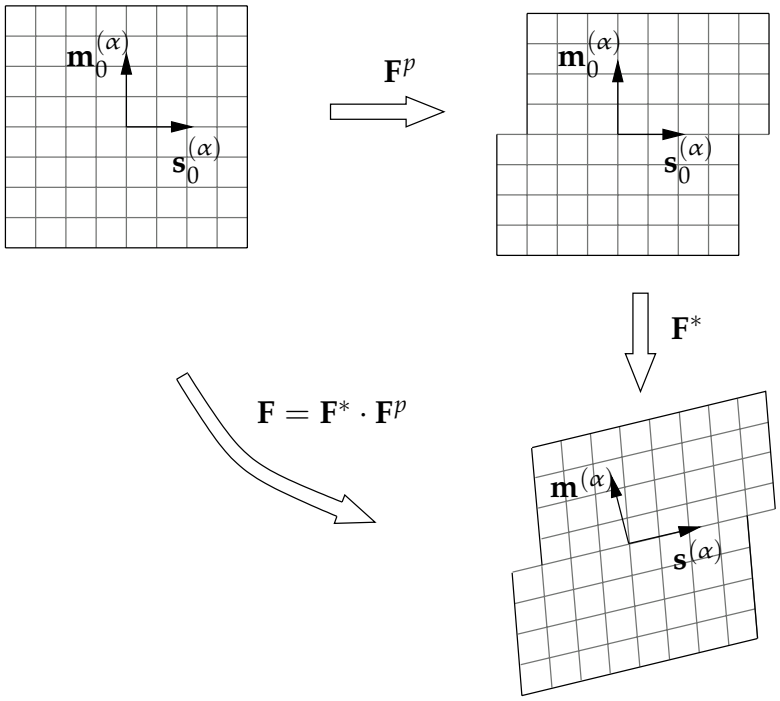

Figure 7.2 The total deformation of the body can be expressed in terms of the slip due to dislocation glide $\mathbf{F}^p$ and the elastic deformation of the lattice $\mathbf{F}^*$. The grid on the body represents the structure of the material. For the sake of clarity, only one slip system is pictured.

where $\hat{\mathbf{u}}(\mathbf{X}, t)$ is the displacement of the material point in the numerical mirror field and $\tilde{\mathbf{u}}(\mathbf{X}, t)$ is the total analytical displacement of this point due to the dislocations.* It should be noted that since the analytical displacement field will only be used in rate form, projected on the deformed configuration, the total value of $\tilde{\mathbf{u}}$ is never known exactly.

At any stage of the deformation history, the total deformation of the material is completely described by the deformation gradient $\mathbf{F}$, see Figure 7.2. The deformation gradient $\mathbf{F}$ is defined as:

$$\mathbf{F} = \frac{\partial \mathbf{x}(\mathbf{X}, t)}{\partial \mathbf{X}} = \nabla_{\mathbf{X}} \mathbf{x}\,, \tag{7.2}$$

*In this derivation, the 'hat' symbol ($\hat{}$) and the 'tilde' symbol ($\tilde{}$) have a different meaning than in the previous chapters. Historically, the symbols are used in partition of unity related as well as discrete dislocation related publications. In order to avoid the introduction of alternative symbols, the standard conventions have been adopted.

where $\nabla_{\mathbf{X}}$ is the differential operator that takes the spatial derivative with respect to the *undeformed* configuration. In the remainder of this chapter, this operator will simply be denoted as $\nabla_{\mathbf{X}} = \nabla$. Each increment of deformation consists of two parts as shown schematically in Figure 7.2. First, the material slips on the currently active slip planes. These slips do not affect the orientation or structure of the crystal lattice and are described by a deformation gradient $\mathbf{F}^p$. Since the bulk material will not deform due to slip, this deformation gradient is equal to the unit tensor $\mathbf{I}$ at all material points except for material points that reside on the dislocation slip traces where $\mathbf{F}^p$ is unbounded. Second, the lattice and material deform together, the elastic response of the lattice and any rigid body rotations are realised. This deformation is denoted by $\mathbf{F}^*$. Note that the deformation gradient $\mathbf{F}^*$ consists of both terms from the numerical 'hat' fields ($\hat{}$) as well as the continuous part of the analytical 'tilde' fields ($\tilde{}$) due the discrete dislocations. The total deformation gradient of the body can be written as, see Figure 7.2:

$$\mathbf{F} = \mathbf{F}^* \cdot \mathbf{F}^p \,. \tag{7.3}$$

At time t the body contains K edge dislocations which are moving with respect to the material with velocities $\mathbf{v}^{(I)}$, where I indicates the dislocation number: $I = 1, \ldots, K$. The change in position of a dislocation gives rise to a displacement rate field $\dot{\tilde{\mathbf{u}}}^{(I)}$. The total displacement rate field at time t of the body is written as the superposition:

$$\dot{\mathbf{u}}(\mathbf{x}, t) = \dot{\hat{\mathbf{u}}}(\mathbf{x}, t) + \dot{\tilde{\mathbf{u}}}(\mathbf{x}, t), \tag{7.4}$$

where $\dot{\hat{\mathbf{u}}}(\mathbf{x}, t)$ is the displacement rate of the numerical field that arises from satisfying the boundary conditions and $\dot{\tilde{\mathbf{u}}}(\mathbf{x}, t)$ is the sum of displacement rates generated by all dislocations:

$$\dot{\tilde{\mathbf{u}}}(\mathbf{x}, t) = \sum_{I=1}^{K} \dot{\tilde{\mathbf{u}}}^{(I)}(\mathbf{x}, t) \,. \tag{7.5}$$

The displacement rate $\dot{\tilde{\mathbf{u}}}^{(I)}$, which contains singular terms along the trace of dislocation I, can be determined numerically, according to:

$$\dot{\tilde{\mathbf{u}}}^{(I)}(\mathbf{x}, t) = \frac{\tilde{\mathbf{u}}^{(I)}(\mathbf{x}, t) - \tilde{\mathbf{u}}^{(I)}(\mathbf{x}, t - \Delta t)}{\Delta t} \,, \tag{7.6}$$

where $\tilde{\mathbf{u}}^{(I)}$ is the displacement field generated by dislocation I.

The stretching and rotation of the lattice of the material $\mathbf{F}^*$ at time t is obtained in an incremental fashion:

$$\mathbf{F}^*(t) = \mathbf{I} + \nabla_{\mathbf{X}}\hat{\mathbf{u}}(t) + \int_{\tau=0}^{t} \nabla_{\mathbf{x}}\dot{\hat{\mathbf{u}}}(\tau) \cdot \mathbf{F}^*(\tau)\mathrm{d}\tau, \tag{7.7}$$

where $\nabla_{\mathbf{x}}$ is the spatial differential operator with respect to the *current* configuration $\partial(\cdot)/\partial\mathbf{x}$. Thus, $\nabla_{\mathbf{x}}\dot{\hat{\mathbf{u}}}$ is the displacement rate gradient not including the slip contribution, which is obtained by the analytical differentiation of the combined displacement rate field of the dislocations $\dot{\tilde{\mathbf{u}}}$. The total displacement of the mirror field $\hat{\mathbf{u}}(t)$ is obtained by the integration of the corresponding displacement rate with respect to time:

$$\hat{\mathbf{u}}(t) = \int_{\tau=0}^{t} \dot{\hat{\mathbf{u}}}\mathrm{d}\tau\,. \tag{7.8}$$

Note that since the stretch in the material is assumed to be small compared to the deformation due to slip, it is allowed to take the Jacobian of the deformation gradient equal to $J = \det(\mathbf{F}^*) \approx 1$. As a result, the deformation gradient of the crystal lattice $\mathbf{F}^*$ can be assumed to be identical to its rotation: $\mathbf{F}^* \approx \mathbf{R}^*$.

Additionally, the corresponding rate of deformation $\hat{\mathbf{D}}$ of the numerical field is defined, which is the symmetric part of the velocity gradient:

$$\hat{\mathbf{D}} = \frac{1}{2}\left(\nabla\dot{\hat{\mathbf{u}}} + \nabla\dot{\hat{\mathbf{u}}}^{\mathrm{T}}\right) \tag{7.9}$$

The material consists of a set of crystallographic planes in which the edge dislocations reside and glide. In the undeformed configuration, the unit normal to slip plane α is denoted by $\mathbf{m}_0^{(\alpha)}$ and $\mathbf{s}_0^{(\alpha)}$ is a unit vector in this slip plane such that $\mathbf{s}_0^{(\alpha)} \times \mathbf{m}_0^{(\alpha)}$ is a unit vector pointing out of the plane, see Figure 7.2. The current orientations of these vectors, which are denoted by $\mathbf{s}^{(\alpha)}$ and $\mathbf{m}^{(\alpha)}$ respectively, are obtained by:

$$\mathbf{s}^{(\alpha)} = \mathbf{F}^* \cdot \mathbf{s}_0^{(\alpha)}\,; \qquad \mathbf{m}^{(\alpha)} = \mathbf{F}^* \cdot \mathbf{m}_0^{(\alpha)}. \tag{7.10}$$

Due to lattice curvature, $\mathbf{s}^{(\alpha)}$ and $\mathbf{m}^{(\alpha)}$ vary with position. Also, we define a unit vector $\mathbf{r}^{(I)}$ such that

$$\mathbf{r}_0^{(I)} = \mathbf{F}^{*-1} \cdot \mathbf{r}^{(I)}\,, \tag{7.11}$$

where $\mathbf{r}^{(I)}$ is a unit vector in the direction of the velocity $\mathbf{v}^{(I)}$ of dislocation I.

In equation (7.3), the term $\mathbf{F}^p$ describes the deformation due to a discrete set of slip traces, which are created by the gliding dislocations. Each dislocation I creates a trace $\Gamma^{(I)}$ from the position of the source it nucleated from to its current position in the domain. The trace represents the jump in the displacement field with the magnitude of a Burgers' vector. Thus, $\mathbf{F}^p$ is equal to the unit tensor $\mathbf{I}$ at all material points except for the ones along the slip traces $\Gamma^{(I)}$, where:

$$\mathbf{F}^p|_{\Gamma^{(I)}} = \mathbf{I} + \lim_{h\to 0} \frac{|\mathbf{b}^{(I)}|}{h} \mathbf{s}^{(\alpha)} \mathbf{m}^{(\alpha)} \text{sign}\left(\mathbf{b}^{(I)} \cdot \mathbf{r}^{(I)}\right), \tag{7.12}$$

where $\mathbf{b}^{(I)}$ is the Burgers' vector of dislocation I on slip system α with length $|\mathbf{b}^{(I)}|$ and h is a width along the slip segment normal $\mathbf{m}^{(\alpha)}$. When the width of the band around the trace is decreased to zero, $\mathbf{F}^p$ is unbounded.* The Burgers' vector $\mathbf{b}^{(I)}$ of dislocation I in the current configuration is related to its Burgers' vector $\mathbf{b}_0^{(I)}$ in the undeformed configuration via:

$$\mathbf{b}^{(I)} = \mathbf{F}^* \cdot \mathbf{b}_0^{(I)}. \tag{7.13}$$

§ 7.2 Equilibrium equations

The total stress in a material point can be written in terms of the Kirchhoff stress $\boldsymbol{\tau}$ as a superposition:

$$\boldsymbol{\tau} = \hat{\boldsymbol{\tau}} + \tilde{\boldsymbol{\tau}}. \tag{7.14}$$

In this equation, $\hat{\boldsymbol{\tau}}$ denotes the numerical stress field that enforces the boundary conditions and $\tilde{\boldsymbol{\tau}}$ is the sum of the analytically known stress fields of dislocations I:

$$\tilde{\boldsymbol{\tau}} = \sum_{I=1}^{K} \tilde{\boldsymbol{\sigma}}^{(I)}. \tag{7.15}$$

The weak formulation of the linear moment balance is equal to:

$$\int_\Omega \nabla_{\mathbf{x}} \delta\hat{\mathbf{u}} : \hat{\boldsymbol{\tau}} \mathrm{d}\Omega = \int_\Gamma \delta\hat{\mathbf{u}} \cdot (\mathbf{t} - \tilde{\mathbf{t}}) \mathrm{d}\Gamma, \tag{7.16}$$

*Note the similarity with the unbounded part of the strain field in the traditional partition of unity approach to cohesive fracture, equation (2.5).

where $\delta\hat{\mathbf{u}}$ is a continuous displacement variation, $\mathbf{t}$ denotes the applied tractions on a surface with the outward normal $\mathbf{n}$ in the current configuration:

$$\mathbf{t} = \boldsymbol{\tau} \cdot \mathbf{n}\,; \qquad \tilde{\mathbf{t}} = \tilde{\boldsymbol{\tau}} \cdot \mathbf{n}\,. \tag{7.17}$$

In equation (7.16), Γ is the portion of the boundary on which tractions are specified and Ω is the area of the body, both in the current configuration.

The integral on the left hand side of the balance equation in (7.16) can be written in the undeformed configuration so as to make the contributions due to slip explicit. Noting the fact that $J \approx 1$, the equation is re-written as:

$$\int_{\Omega_0} \left(\nabla\delta\hat{\mathbf{u}} : \hat{\mathbf{S}} \cdot \mathbf{F}^{\mathrm{T}}\right) \mathrm{d}\Omega = \int_{\Gamma} \delta\hat{\mathbf{u}} \cdot (\mathbf{T} - \tilde{\mathbf{T}}) \mathrm{d}\Gamma, \tag{7.18}$$

where Ω_0 denotes the area in the undeformed configuration and $\hat{\mathbf{S}}$ is the second Piola-Kirchhoff stress related to $\hat{\boldsymbol{\tau}}$ via

$$\hat{\boldsymbol{\tau}} = \mathbf{F} \cdot \hat{\mathbf{S}} \cdot \mathbf{F}^{\mathrm{T}}\,. \tag{7.19}$$

By isolating small areas around the slip traces $\Gamma^{(I)}$, which are assumed to have a width $h \to 0$ along the normal $\mathbf{m}^{(\alpha)}$ and by employing the fact that $\mathbf{F} \approx \mathbf{F}^*$ on material points that are not lying on these slip traces and using equation (7.12) for the points on these slip traces, the equilibrium equation can be written as:

$$\begin{aligned}\int_{\Omega_0\backslash\Gamma_0} \nabla\delta\hat{\mathbf{u}} :\hat{\mathbf{S}} \cdot \mathbf{F}^{*\mathrm{T}} \mathrm{d}\Omega + \sum_{I=1}^{N} \int_{\Gamma_0^{(I)}} \nabla\delta\hat{\mathbf{u}} : \hat{\mathbf{S}} \cdot (\mathbf{F}^* \cdot \mathbf{F}^{(I)})^{\mathrm{T}} \mathrm{d}\Gamma = \\ \int_{\Gamma} \delta\hat{\mathbf{u}} \cdot \left(\mathbf{T} - \tilde{\mathbf{T}}\right) \mathrm{d}\Gamma,\end{aligned} \tag{7.20}$$

where $\Omega_0\backslash\Gamma_0$ denotes the area in the undeformed configuration excluding the slip segments. In the second left-hand-term of the equation, $\mathbf{F}^{(I)}$ denotes the displacement jump at the slip trace $\Gamma^{(I)}$ which is equal to, see equation (7.12):

$$\mathbf{F}^{(I)} = |\mathbf{b}^{(I)}|\, \mathbf{s}^{(\alpha)} \mathbf{m}^{(\alpha)} \mathrm{sign}\left(\mathbf{b}^{(I)} \cdot \mathbf{r}^{(I)}\right). \tag{7.21}$$

The integral on the right-hand-side of equation (7.20) is over the surface Γ on which tractions are specified in the current configuration. Due to slip, interior material points can become boundary points when dislocations exit the domain. Hence, this term can be rewritten as:

$$\int_{\Gamma} \delta\hat{\mathbf{u}} \cdot \left(\mathbf{T} - \tilde{\mathbf{T}}\right) \mathrm{d}\Gamma = \int_{\Gamma_0} \delta\hat{\mathbf{u}} \cdot \left(\mathbf{T} - \tilde{\mathbf{T}}\right) \mathrm{d}\Gamma + \sum_{I=1}^{M} \delta\hat{\mathbf{u}} \cdot \tilde{\boldsymbol{\tau}} \mathbf{m}^{(\alpha)} \cdot \mathbf{b}^{(I)} \mathbf{s}^{(\alpha)}\,, \tag{7.22}$$

where Γ_0 is the boundary on which tractions are specified in the undeformed configuration, M the number of dislocations that have exited the domain and $\mathbf{m}^{(\alpha)}$ is the slip plane normal at the slip step in the current configuration. It is assumed here that the surface steps due to the dislocations are traction free and that $\tilde{\boldsymbol{\tau}}$ is a constant over the individual slip steps.

§ 7.3 Implementation

In the current model, attention is restricted to isotropic elastic behaviour of the lattice. The strain rate $\dot{\mathbf{S}}$ can be written as:

$$\dot{\mathbf{S}} = \mathbf{L} : \dot{\mathbf{E}}^* \,. \tag{7.23}$$

In this equation, $\dot{\mathbf{E}}^*$ is the rate of the Green-Lagrange strain of the lattice, with:

$$\mathbf{E}^* = \frac{1}{2}\left((\mathbf{F}^*)^{\mathrm{T}} \cdot \mathbf{F}^* - \mathbf{I}\right) , \tag{7.24}$$

and $\mathbf{L}$ is the fourth order tensor of elastic moduli, which is defined as:

$$\mathbf{L} = \lambda \mathbf{I} \otimes \mathbf{I} + 2\mu \mathbf{I}' \,. \tag{7.25}$$

In this constitutive relation, λ and μ are the Lamé constants and $\mathbf{I}$ and $\mathbf{I}'$ are a second and a fourth order unit tensor respectively. The stress rate $\hat{\dot{\mathbf{S}}}$ associated with the rate of the numerical mirror displacement field $\dot{\hat{\mathbf{u}}}$ is given by:

$$\hat{\dot{\mathbf{S}}} = \mathbf{L} : \left(\mathbf{F}^{*\mathrm{T}} \cdot \hat{\mathbf{D}} \cdot \mathbf{F}^*\right) , \tag{7.26}$$

where $\hat{\mathbf{D}}$ is the rate of deformation of the numerical field, equation (7.9).

The constitutive relations that govern the nucleation of a dislocation, its subsequent glide and pinning at obstacles are in general identical to the relations for small strain analyses as presented by van der Giessen and Needleman (1995). A significant difference in this finite strain model is that the underlying lattice is subject to deformations and that the slip systems are rotating as well. As a result, the relative positions of dislocations, nucleation sources and obstacles vary with the deformation state as well as with the local orientation of the slip system.

The nucleation and the subsequent glide of a dislocation J is governed by a Peach-Koehler force $f^{(J)}$, which can be written as:

$$f^{(J)} = \mathbf{m}^{(\alpha)} \cdot \left(\hat{\mathbf{S}} + \sum_{I \neq J} \tilde{\mathbf{S}}^{(I)} \right) \cdot \mathbf{b}^{(\alpha)} \,. \tag{7.27}$$

The direction of the force is in the current orientation of the slip plane $\mathbf{s}^{(\alpha)}$. New dislocation pairs are generated by simulating Frank-Read sources. The initial dislocation segment of a Frank-Read source bows out until it produces a new dislocation loop and a replica of itself. The Frank-Read source is modelled in terms of a critical value of the Peach-Koehler force, the time it takes to generate a dislocation loop and the size of the generated loop. In two dimensions, this is simulated by point sources which generate a dislocation dipole when the magnitude of the Peach-Koehler force at the source exceeds a critical value τ_{nuc} during a period of time Δt_{nuc}. The distance L_{nuc} between the two dislocations at nucleation is set by:

$$L_{\text{nuc}} = \frac{\mu}{2\pi(1-\nu)} \frac{|\mathbf{b}|}{\tau_{\text{nuc}}} \,. \tag{7.28}$$

At this distance, the shear stress of one dislocation acting on the other is balanced by the slip plane shear stress.

It is assumed that dislocations are only allowed to glide along slip planes. The magnitude glide velocity of the dislocation, $|\mathbf{v}^{(I)}|$ is taken to be linearly related to the Peach-Koehler force:

$$|\mathbf{v}^{(I)}| = B f^{(I)}, \tag{7.29}$$

where B is the drag coefficient. Obviously, the dislocation glides in the current direction of the slip plane $\mathbf{s}^{(\alpha)}$.

Since nucleation sources and obstacles are tied to the lattice of the material, their positions follow the corresponding material points. Dislocations however glide with respect to the material with a velocity $\mathbf{v}^{(I)}$. In order to obtain the position of a dislocation I in the current configuration, one first must know its position in the undeformed frame of reference $\mathbf{X}^{(I)}$ at time t, which can be determined in an incremental fashion:

$$\mathbf{X}^{(I)} = \mathbf{X}^{(I)}_{\text{nuc}} + \int_{\tau=t_{\text{nuc}}}^{t} \mathbf{F}^{-1}(\tau) \cdot \mathbf{v}^{(I)}(\tau) d\tau \,, \tag{7.30}$$

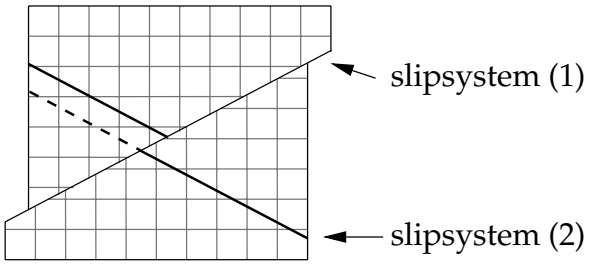

Figure 7.3 Cross slip in a body with 2 active slip planes. Due to the glide of dislocations along slip plane (1), slip plane (2) denoted by the bold line has shifted. When a dislocation on this plane crosses slip plane (1), it will continue to glide along the dashed line. Note that for the sake of clarity, the deformation of the lattice $\mathbf{F}^*$ is not shown here.

where $\mathbf{X}_{\text{nuc}}^{(I)}$ is the position of the parent source in the undeformed configuration where dislocation I was nucleated; t_{nuc} is the time of nucleation. Since the glide velocity of the dislocation $\mathbf{v}^{(I)}$ is expressed in the deformed configuration, it needs to be transformed into the undeformed frame of reference using the total deformation gradient $\mathbf{F}(\tau)$ of the lattice at which dislocation I was located at time τ.

In the case the material only contains one active slip system, dislocation I does not cross the slip traces of dislocations tied to other slip systems, so that in equation (7.30), the deformation gradient $\mathbf{F}$ can be replaced by $\mathbf{F}^*$. When the material has multiple slip systems, the displacement discontinuities due to dislocation glide at different slip systems may give rise to cross-slip, which contributes to an additional motion of a dislocation, see Figure 7.3. Due to the glide of a dislocation, the entire lattice on the other side of the dislocation trace has an additional displacement with magnitude $|\mathbf{b}|$ with respect to the undeformed configuration. When determining the position of a dislocation in the undeformed frame of reference, equation (7.30), this effect must be compensated for.

In the original formulation by van der Giessen and Needleman (1995), dislocations, nucleation sources and obstacles are assumed to reside on a limited number of slip planes. Whereas in reality, the spacing between slip planes in a material is equal to one Burgers' vector, in the discrete dislocation models the spacing between active slip planes is set to 60 Burgers' vectors. Annihilation and pinning of dislocations is determined by measuring the relative distance:

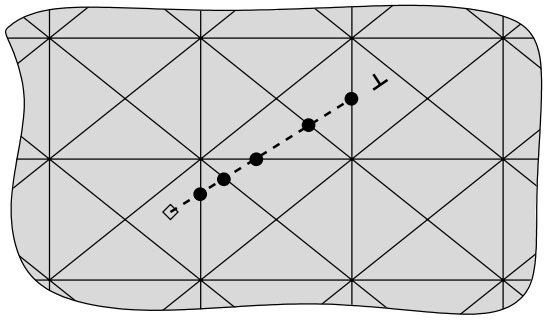

Figure 7.4 Position of the trace (dashed line) generated by a dislocation in the finite element mesh. The trace starts at the nucleation source of the dislocation, denoted by the diamond and is supported by the intersections of the dislocation with element boundaries.

when two dislocations with opposite signs are within a specific distance of $L_e = 6|\mathbf{b}|$, they are annihilated. When a dislocation approaches an obstacle within a distance $2|\mathbf{b}|$ it is pinned to this obstacle. It is only allowed to pass if the Peach-Koehler force exceeds an obstacle depending strength τ_{obs}.

In the proposed finite strain model, this approach cannot be followed. Due to cross-slip, dislocations will leave their original slip planes to end up at planes that are not accounted for in the model. As a result, the chances of meeting obstacles or other dislocations decrease significantly and the original constitutive relations that govern pinning and annihilation will predict a different behaviour. An alternative approach is to increase the obstacle density in the model and no longer assign individual obstacles to specific slip planes. Another alternative is to use different cut-off distances in the aforementioned constitutive relations.

The method can be implemented in a three node finite element using standard iso-parametric interpolation functions. An advantage of this approach is that the numerical parts of the deformation gradient and the stress field are constant within an element, which avoids the use of additional interpolation schemes to determine the exact stress state at a dislocation, nucleation source or an obstacle.

The slip trace terms $\Gamma^{(I)}$ in the equilibrium equation (7.20) are integrated as line integrals, in a similar fashion as the cohesive terms in the partition of

unity cohesive crack formulation, e.g. equation (2.37). This implies that the position of a trace generated by a moving dislocation must be known exactly. When a new dislocation is nucleated, the position of the corresponding nucleation source is stored as the starting point of the line representing the trace, see Figure 7.4. Each time that the dislocation crosses the boundary of an element, the intersection is stored and the line is augmented. This is repeated until the dislocation leaves the domain.

For practical reasons, the line is only extended when the corresponding dislocation crosses an element. As a result, a small error is introduced since the contribution of the discontinuity just behind the dislocation is neglected. In addition, since the lines are assumed to be straight within the element, the effect of cross-slip is neglected and the numerical representation of the slip trace is longer than the actual slip trace.

§ 7.4 Future prospects

In this chapter, an alternative approach is presented to model discrete dislocations in a finite strain kinematic framework. As opposed to the work by Deshpande *et al.* (2003b), the new model explicitly takes into account the effects of slip generated by gliding dislocations. To this end, the deformation gradient is split into an elastic part and an unbounded part that represents the slip displacement. The performance of the model remains to be demonstrated.

In principle, the model can be coupled with the cohesive segments model as discussed in Chapter 5 to arrive at a general tool to simulate crack propagation that is driven by dislocation glide. Additionally, since the creation of new surfaces at free edges is accounted for, the combined model is an ideal candidate to study fatigue crack initiation.

Chapter 8

Conclusions

Crack growth in solid materials can be modelled with the cohesive zone approach. In this approach, the micro-separations in the process zone that set the fracture behaviour of the material are lumped in a single plane ahead of the dominant crack tip. In traditional finite element models, this cohesive zone is represented by interface elements. These elements consist of two surfaces that are connected to the adjacent continuum elements that represent the bulk material. The relative distance between the two surfaces, which represents the opening of the element, is governed by an additional constitutive relation. This cohesive constitutive relation, together with a constitutive relation for the bulk material and the appropriate balance laws and boundary and initial conditions, completely specify the fracture behaviour of the material.

The cohesive zone approach has proven to be a very robust numerical technique for the analysis of fracture in brittle materials. Nevertheless, it has an important drawback. The trajectory of the crack must be known beforehand and is restricted to the position of interface elements in the finite element mesh. Moreover, in order to ensure a perfect bond prior to cracking, the interface elements are equipped with an initial dummy stiffness, which increases the overall compliance of the bulk material and influences the numerical results, at least in a qualitative sense.

The partition of unity property of finite element shape functions offers the possibility to model a cohesive zone as a discontinuity in the displacement field by adding a second displacement field to the regular field on one side of the domain only. This additional field is supported by extra degrees of free-

dom, which are added to the existing nodes of the finite element mesh. The opening of the cohesive zone is equal to the magnitude of the additional field at the discontinuity. An important feature of the partition of unity method is that the discontinuity can be added or extended during a simulation, irrespective of the structure of the underlying finite element mesh. This allows for a truly mesh-independent representation of a crack. Moreover, since the cohesive zone is only created upon fracture, the constitutive relation no longer needs an initial dummy stiffness to model a perfect bond.

In principle, the partition of unity method does not impose any restrictions on the underlying kinematic relations of the finite element formulation. In chapter 3 of this thesis, the method has been applied to a geometrically nonlinear solid-like shell element to analyse delamination growth in laminates. The kinematic relations of the original solid-like shell element are based on a classical shell theory. In addition, the element is equipped with extra degrees of freedom to construct a second-order displacement field in thickness direction, the so-called stretch of the element, in order to avoid Poisson thickness locking. As a result, the element can be used to model relatively thin structures. Apart from that, the element is equipped with an assumed natural strain formulation to overcome transverse shear locking.

In the enhanced solid-like shell element, the discontinuous displacement field has been carefully elaborated throughout all aspects of the kinematic formulation, including the alternative strain relations. The performance of the element has been demonstrated by two small examples, which clearly show that the enhanced element inherits all special properties: it can still be used in thin applications and, even more important, it allows for the simulation of local buckling in combination with delamination growth, which has been demonstrated in the final example of the chapter.

An important problem of the current implementation is related to delamination growth under mixed-mode conditions. In order to avoid the use of additional formulations to determine whether a discontinuity needs to be extended, the criterion that controls the extension of a discontinuity is only based on the stress state in the delamination front. In pure mode-I delamination cases, this approach works well, but in the complex cases as presented in chapter 4, the approach fails to predict the instant of delamination propagation correctly. Here, the discontinuity is inserted in the element beforehand,

as if it were a traditional interface element. A cohesive constitutive relation with an initial dummy stiffness is used to model the delamination. Although in this way, many of the advantages of the partition of unity method were negated, the large models in this chapter clearly show the robustness of the method.

The cohesive segments method, presented in chapter 5, is an extension of the partition of unity approach and allows for the simulation of multiple cracks in a domain. Each crack is modelled as a discontinuity by using as many additional displacement fields, which are supported by unique sets of additional degrees of freedom. The method allows for the simulation of the nucleation of new cracks, the coalescence of cracks and crack branching. In all cases, the same stress based criterion is used to add or extend a cohesive segment. Crack branching is therefore a natural outcome of the loading process, without using additional criteria.

The cohesive segments method can be used to simulate the diffuse crack patterns on the microscopic level that can be observed in structural materials such as fibre reinforced composites. Since the topology of the internal, heterogeneous structure is defined by cohesive segments as well, it is even possible to use structured meshes, which are easy to generate. In order to solve problems with multiple propagating cracks, the energy constraint solution method has been implemented, which appears to be robust. Unfortunately, since cohesive segments are only allowed to propagate into the next element only, the maximum allowable incremental path parameter is limited.

In chapter 6, the cohesive segments method has been extended to simulate fast crack growth in brittle materials. The governing system of equations is solved using an explicit time integration technique. Traditionally, the computational effort is reduced by lumping the mass matrix. In the cohesive segments method, this cannot be done. The full mass matrix of an element with a discontinuity contains crucial information on the coupling of the regular and additional displacement terms. By lumping the mass matrix, this information is lost and spurious transfer of strain energy across a discontinuity is observed. When a different jump function is chosen, for example a unit-symmetric function, this problem is only partly solved. Hence, in all simulations, the computationally more expensive consistent mass matrix has been used.

The critical time step in an explicit transient analysis is roughly equal to the time needed for a stress wave to cross a single element. However, when an element is split by a discontinuity, the equivalent length of the two remaining parts, at least from a kinematic point of view, is smaller than the original length of the element. In the case of a discontinuity crossing an element near one of its boundaries, the equivalent length approaches zero, hence decreasing the critical time step. In order to avoid the use of extremely small time steps in the solution procedure, an offset criterion is used to keep a discontinuity away from the nodes in the domain. This implies that in some cases, the direction of the extension of a segment is slightly modified, but for small offset values, the corresponding error is negligible.

The dynamic shear fracture example clearly shows the benefits of the cohesive segments method. The propagating crack follows the exact angle as observed in experiments and predicted in a linear elastic fracture model. The transit of reflected stress waves gives rise to small disturbances in the orientation of the propagating crack, which are neatly captured by the model. Even the adiabatic shear crack, which occurs at high impact loads can be simulated. The crack branching example however uncovers one of the deficiencies of the current model. The creation of a new segment and the propagation of an existing segment are governed by the same stress based nucleation criterion. In the latter case, an averaged stress state is used, whereas the nucleation of a new segment is based on the exact stress state in a single integration point. The averaged stress in the vicinity of the terminus of a cohesive segment is, by definition, smaller than the actual stress. As a result, a cohesive segment is always extended slightly too late, which in principle is not a serious problem except in the case of crack branching. In this case, the propagation of existing segments is competing with the nucleation of new segments.

The partition of unity approach to cohesive fracture has proven to be a suitable tool for the simulation of crack growth in arbitrary directions, on many levels of observation. However, the elegance of the mathematical formulation is not reflected in the implementation. When a discontinuity is extended into the next element, the nodes that support this element will be enhanced with additional degrees of freedom. Subsequently, all elements that are connected to these nodes, including the one that contains the discontinuity, will obtain an augmented system of equations. Obviously, this update operation requires

some exchange of data between the elements and nodes. In most commercial finite element codes this inter-element communication is not provided, which hampers an efficient implementation of the method in these codes. In addition, in order to perform an accurate numerical integration, the element that is crossed by a discontinuity must be divided in a number of subelements that are integrated separately. To this end, new integration points have to be created, and possible material history parameters must be reallocated. In that respect, the implementation of the partition of unity approach to cohesive fracture can be considered as a single element remeshing technique.

Apart from the issues related to the implementation, the present implementation can be improved. The current algorithm that detects the direction in which a discontinuity needs to be extended is far from robust. Future efforts should therefore be directed towards new crack propagation algorithms. This will most likely also change the way the stress fields in the vicinity of the tip are represented, since the resolution of the finite element mesh is too small to capture the large stress gradients in those regions. Recently, a remedy for this problem has been presented by Xiao and Karihaloo (2006). Here, the stresses near the tip are corrected by a statically admissible field that meets the tractions at the edges of the discontinuity and uses moving least squares to fit the stresses at the existing integration points of the model. In principle, the method allows to determine the stress state at the tip of a segment more accurately, such that the use of an averaging algorithm is avoided. As a result, the nucleation and extension of a cohesive segment are completely equivalent, which enables a quantitative analysis of diffuse fracture problems.

Practical considerations refrained from using the partition of unity in the finite strain dislocation model as described in chapter 7. In theory, the method can be used to enhance the finite element displacement field with the displacement field generated by the individual dislocations. But in practice, this would result in a large, inefficient numerical code. The displacement field of a single dislocation decays with the order of inverse distance, which implies that the nodes in a large area around the dislocation need to be enhanced by additional degrees of freedom. Moreover, taking into account that a standard specimen can contain hundreds of dislocations, which all move through the specimen as well, it is not hard to imagine that computational overhead is

enormous.

Nevertheless, the need to explicitly take into account the contribution of slip in the finite strain discrete dislocation model is evident. In the original formulation, the slip displacement, accumulated by the collective motion of dislocations, was smeared out over the element. As a result, the deformation gradient, which is supposed to remain relatively small, is too large. In the proposed model, the deformation gradient is split into an elastic part and an unbounded part related to the slip displacement. The regular part of the displacement field generated by dislocations is dealt with in the same way as the original discrete dislocation models. The creation of new surfaces at free edges is taken into account, which provides a firm basis for the combined analysis of micro-crack nucleation driven by dislocation glide.

Appendix A

Visualisation of a discontinuity

When the cohesive zone in the finite element is modelled by means of interface elements, the position of the crack in the deformed specimen is visible as a gap between elements (Xu and Needleman 1994, Camacho and Ortiz 1996). In the partition of unity approach, where a cohesive zone is modelled as a jump in the displacement field of continuum elements, this is not the case. Here, the topology of the mesh is by no means related to the location of a cohesive zone and the trajectory of the crack can only be revealed vaguely by following the highly distorted elements in the deformed mesh, as demonstrated in Figure A.1.

As an alternative, the position of the crack in the deformed specimen can be shown by creating a second mesh, which is derived from the original finite element mesh. This *post-processing mesh* is used for visualisation purposes only and is not involved in any numerical operation. As a result, the topology of this mesh can be modified endlessly without losing computational efficiency. Moreover, the elements in the post-processing mesh do not have to satisfy quality requirements regarding aspect ratios.

In this Appendix, the technique to create a post-processing mesh of a specimen with a discontinuity is explained. In the second section, an extension of this technique to visualise multiple interacting discontinuities is presented.

§ A.1 A single discontinuity

Consider the situation depicted in Figure A.2. The triangular finite element mesh is crossed by a discontinuity dividing the domain in two parts denoted

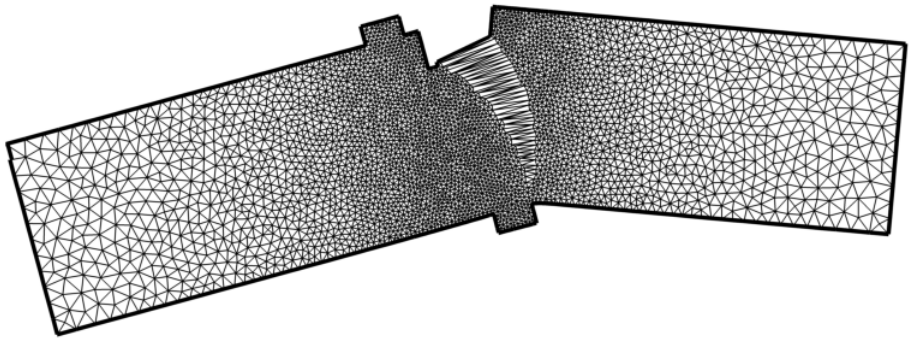

Figure A.1 The single edge notched beam in deformed configuration (Wells and Sluys, 2001). The displacements are magnified by a factor 100. The crack crosses the highly distorted elements.

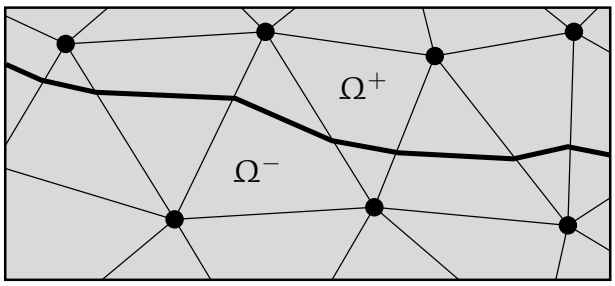

Figure A.2 Detail of a triangular finite element mesh that is crossed by a single discontinuity (bold line) dividing it into an Ω^+ and an Ω^- part.

Ω^+ and an Ω^-. Due to the corresponding discontinuous displacement field, each part of the domain is able to move independently. To facilitate this behaviour, the elements that contain the discontinuity are cut in two parts, see Figure A.3. At each intersection of the discontinuity, a pair of two nodes is created. The two nodes in a pair have identical positions in the undeformed configuration, but they are subjected to different displacement fields.

For a more elaborated explanation, consider the element ABC in Figure A.4. The original element is replaced by two new elements representing the $\mathcal{V}^+$ and the $\mathcal{V}^-$ part of the original element. In the post-processing mesh, two pairs of new nodes are created at the intersection of edges AB and BC and the discontinuity. On edge AB, these new nodes are called P and P', on edge BC they are denoted Q and Q'. Both P' and Q' are part of the Ω^+ part of the

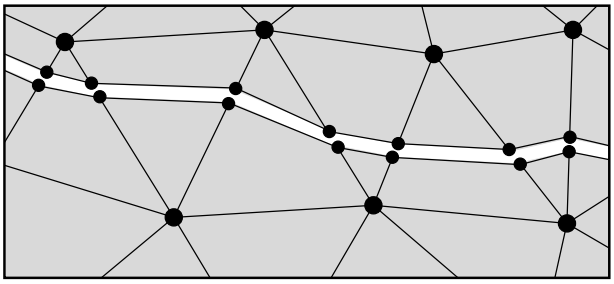

Figure A.3 Visualisation of the discontinuity in the triangular mesh. The smaller grey dots denote the new post-processing nodes. For reasons of clarity, the two additional nodes that form a pair are drawn with a small offset. In reality, the two nodes in a pair have identical coordinates in the undeformed position.

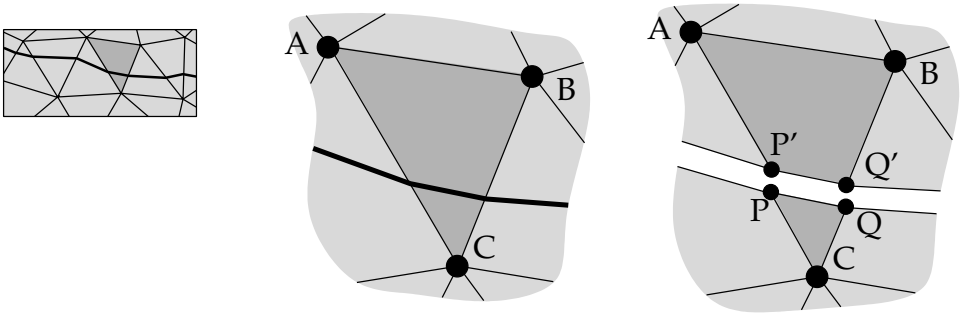

Figure A.4 The element ABC is crossed by the discontinuity and is split in two parts. At the intersection of the discontinuity with edge AC the nodes P and P′ are created, on the intersection of the discontinuity with BC, the Q and Q′ are created.

domain, whereas P and Q belong to the Ω^- part.

The displacement $\mathbf{u}_i$ of node i consists of the regular degrees of freedom $\mathbf{a}_i$ and the additional degrees of freedom $\mathbf{b}_i$ multiplied with the enhanced basis function $\mathcal{H}_{\Gamma_\mathrm{d}}(\mathbf{x}_i)$:

$$\mathbf{u}_i = \mathbf{a}_i + \mathcal{H}_{\Gamma_\mathrm{d}}(\mathbf{x}_i)\mathbf{b}_i\,, \tag{A.1}$$

where $\mathbf{x}_i$ is the original position of node i. In the example in Figure A.4, node A resides in the Ω^+ part of the domain and node C is in the Ω^- part. Using the standard Heaviside jump function as stated in equation (2.4), the total

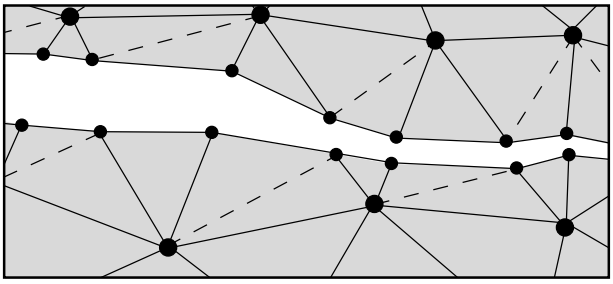

Figure A.5 The deformed visualisation mesh. Since most visualisation tools are not able to handle meshes that consist of elements with various number of supporting nodes, all four node elements are triangulated. The element boundaries that are created in this procedure are dashed.

displacements of nodes A and C are equal to:

$$\mathbf{u}_\mathrm{A} = \mathbf{a}_\mathrm{A} + \mathbf{b}_\mathrm{A}\,; \qquad \mathbf{u}_\mathrm{C} = \mathbf{a}_\mathrm{C}\,. \tag{A.2}$$

The displacement of the new nodes can be derived from the displacement of the adjacent nodes using the corresponding shape functions, equation (2.22). In case of nodes P and P', which are located in point $\mathbf{x}_P$, the only shape functions that have non-zero contributions belong to nodes A and C. Hence, equation (2.22) reduces to:

$$\mathbf{u}(\mathbf{x}_\mathrm{P}) = \phi_\mathrm{A}(\mathbf{x}_\mathrm{P})\left(\mathbf{a}_\mathrm{A} + \mathcal{H}^+\mathbf{b}_\mathrm{A}\right) + \phi_\mathrm{C}(\mathbf{x}_\mathrm{P})\left(\mathbf{a}_\mathrm{C} + \mathcal{H}^-\mathbf{b}_\mathrm{C}\right) \tag{A.3}$$

where ϕ_A and ϕ_C are the shape functions that correspond to node A and C, respectively, and $\mathcal{H}^+$ and $\mathcal{H}^-$ are defined in (2.2).

The procedure is demonstrated by means of the single edge notched beam example from chapter 2. A detail of the deformed post-processing mesh is shown in Figure A.6. In order to get a better perception of the crack, the displacements are magnified by a factor 100. The stress state at integration points is extrapolated into the nodes in the conventional way.

§ A.2 Multiple discontinuities

The procedure can be repeated in case an element is crossed by a discontinuity more than once. Consider the situation shown in Figure A.7 in which a second

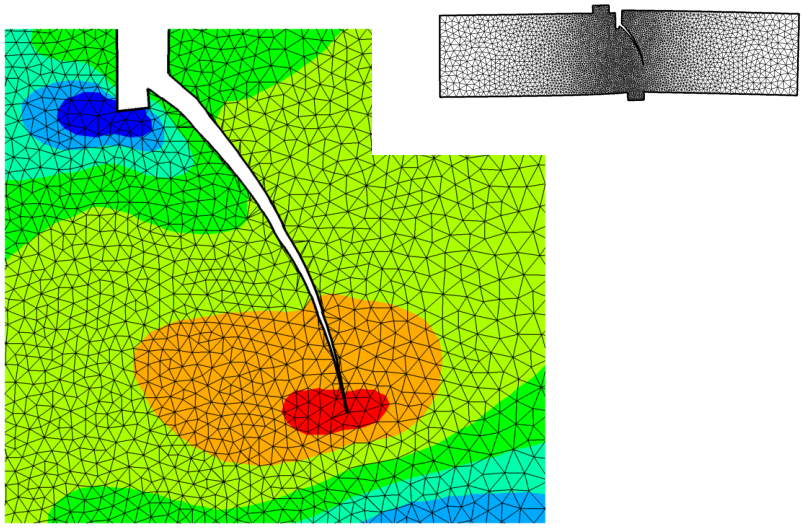

Figure A.6 Detail of the deformed post-processing mesh of the single edge notched beam. The displacements are magnified by a factor 100. Note the smaller triangulated elements near the crack surface.

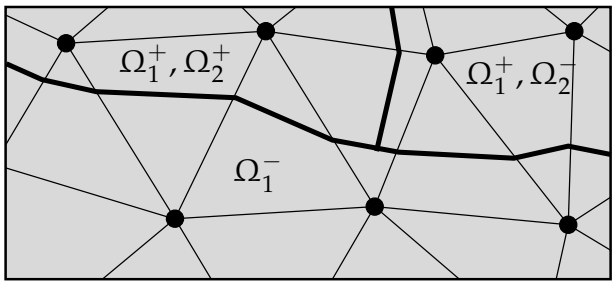

Figure A.7 Detail of a triangular mesh with two discontinuities, denoted by the bold lines. Discontinuity 1 divides the mesh into an Ω_1^+ and an Ω_1^- part. Discontinuity 2, which is added later, touches discontinuity 1 and devides the Ω_1^+ part into an Ω_2^+ and Ω_2^- part.

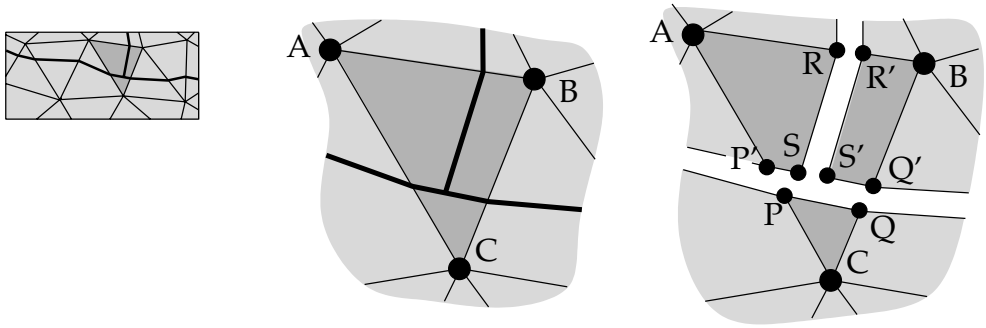

Figure A.8 The element ABC is crossed by two discontinuities. At the intersection of the second discontinuity with vertex AB the two nodes R and R′ are created, at the intersection with vertex PP′ the new nodes are called S and S′.

discontinuity touches the initial discontinuity inside the element of interest ABC. The part of the mesh below the initial discontinuity is now denoted as Ω_1^-, whereas the part above is Ω_1^+. In addition, due to the new discontinuity, the area on the left is enhanced for a second time and denoted by Ω_2^+, while the other side of this discontinuity is called Ω_2^-.

The second discontinuity is visualised by creating two new pairs of nodes: R and R′ on the vertex AB and Q and Q′ on the vertex PP′, see Figure A.8. The position of the nodes can be determined by applying equation (5.13) in a similar fashion as explained before. A remark must be made with respect to nodes S and S′. Since these nodes reside in the element (and not on one of the original vertices), their displacements consist of the regular displacements $\mathbf{a}_i$ and additional displacements $\mathbf{b}_{i1}$ and $\mathbf{b}_{i2}$ of all three nodes of the element in combination with the correct shape functions and the corresponding value for the enhancement function.

As a rule of thumb, in complex situations as described here, the enhancement functions of an additional node are identical to the enhancement functions of the regular node in the same sub-element. For example, the enhancement functions of node S′ are equal to the enhancement functions of node B.

Appendix B

Kinematic relations of the solid-like shell element

The calculation of the element internal force vector and the incremental strain field requires a straightforward derivation of kinematic relations. In this appendix, these derivations are elaborated for the solid-like shell element. In addition, the assumed natural shear strains which are needed for the eight node element are presented.

§ B.1 Variational and incremental strain fields

The variation of the discontinuous strain field $\delta\boldsymbol{\gamma}$ can be derived from the strain field $\boldsymbol{\gamma}$ in equation (3.28) in terms of the displacement components:

$$
\begin{aligned}
2\delta\epsilon_{\alpha\beta} &= \mathbf{e}_\beta\cdot(\delta\hat{\mathbf{u}}_{0,\alpha}+\mathcal{H}_{\Gamma_{d,0}}\delta\tilde{\mathbf{u}}_{0,\alpha}) + \mathbf{e}_\alpha\cdot(\delta\hat{\mathbf{u}}_{0,\beta}+\mathcal{H}_{\Gamma_{d,0}}\delta\tilde{\mathbf{u}}_{0,\beta})\,;\\
2\delta\epsilon_{\alpha 3} &= \mathbf{d}\cdot(\delta\hat{\mathbf{u}}_{0,\alpha}+\mathcal{H}_{\Gamma_{d,0}}\delta\tilde{\mathbf{u}}_{0,\alpha}) + \mathbf{e}_\alpha\cdot(\delta\hat{\mathbf{u}}_1+\mathcal{H}_{\Gamma_{d,0}}\delta\tilde{\mathbf{u}}_1)\,;\\
2\delta\epsilon_{33} &= 2\mathbf{d}\cdot(\delta\hat{\mathbf{u}}_1+\mathcal{H}_{\Gamma_{d,0}}\delta\tilde{\mathbf{u}}_1)\,;\\
2\delta\rho_{\alpha\beta} &= \mathbf{e}_\beta\cdot(\delta\hat{\mathbf{u}}_{1,\alpha}+\mathcal{H}_{\Gamma_{d,0}}\delta\tilde{\mathbf{u}}_{1,\alpha}) + \mathbf{e}_\alpha\cdot(\delta\hat{\mathbf{u}}_{1,\beta}+\mathcal{H}_{\Gamma_{d,0}}\delta\tilde{\mathbf{u}}_{1,\beta}) +\\
&\quad \mathbf{d}_{,\alpha}\cdot(\delta\hat{\mathbf{u}}_{0,\beta}+\mathcal{H}_{\Gamma_{d,0}}\delta\tilde{\mathbf{u}}_{0,\beta}) + \mathbf{d}_{,\beta}\cdot(\delta\hat{\mathbf{u}}_{0,\alpha}+\mathcal{H}_{\Gamma_{d,0}}\delta\tilde{\mathbf{u}}_{0,\alpha})\\
&\quad - \bar{G}^\lambda_\alpha[\mathbf{e}_\beta\cdot(\delta\hat{\mathbf{u}}_{0,\lambda}+\mathcal{H}_{\Gamma_{d,0}}\delta\tilde{\mathbf{u}}_{0,\lambda}) + \mathbf{e}_\lambda\cdot(\delta\hat{\mathbf{u}}_{0,\beta}+\mathcal{H}_{\Gamma_{d,0}}\delta\tilde{\mathbf{u}}_{0,\beta})]\\
&\quad - \bar{G}^\lambda_\beta[\mathbf{e}_\alpha\cdot(\delta\hat{\mathbf{u}}_{0,\lambda}+\mathcal{H}_{\Gamma_{d,0}}\delta\tilde{\mathbf{u}}_{0,\lambda}) + \mathbf{e}_\lambda\cdot(\delta\hat{\mathbf{u}}_{0,\alpha}+\mathcal{H}_{\Gamma_{d,0}}\delta\tilde{\mathbf{u}}_{0,\alpha})]\,;\\
2\delta\rho_{\alpha 3} &= \mathbf{d}\cdot(\delta\hat{\mathbf{u}}_{1,\alpha}+\mathcal{H}_{\Gamma_{d,0}}\delta\tilde{\mathbf{u}}_{1,\alpha}) + \mathbf{d}_{,\alpha}\cdot(\delta\hat{\mathbf{u}}_1+\mathcal{H}_{\Gamma_{d,0}}\delta\tilde{\mathbf{u}}_1)\,;\\
2\delta\rho_{33} &= -8\mathbf{u}_2\cdot(\delta\hat{\mathbf{u}}_1+\mathcal{H}_{\Gamma_{d,0}}\delta\tilde{\mathbf{u}}_1) - 4\mathbf{d}\cdot\mathbf{d}(\delta\hat{w}+\mathcal{H}_{\Gamma_{d,0}}\delta\tilde{w})\,,
\end{aligned}
\tag{B.1}
$$

where $\mathbf{e}_\alpha$, $\mathbf{d}$, $\mathbf{d}_{,\alpha}$ and $\mathbf{u}_2$ denote the *current* orientation of the base vectors and internal stretch:

$$\begin{aligned}
\mathbf{e}_\alpha &= \mathbf{E}_\alpha + \hat{\mathbf{u}}_{0,\alpha} + \mathcal{H}_{\Gamma_{\mathrm{d},0}}\tilde{\mathbf{u}}_{0,\alpha}\,;\\
\mathbf{d} &= \mathbf{D} + \hat{\mathbf{u}}_1 + \mathcal{H}_{\Gamma_{\mathrm{d},0}}\tilde{\mathbf{u}}_1\,;\\
\mathbf{d}_{,\alpha} &= \mathbf{D}_{,\alpha} + \hat{\mathbf{u}}_{1,\alpha} + \mathcal{H}_{\Gamma_{\mathrm{d},0}}\hat{\mathbf{u}}_{1,\alpha}\,;\\
\mathbf{u}_2 &= \hat{\mathbf{u}}_2 + \mathcal{H}_{\Gamma_{\mathrm{d},0}}\tilde{\mathbf{u}}_2\,.
\end{aligned} \tag{B.2}$$

In an incremental iterative solution scheme, the strain increment $\Delta\boldsymbol{\gamma}$ with respect to the previous converged solution is normally needed. It can be derived as:

$$\begin{aligned}
2\Delta\epsilon_{\alpha\beta} &= \mathbf{e}_\alpha\cdot\Delta\mathbf{u}_{0,\beta} + \mathbf{e}_\beta\cdot\Delta\mathbf{u}_{0,\alpha} + \Delta\mathbf{u}_{0,\alpha}\cdot\Delta\mathbf{u}_{0,\beta}\,;\\
2\Delta\epsilon_{\alpha 3} &= \mathbf{e}_\alpha\cdot\Delta\mathbf{u}_1 + \mathbf{d}\cdot\Delta\mathbf{u}_{0,\alpha} + \Delta\mathbf{u}_{0,\alpha}\cdot\Delta\mathbf{u}_1\,;\\
2\Delta\epsilon_{33} &= 2\mathbf{d}\cdot\Delta\mathbf{u}_1 + 2\Delta\mathbf{u}_1\cdot\Delta\mathbf{u}_1\,;\\
2\Delta\rho_{\alpha\beta} &= \mathbf{e}_\beta\cdot\Delta\mathbf{u}_{1,\alpha} + \mathbf{d}_{,\alpha}\cdot\Delta\mathbf{u}_{0,\beta} + \Delta\mathbf{u}_{1,\alpha}\cdot\Delta\mathbf{u}_{0,\beta}\\
&\quad + \mathbf{e}_\alpha\cdot\Delta\mathbf{u}_{1,\beta} + \mathbf{d}_{,\beta}\cdot\Delta\mathbf{u}_{0,\alpha} + \Delta\mathbf{u}_{1,\beta}\cdot\Delta\mathbf{u}_{0,\alpha}\\
&\quad - \bar{G}^\lambda_\alpha[\mathbf{e}_\beta\cdot\Delta\mathbf{u}_{0,\lambda} + \mathbf{e}_\lambda\cdot\Delta\mathbf{u}_{0,\beta} + \Delta\mathbf{u}_{0,\lambda}\cdot\Delta\mathbf{u}_{0,\beta}]\\
&\quad - \bar{G}^\lambda_\beta[\mathbf{e}_\alpha\cdot\Delta\mathbf{u}_{0,\lambda} + \mathbf{e}_\lambda\cdot\Delta\mathbf{u}_{0,\alpha} + \Delta\mathbf{u}_{0,\lambda}\cdot\Delta\mathbf{u}_{0,\alpha}]\,;\\
2\Delta\rho_{\alpha 3} &= \mathbf{d}_{,\alpha}\cdot\Delta\mathbf{u}_1 + \mathbf{d}\cdot\Delta\mathbf{u}_{1,\alpha} + \Delta\mathbf{u}_{1,\alpha}\cdot\Delta\mathbf{u}_1\,;\\
2\Delta\rho_{33} &= -4\mathbf{d}\cdot\Delta\mathbf{u}_1 - 2w\Delta\mathbf{u}_1\cdot\mathbf{u}_1 - 2\Delta w\mathbf{d}\cdot\mathbf{d}\\
&\quad - 4\Delta w\mathbf{u}_1\cdot\mathbf{d} - 2\Delta w\Delta\mathbf{u}_1\cdot\Delta\mathbf{u}_1\,,
\end{aligned} \tag{B.3}$$

where $\mathbf{e}_\alpha$, $\mathbf{d}$, $\mathbf{d}_{,\alpha}$ and $\mathbf{u}_2$ are the orientation of the base vectors and internal stretch in the *previous* converged solution and $\Delta\mathbf{u}_1$, $\Delta\mathbf{u}_{1,\alpha}$, $\Delta\mathbf{u}_{1,\alpha}$, $\Delta\mathbf{d}_{,\alpha}$ and Δw are:

$$\begin{aligned}
\Delta\mathbf{u}_1 &= \Delta\hat{\mathbf{u}}_1 + \mathcal{H}_{\Gamma_{\mathrm{d},0}}\Delta\tilde{\mathbf{u}}_1\,;\\
\Delta\mathbf{u}_{0,\alpha} &= \Delta\hat{\mathbf{u}}_{0,\alpha} + \mathcal{H}_{\Gamma_{\mathrm{d},0}}\Delta\tilde{\mathbf{u}}_{0,\alpha}\,;\\
\Delta\mathbf{u}_{1,\alpha} &= \Delta\hat{\mathbf{u}}_{1,\alpha} + \mathcal{H}_{\Gamma_{\mathrm{d},0}}\Delta\tilde{\mathbf{u}}_{1,\alpha}\,;\\
\Delta\mathbf{d}_{,\alpha} &= \Delta\hat{\mathbf{d}}_{,\alpha} + \mathcal{H}_{\Gamma_{\mathrm{d},0}}\Delta\tilde{\mathbf{d}}_{,\alpha}\,;\\
\Delta w &= \Delta\hat{w} + \mathcal{H}_{\Gamma_{\mathrm{d},0}}\Delta\tilde{w}\,.
\end{aligned} \tag{B.4}$$

§ B.2 Derivation of the **B** matrix.

The variational strains as derived in equation (B.1) can be split in terms of regular and additional variational displacement components and written in the following matrix notation:

$$\begin{aligned}\delta\boldsymbol{\gamma} = \mathbf{H}^1\delta\hat{\mathbf{u}}_1+\mathbf{H}^0_1\delta\hat{\mathbf{u}}_{0,1}+\mathbf{H}^1_1\delta\hat{\mathbf{u}}_{1,1}+\mathbf{H}^0_2\delta\hat{\mathbf{u}}_{0,2}+\mathbf{H}^1_2\delta\hat{\mathbf{u}}_{1,2}+\mathbf{H}^w\delta\hat{w}+\\ \mathcal{H}_{\Gamma_{\mathrm{d},0}}(\mathbf{H}^1\delta\hat{\mathbf{u}}_1+\mathbf{H}^0_1\delta\hat{\mathbf{u}}_{0,1}+\mathbf{H}^1_1\delta\hat{\mathbf{u}}_{1,1}+\mathbf{H}^0_2\delta\hat{\mathbf{u}}_{0,2}+\mathbf{H}^1_2\delta\hat{\mathbf{u}}_{1,2}+\mathbf{H}^w\delta\hat{w})\,,\end{aligned} \tag{B.5}$$

where,

$$\mathbf{H}^1=\begin{bmatrix}\mathbf{0}\\ \mathbf{0}\\ \mathbf{d}^{\mathrm{T}}-4\zeta w\mathbf{d}^{\mathrm{T}}\\ \mathbf{0}\\ \mathbf{e}_2^{\mathrm{T}}+\zeta\mathbf{d}_{,2}^{\mathrm{T}}\\ \mathbf{e}_1^{\mathrm{T}}+\zeta\mathbf{d}_{,1}^{\mathrm{T}}\end{bmatrix}\qquad \mathbf{H}^1_1=\begin{bmatrix}\zeta\mathbf{e}_1^{\mathrm{T}}\\ \mathbf{0}\\ \mathbf{0}\\ \zeta\mathbf{e}_2^{\mathrm{T}}\\ \mathbf{0}\\ \zeta\mathbf{d}^{\mathrm{T}}\end{bmatrix}\qquad \mathbf{H}^1_2=\begin{bmatrix}\mathbf{0}\\ \zeta\mathbf{e}_2^{\mathrm{T}}\\ \mathbf{0}\\ \zeta\mathbf{e}_1^{\mathrm{T}}\\ \zeta\mathbf{d}^{\mathrm{T}}\\ \mathbf{0}\end{bmatrix}\qquad \mathbf{H}^w=\begin{bmatrix}0\\ 0\\ -2\zeta\mathbf{d}\cdot\mathbf{d}\\ 0\\ 0\\ 0\end{bmatrix}$$

$$\mathbf{H}^1_1=\begin{bmatrix}\mathbf{e}_1^{\mathrm{T}}+\zeta(\mathbf{d}_{,1}^{\mathrm{T}}-2\mathbf{e}_1^{\mathrm{T}}\bar{G}_1^1-\mathbf{e}_2^{\mathrm{T}}\bar{G}_1^2)\\ -\zeta\mathbf{e}_2^{\mathrm{T}}\bar{G}_2^1\\ \mathbf{0}\\ \mathbf{e}_2^{\mathrm{T}}+\zeta(\mathbf{d}_{,2}^{\mathrm{T}}-\mathbf{e}_2^{\mathrm{T}}\bar{G}_1^1-2\mathbf{e}_1^{\mathrm{T}}\bar{G}_2^1-\mathbf{e}_2^{\mathrm{T}}\bar{G}_2^2)\\ \mathbf{0}\\ \mathbf{d}^{\mathrm{T}}\end{bmatrix}\qquad \mathbf{H}^1_2=\begin{bmatrix}-\zeta\mathbf{e}_1^{\mathrm{T}}\bar{G}_1^2\\ \mathbf{e}_2^{\mathrm{T}}(\mathbf{d}_{,2}^{\mathrm{T}}-\mathbf{e}_1^{\mathrm{T}}\bar{G}_2^1-2\mathbf{e}_2^{\mathrm{T}}\bar{G}_2^2)\\ \mathbf{0}\\ \mathbf{e}_1^{\mathrm{T}}+\zeta(\mathbf{d}_{,1}^{\mathrm{T}}-\mathbf{e}_1^{\mathrm{T}}\bar{G}_1^1-2\mathbf{e}_2^{\mathrm{T}}\bar{G}_1^2-\mathbf{e}_1^{\mathrm{T}}\bar{G}_2^2)\\ \mathbf{d}^{\mathrm{T}}\\ \mathbf{0}\end{bmatrix}.$$

The variational displacement vectors can be obtained from the nodal degrees of freedom via the shape functions as defined in equations (3.44) to (3.47).

$$\begin{aligned}\delta\hat{\mathbf{u}}_1 &= \mathbf{N}_1\delta\mathbf{a}; & \delta\tilde{\mathbf{u}}_1 &= \mathbf{N}_1\delta\mathbf{b};\\ \delta\hat{\mathbf{u}}_{0,\alpha} &= \mathbf{N}_{0,\alpha}\delta\mathbf{a}; & \delta\tilde{\mathbf{u}}_{0,\alpha} &= \mathbf{N}_{0,\alpha}\delta\mathbf{b};\\ \delta\hat{\mathbf{u}}_{1,\alpha} &= \mathbf{N}_{1,\alpha}\delta\mathbf{a}; & \delta\tilde{\mathbf{u}}_{1,\alpha} &= \mathbf{N}_{1,\alpha}\delta\mathbf{b};\\ \delta\hat{w} &= \mathbf{N}_w\delta\mathbf{p}; & \delta\tilde{w} &= \mathbf{N}_w\delta\mathbf{q};\end{aligned} \tag{B.6}$$

Substituting these equations into (B.5) gives:

$$\delta\boldsymbol{\gamma} = \mathbf{B}_u\delta\mathbf{a} + \mathbf{B}_w\delta\mathbf{p} + \mathcal{H}_{\Gamma_{\mathrm{d},0}}(\mathbf{B}_u\delta\mathbf{b} + \mathbf{B}_w\delta\mathbf{q})\,. \tag{B.7}$$

where $\mathbf{B}_u$ and $\mathbf{B}_w$ are defined as:

$$\begin{aligned}\mathbf{B}_u &= \mathbf{H}^1\mathbf{N}_1 + \mathbf{H}^0_1\mathbf{N}_{0,1} + \mathbf{H}^1_1\mathbf{N}_{1,1} + \mathbf{H}^0_2\mathbf{N}_{0,2} + \mathbf{H}^1_2\mathbf{N}_{1,2}\,;\\ \mathbf{B}_w &= \mathbf{H}_w\mathbf{N}_w\,.\end{aligned} \tag{B.8}$$

Note that the matrices $\mathbf{B}_u$ and $\mathbf{B}_w$ are identical for the regular displacement terms $\mathbf{a}$ and $\mathbf{p}$ as well as the additional terms $\mathbf{b}$ and $\mathbf{q}$. The matrices $\mathbf{B}_u$ and $\mathbf{B}_w$ are still defined in the iso-parametric frame of reference and must be transformed in the element local system $\mathbf{l}_j$, using the transformation tensor T^i_k in equation (3.29).

§ B.3 Stress dependent part of the stiffness matrix

The derivative of the variational strains with respect to the displacement field is equal to:

$$\begin{aligned}
2d(\delta\epsilon_{\alpha\beta}) &= (\delta\hat{\mathbf{u}}_{0,\alpha} + \mathcal{H}_{\Gamma_{\mathrm{d},0}}\delta\tilde{\mathbf{u}}_{0,\alpha})\cdot(d\hat{\mathbf{u}}_{0,\beta}+\mathcal{H}_{\Gamma_{\mathrm{d},0}}d\tilde{\mathbf{u}}_{0,\beta})\\
&\quad + (\delta\hat{\mathbf{u}}_{0,\beta} + \mathcal{H}_{\Gamma_{\mathrm{d},0}}\delta\tilde{\mathbf{u}}_{0,\beta})\cdot(d\hat{\mathbf{u}}_{0,\alpha}+\mathcal{H}_{\Gamma_{\mathrm{d},0}}d\tilde{\mathbf{u}}_{0,\alpha})\,;\\
2d(\delta\epsilon_{\alpha 3}) &= (\delta\hat{\mathbf{u}}_{0,\alpha} + \mathcal{H}_{\Gamma_{\mathrm{d},0}}\delta\tilde{\mathbf{u}}_{0,\alpha})\cdot(d\hat{\mathbf{u}}_{1}+\mathcal{H}_{\Gamma_{\mathrm{d},0}}d\tilde{\mathbf{u}}_{1})\\
&\quad + (\delta\hat{\mathbf{u}}_{1} + \mathcal{H}_{\Gamma_{\mathrm{d},0}}\delta\tilde{\mathbf{u}}_{1})\cdot(d\hat{\mathbf{u}}_{0,\alpha}+\mathcal{H}_{\Gamma_{\mathrm{d},0}}d\tilde{\mathbf{u}}_{0,\alpha})\,;\\
2d(\delta\epsilon_{33}) &= 2(\delta\hat{\mathbf{u}}_{1} + \mathcal{H}_{\Gamma_{\mathrm{d},0}}\delta\tilde{\mathbf{u}}_{1})\cdot(d\hat{\mathbf{u}}_{1}+\mathcal{H}_{\Gamma_{\mathrm{d},0}}d\tilde{\mathbf{u}}_{1})\,;\\
2d(\delta\rho_{\alpha\beta}) &= (\delta\hat{\mathbf{u}}_{1,\alpha} + \mathcal{H}_{\Gamma_{\mathrm{d},0}}\delta\tilde{\mathbf{u}}_{1,\alpha})\cdot(d\hat{\mathbf{u}}_{0,\beta}+\mathcal{H}_{\Gamma_{\mathrm{d},0}}d\tilde{\mathbf{u}}_{0,\beta})\\
&\quad + (\delta\hat{\mathbf{u}}_{1,\beta} + \mathcal{H}_{\Gamma_{\mathrm{d},0}}\delta\tilde{\mathbf{u}}_{1,\beta})\cdot(d\hat{\mathbf{u}}_{0,\alpha}+\mathcal{H}_{\Gamma_{\mathrm{d},0}}d\tilde{\mathbf{u}}_{0,\alpha})\\
&\quad + (\delta\hat{\mathbf{u}}_{0,\alpha} + \mathcal{H}_{\Gamma_{\mathrm{d},0}}\delta\tilde{\mathbf{u}}_{0,\alpha})\cdot(d\hat{\mathbf{u}}_{1,\beta}+\mathcal{H}_{\Gamma_{\mathrm{d},0}}d\tilde{\mathbf{u}}_{1,\beta})\\
&\quad + (\delta\hat{\mathbf{u}}_{0,\beta} + \mathcal{H}_{\Gamma_{\mathrm{d},0}}\delta\tilde{\mathbf{u}}_{0,\beta})\cdot(d\hat{\mathbf{u}}_{1,\alpha}+\mathcal{H}_{\Gamma_{\mathrm{d},0}}d\tilde{\mathbf{u}}_{1,\alpha})\\
&\quad - \bar{G}^\lambda_\alpha[(\delta\hat{\mathbf{u}}_{0,\lambda} + \mathcal{H}_{\Gamma_{\mathrm{d},0}}\delta\tilde{\mathbf{u}}_{0,\lambda})\cdot(d\hat{\mathbf{u}}_{0,\beta}+\mathcal{H}_{\Gamma_{\mathrm{d},0}}d\tilde{\mathbf{u}}_{0,\beta})\\
&\qquad + (\delta\hat{\mathbf{u}}_{0,\beta} + \mathcal{H}_{\Gamma_{\mathrm{d},0}}\delta\tilde{\mathbf{u}}_{0,\beta})\cdot(d\hat{\mathbf{u}}_{0,\lambda}+\mathcal{H}_{\Gamma_{\mathrm{d},0}}d\tilde{\mathbf{u}}_{0,\lambda})]\\
&\quad - \bar{G}^\lambda_\beta[(\delta\hat{\mathbf{u}}_{0,\alpha} + \mathcal{H}_{\Gamma_{\mathrm{d},0}}\delta\tilde{\mathbf{u}}_{0,\alpha})\cdot(d\hat{\mathbf{u}}_{0,\lambda}+\mathcal{H}_{\Gamma_{\mathrm{d},0}}d\tilde{\mathbf{u}}_{0,\lambda})\\
&\qquad + (\delta\hat{\mathbf{u}}_{0,\lambda} + \mathcal{H}_{\Gamma_{\mathrm{d},0}}\delta\tilde{\mathbf{u}}_{0,\lambda})\cdot(d\hat{\mathbf{u}}_{0,\alpha}+\mathcal{H}_{\Gamma_{\mathrm{d},0}}d\tilde{\mathbf{u}}_{0,\alpha})]\,;
\end{aligned} \tag{B.9}$$

$$
\begin{aligned}
2d(\delta\rho_{\alpha 3}) &= (\delta\hat{\mathbf{u}}_{1,\alpha} + \mathcal{H}_{\Gamma_{\mathrm{d},0}}\delta\tilde{\mathbf{u}}_{1,\alpha})\cdot(d\hat{\mathbf{u}}_1 + \mathcal{H}_{\Gamma_{\mathrm{d},0}}d\tilde{\mathbf{u}}_1) \\
&\quad + (\delta\hat{\mathbf{u}}_1 + \mathcal{H}_{\Gamma_{\mathrm{d},0}}\delta\tilde{\mathbf{u}}_1)\cdot(d\hat{\mathbf{u}}_{1,\alpha} + \mathcal{H}_{\Gamma_{\mathrm{d},0}}d\tilde{\mathbf{u}}_{1,\alpha})\,; \\
2d(\delta\rho_{33}) &= -8\big[(\delta\hat{\mathbf{u}}_1 + \mathcal{H}_{\Gamma_{\mathrm{d},0}}\delta\tilde{\mathbf{u}}_1)\cdot\mathbf{d}\,(d\hat{w} + \mathcal{H}_{\Gamma_{\mathrm{d},0}}d\tilde{w}) \\
&\quad + (\delta\hat{w} + \mathcal{H}_{\Gamma_{\mathrm{d},0}}\delta\tilde{w})\mathbf{d}\cdot(d\hat{\mathbf{u}}_1 + \mathcal{H}_{\Gamma_{\mathrm{d},0}}d\tilde{\mathbf{u}}_1) \\
&\quad + w(\delta\hat{\mathbf{u}}_1 + \mathcal{H}_{\Gamma_{\mathrm{d},0}}\delta\tilde{\mathbf{u}}_1)\cdot(\hat{\mathbf{u}}_1 + \mathcal{H}_{\Gamma_{\mathrm{d},0}}\tilde{\mathbf{u}}_1)\big]\,.
\end{aligned}
\tag{B.9}
$$

These relations can be written as a function of the nodal degrees of freedom **a** and **b** and the internal degrees of freedom **p** and **q** by using the shape functions as defined in equations (3.44), (3.45) and (3.47).

$$
\begin{aligned}
2d(\delta\epsilon_{\alpha\beta}) &= (\delta\mathbf{a} + \mathcal{H}_{\Gamma_{\mathrm{d},0}}\delta\mathbf{b})^{\mathrm{T}}\mathbf{N}_{0,\alpha}^{\mathrm{T}}\mathbf{N}_{0,\beta}(d\mathbf{a} + \mathcal{H}_{\Gamma_{\mathrm{d},0}}d\mathbf{b}) \\
&\quad + (\delta\mathbf{a} + \mathcal{H}_{\Gamma_{\mathrm{d},0}}\delta\mathbf{b})^{\mathrm{T}}\mathbf{N}_{0,\beta}^{\mathrm{T}}\mathbf{N}_{0,\alpha}(d\mathbf{a} + \mathcal{H}_{\Gamma_{\mathrm{d},0}}d\mathbf{b})\,; \\
2d(\delta\epsilon_{\alpha 3}) &= (\delta\mathbf{a} + \mathcal{H}_{\Gamma_{\mathrm{d},0}}\delta\mathbf{b})^{\mathrm{T}}\mathbf{N}_{0,\alpha}^{\mathrm{T}}\mathbf{N}_{1}(d\mathbf{a} + \mathcal{H}_{\Gamma_{\mathrm{d},0}}d\mathbf{b}) \\
&\quad + (\delta\mathbf{a} + \mathcal{H}_{\Gamma_{\mathrm{d},0}}\delta\mathbf{b})^{\mathrm{T}}\mathbf{N}_{1}^{\mathrm{T}}\mathbf{N}_{0,\alpha}(d\mathbf{a} + \mathcal{H}_{\Gamma_{\mathrm{d},0}}d\mathbf{b})\,; \\
2d(\delta\epsilon_{33}) &= 2(\delta\mathbf{a} + \mathcal{H}_{\Gamma_{\mathrm{d},0}}\delta\mathbf{b})^{\mathrm{T}}\mathbf{N}_{1}^{\mathrm{T}}\mathbf{N}_{1}(d\mathbf{a} + \mathcal{H}_{\Gamma_{\mathrm{d},0}}d\mathbf{b})\,; \\
2d(\delta\rho_{\alpha\beta}) &= (\delta\mathbf{a} + \mathcal{H}_{\Gamma_{\mathrm{d},0}}\delta\mathbf{b})^{\mathrm{T}}\mathbf{N}_{1,\alpha}^{\mathrm{T}}\mathbf{N}_{0,\beta}(d\mathbf{a} + \mathcal{H}_{\Gamma_{\mathrm{d},0}}d\mathbf{b}) \\
&\quad + (\delta\mathbf{a} + \mathcal{H}_{\Gamma_{\mathrm{d},0}}\delta\mathbf{b})^{\mathrm{T}}\mathbf{N}_{0,\beta}^{\mathrm{T}}\mathbf{N}_{1,\alpha}(d\mathbf{a} + \mathcal{H}_{\Gamma_{\mathrm{d},0}}d\mathbf{b}) \\
&\quad + (\delta\mathbf{a} + \mathcal{H}_{\Gamma_{\mathrm{d},0}}\delta\mathbf{b})^{\mathrm{T}}\mathbf{N}_{0,\alpha}^{\mathrm{T}}\mathbf{N}_{1,\beta}(d\mathbf{a} + \mathcal{H}_{\Gamma_{\mathrm{d},0}}d\mathbf{b}) \\
&\quad + (\delta\mathbf{a} + \mathcal{H}_{\Gamma_{\mathrm{d},0}}\delta\mathbf{b})^{\mathrm{T}}\mathbf{N}_{1,\beta}^{\mathrm{T}}\mathbf{N}_{0,\alpha}(d\mathbf{a} + \mathcal{H}_{\Gamma_{\mathrm{d},0}}d\mathbf{b}) \\
&\quad - (\delta\mathbf{a} + \mathcal{H}_{\Gamma_{\mathrm{d},0}}\delta\mathbf{b})^{\mathrm{T}}\mathbf{C}_{\alpha}^{\mathrm{T}}\mathbf{N}_{1,\beta}(d\mathbf{a} + \mathcal{H}_{\Gamma_{\mathrm{d},0}}d\mathbf{b}) \\
&\quad - (\delta\mathbf{a} + \mathcal{H}_{\Gamma_{\mathrm{d},0}}\delta\mathbf{b})^{\mathrm{T}}\mathbf{C}_{\beta}^{\mathrm{T}}\mathbf{N}_{0,\alpha}(d\mathbf{a} + \mathcal{H}_{\Gamma_{\mathrm{d},0}}d\mathbf{b}) \\
&\quad - (\delta\mathbf{a} + \mathcal{H}_{\Gamma_{\mathrm{d},0}}\delta\mathbf{b})^{\mathrm{T}}\mathbf{N}_{0,\alpha}^{\mathrm{T}}\mathbf{C}_{\beta}(d\mathbf{a} + \mathcal{H}_{\Gamma_{\mathrm{d},0}}d\mathbf{b}) \\
&\quad - (\delta\mathbf{a} + \mathcal{H}_{\Gamma_{\mathrm{d},0}}\delta\mathbf{b})^{\mathrm{T}}\mathbf{N}_{0,\beta}^{\mathrm{T}}\mathbf{C}_{\alpha}(d\mathbf{a} + \mathcal{H}_{\Gamma_{\mathrm{d},0}}d\mathbf{b})\,; \\
2d(\delta\rho_{\alpha 3}) &= (\delta\mathbf{a} + \mathcal{H}_{\Gamma_{\mathrm{d},0}}\delta\mathbf{b})^{\mathrm{T}}\mathbf{N}_{1,\alpha}^{\mathrm{T}}\mathbf{N}_{1}(d\mathbf{a} + \mathcal{H}_{\Gamma_{\mathrm{d},0}}d\mathbf{b}) \\
&\quad + (\delta\mathbf{a} + \mathcal{H}_{\Gamma_{\mathrm{d},0}}\delta\mathbf{b})^{\mathrm{T}}\mathbf{N}_{1}^{\mathrm{T}}\mathbf{N}_{1,\alpha}(d\mathbf{a} + \mathcal{H}_{\Gamma_{\mathrm{d},0}}d\mathbf{b})\,; \\
2d(\delta\rho_{33}) &= (\delta\mathbf{a} + \mathcal{H}_{\Gamma_{\mathrm{d},0}}\delta\mathbf{b})^{\mathrm{T}}\mathbf{N}_{1}^{\mathrm{T}}\mathbf{d}\mathbf{N}_{w}(d\mathbf{a} + \mathcal{H}_{\Gamma_{\mathrm{d},0}}d\mathbf{b}) \\
&\quad + (\delta\mathbf{a} + \mathcal{H}_{\Gamma_{\mathrm{d},0}}\delta\mathbf{b})^{\mathrm{T}}\mathbf{N}_{w}^{\mathrm{T}}\mathbf{d}^{\mathrm{T}}\mathbf{N}_{1}(d\mathbf{a} + \mathcal{H}_{\Gamma_{\mathrm{d},0}}d\mathbf{b}) \\
&\quad + w(\delta\mathbf{a} + \mathcal{H}_{\Gamma_{\mathrm{d},0}}\delta\mathbf{b})^{\mathrm{T}}\mathbf{N}_{1}^{\mathrm{T}}\mathbf{N}_{1}(d\mathbf{a} + \mathcal{H}_{\Gamma_{\mathrm{d},0}}d\mathbf{b})\,,
\end{aligned}
\tag{B.10}
$$

where

$$
\mathbf{C}_{\alpha} = \bar{G}_{\alpha}^{1}\mathbf{N}_{0,1} + \bar{G}_{\alpha}^{2}\mathbf{N}_{0,2}\,. \tag{B.11}
$$

The incremental change of the virtual strains still refers to the covariant components. However, the stress components are referred to the local system $\mathbf{l}_j$. Hence, for the set-up of the stress dependent part of the stiffness matrix $\mathbf{K}^{\mathrm{g}}$ the factor ω^{ij} is introduced as:

$$\omega^{mn} = T_k^m T_l^n \boldsymbol{\sigma}_{kl} \,. \tag{B.12}$$

Elaboration of equations (B.10) and equation (B.12) gives the following matrices:

$$\begin{aligned}
\mathbf{A}_{uu}^{\mathrm{g}} =& \omega^{11}\mathbf{N}_{0,1}^{\mathrm{T}}\mathbf{N}_{0,1} + \omega^{22}\mathbf{N}_{0,2}^{\mathrm{T}}\mathbf{N}_{0,2} + \omega^{33}\mathbf{N}_{1}^{\mathrm{T}}\mathbf{N}_{1} \\
&+ \omega^{12}\left(\mathbf{N}_{0,1}^{\mathrm{T}}\mathbf{N}_{0,2} + \mathbf{N}_{0,2}^{\mathrm{T}}\mathbf{N}_{0,1}\right) \\
&+ \omega^{23}\left(\mathbf{N}_{0,2}^{\mathrm{T}}\mathbf{N}_{1} + \mathbf{N}_{1}^{\mathrm{T}}\mathbf{N}_{0,2}\right) + \omega^{13}\left(\mathbf{N}_{0,1}^{\mathrm{T}}\mathbf{N}_{1} + \mathbf{N}_{1}^{\mathrm{T}}\mathbf{N}_{0,1}\right) \\
&+ \zeta\omega^{11}\left(\mathbf{N}_{1,1}^{\mathrm{T}}\mathbf{N}_{0,1} + \mathbf{N}_{0,1}^{\mathrm{T}}\mathbf{N}_{1,1} - \mathbf{C}_{1}^{\mathrm{T}}\mathbf{N}_{0,1} - \mathbf{N}_{0,1}^{\mathrm{T}}\mathbf{C}_{1}\right) \\
&+ \zeta\omega^{22}\left(\mathbf{N}_{1,2}^{\mathrm{T}}\mathbf{N}_{0,2} + \mathbf{N}_{0,2}^{\mathrm{T}}\mathbf{N}_{1,2} - \mathbf{C}_{2}^{\mathrm{T}}\mathbf{N}_{0,2} - \mathbf{N}_{0,2}^{\mathrm{T}}\mathbf{C}_{2}\right) \\
&- \zeta\omega^{33}4w\mathbf{N}_{1}^{\mathrm{T}}\mathbf{N}_{1} \\
&+ \zeta\omega^{23}\left(\mathbf{N}_{1,2}^{\mathrm{T}}\mathbf{N}_{1} + \mathbf{N}_{1}^{\mathrm{T}}\mathbf{N}_{1,2}\right) + \zeta\omega^{13}\left(\mathbf{N}_{1,1}^{\mathrm{T}}\mathbf{N}_{1} + \mathbf{N}_{1}^{\mathrm{T}}\mathbf{N}_{1,1}\right) \\
&+ \zeta\omega^{12}\Big(\mathbf{N}_{1,1}^{\mathrm{T}}\mathbf{N}_{0,2} + \mathbf{N}_{1,2}^{\mathrm{T}}\mathbf{N}_{0,1} + \mathbf{N}_{0,1}^{\mathrm{T}}\mathbf{N}_{1,2} + \mathbf{N}_{0,2}^{\mathrm{T}}\mathbf{N}_{1,1} \\
&- \mathbf{C}_{1}^{\mathrm{T}}\mathbf{N}_{0,2} - \mathbf{C}_{2}^{\mathrm{T}}\mathbf{N}_{0,1} - \mathbf{N}_{0,1}^{\mathrm{T}}\mathbf{C}_{2} - \mathbf{N}_{0,2}^{\mathrm{T}}\mathbf{C}_{1}\Big) \,; \\
\mathbf{A}_{wu}^{\mathrm{g}} =& -\zeta\omega^{33}4\mathbf{N}_{w}^{\mathrm{T}}\mathbf{d}^{\mathrm{T}}\mathbf{N}_{1} \,; \\
\mathbf{A}_{uw}^{\mathrm{g}} =& -\zeta\omega^{33}4\mathbf{N}_{1}^{\mathrm{T}}\mathbf{d}^{\mathrm{T}}\mathbf{N}_{w} \,; \\
\mathbf{A}_{ww}^{\mathrm{g}} =& \mathbf{0} \,.
\end{aligned} \tag{B.13}$$

§ B.4 Assumed natural strains

It was noted by Parisch (1995) that the eight node shell element, which can be compared with an original four node shell element suffers from shear locking: the shear stiffness is overestimated. As proposed by Bathe and Dvorkin

(1986), an assumed natural strain approach is applied to overcome this problem. Here, the strain terms ϵ_{a3} are replaced by an alternative strain, determined in four tying points located at the mid-surface of the element as shown in figure 3.9. The strains are defined as:

$$\begin{aligned}\epsilon_{23} =& \chi_C \hat{\epsilon}^C_{23} + \chi_A \hat{\epsilon}^A_{23} + \mathcal{H}_{\Gamma_{\mathrm{d},0}}(\chi_C \tilde{\epsilon}^C_{23} + \chi_A \tilde{\epsilon}^A_{23})\,; \\ \epsilon_{13} =& \chi_B \hat{\epsilon}^B_{13} + \chi_D \hat{\epsilon}^D_{13} + \mathcal{H}_{\Gamma_{\mathrm{d},0}}(\chi_C \tilde{\epsilon}^B_{13} + \chi_A \tilde{\epsilon}^D_{13})\,.\end{aligned} \tag{B.14}$$

The virtual strains in tying point S can be written directly in terms of the regular and enhanced variational degrees of freedom $\delta\mathbf{a}$ and $\delta\mathbf{b}$:

$$2\delta\epsilon^S_{\alpha 3} = \mathbf{B}^{\mathrm{ANS}}_u \begin{bmatrix} \delta\mathbf{a}_J \\ \delta\mathbf{a}_K \\ \delta\mathbf{a}_L \\ \delta\mathbf{a}_M \end{bmatrix} + \mathcal{H}_{\Gamma_{\mathrm{d},0}} \mathbf{B}^{\mathrm{ANS}}_u \begin{bmatrix} \delta\mathbf{b}_J \\ \delta\mathbf{b}_K \\ \delta\mathbf{b}_L \\ \delta\mathbf{b}_M \end{bmatrix}, \tag{B.15}$$

where the superscripts J, K, L and M represent the nodes which span the side on which the sampling point S is located, see also Table B.1. The matrix $\mathbf{B}^{\mathrm{ANS}}_u$ replaces the terms that are related to the membrane strains ϵ_{13} and ϵ_{23} in equation (B.8) and is equal to:

$$\mathbf{B}^{\mathrm{ANS}}_u = \frac{1}{4}[(\mathbf{e}-\mathbf{d}), (-\mathbf{e}-\mathbf{d}), (\mathbf{e}+\mathbf{d}), (-\mathbf{e}+\mathbf{d})]^S\,, \tag{B.16}$$

where,

$$\mathbf{e}^S = \frac{1}{4}(-\mathbf{x}_J - \mathbf{x}_K + \mathbf{x}_L + \mathbf{x}_M)\,; \qquad \mathbf{d}^S = \frac{1}{4}(\mathbf{x}_J - \mathbf{x}_K + \mathbf{x}_L - \mathbf{x}_M)\,. \tag{B.17}$$

where for example, $\mathbf{x}_J$ is the position of node J in deformed configuration:

$$\mathbf{x}_J = \mathbf{X}_J + \mathbf{a}_J + \mathcal{H}_{\Gamma_{\mathrm{d},0}} \mathbf{b}_J\,. \tag{B.18}$$

Furthermore, the terms in the geometric part of the stiffness matrix $\mathbf{K}^{\mathrm{g}}$ in equation (3.69) that correspond to the shear stresses ω^{13} and ω^{23} are replaced

Point	**Coordinates**		**Corresponding nodes**			
	ξ	η	J	K	L	M
A	0.0	-1.0	5	1	6	2
B	1.0	0.0	6	2	7	3
C	0.0	1.0	8	4	7	3
D	-1.0	0.0	5	1	8	4

Table B.1 Position of tying points and the corresponding node numbers.

by:

$$\mathbf{K}^{\mathrm{g,ANS}} = \begin{bmatrix} \int_\Omega \mathbf{A}_{uu}^{\mathrm{ANS}} \mathrm{d}\Omega & \int_{\Omega^+} \mathbf{A}_{uu}^{\mathrm{ANS}} \mathrm{d}\Omega & \mathbf{0} & \mathbf{0} \\ \int_{\Omega^+} \mathbf{A}_{uu}^{\mathrm{ANS}} \mathrm{d}\Omega & \int_{\Omega^+} \mathbf{A}_{uu}^{\mathrm{ANS}} \mathrm{d}\Omega & \mathbf{0} & \mathbf{0} \\ \mathbf{0} & \mathbf{0} & \mathbf{0} & \mathbf{0} \\ \mathbf{0} & \mathbf{0} & \mathbf{0} & \mathbf{0} \end{bmatrix}, \tag{B.19}$$

where,

$$\mathbf{A}_{uu}^{\mathrm{ANS}} = \omega^{23}(\chi_B \mathbf{H}_{23}^B + \chi_D \mathbf{H}_{23}^D) + \omega^{13}(\chi_A \mathbf{H}_{13}^A + \chi_C \mathbf{H}_{13}^C)\,, \tag{B.20}$$

where $\mathbf{H}_{\alpha 3}^S$ represents the mapping matrices and is obtained by expanding the terms of the compact matrix $\bar{\mathbf{H}}_{\alpha 3}^S$ to the correct nodal degrees of freedom

according to Table B.1(Parisch 1995).

$$\bar{\mathbf{H}}^{S}_{\alpha 3} = \frac{1}{8}\begin{bmatrix} -\mathbf{I}_3 & \mathbf{0} & \mathbf{0} & \mathbf{I}_3 \\ \mathbf{0} & \mathbf{I}_3 & -\mathbf{I}_3 & \mathbf{0} \\ \mathbf{0} & -\mathbf{I}_3 & \mathbf{I}_3 & \mathbf{0} \\ \mathbf{I}_3 & \mathbf{0} & \mathbf{0} & -\mathbf{I}_3 \end{bmatrix}, \tag{B.21}$$

where $\mathbf{I}_3$ is a three-dimensional unit matrix.

Appendix C

A solution algorithm to solve an augmented system of equations

In the solution procedure as described in section 5.5, the system of equations is augmented with an additional degree of freedom, the load factor. The constraint equation that relates this additional unknown to the displacement degrees of freedom gives rise to an additional column and row in the Jacobian of the system, hence destroying the banded structure of the original matrix. The time needed to solve a system of equations with a direct solver increases with the width of the matrix. In the current situation, the time required to solve the augmented system would become undesirably long. In this section, an alternative procedure, where the banded structure of the matrix is not affected, is presented (Díez 1996, Gutiérrez and de Borst 1998).

§ C.1 General case

The augmented system of equilibrium equations as presented in (5.49) and (5.50) can be written in a general form as:

$$\mathbf{A}\mathbf{x} = \mathbf{y} \tag{C.1}$$

where $\mathbf{A}$ is the Jacobian of the system; $\mathbf{x}$ contains the unknowns and $\mathbf{y}$ is the right hand side:

$$\mathbf{A} = \begin{bmatrix} \mathbf{K} & \mathbf{h} \\ \mathbf{g}^{\mathrm{T}} & w \end{bmatrix} \; ; \qquad \mathbf{x} = \begin{bmatrix} \Delta\mathbf{d} \\ \Delta\lambda \end{bmatrix} \; ; \qquad \mathbf{y} = \begin{bmatrix} \mathbf{r} \\ q \end{bmatrix} \tag{C.2}$$

Here, $\mathbf{K}$ represents the non-singular stiffness matrix of the system with dimensions $N \times N$. The column vector $\mathbf{h}$, the row vector $\mathbf{g}$ and scalar w are defined in equation (5.50). Vector $\Delta\mathbf{d}$ contains the incremental displacement degrees of freedom (both regular and enhanced), $\Delta\lambda$ is the increment of the load factor. Finally, $\mathbf{r}$ denotes the residual force vector of the system and q can be found in equation (5.48).

In order to solve the augmented system of equations, the inverse of Jacobian $\mathbf{A}$ is needed. This inverse can be obtained by using the Sherman-Morrison formula for the evaluation of a non-singular matrix plus a rank 1 matrix:

$$\left(\mathbf{C} + \mathbf{u}\mathbf{v}^{\mathrm{T}}\right)^{-1} = \mathbf{C}^{-1} - \frac{\mathbf{C}^{-1}\mathbf{u}\mathbf{v}^{\mathrm{T}}\mathbf{C}^{-1}}{1 - \mathbf{v}^{\mathrm{T}}\mathbf{C}^{-1}\mathbf{u}}\,. \tag{C.3}$$

The Jacobian $\mathbf{A}$ of the augmented system can be written as the sum of four matrices $\mathbf{A}_i$, $i = 1..4$, according to:

$$\begin{bmatrix} \mathbf{K} & \mathbf{h} \\ \mathbf{g}^{\mathrm{T}} & w \end{bmatrix} = \begin{bmatrix} \mathbf{K} & \mathbf{0}_{N\times 1} \\ \mathbf{0}_{1\times N} & 1 \end{bmatrix} + \begin{bmatrix} \mathbf{0}_{N\times N} & \mathbf{h} \\ \mathbf{0}_{1\times N} & 0 \end{bmatrix} + \begin{bmatrix} \mathbf{0}_{N\times N} & \mathbf{0}_{N\times 1} \\ \mathbf{g}^{\mathrm{T}} & -1 \end{bmatrix} + \begin{bmatrix} \mathbf{0}_{N\times N} & \mathbf{0}_{N\times 1} \\ \mathbf{0}_{1\times N} & w \end{bmatrix}. \tag{C.4}$$

In this equation, $\mathbf{0}_{i\times j}$ represents a zero matrix with i rows and j columns. In order to be able to use the matrices in the Sherman-Morrison formula, the second, third and fourth term of the equation may be decomposed into a vector product:

$$\mathbf{A}_2 = \begin{bmatrix} \mathbf{h} \\ 0 \end{bmatrix} \begin{bmatrix} \mathbf{0}_{1\times N} & 1 \end{bmatrix} \;;\quad \mathbf{A}_3 = \begin{bmatrix} \mathbf{0}_{N\times 1} \\ 1 \end{bmatrix} \begin{bmatrix} \mathbf{g}^{\mathrm{T}} & -1 \end{bmatrix} \;;\quad \mathbf{A}_4 = \begin{bmatrix} \mathbf{0}_{N\times 1} \\ w \end{bmatrix} \begin{bmatrix} \mathbf{0}_{1\times N} & 1 \end{bmatrix}. \tag{C.5}$$

Using equation (C.3), the inverse of the two first terms of equation (C.5) can be obtained:

$$\mathbf{A}_{12}^{-1} = \left(\mathbf{A}_1 + \mathbf{A}_2\right)^{-1} = \begin{bmatrix} \mathbf{K}^{-1} & -\mathbf{K}^{-1}\mathbf{h} \\ \mathbf{0} & 1 \end{bmatrix}. \tag{C.6}$$

The inverse of the first three parts of the Jacobian can be expressed as:

$$\mathbf{A}_{123}^{-1} = \left(\mathbf{A}_1 + \mathbf{A}_2 + \mathbf{A}_3\right)^{-1} = \left(\mathbf{A}_{12} + \mathbf{A}_3\right)^{-1}. \tag{C.7}$$

Substitution of equation (C.6) yields:

$$\mathbf{A}_{123}^{-1} = \begin{bmatrix} \mathbf{K}^{-1} & \mathbf{0}_{N\times 1} \\ \mathbf{0}_{1\times N} & 1 \end{bmatrix} - \frac{1}{\mathbf{g}^{\mathrm{T}}\mathbf{K}^{-1}\mathbf{h}} \begin{bmatrix} \mathbf{K}^{-1}\mathbf{h}\mathbf{g}^{\mathrm{T}}\mathbf{K}^{-1} & -\mathbf{K}^{-1}\mathbf{h} \\ -\mathbf{g}^{\mathrm{T}}\mathbf{K}^{-1} & 1+\mathbf{g}^{\mathrm{T}}\mathbf{K}^{-1}\mathbf{h} \end{bmatrix}. \tag{C.8}$$

Similarly, the fourth term can be added to obtain the complete inverse of the Jacobian:

$$\mathbf{A}^{-1} = \begin{bmatrix} \mathbf{K}^{-1} & \mathbf{0}_{N\times 1} \\ \mathbf{0}_{1\times N} & 1 \end{bmatrix} - \frac{1}{\mathbf{g}^{\mathrm{T}}\mathbf{K}^{-1}\mathbf{h} - w} \begin{bmatrix} \mathbf{K}^{-1}\mathbf{h}\mathbf{g}^{\mathrm{T}}\mathbf{K}^{-1} & -\mathbf{K}^{-1}\mathbf{h} \\ -\mathbf{g}^{\mathrm{T}}\mathbf{K}^{-1} & 1+\mathbf{g}^{\mathrm{T}}\mathbf{K}^{-1}\mathbf{h} - w \end{bmatrix}. \tag{C.9}$$

Multiplying this equation by the right hand side vector $\mathbf{y}$, equation (C.2) and reordening gives the total solution of the augmented system.

$$\begin{bmatrix} \Delta\mathbf{d} \\ \Delta\lambda \end{bmatrix} = \begin{bmatrix} \mathbf{K}^{-1}\mathbf{r} \\ q \end{bmatrix} - \frac{1}{\mathbf{g}^{\mathrm{T}}\mathbf{K}^{-1}\mathbf{h} - w} \begin{bmatrix} \mathbf{K}^{-1}\mathbf{h}\mathbf{g}^{\mathrm{T}}\mathbf{K}^{-1}\mathbf{r} - \mathbf{K}^{-1}\mathbf{h}q \\ -\mathbf{g}^{\mathrm{T}}\mathbf{K}^{-1}\mathbf{r} + [1+\mathbf{g}^{\mathrm{T}}\mathbf{K}^{-1}\mathbf{h} - w]q \end{bmatrix}. \tag{C.10}$$

Note that in the equation above, the inverse of the stiffness matrix $\mathbf{K}$ is always multiplied by the vectors $\mathbf{r}$ or $\mathbf{h}$. These combinations can be replaced by the vectors $\mathbf{d}_I$ and $\mathbf{d}_{II}$, respectively, which can be obtained by solving the following two systems of equations.

$$\mathbf{K}\mathbf{d}_I = \mathbf{r}\,; \qquad \mathbf{K}\mathbf{d}_{II} = \mathbf{h}\,. \tag{C.11}$$

Substitution of $\mathbf{d}_I$ and $\mathbf{d}_{II}$ into equation (C.10) and introducing the scalar product notation yields:

$$\begin{bmatrix} \Delta\mathbf{d} \\ \Delta\lambda \end{bmatrix} = \begin{bmatrix} \mathbf{d}_I \\ q \end{bmatrix} - \frac{1}{\mathbf{g}\cdot\mathbf{d}_{II} - w} \begin{bmatrix} \mathbf{d}_{II}[\mathbf{g}\cdot\mathbf{d}_I - q] \\ -\mathbf{g}\cdot\mathbf{d}_I + [1+\mathbf{g}\cdot\mathbf{d}_{II} - w]q \end{bmatrix} \tag{C.12}$$

Hence, the total solution of the augmented system of equations is obtained by solving the two systems of equations (C.11). These equations share the same Jacobian with a relatively good band structure: the original stiffness matrix. When using a direct solver, this matrix needs to be decomposed only once. Since the decomposition of the matrix roughly takes about 90% of the total solution time, the current approach is considerable faster than solving the augmented system of equations in a single procedure.

§ C.2 Prescribed displacements

Alternatively, a specimen can be loaded by prescribing the displacements of a selected group of nodes. A technique to solve such an augmented system is presented by Verhoosel *et al.* (2006). The solution vector that contains all degrees of freedom, can be written as:

$$\mathbf{d} = \begin{bmatrix} \mathbf{d}_\mathrm{f} \\ \mathbf{d}_\mathrm{p} \end{bmatrix}, \tag{C.13}$$

where $\mathbf{d}_\mathrm{f}$ is a vector with length N_f representing the 'free' degrees of freedom, which are still part of the solution space, $\mathbf{d}_\mathrm{p}$ is a vector with length N_p denoting the prescribed degrees of freedom and $N_\mathrm{f} + N_\mathrm{p} = N$, where N is the total number of degrees of freedom. The prescribed degrees of freedom can be written in terms of a unit prescribed displacement vector $\bar{\mathbf{d}}_\mathrm{p}$ times the load factor λ, according to:

$$\mathbf{d}_\mathrm{p} = \lambda \bar{\mathbf{d}}_\mathrm{p} \,. \tag{C.14}$$

Accordingly, the augmented system of equations as presented in (5.50) can be written in terms of the free and prescribed degrees of freedom as well:

$$\begin{bmatrix} \mathbf{K}_\mathrm{ff} & \mathbf{K}_\mathrm{fp} & \mathbf{h}_\mathrm{f} \\ \mathbf{K}_\mathrm{pf} & \mathbf{K}_\mathrm{pp} & \mathbf{h}_\mathrm{p} \\ \mathbf{g}_\mathrm{f}^\mathrm{T} & \mathbf{g}_\mathrm{p}^\mathrm{T} & w \end{bmatrix} \begin{bmatrix} \Delta\mathbf{d}_\mathrm{f} \\ \Delta\mathbf{d}_\mathrm{p} \\ \Delta\lambda \end{bmatrix} = \begin{bmatrix} \mathbf{r}_\mathrm{f} \\ \mathbf{r}_\mathrm{p} \\ q \end{bmatrix}, \tag{C.15}$$

where $\Delta\mathbf{d}_\mathrm{p}$ can be replaced by, see equation (C.14):

$$\Delta\mathbf{d}_\mathrm{p} = \Delta\lambda \bar{\mathbf{d}}_\mathrm{p} \,. \tag{C.16}$$

These prescribed degrees of freedom can be eliminated from the system of equations by condensation:

$$\begin{bmatrix} \mathbf{K}_\mathrm{ff} & \mathbf{h}_\mathrm{f} \\ \mathbf{g}_\mathrm{f}^\mathrm{T} & w \end{bmatrix} \begin{bmatrix} \Delta\mathbf{d}_\mathrm{f} \\ \Delta\lambda \end{bmatrix} = \begin{bmatrix} \mathbf{r}_\mathrm{f} - \mathbf{K}_\mathrm{fp}(\Delta\lambda\bar{\mathbf{d}}_\mathrm{p}) \\ q - \mathbf{g}_\mathrm{p}^\mathrm{T}(\Delta\lambda\bar{\mathbf{d}}_\mathrm{p}) \end{bmatrix}. \tag{C.17}$$

A degree of freedom that is prescribed cannot be subjected to an external force, such that $\mathbf{g}_\mathrm{p} = \frac{1}{2}\lambda\bar{\mathbf{f}}_\mathrm{p}$ is equal to zero. As a result, the term $\mathbf{g}_\mathrm{p}^\mathrm{T}(\Delta\lambda\bar{\mathbf{d}}_\mathrm{p})$ in the right-hand-side of equation (C.17) is identical to zero too.

The condensed system of equations now has the same form as the system in equation (C.14) and the solution is identical to the one presented in equation (C.12), where:

$$\mathbf{d}_{I\mathrm{f}} = \mathbf{K}_{\mathrm{ff}}^{-1}\mathbf{r}_\mathrm{f} - \mathbf{K}_{\mathrm{ff}}^{-1}\mathbf{K}_{\mathrm{fp}}(\Delta\lambda\mathbf{d}_\mathrm{p})\,; \qquad \mathbf{d}_{II\mathrm{f}} = \mathbf{K}_{\mathrm{ff}}^{-1}\mathbf{h}_\mathrm{f}\,. \tag{C.18}$$

From an implementation point of view, the prescribed degrees of freedom are dealt with in the solver of the finite element code. The degrees of freedom that have a fixed value beforehand, are given as an input to the solver together with the Jacobian of the system and the right-hand-side vector. In this particular case, the final solution of the problem is composed of two vectors $\mathbf{d}_I$ and $\mathbf{d}_{II}$ which are obtained by solving two systems of equations independently. In the following derivation, the corresponding prescribed degrees of freedom $\mathbf{d}_{I\mathrm{p}}$ and $\mathbf{d}_{II\mathrm{p}}$ are obtained.

Consider a regular system of equations with a positive definite Jacobian $\mathbf{A}$ with dimensions $N \times N$ and a right hand side $\mathbf{y}$ that consists of a N_p prescribed degrees of freedom vector $\mathbf{x}_\mathrm{p}$:

$$\begin{bmatrix} \mathbf{A}_{\mathrm{ff}} & \mathbf{A}_{\mathrm{fp}} \\ \mathbf{A}_{\mathrm{pf}} & \mathbf{A}_{\mathrm{pp}} \end{bmatrix} \begin{bmatrix} \mathbf{x}_\mathrm{f} \\ \mathbf{x}_\mathrm{p} \end{bmatrix} = \begin{bmatrix} \mathbf{y}_\mathrm{f} \\ \mathbf{y}_\mathrm{p} \end{bmatrix}. \tag{C.19}$$

The solution $\mathbf{x}_\mathrm{f}$ of this system is equal to:

$$\mathbf{x}_\mathrm{f} = \mathbf{A}_{\mathrm{ff}}^{-1}\mathbf{y}_\mathrm{f} - \mathbf{A}_{\mathrm{ff}}^{-1}\mathbf{A}_{\mathrm{fp}}\mathbf{x}_\mathrm{p}\,. \tag{C.20}$$

When comparing this solution to the expression for $\mathbf{d}_{I\mathrm{f}}$, equation (C.18), it is clear that the corresponding prescribed term $\mathbf{d}_{I\mathrm{p}}$, which can be used as input to solve for $\mathbf{d}_{I\mathrm{f}}$, is equal to the total incremental prescribed displacement:

$$\mathbf{d}_{I\mathrm{p}} = \Delta\lambda\mathbf{u}_\mathrm{p}\,. \tag{C.21}$$

When comparing the solution in equation (C.19) with the expression for $\mathbf{d}_{II\mathrm{f}}$ in (C.18), it follows that:

$$\mathbf{d}_{II\mathrm{p}} = \mathbf{0}\,. \tag{C.22}$$

Bibliography

G. Alfano and M.A. Crisfield, 2001. Finite element interface models for the delamination analysis of laminated composites. *International Journal for Numerical Methods in Engineering*, 50 (7), 1701–1736.

O. Allix and A. Corigliano, 1999. Geometrical and interfacial non-linearities in the analysis of delamination in composites. *International Journal of Solids and Structures*, 36, 2189–2216.

O. Allix and P. Ladevèze, 1992. Interlaminar interface modelling for the prediction of delamination. *Composite Structures*, 22 (4), 235–242.

J.J.M. Arata, K.S. Kumar, W.A. Curtin, and A. Needleman, 2001. Crack growth in lamellar titanium aluminide. *International Journal of Fracture*, 111, 163–189.

H. Askes, 2000. *Advanced spatial discretisation strategies for localised failure - mesh adaptivity and meshless methods*. Dissertation, Delft University of Technology, Delft, The Netherlands.

H. Askes and A. Rodríguez-Ferran, 2001. A combined rh-adaptive scheme based on domain subdivision. Formulation and linear examples. *International Journal for Numerical Methods in Engineering*, 51 (3), 253–273.

I. Babuška and J.M. Melenk, 1997. The Partition of Unity Method. *International Journal for Numerical Methods in Engineering*, 40 (4), 727–758.

G.I. Barenblatt, 1962. The mathematical theory of equilibrium cracks in brittle fracture. *Advances in Applied Mechanics*, 7, 55–129.

K.J. Bathe, 1996. *Finite Element Procedures*. Upper Saddle River, NJ, USA, Prentice Hall, Inc.

K.J. Bathe and E. Dvorkin, 1986. A formulation of general shell elements - The use of mixed interpolation of tensorial components. *International Journal for Numerical Methods in Engineering*, 22 (3), 697–722.

T. Belytschko and T. Black, 1999. Elastic crack growth in finite elements with minimal remeshing. *International Journal for Numerical Methods in Engineering*, 45 (5), 601–620.

T. Belytschko, R.L. Chiapetta, and H.D. Bartel, 1976. Efficient large scale nonlinear transient analysis by finite elements. *International Journal for Numerical Methods in Engineering*, 10 (3), 579–596.

T. Belytschko, J. Fish, and B.E. Engelman, 1988. A finite element with embedded localization zones. *Computer Methods in Applied Mechanics and Engineering*, 70, 59–89.

T. Belytschko, Y. Krongauz, D. Organ, M. Fleming, and P. Krysl, 1996. Meshless methods: An overview and recent developments. *Computer Methods in Applied Mechanics and Engineering*, 193, 3–47.

T. Belytschko, W.K. Liu, and B. Moran, 2000. *Nonlinear Finite Elements for Continua and Structures*. England, John Wiley and Sons Ltd.

M. Bisschoff and E. Ramm, 1997. Shear deformable shell elements for large strains and rotations. *International Journal for Numerical Methods in Engineering*, 40 (23), 4427–4449.

J. Bisschop, 2002. *Drying shrinkage microcracking in cement-based materials*. Dissertation, Delft University of Technology, Delft, The Netherlands.

R. de Borst, 1987. Computation of post-bifurcation and post-failure behaviour of strain-softening solids. *Computers & Structures*, 25, 211–224.

R. de Borst and H.B. Muhlhaus, 1992. Gradient-dependent plasticity: formulation and algorithmic aspects. *International Journal for Numerical Methods in Engineering*, 35 (3), 521–539.

R. de Borst and J.J.C. Remmers, 2006. Computational modeling of delamination. *Composite Science and Technology*, 66 (6), 713–722.

R. de Borst, J.J.C. Remmers, and A. Needleman, 2006. Mesh-independent discrete numerical representations of cohesive-zone models. *Engineering Fracture Mechanics*, 73 (2), 160–177.

R. de Borst, J.J.C. Remmers, A. Needleman, and M.A. Abellan, 2004. Discrete vs smeared crack models for concrete fracture: Bridging the gap. *International Journal for Numerical and Analytical Methods in Geomechanics*, 28 (7-8), 583–607.

O.J. Bosker, 1998. Growth of debonds in Glare, Part I (no moisture absorption). Technical Report B2V-98-24, Delft University of Technology.

O.J. Bosker, 2000. Growth of debonds in Glare, Part II (with moisture absorption). Technical Report B2V-00-08, Delft University of Technology.

K.B. Broberg, 1999. *Cracks and Fracture*. San Diego, CA, USA, Acedemic Press.

G.T. Camacho and M. Ortiz, 1996. Computational modelling of impact damage in brittle materials. *International Journal of Solids and Structures*, 33, 2899–2938.

P.P. Camanho, C.G. Davila, and M.F. de Moura, 2003. Numerical simulation of mixed-mode progressive delamination in composite materials. *Journal of composite materials*, 37 (16), 1415–1438.

H.H.M. Cleveringa, E. van der Giessen, and A. Needleman, 2001. A Discrete Dislocation Analysis of Rate Effects on Mode I Crack Growth. *Materials Science and Engineering A*, 317, 37–43.

D. Coker, A.J. Rosakis, and A. Needleman, 2003. Dynamic crack growth along a polymer composite-homalite interface. *Journal of the Mechanics and Physics of Solids*, 51 (3), 425–460.

R.J. Cope, P.V. Rao, L.A. Clark, and P. Norris, 1980. Modelling of reinforced concrete behaviour for finite element analysis of bridge slabs. In *Numerical Methods for Non-Linear Problems.*, C. Taylor, E. Hinton, and D.R.J. Owen, Eds., 457–470. Pineridge Press, Swansea.

M.A. Crisfield, 1982. Accelerated solution techniques and concrete cracking. *Computer Methods in Applied Mechanics and Engineering*, 33 (1-3), 585–607.

C. Daux, N. Moës, J. Dolbow, N. Sukumar, and T. Belytschko, 2000. Arbitrary branched and intersecting cracks with the extended finite element method. *International Journal for Numerical Methods in Engineering*, 48 (12), 1741–1760.

M.S. Daw, 1990. The embedded atom method: a review. *Many-Atom Interactions in Solids, Spring Proceedings in Physics*, 48, 49–63.

V.S. Deshpande, A. Needleman, and E. van der Giessen, 2003a. Scaling of discrete dislocation predictions for near-threshold fatigue crack growth. *Acta Materialia*, 51 (15), 4637–4651.

V.S. Deshpande, A. Needleman, and E. van der Giessen, 2003b. Finite strain dislocation plasticity. *Journal of the Mechanics and Physics of Solids*, 51, 2057–2083.

B. Devincre and L.P. Kubin, 1994. Simulation of forest interactions and strain-hardening in fcc crystals. *Modelling and Simulation in Materials Science and Engineering*, 2 (3A), 559–570.

P. Díez, 1996. *Un nuevo estimador de error para el método de los elementos finitos*. Dissertation, Universidad Politécnica de Cataluña.

D.S. Dugdale, 1960. Yielding of steel sheets containing slits. *Journal of the Mechanics and Physics of Solids*, 8, 100–108.

M.L. Falk, A. Needleman, and J.R. Rice, 2001. A critical evaluation of cohesive zone models of dynamic fracture. *Journal de Physique IV*, 11 Pr5, 43–50.

D. Farkas, M. Duranduru, W.A. Curtin, and C. Ribbens, 2001. Multiple-dislocation emission from the crack tip in the ductile fracture of Al. *Phylosofical Magazine A*, 81 (5), 1241–1255.

L.B. Freund, 1998. *Dynamic Fracture Mechanics*. Cambridge, Cambridge University Press.

H.J. Gao, 1993. Surface roughening and branching instabilities in dynamic fracture. *Journal of the Mechanics and Physics of Solids*, 41, 457–486.

M.G.D. Geers, 1999a. Enhanced solution control for physically and geometrically non-linear problems. Part I- The subplane control method. *International Journal for Numerical Methods in Engineering*, 46 (2), 177–204.

M.G.D. Geers, 1999b. Enhanced solution control for physically and geometrically non-linear problems. Part I- Comparative performance analysis. *International Journal for Numerical Methods in Engineering*, 46 (2), 205–230.

E. van der Giessen and A. Needleman, 1995. Discrete dislocation plasticity - a simple planar model. *Modelling and Simulation in Materials Science and Engineering*, 3 (5), 689–735.

Y. Goto, Y. Watanaber, T. Kasugai, and M. Obata, 1992. Elastic Buckling Phenomenon Applicable to Deployable Rings. *International Journal of Solids and Structures*, 27 (7), 893–909.

A.A. Griffith, 1920. The phenomena of rupture and flow in solids. *Phylosophical Transactions*, 221, 163–198.

P. A. Guidault, O. Allix, L. Champaney, and C. Cornuault, 2006. A micro-macro partition of unity method for crack propagation. In *Proceedings of ECF 16 - 16th European Conference of Fracture*, Alexandroupolis, Greece.

M.A. Gutiérrez, 2004. Energy release control for numerical simulations of failure in quasi-brittle solids. *Communications in Numerical Methods in Engineering*, 20, 19–29.

M.A. Gutiérrez and R. de Borst, 1998. Studies in material parameter sensitivity of softening solids. *Computer Methods in Applied Mechanics and Engineering*, 162, 337–350.

F. Hashagen, 1998. *Numerical Analysis of Failure Mechanisms in Fibre Metal Laminates*. Dissertation, Delft University of Technology, Delft, The Netherlands.

F. Hashagen and R. de Borst, 2001. Enhancement of the Hoffman yield criterion with an anisotropic hardening model. *Composite Structures*, 79 (6), 637–651.

F. Hashagen, R. de Borst, and T.J. de Vries, 1999. Delamination behavior of spliced Fiber Metal Laminates. Part 2. Numerical investigation. *Composite Structures*, 46 (2), 147–162.

A. Hillerborg, M. Modeér, and P.E. Petersson, 1976. Analysis of crack formation and crack growth in concrete by means of fracture mechanics and finite elements. *Cement and Concrete Research*, 6, 773–782.

J.P. Hirth and J. Lothe, 1982. *Theory of Dislocations*. John Wiley & Sons Inc, 2nd Edition.

P.A. Hooijmeijer and O.J. Bosker, 2000. Debond Growth in Glare under compression and tension fatigue loading and elevated temperature. Technical Report B2V-00-61, Delft University of Technology.

J.W. Hutchinson and A.G. Evans, 2000. Mechanics of materials: top–down approaches to fracture. *Acta Materialia*, 48, 125–135.

C.E. Inglis, 1913. Stresses in a plate due to the presence of cracks and sharp corners. *Transactions of the Institute of Naval Architects*, 55, 219–241.

A.R. Ingraffea and V. Saouma, 1985. Numerical modelling of discrete crack propagation in reinforced and plain concrete. In *Fracture Mechanics of Concrete*, 171–225. Martinus Nijhoff Publishers, Dordrecht.

G.R. Irwin, 1957. Analysis of stresses and strains near the end of a crack traversing a plate. *J. Appl. Mech.-T.ASME*, 24, 361–364.

M. Jirásek, 1998. Embedded crack models for concrete fracture. In *EURO-C 1998 Computer Modelling of Concrete Structures*, 291–300, Rotterdam. Balkema.

T.W. de Jong, E. Kroon, and J. Sinke, 2001. Formability. In *Fibre Metal Laminates an Introduction*, A. Vlot and J.W. Gunnink, Eds., hoofdstuk 22, 337–354. Kluwer Academic Publishers, Dordrecht, The Netherlands.

L.M. Kachanov, 1988. *Delamination Buckling of Composite Materials*. Dordrecht, The Netherlands, Kluwer Academic Publishers.

J.F. Kalthoff and A. Bürgel, 2004. Influence of loading rate on shear fracture toughness for failure mode transition. *International Journal of Impact Engineering*, 30, 957–971.

J.K. Kalthoff and S. Winkler, 1988. Failure mode transition at high rates of loading. In *Proceedings of the International Conference on Impact Loading and Dynamic Behaviour of Materials*, 43–56. Deutsche Gesellshaft für Metallkunde.

P.A. Klein, J.W. Foulk, E.P. Chen, S.A. Wimmer, and H.J. Gao, 2001. Physics based modelling of brittle fracture: cohesive formulations and the application of meshfree methods. *Theoretical and Applied Fracture Mechancics*, 37, 99–166.

S. Klinkel, F. Gruttmann, and W. Wagner, 1999. A continuum based three-dimensional shell element for laminated structures. *Computers & Structures*, 71(1), 43–62.

H.A.J. Knops, 1994. *Numerical Simulation of Crack Growth in Pressurized Fuselages*. Dissertation, Delft University of Technology, Delft, The Netherlands.

V. Kouznetsova, M.G.D. Geers, and W.A.M. Brekelmans, 2002. Multi-scale constitutive modelling of heterogeneous materials with a gradient-enhanced computational homogenization scheme. *International Journal for Numerical Methods in Engineering*, 54 (8), 1235–1260.

E. Kuhl, E. Ramm, and R. de Borst, 2000. An anisotropic gradient damage model for quasi-brittle materials. *Computer Methods in Applied Mechanics and Engineering*, 183, 87–103.

J. Lemaitre and J.L. Chaboche, 1990. *Mechanics of Solid Materials*. Cambridge, UK, Cambridge University Press.

S.F. Li, W.K. Liu, A.J. Rosakis, T. Belytschko, and W. Hao, 2002. Mesh free Galerkin simulation of dynamic shear band propagation and failure mode transition. *International Journal of Solids and Structures*, 39, 1213–1240.

L.E. Malvern, 1969. *Introduction to the mechanics of a continuous meduium*. Prentice Hall, Inc.

R. Marissen, 1988. *Fatigue crack growth in Arall a hybrid aluminium-aramid composite material*. Dissertation, Delft University of Technology, Delft, The Netherlands.

J.J. Mason, A.J. Rosakis, and G. Ravichandran, 1994. Full field measurements of the dynamic deformation field around a growing adiabatic shear band at the tip of a dynamically loaded crack or notch. *Journal of the Mechanics and Physics of Solids*, 42, 1679–1697.

J. Mazars, 1984. *Application de la mécanique de l'endommagement au comportement non linéaire et à la rupture du béton de structure*. Dissertation, Université Paris VI, Paris, France.

J. Mazars and G. Pijaudier-Cabot, 1989. Continuum damage theory – application to concrete. *ASCE Journal of Engineering Mechanics*, 115, 345–365.

J.G.M. van Mier, 1997. *Fracture Processes of Concrete*. Boca Raton, Florida, CRC Press.

N. Moës and T. Belytschko, 2002. Extended finite element method for cohesive crack growth. *Engineering Fracture Mechanics*, 69, 813–833.

N. Moës, M. Cloirec, P. Cartraud, and J.F. Remacle, 2003. A computational approach to handle complex microstructure geometries. *Computer Methods in Applied Mechanics and Engineering*, 192 (28-30), 3163–3177.

N. Moës, J. Dolbow, and T. Belytschko, 1999. A Finite Element Method for Crack Growth without Remeshing. *International Journal for Numerical Methods in Engineering*, 46 (1), 131–150.

N. Moës, A. Gravouil, and T. Belytschko, 2002. Non-planar 3D crack growth by the extended finite element and level sets - Part I: Mechanical model. *International Journal for Numerical Methods in Engineering*, 53 (11), 2549–2568.

E.A. Munts, S.J. Hulshoff, and R. de Borst, 2003. The partition-of-unity method for linear diffusion and convection problems: accuracy, stabilization and multiscale interpretation. *International Journal for Numerical Methods in Fluids*, 43 (2), 199–213.

F.R.N. Nabarro, 1967. *Theory of Crystal Dislocations*. Oxford, Oxford University Press.

P.M. Naghdi, 1972. The theory of shells and plates. In *Encyclopedia of physics*, S. Flügge, Eds., deel VIa/2. Springer-Verlag, Berlin/Heidelberg/New York.

A. Needleman, 1987. A continuum model for void nucleation by inclusion debonding. *Journal of Applied Mechanics*, 54, 525–531.

A. Needleman and V. Tvergaard, 1995. Analysis of a brittle-ductile transition under dynamic shear loading. *International Journal of Solids and Structures*, 32, 2571–2590.

D. Ngo and A.C. Scordelis, 1967. Finite element analysis of reinforced concrete beams. *Journal of the American Concrete Institute*, 64, 152–163.

R.W. Ogden, 1984. *Non-Linear Elastic Deformations*. Ellis Horwood Limited.

M. Ortiz, Y. Leroy, and A. Needleman, 1987. A finite element method for localized failure analysis. *Computer Methods in Applied Mechanics and Engineering*, 61, 189–214.

K.D. Papoulia, S.H. Sam, and S.A. Vavasis, 2003. Time-continuous cohesive interface finite elements in explicit dynamics. *International Journal for Numerical Methods in Engineering*, 58 (5), 679–701.

H. Parisch, 1995. A Continuum-Based Shell Theory for Non-Linear Applications. *International Journal for Numerical Methods in Engineering*, 38 (11), 1855–1883.

K.C. Park, 1975. An Improved Stiffly Stable Method for Direct Integration of Nonlinear Structural Dynamic Equations. *Journal of Applied Mechanics*, 42, 464–470.

R.H.J. Peerlings, R. de Borst, W.A.M. Brekelmans, and M.G.D. Geers, 1998. Gradient-enhanced modelling of concrete fracture. *Mechanics of Cohesive-frictional Materials*, 3, 323–342.

R.H.J. Peerlings, R. de Borst, W.A.M. Brekelmans, and H.P.J. de Vree HPJ, 1996. Gradient-enhanced damage for quasi-brittle materials. *International Journal for Numerical Methods in Engineering*, 39 (19), 3391–3403.

G. Pijaudier-Cabot and Z.P. Bažant, 1987. Nonlocal damage theory. *ASCE Journal of Engineering Mechanics*, 113, 1512–1533.

W.H. Press, B.P. Flannery, and W.T. Vetterling S.A. Teukolsky, 1988. *Numerical Recipes in C : The Art of Scientific Computing*. Cambridge University Press.

E. Ramm, 1981. Strategies for tracing ther nonlinear response near limit points. In *Nonlinear finite element analysis in Structural Mechanics*, W. Wunderlich, E. Stein, and K.J. Bathe, Eds. Springer, Berlin.

Y.R. Rashid, 1968. Analysis of reinforced concrete pressure vessels. *Nuclear Engineering and Design*, 7, 334–344.

K. Ravi-Chandar, 1995. On the failure mode transitions in polycarbonate under dynamic mixed-mode loading. *International Journal of Solids and Structures*, 32, 925–938.

K. Ravi-Chandar and W.G. Knauss, 1984. An experimental investigation into dynamic fracture: I: Crack initiation and arrest. *International Journal of Fracture*, 25 (4), 247–262.

G. Rebel, 1998. *Finite Rotation Shell Theory Including Drill Rotations and its Finite Element Implementation*. Dissertation, Delft University of Technology, Delft, The Netherlands.

J.J.C. Remmers, G.N. Wells, and R. de Borst, 2001. Analysis of delamination growth with discontinuous finite elements. In *Proceedings of the second European Conference on Computational Mechanics*, Cracow. CDROM.

J.J.C. Remmers and R. de Borst, 2001a. Numerical Modelling: Delamination buckling. In *Fibre Metal Laminates - an introduction*, A. Vlot and J.W. Gunnink, Eds., 281–297, Dordrecht. Kluwer Academic Publishers.

J.J.C. Remmers and R. de Borst, 2001b. Delamination Buckling in Fibre-Metal Laminates. *Composite Science and Technology*, 61 (15), 2207–2213.

J.J.C. Remmers, R. de Borst, and A. Needleman, 2003a. A cohesive segments method for the simulation of crack growth. *Computational Mechanics*, 31, 69–77.

J.J.C. Remmers, G.N. Wells, and R. de Borst, 2003b. A discontinuous solid-like shell element for arbitrary delaminations. *International Journal for Numerical Methods in Engineering*, 58 (13), 2013–2040.

J. Réthoré, A. Gravouil, and A. Combescure, 2005. An energy-conserving scheme for dynamic crack growth using the extended finite element method. *International Journal for Numerical Methods in Engineering*, 63 (5), 631–659.

J.R. Rice, 1968. A path independent integral and the approximate analysis of strain concentrations by notches and cracks. *Journal of Applied Physics*, 35, 379–386.

E. Riks, 1979. An incremental approach to the solution of snapping and buckling problems. *International Journal of Solids and Structures*, 15, 529–551.

E. Riks and C.C. Rankin, 1997. Computer simulation of the buckling behavior of thin shells under quasi static loads. *Archives of computational methods in engineering*, 4 (4), 325–351.

S. Rinderknecht, 1994. *Delamination in Faserverbundplatten, ein vereinfachtes Berechnungsmodell*. Dissertation, Universität Stuttgart, Stuttgart, Germany.

G.H.J.J. Roebroeks, 1997. Aircraft Fire Safety. In *AGARD Conference Proceedings 587*, 26/1–26/13. AGARD.

J.G. Rots, 1986. Strain-softening analysis of concrete fracture specimens. In *Fracture Toughness and Fracture Energy of Concrete.*, F.H. Wittman, Eds., 137–148, Amsterdam. Elsevier Sciennce Publishers.

J. Rots, 1988. *Computational modelling of concrete fracture*. Dissertation, Delft University of Technology, Delft, The Netherlands.

J.G. Rots, 1991. Smeared and discrete representations of localized fracture. *International Journal of Fracture*, 51, 45–59.

J.C.J. Schellekens and R. de Borst, 1993. On the numerical integration of interface elements. *International Journal for Numerical Methods in Engineering*, 36 (1), 43–66.

J.C.J. Schellekens, 1992. *Computational Strategies for Composite Structures*. Dissertation, Delft University of Technology, Delft, The Netherlands.

J.C.J. Schellekens and R. de Borst, 1993. A nonlinear finite-element approach for the analysis of mode-I free edge delamination in composites. *International Journal of Solids and Structures*, 30 (9), 1239–1253.

J.C.J. Schellekens and R. de Borst, 1994. Free edge delamination in carbon-epoxy laminates: a novel numerical/experimental approach. *Composite Structures*, 28, 357–373.

J.H.A. Schipperen, 2000. Mixed Mode Delamination in Graphite-Epoxy Prepregs: A Numerical Analysis. In *Proceedings of ECCOMAS*, Barcelona.

J.H.A. Schipperen and R. de Borst, 2001. A numerical analysis of mixed-mode delamination in carbon-epoxy prepregs. *Composite Structures*, 54 (4), 445–451.

E. Schlangen, 1993. *Experimental ad numerical analysis of fracture processes in concrete*. Dissertation, Delft University of Technology, Delft, The Netherlands.

L.E. Shilkrot, R.E. Miller, and W.A. Curtin, 2004. Multiscale plasticity modeling: coupled atomistics and discrete dislocation mechanics. *Journal of the Mechanics and Physics of Solids*, 52 (4), 755–787.

K.N. Shivakumar and J.D. Whitcomb, 1985. Buckling of a sublaminate in a quasi-isotropic composite laminates. *Journal of Composite Materials*, 19, 2–18.

J.C. Simo and D.D. Fox, 1989. On a stress resultant geometrically exact shell model, Part I: Formulation and Optimal representation. *Computer Methods in Applied Mechanics and Engineering*, 72, 267–304.

J.C. Simo, J. Oliver, and F. Armero, 1993. An analysis of strong discontinuities induced by softening relations in rate-independent solids. *Computational Mechanics*, 12, 277–296.

A. Simone, J.J.C. Remmers, and G.N. Wells, 2001. An interface element based on the partition of unity. Technical Report CM2001-007, Delft University of Technology, Delft, The Netherlands.

A. Simone and L.J. Sluys, 2004. The use of displacement discontinuities in a rate-dependent medium. *Computer Methods in Applied Mechanics and Engineering*, 193 (27-29), 3015–3033.

M.G.A. Tijssens, L.J. Sluys, and E. van der Giessen., 2001. Simulation of fracture in cementitious composites with explicit modeling of microstructural features. *Engineering Fracture Mechanics*, 68, 1245–1263.

G. Ventura, B. Moran, and T. Belytschko, 2005. Dislocations by partition of unity. *International Journal for Numerical Methods in Engineering*, 62 (11), 1463–1487.

M.L.C.E. Verbruggen, 1986. Aramid Reinforced Aluminium Laminates: ARALL, Adhesion problems and environmental effects. Technical Report LR 503, Delft University of Technology.

C.V. Verhoosel, J.J.C. Remmers, and M.A. Gutiérrez, 2006. The energy release control arc-length method for the simulation of brittle and ductile fracture. *in preparation*.

A. Vlot, 1991. *Low velocity impact loading in fibre reinforced aluminium laminates and other aircraft sheet materials*. Dissertation, Delft University of Technology, Delft, The Netherlands.

A. Vlot, 2001. Historical Overview. In *Fibre Metal Laminates an Introduction*, A. Vlot and J.W. Gunnink, Eds., hoofdstuk 1, 3–22. Kluwer Academic Publishers, Dordrecht, The Netherlands.

L.B. Vogelesang, J. Schijve, and R. Fredell, 1995. Fibre-metal laminates: damage tolerant aerospace materials. *Case Studies in Manufacturing with Advanced Materials*, 2, 253–271.

G.N. Wells, R. de Borst, and L.J. Sluys, 2002. A consistent geometrically nonlinear approach for delamination. *International Journal for Numerical Methods in Engineering*, 54 (9), 1333–1355.

G.N. Wells, J.J.C. Remmers, L.J. Sluys, and R. de Borst, 2003. A large strain discontinuous finite element approach to laminated composites. In *IUTAM symposium on computational mechanics of solid materials at large strains*, 355–364, Stuttgart.

G.N. Wells and L.J. Sluys, 2001a. A new method for modelling cohesive cracks using finite elements. *International Journal for Numerical Methods in Engineering*, 50 (12), 2667–2682.

G.N. Wells and L.J. Sluys, 2001b. Three-dimensional embedded discontinuity model for brittle fracture. *International Journal of Solids and Structures*, 38 (5), 897–913.

G.N. Wells, L.J. Sluys, and R. de Borst, 2002. Simulating the propagation of displacement discontinuities in a regularized strain-softening medium. *International Journal for Numerical Methods in Engineering*, 53 (5), 1235–1256.

Q.Z. Xiao and B.L. Karihaloo, 2006. Improving the accuracy of XFEM crack field using higher order quadrature and statically admissible stress recovery. *International Journal for Numerical Methods in Engineering*, 66 (9), 1378–1410.

X.P. Xu and A. Needleman, 1993. Void nucleation by inclusion debonding in a crystal matrix. *Modelling and Simulation in Materials Science and Engineering*, 1, 111–132.

X.P. Xu and A. Needleman, 1994. Numerical simulations of fast crack growth in brittle solids. *Journal of the Mechanics and Physics of Solids*, 42, 1397–1434.

X.P. Xu and A. Needleman, 1996. Numerical simulations of dynamic crack growth along an interface. *International Journal of Fracture*, 74, 289–324.

Summary

Discontinuities in materials and structures

A unifying computational approach

Joris J.C. Remmers

In order to arrive at an efficient and safe design of structures, a complete understanding of the behaviour of the materials, including their failure mechanisms, is a requisite. These failure mechanisms can be studied at different levels of observation. On the structural level, fracture can be regarded as a single crack or defect, which propagates through the material or along an interface under the action of external forces. On smaller levels of observation, the area ahead of the apparent crack tip, the process zone, contains a collection of micro-cracks that nucleate, grow and coalescence in order to form the dominant crack. The mechanisms that cause nucleation of micro-separations in the process zone can be traced back to even smaller levels of observation. In crystalline solids such as metals, the collective glide of dislocations in the atomic structure gives rise to small imperfections at the free edges of the material, which in turn trigger the nucleation of micro-separations.

From a mathematical point of view, interface cracks, interacting micro-separations in the process zone and slip planes created by gliding dislocations can be considered as jumps in the displacement field of the specimen. This is in contradiction with the assumption stated in classical formulations, in which the material is regarded as a continuum with smooth displacement fields. A possible solution to this is to smear out displacement jumps. In some

cases however, this technique cannot be used. In brittle materials, where the process zone is relatively narrow compared to the structural dimensions, neglecting the discontinuous nature of a crack leads to numerical deficiencies. In finite strain discrete dislocation models, the effect of smearing the displacement jump gives rise to spurious stresses in the surrounding material.

An alternative is to model the discontinuous displacement fields explicitly by exploiting the partition of unity property of finite element shape functions. In this approach, the displacement jump is represented by adding a second displacement field multiplied with a step function on top of the existing base field. The second displacement field is supported by additional sets of degrees of freedom, which are added to the existing nodes of the finite element mesh.

This approach has a number of advantages, in particular for the analysis of crack growth in a cohesive surface framework. First, the discontinuity can be introduced and extended irrespective of the structure of the underlying finite element mesh. This enables the simulation of crack propagation in arbitrary directions and avoids the use of initial cohesive dummy stiffnesses to model a perfect bond prior to cracking. Moreover, since the new degrees of freedom are added to existing nodes, the topology of the finite element mesh does not change. Finally, the computational effort remains relatively small since the system is only augmented when the crack propagates.

In this thesis, the partition of unity method has been implemented to analyse fracture processes at various levels of observation. In chapter 3, a discontinuous solid-like shell element has been presented that allows for the simulation of delamination growth. The kinematic relations of the original solid-like shell element are chosen such that the element can be used to model very thin structures. In the discontinuous solid-like shell element, these kinematic relations are meticulously enhanced to incorporate a displacement jump. It has been demonstrated that the new element inherits the advantageous properties of the original solid-like shell element. It can even be used to analyse delamination buckling growth in a bi-layer material with only one element in thickness direction. In chapter 4, the discontinuous solid-like shell element has been used to study the delamination buckling behaviour of fibre-metal laminates under various loading conditions.

In chapter 5 the partition of unity method has been extended to the cohesive segments method that allows for the simulation of the nucleation, growth

and coalescence of multiple interacting cracks. In this chapter, special attention is paid to a solution technique that is able to solve this highly nonlinear system of equations. To this end, the energy release control path-following method has been used, in which the constraint equation is based on the maximum energy dissipation of the system.

Diffuse fracture phenomena also play an important role in dynamic fracture. In chapter 6, the application of the cohesive segments method for transient simulations is discussed. The stability and accuracy of the explicit time integration scheme is investigated in detail. It has been demonstrated that adding degrees of freedom during a simulation does not affect the energy balance of the system. However, it is not possible to use a diagonal mass matrix to solve the system of equations. By lumping the mass matrix, information regarding the coupling of regular and additional degrees of freedom is lost. The performance of the method is demonstrated in a dynamic shear failure example. The method appears to be able to capture both the cleavage as well as the adiabatic shear failure mode. The possibility to capture crack branching has been shown in a second example. Unfortunately, due to the averaging technique to determine the stress at the tip of a segment, the nucleation of a new segment is biased over the propagation of an existing segment, which hampers a quantitative analysis.

In principle, the partition of unity method is a suitable candidate to incorporate the discontinuous fields generated by dislocations in the finite element solution. Unfortunately, this appears to be inefficient for a number of reasons. Since a typical model consists of hundreds of interacting dislocations with long range effects, the number of additional degrees of freedom would become very large. In addition, it is questionable whether the resolution of the mesh is sufficient to model dislocation pile-up correctly.

In the method that is proposed in chapter 7, the deformation gradient is split into an elastic part and an unbounded part related to the slip displacement. The regular part of the displacement field generated by dislocations is dealt with in the same way as the original small strain discrete dislocation models, albeit in an incremental fashion. The creation of new surfaces at free edges is taken into account, which provides a firm basis for the combined analysis of micro-crack nucleation driven by dislocation glide.

Samenvatting

Discontinuiteiten in materialen en constructies

Een generaliserende numerieke benadering

Joris J.C. Remmers

Om tot een efficiënt en veilig ontwerp van constructies te komen is een volledig begrip van het materiaal gedrag, inclusief het bezwijkgedrag, vereist. Dit bezwijkgedrag kan worden bestudeerd op verschillende lengteschalen. Op het niveau van de constructie is het bezwijken zichtbaar als een enkele scheur die zich voortplant door het materiaal of langs een grensvlak. Op lagere schaalniveau's blijkt echter dat het gebied voor de scheur tip, de proces zone, bestaat uit een verzameling microscheuren die door samengroeien een dominante scheur vormen. Het mechanisme dat het ontstaan van deze microscheuren veroorzaakt, kan worden herleid naar nog lagere schaalniveau's. In kristallijne materialen zoals metalen, leidt het collectief bewegen van dislocaties tot kleine imperfecties aan de vrije rand van het materiaal. Deze imperfecties geven op hun beurt weer aanleiding tot het ontstaan van microscheuren.

Vanuit een wiskundig oogpunt kunnen scheuren langs grensvlakken, microscheuren in de proces zone en schuifvlakken ten gevolge van het verplaatsen van dislocaties worden beschouwd als sprongen in het verplaatsingsveld. Dit is in tegenspraak met de klassieke formuleringen in de mechanica, waarin wordt aangenomen dat het materiaal een continuüm en het verplaatsingsveld glad is. Een mogelijke oplossing is om het effect van de discontinuïteit

uit te smeren over een bepaalde breedte, zodanig dat het verplaatsingsveld zijn continue karakter behoudt. In sommige gevallen kan echter niet voor deze aanpak worden gekozen. In brosse materialen, waarin de proces zone relatief smal is, leidt dit onherroepelijk tot numerieke problemen. In het geval van een eindige rek formulering in een discreet dislocatie model geeft het uitsmeren van de sprong in het verplaatsingsveld aanleiding tot oneigenlijke spanningen in het omliggende materiaal.

Eén van de alternatieven om het discontinue verplaatsingsveld expliciet te modelleren is door gebruik te maken van de 'partition of unity' eigenschap van standaard eindige elementen interpolatie-functies. In deze aanpak wordt de sprong in het verplaatsingsveld gerepresenteerd door een tweede verplaatsingsveld, vermenigvuldigd met een stap functie, toe te voegen aan het bestaande basis veld. Dit tweede verplaatsingsveld wordt ondersteund door extra vrijheidsgraden die worden toegevoegd aan de reeds bestaande knooppunten van het eindige elementen rooster.

Deze benadering heeft een aantal voordelen, in het bijzonder voor het modelleren van scheurgroei met behulp van de cohesieve zone formulering. Op de eerste plaats kan de discontinuïteit op elke gewenste positie in het model worden toegevoegd of uitgebreid, ongeacht de structuur van het onderliggende eindige elementen rooster. Hierdoor is het mogelijk om scheurvoortplanting in willekeurige richtingen te simuleren en wordt het gebruik van initiële cohesieve stijfheden voorkomen. Bovendien blijft de oorspronkelijke topologie van het eindige elementen rooster behouden omdat de nieuwe vrijheidsgraden worden toegevoegd aan bestaande knooppunten. Tenslotte is de methode relatief goedkoop omdat er enkel vrijheidsgraden worden toegevoegd als de scheur zich ook daadwerkelijk voortplant.

In dit proefschrift is de partition of unity methode gebruikt om scheurgroeiprocessen op verschillende lengteschalen te analyseren. In hoofdstuk 3 wordt een discontinu 'solid-like shell' element gepresenteerd waarmee het mogelijk is om delaminatiegroei langs een grensvlak in een laminaat te analyseren. De kinematische relaties van het oorspronkelijke solid-like shell element zijn zodanig gekozen dat het element gebruikt kan worden om zeer dunne constructies mee te modelleren. In het discontinue solid-like shell element zijn deze kinematische relaties zorgvuldig uitgewerkt zodat ze een discontinu verplaatsingsveld representeren. Het is aangetoond dat dit nieuwe element

dezelfde gunstige eigenschappen heeft als het oorspronkelijke element. Het kan zelfs gebruikt worden om delaminatie-knik in een laminaat te analyseren door slechts één element in de dikte-richting te gebruiken. In hoofdstuk 4 is het discontinue solid-like shell element gebruikt om het delaminatie-knik gedrag van vezel-metaal laminaten voor verschillende belastingen te bestuderen.

In hoofdstuk 5 is de partition of unity methode omgevormd tot de cohesieve segmenten methode die in staat is om zowel het ontstaan, het groeien en het samengroeien van meerdere microscheuren te modelleren. Hierbij is in het bijzonder aandacht geschonken aan een techniek die in staat is om dit niet-lineaire stelsel vergelijkingen op een efficiënte manier op te lossen. Hier is gekozen voor een padvolg methode die stuurt op de maximale energie dissipatie van het systeem.

Diffuse scheurpatronen spelen ook een belangrijke rol in snelle scheurvoortplanting. In hoofdstuk 6 wordt de toepassing van de cohesieve segmenten methode voor transiënte berekeningen besproken. Met name de stabiliteit en de nauwkeurigheid van de methode is uitgebreid bestudeerd. Het wordt aangetoond dat het toevoegen van vrijheidsgraden tijdens een simulatie geen invloed heeft op de energie balans van het systeem. Het blijkt echter niet mogelijk te zijn om een diagonale massa matrix te gebruiken bij het oplossen van het stelsel vergelijkingen. Door de massa matrix te diagonaliseren gaat de informatie over de koppeling van reguliere en additionele vrijheidsgraden verloren.

De eigenschappen van het model worden gedemonstreerd in een dynamische afschuif scheurgroei voorbeeld. De methode is in staat om zowel mode-I scheurgroei als adiabatische mode-II scheurvorming te kunnen beschrijven. De mogelijkheid om scheurvertakking te modelleren is besproken in een tweede voorbeeld. Het is echter moeilijk om deze berekening op waarde te schatten. Door het middelen van de spanningen in de buurt van de scheur tip, is de creatie van een nieuw segment eenvoudiger dan het groeien van een bestaand segment.

In principe is de partition of unity methode een geschikte manier om de discontinue velden veroorzaakt door dislocaties in het eindige elementen model te beschrijven. Dit blijkt echter erg inefficiënt te zijn. Omdat een standaard model uit honderden dislocaties kan bestaan en de effecten van een disloca-

tie op grote afstand merkbaar zijn, zou het aantal extra vrijheidsgraden dat nodig is om deze effecten op een juiste manier te representeren zeer groot worden. Bovendien is het maar de vraag of de resolutie van het eindige elementen rooster voldoende is om het effect van opgestapelde dislocaties, een zogenaamde 'pile-up', met voldoende nauwkeurigheid te representeren.

In de alternatieve methode die wordt gepresenteerd in hoofdstuk 7 is de vervormingsgradiënt gesplitst in een elastisch deel en een onbegrensd deel dat de afschuif sprong vertegenwoordigt. Het reguliere gedeelte van het verplaatsingsveld dat gegenereerd wordt door de dislocaties wordt op dezelfde manier beschreven als in de conventionele, kleine rek formulering, zij het op een incrementele manier. Het ontstaan van nieuwe oppervlakken aan de vrije randen van het proefstuk is ook beschouwd. Het model biedt daarom een goede basis voor een gecombineerde analyse van het ontstaan van de door dislocatie veroorzaakte microscheuren.

Curriculum Vitæ

JORIS JOHANNES CORNELIS REMMERS

born May 28, 1974 in Tilburg, The Netherlands

Since July 2006:	Assistant Professor, Faculty of Aerospace Engineering, Delft University of Technology.
Jan. 2003 - June 2006:	Research Associate, Faculty of Aerospace Engineering, Delft University of Technology.
Jan. 1999 - Dec. 2002:	Ph.D. Candidate, Faculty of Aerospace Engineering, Delft University of Technology.
Sept. 1997 - June 1998:	Student Assistant at the Faculty of Aerospace Engineering, Delft University of Technology.
Sept. 1992 - Oct. 1998:	M.Sc. Aerospace Engineering, Delft University of Technology. Graduation thesis on the development of a nonlinear beam element and the simulation of mode-jumping.
Sept. 1986 - June 1992:	VWO, Cobbenhagen College, Tilburg.